*Plasma Physics Reports, Vol. 31, No. 1, 2005, pp. 1–2. Translated from Fizika Plazmy, Vol. 31, No. 1, 2005, pp. 3–5.*


# 30th Anniversary of Our Journal

The journal *Fizika plazmy* (*Plasma Physics Reports*, the former *Soviet Journal of Plasma Physics*) was founded in 1975, almost a quarter of century after the beginning of studies (May, 1951) on magnetic confinement of high-temperature plasmas with the aim of producing controlled thermonuclear reactions (initially, for military purposes). The founders of this field of research, A.D. Sakharov and I.E. Tamm, planned to produce tritium for hydrogen bombs in the deuterium plasma of a controlled fusion reactor. Soon after V.L. Ginzburg proposed using lithium in thermonuclear weapons (lithium nuclei decay into helium and tritium nuclei under the action of neutrons), the studies on controlled fusion reactors switched to peaceful purposes. However, investigations aimed at military purposes continued in the Soviet Union, the United States, and Great Britain under the higher classification code. The studies on controlled nuclear fusion (CNF) began to be declassified only after I.V. Kurchatov's report *On the Possibility of Producing Thermonuclear Reactions in a Gas Discharge* (Harwell, 1956). At the subsequent Symposium on Electromagnetic Phenomena in Cosmical Physics (Stockholm, 1956) and the Third International Conference on Phenomena in Ionized Gazes (Venice, 1957), the presented reports allowed the participants to guess those who worked on the CNF problem. The first papers of English and American scientists on this problem were published in the January issue of *Nature* for 1957, in connection with the sensational results achieved in Harwell in the ZETA toroidal device (later, the optimistic interpretation of these results turned out to be erroneous).

The year 1957 was successful for the development of science in Russia. An epochal event was the launch of the first satellite. A large synchrophasotron—an accelerator with a perimeter of 200 m—was put into operation, thus confirming the self-phasing mechanism discovered by V.I. Veksler. This opened the way for substantially increasing the energy of elementary particles and, thereby, for penetrating into the very fundamentals of nature. In response to Harwell's report by Kurchatov, the Unites States proposed holding the international conference on CNF in Geneva in 1958. To demonstrate their advances in this area, the American scientists presented full-scale operable experimental devices. The culmination of the conference was L. Spitzer's stellarator. A remarkable advantage of this toroidal magnetic confinement system is that, in contrast to the ZETA and tokamak-type systems, no plasma current is required to be excited in it (note that the term *tokamak* was proposed by I.N. Golovin at the end of 1957, but it came into use much later). However, the results on plasma confinement achieved in American stellarators appeared to be unsuccessful. Over the next ten years, this was attributed to anomalous diffusion and/or the inevitable Bohm diffusion.

Nevertheless, in spite of pessimistic expectations of some scientists, the field of CNF research expanded considerably after the Geneva conference. It was decided to hold regular International Conferences on Plasma Physics and Controlled Nuclear Fusion Research. The first such conference was held in Salzburg in 1962; the second, in London in 1965; the third, in Novosibirsk in 1968; the fourth, in Madison in 1971; and the fifth, in Kyoto in 1974 (subsequent conferences were held every two years). The scope of investigations on CNF in the Soviet Union in these years may be glimpsed from the summarizing theoretical reviews published in the first eight volumes of *Reviews of Plasma Physics* edited by M.A. Leontovich. Over fifteen years, different methods of plasma confinement (including high-frequency methods) were tested in the Soviet Union and the United States.

Since 1965, the studies in the T-3 tokamak began to show progress in plasma confinement and heating. At the 1968 Novosibirsk Conference, it was reported that an electron temperature of about 1 keV in the T-3 tokamak had been attained. In 1969, English scientists performed local Thomson-scattering measurements of the temperature in T-3 and confirmed that high plasma temperature had actually been attained. As a result, studies on magnetic fusion research concentrated mainly on tokamaks.

To intensify research on plasma physics in the Soviet Union, M.S. Rabinovich, the head of the Plasma Physics Laboratory at the Lebedev Physical Institute of the USSR Academy of Sciences, proposed creating the Academic Scientific Council on the Complex Problem "Plasma Physics" and to found the journal *Fizika Plazmy*. At that time, there were the following journals on CNF and plasma physics:

*Physics of Fluids*, an American journal founded in 1958 (on the basis of the plasma subjects, a separate journal *Physics of Plasmas* was then formed in 1994);

*Plasma Physics–Accelerator–Thermonuclear Research*, a European journal founded in 1958 (since 1984, it has been published under the title *Plasma Physics and Controlled Fusion*);

*Nuclear Fusion*, an IAEA journal founded in 1960; and

1063-780X/05/3101-0001$26.00 

*Journal of Plasma Physics*, an English journal founded in 1960.

Rabinovich worked under the leadership of Veksler and took part in performing the calculations for the motion of charged particles in accelerators. After theoretical studies for the Dubna synchrophasotron had been successfully completed in 1957, he recognized the importance of the CNF problem and switched to it. He organized studies on magnetic plasma confinement in a stellarator with a circular magnetic axis at the Lebedev Physical Institute (in contrast to the racetrack geometry of the Princeton C stellarator with a two- and three-pole windings on the semicircular segments of the system). At the beginning of 1960s, Kurchatov, the leader of the Soviet thermonuclear program, initiated stellarator studies at the Kharkov Institute for Physics and Technology. Among the institutions involved in CNF research, there were also the Institute of Nuclear Fusion (Novosibirsk), the Ioffe Physicotechnical Institute (Leningrad), the Leningrad Polytechnic Institute, the Sukhumi Physicotechnical Institute, the Institute of Applied Physics (Nizhni Novgorod), and the Institute of Plasma Physics (Kiev). In 1960s, the program on inertial confinement fusion (including laser fusion) was initiated. In the course of investigations, a variety of possible plasma applications (in addition to the CNF problem) were revealed: the idea arose of using plasma to directly transform heat into electric energy, plasmochemistry and relativistic plasma electronics started to develop, the plasma processing of metals came into use, compact plasma thrusters for space vehicles were created, etc. Plasma physics incorporated certain fields of atomic and molecular physics. All these plasma applications initiated the development of specific plasma diagnostics. Interest in the studies and applications of this fourth state of matter naturally resulted in the foundation of the academic journal *Fizika plazmy*, and M.S. Rabinovich became its first editor-in-chief.

The first volume of *Fizika plazmy* appeared in 1975. In the fifth issue of this volume, the remarkable paper by B.B. Kadomtsev *Disruption Instability in Tokamaks* was published. This paper stimulated a large number of studies on active plasma processes in nuclear fusion devices. Along with papers by Soviet scientists, the journal also published those by foreign authors. Special issues were devoted to the jubilees of scientists that had greatly contributed to plasma physics. Unfortunately, Rabinovich, the founder of our journal, died after an extended illness in 1982.

Over thirty years, the scope of our journal progressively expanded. Problems similar to those that arise in investigating magnetized plasma in fusion devices also appear in studying highly ionized space plasma. For example, giant magnetic tubes floating to the surface of the Sun are generated in its interior. When the ends of such two tubes (visible as sun spots) with oppositely directed magnetic fields approach one another, the magnetic field annihilates and its energy is transformed into a plasma particle flow that crumples the Earth's magnetosphere, thus creating a magnetic storm.

In recent years, technological problems of microelectronics have stimulated the development of dusty plasma physics. It turned out that micron-size dust grains immersed in plasma acquire an enormous electric charge. For this reason, the properties of the ambient plasma can change radically even at a relatively low dust concentration. Moreover, the interaction between dust grains appears to be very strong, so the dust is frequently in a liquid or crystalline state. This makes it possible to study phase transformations on a kinetic level. In this way, concepts characteristic of the physics of condensed states were introduced in plasma physics. Our journal has devoted much attention to the problems of dusty plasma from the very beginning of the development of this branch of plasma physics.

To give an idea of the scope of our journal, we list its rubrics (in the alphabetic order):

Beams in Plasma, Charged Particle Motion, Charged Plasma, Dusty Plasma, Elementary Processes in Plasma, Ion and Plasma Sources, Ionospheric Plasma, Isotope Separation, Laser Plasma, Low-Temperature Plasma, Magnetic Confinement Systems, Magnetohydrodynamics, Magnetospheric Plasma, Nonideal Plasma, Nonlinear Phenomena, Particle Acceleration in Plasma, Plasma Accelerators, Plasma Diagnostics, Plasma Dynamics, Plasma Electronics, Plasma Instability, Plasma Kinetics, Plasma Optics, Plasma Oscillations and Waves, Plasma Turbulence, Plasma–Wall Interactions, Radiation in Plasma, Solid-State Plasma, Space Plasma, Stellarators, Symmetries and Conservation Laws, Thermonuclear Plasma, Tokamaks, Transport Processes, and Wall Plasma.

Because of the complexity of high-temperature plasma physics, it has always been impossible to foresee the rate of progress toward a controlled fusion reactor. Nevertheless, the information obtained over long years of tokamak studies has made it possible to begin construction of the large international tokamak experimental reactor (ITER) over the following decade. At the same time, the further development of plasma physics will definitely require even more profound investigations into this state of matter so prevalent in nature and its various applications.

*Editorial Board*

*Plasma Physics Reports, Vol. 31, No. 1, 2005, pp. 14–25. Translated from Fizika Plazmy, Vol. 31, No. 1, 2005, pp. 17–29.*


**STELLARATORS**

# Steady Solutions to Neoclassical Transport Equations and the Absence of Bifurcated States

**L. M. Kovrizhnykh**

*Prokhorov Institute of General Physics, Russian Academy of Sciences, ul. Vavilova 38, Moscow, 119991 Russia*

Received July 22, 2004; in final form, August 19, 2004

**Abstract**—The question of whether two-valued solutions can exist for an ambipolar electric field in stellarators and rippled tokamaks is considered. Steady solutions to transport equations in the limit of infrequent collisions are obtained in the purely neoclassical transport theory (that is, without allowance for possible anomalous losses). It is shown that, given the particle and heat sources, these equations have only one steady continuous solution, i.e., the steady states are nonbifurcating. © *2005 Pleiades Publishing, Inc.*

## 1. INTRODUCTION

In the classical theory of transport processes, the electron and ion diffusion coefficients are independent of the ambipolar electric field $E$ and the magnitude of this field is unambiguously determined by the ambipolarity condition, which implies that the electric current component normal to the magnetic surface equals zero. In neoclassical theory, however, the diffusion coefficients (as well as the thermal conductivity) in the limit of infrequent collisions depend on the electric field $E$ (see, e.g., [1, 2]). As a result, the ambipolarity condition yields a cubic (rather than linear) equation for the field $E$. In a certain range of plasma density and electron and ion plasma temperatures, this equation can have three different steady solutions, $E_3 \le E_2 \le E_1$, two of which, $E_1$ and $E_3$, are stable and one of which, $E_2$, is unstable. On the other hand, since the condition for the existence of three real solutions depends on the values of the plasma parameters, which, in turn, are functions of the minor radius $r$,[1] it may be that the solutions $E_1$ and $E_2$ vanish (or, more precisely, become complex) at a certain radius $r = r_1$; as a result, in the region $r > r_1$, there exists only one real solution $E_3$. Thus, it might well be possible that, along with the stable solution $E_3$, there also exists a solution that coincides with $E_1$ and with $E_3$ in the regions $r < r_1$ and $r > r_1$, respectively, and, at the boundary between these regions, jumps from one solution to another (this issue will be addressed in more detail in Section 3).

The possible existence of two-valued solutions for the ambipolar electric field was pointed out as early as 1969 in one of the first papers by the author on the neoclassical transport theory [3], but the relevant phenomenon (it seems appropriate to call it the bifurcation of the steady state) has long been deprived of attention. Interest in it has been revived by the discovery of improved confinement regimes and by subsequent attempts to explain L–H transitions theoretically. Indeed, in view of the stabilizing role of the shear of poloidal plasma rotation, it is tempting to connect the L- and H-regimes with the existence of the above two-valued solutions for the ambipolar electric field. Attempts to explain L–H transitions on the basis of such two-valued solutions for the field $E$ were made in quite a number of papers (see review [4] and the literature cited therein).

In the author's opinion, however, these attempts are physically unjustified because a more careful analysis shows that two-valued solutions (and especially discontinuity solutions) for the ambipolar electric field do not exist. We have now to see why the assertion that there can exist bifurcated steady states is incorrect. First of all, the ambipolarity equation was solved under the assumption that it permits discontinuous solutions for the electric field $E$. However, this assumption is in conflict with the continuity equations (i.e., the diffusion and heat conduction equations). The reason is that, at magnetic surfaces at which the field $E$ undergoes discontinuous jumps, the particle and energy fluxes also turn out to be discontinuous and, accordingly, the particle and heat sources at these surfaces should have singularities of the δ-function type, which is, however, hardly possible from the physical point of view. Such discontinuous solutions arise because the ambipolarity equation was solved under the assumption that the plasma density and temperature are prescribed functions of radius and are independent of the ambipolar electric field. As a result, depending on the initial conditions, the ambipolarity equation admits *an infinite set of solutions, each having a jump discontinuity at any arbitrary number of prechosen points.* Also noteworthy is the fact that to each of these solutions correspond *their own* particle and heat sources. Consequently, even if, for prescribed density and temperature profiles, the ambipolarity equation has two continuous solutions,

[1] In what follows, the cross sections of the magnetic surfaces will be assumed, for simplicity, to be circles of radius $r$.

there is no bifurcation because the two corresponding plasma states refer to *different particle and heat sources.* Finally, it is not a priori obvious that the transport equations admit steady solutions with arbitrarily chosen density and temperature profiles.

Another method for finding steady solutions without producing discontinuous ones consists in simultaneously solving the ambipolarity equation, diffusion equation, and heat conduction equation for prescribed particle and heat sources. Such a self-consistent solution will be obtained below (see Section 4), and it will be shown that, in a steady state, the ambipolar electric field is a two-valued function of radius. The stability analysis of these two solutions (see Section 5) shows, however, that only one of them is stable. Hence, *in purely neoclassical transport theory, the steady solutions are nonbifurcating*, and, in order to explain the existence of L- and H-regimes, it is necessary to go beyond the scope of neoclassical theory and to invoke some other physical processes.

The paper is organized as follows. In Section 2, the basic equations are presented and the model used to describe transport coefficients is discussed. In Section 3, the solutions to the ambipolarity equation are analyzed for prescribed profiles of the plasma density and plasma temperatures. It is shown that, in a certain range of density and temperatures, this equation admits solutions having a discontinuity at any arbitrary number of prechosen magnetic surfaces. The number of discontinuities and their positions are determined by the initial magnitude of the electric field; moreover, the particle and heat sources that correspond to each of these solutions are different. In Section 4, an analysis is made of a complete set of time-independent transport equations that consists of the ambipolarity equation, as well as of the equations for the electric field $E$, plasma density, and plasma temperatures. Also, expressions for the steady-state ambipolar electric field as a function of the plasma density and plasma temperatures and of the particle and heat sources are presented. Section 5 is devoted to analyzing the stability of the solutions derived in Section 4. It is shown that, of the two steady solutions, only one is stable, namely, that corresponding to the weaker ambipolar electric field. The final section summarizes the results obtained and presents the main conclusions.

## 2. BASIC EQUATIONS

We are interested in toroidal confinement systems such as a conventional stellarator in which the helical magnetic field is specified by a single harmonic with an amplitude equal to $\varepsilon x^l B_0$, where $x = r/r_0$ with $r_0$ being the radius of the plasma column, $l$ is the number of helical field periods along the poloidal direction, and $B_0$ is the toroidal magnetic field. However, if we set $l = 0$ in the formulas presented below, then we arrive at the results that are also valid for a rippled tokamak, because the transport coefficients for a conventional stellarator and for a rippled tokamak exhibit the same functional dependence on the electric field, plasma density, and plasma temperatures. We assume that the ions are singly charged. We also restrict ourselves to considering a regime in which collisions are sufficiently infrequent for the main contribution to the transport coefficients to come from locally trapped particles; it is in this case that the ambipolarity equation can lead to two-valued solutions for the ambipolar electric field.

Under these assumptions, the set of equations describing the spatiotemporal behavior of the particle density $N(x, t)$, electron and ion temperatures $T_j(x, t)$ ($j = e, i$), and ambipolar electric field $E$ can be written in the form

$$S_e = S_i, \tag{1}$$

$$\frac{\partial \rho}{\partial \tau} + \frac{1}{x}\frac{\partial}{\partial x} x(S_j - S^{\text{ext}}) = 0, \tag{2}$$

$$1.5\frac{\partial(\rho t_j)}{\partial \tau} + \frac{1}{x}\frac{\partial}{\partial x} x(\Pi_j - \Pi_j^{\text{ext}}) = 0. \tag{3}$$

Here, $\rho = N/N_0$ is the dimensionless density, $t_j = T_j/T_0$ stands for the dimensionless electron ($j = e$) and ion ($j = i$) temperatures, and $\tau = \omega_0 t$ is the time in units of $\omega_0^{-1}$ (the definition of the frequency $\omega_0$ will be given below, after formula (11)). The values of $N_0$ and $T_0$ are arbitrary; they can be chosen to equal, say, the density and temperature of one of the components of the plasma at its boundary (i.e., at $x = 1$). The functions $S^{\text{ext}}(x, t)$ and $\Pi_j^{\text{ext}}(x, t)$ account for the external particle and heat sources and are related to the density of the particles injected into the plasma per unit time, $\delta N/\delta t$, and to the energy density absorbed by the electrons and ions, $\delta W/\delta t$, through the following obvious relationships:

$$\frac{\delta N}{\delta t} = \frac{N_0\omega_0}{x}\frac{\partial}{\partial x} x S^{\text{ext}}(x), \tag{4}$$

$$\frac{\delta W_j}{\delta t} = \frac{N_0 T_0 \omega_0}{x}\frac{\partial}{\partial x} x \Pi_j^{\text{ext}}(x). \tag{5}$$

The dimensionless particle and heat fluxes, $S_j$ and $\Pi_j$, have the form[2]

$$S_j = -D_j\left(\frac{\rho'}{\rho} + b_j^{(1)}\frac{t_j'}{t_j} - \frac{e_j}{e_i}\frac{V}{t_j}\right) + D_0\rho\frac{\partial V}{\partial \tau}\frac{e_j m_j}{e_i m_i}, \tag{6}$$

$$\Pi_j = -K_j\left(\frac{\rho'}{\rho} + b_j^{(2)}\frac{t_j'}{t_j} - \frac{e_j}{e_i}\frac{V}{t_j}\right) + 1.5D_0\rho t_j\frac{\partial V}{\partial \tau}\frac{e_j m_j}{e_i m_i}, \tag{7}$$

[2] As usual, we assume that the transverse dielectric constant $\varepsilon_\perp = 4\pi m_i c^2 N B_0^{-2}$ is much larger than unity; here, $m_i$ is the mass of an ion and $c$ is the speed of light.

where the prime denotes the derivative with respect to the dimensionless radial coordinate $x$ and $e_j$ and $m_j$ are the charge and mass of a plasma particle of species $j$.

The first terms on the right-hand sides of formulas (6) and (7) account for diffusive particle and energy fluxes. The second terms, which are proportional to the time derivatives of the dimensionless ambipolar electric field, $V = e_i r_0 E/T_0$, describe convective particle and energy fluxes associated with the polarization currents. In what follows, by virtue of the smallness of the electron-to-ion mass ratio $m_e/m_i$, we will ignore the electron polarization current. The coefficient in the last terms on the right-hand sides of formulas (6) and (7) is small, $D_0 = (\rho_L/r_0)^2 \ll 1$; it is defined as the squared ratio of the ion gyroradius $\rho_L$ at the temperature $T_0$ to the plasma radius $r_0$. The expressions for the diffusion coefficients $D_j$ and thermal conductivities $K_j$ can be written as

$$D_i = \frac{x^{2-0.5l}\rho^2 t_i^{0.5}}{V_i^2 + u^2\rho^2 t_i^{-3} x^{2-2l}}, \quad (8)$$

$$D_e = \frac{\mu x^{2-0.5l}\rho^2 t_e^{0.5}}{V_e^2 + 0.9\mu^2 u^2\rho^2 t_e^{-3} x^{2-2l}}, \quad (9)$$

$$K_i = \frac{2.25 x^{2-0.5l}\rho^2 t_i^{1.5}}{V_i^2 + 0.46 u^2\rho^2 t_i^{-3} x^{2-2l}}, \quad (10)$$

$$K_e = \frac{2.1\mu x^{2-0.5l}\rho^2 t_e^{1.5}}{V_e^2 + 0.38\mu^2 u^2\rho^2 t_e^{-3} x^{2-2l}}. \quad (11)$$

These expressions were obtained by approximating more exact formulas presented in [5]. The approximations were constructed for different limits in the collision frequency $\nu$ in such a way that, for $\nu \longrightarrow 0$ and $\nu \longrightarrow \infty$, expressions (8)–(11) pass over to the corresponding expressions obtained in [5]. Here, $V_j = V + \varepsilon l x^{l-1} t_j e_j/e_i$, $u = \sqrt{0.2}\,\nu_0/(\varepsilon\omega_i D_0)$, $\nu_0$ is the ion–ion collision frequency at a density $N_0$ and temperature $T_0$, $\omega_i$ is the ion gyrofrequency at a temperature $T_0$, $\omega_0 = 1.34 r_0^2 \nu_0/(R^2\varepsilon^{0.5})$, $R$ is the major radius of the torus, and $\mu = 2.41(m_i/m_e)^{0.5} \cong 102$. The coefficients $b_j^{(1,2)}$ in expressions (6) and (7) for the particle and energy fluxes are not generally constant; their values depend on the relationship between the first and second terms in the denominators in the expressions for $D_j$ and $K_j$. Thus, for plasma parameters such that the first terms, $V_j^2$, predominate over the second ones, we have

$$b_i^{(1)} \cong 0.75, \quad b_e^{(1)} \cong 0.6, \quad b_i^{(2)} \cong 1.4, \quad b_e^{(2)} \cong 1.44.$$

In the opposite case, i.e., when the first terms can be ignored in comparison to the second ones, the coefficients are

$$b_i^{(1)} \cong 3.4, \quad b_e^{(1)} \cong 3.84, \quad b_i^{(2)} \cong 4.5, \quad b_e^{(2)} \cong 4.4.$$

As will be clear later, the first terms in the denominators are dominant for the ion plasma component, while the second play the dominant role for the electron plasma component. So, for further analysis, we set

$$b_i^{(1)} \cong 0.75, \quad b_i^{(2)} \cong 1.4, \quad b_e^{(1)} \cong 3.84, \quad b_e^{(2)} \cong 4.4.$$

However, the numerical values of these coefficients do not change the final conclusions of this study. Note also that expressions (6)–(11) for the fluxes coincide qualitatively with those presented in the review by Fujisawa [4].

It should also be pointed out that, if we express the temperature $T_0$, magnetic field $B_0$, and radii $R$ and $r_0$ in keV, T, and cm, respectively, the density $N_0$ being expressed in units of $10^{13}$ cm$^{-3}$, then we can introduce the dimensionless quantities $D_0 = 0.104\, T_0 r_0^{-2} B_0^{-2}$ and $u = 1.42 \times 10^{-5} r_0^2 N_0 B_0 \varepsilon^{-1} T_0^{-2.5}$. Note that the collision frequency

$$\nu_0\ [\mathrm{s}^{-1}] = 3.16 \times 10^2 N_0 T_0^{-1.5} \quad (12)$$

is a dimensional quantity.

The applicability condition for formulas (8)–(11), i.e., the condition for the plasma to be in the superbanana diffusion regime, is given by the inequality

$$N_0\rho \ll 1.7 \times 10^5 T_0^2 t_j^2 M R^{-1} (\varepsilon x^l)^{1.5}, \quad (13)$$

where $M$ is the number of helical field periods along the toroidal direction.

Having made these remarks, we now turn to the analysis of Eqs. (1)–(3), which, in the steady-state case, have a fairly simple form:

$$S_e = S_i; \quad S_j = S^{\mathrm{ext}}; \quad \Pi_j = \Pi_j^{\mathrm{ext}}. \quad (14)$$

Moreover, in the absence of external charge sources (i.e., for $S_e^{\mathrm{ext}} = S_i^{\mathrm{ext}} = S^{\mathrm{ext}}$), the first of these equations (the ambipolarity condition) is a consequence of the last two equations, which are the time-independent electron and ion diffusion equations.

As was mentioned in the Introduction, the set of equations (14) can be solved in two ways. The first way is simpler because it requires solving a third-order algebraic equation rather than a set of differential equations. In this way, we have to specify the functions $\rho(x)$ and $t_j(x)$, to substitute then into the ambipolarity equation $S_e = S_i$, and to solve the resulting algebraic equation for $V$. Inserting the solution obtained, $V(x)$, into the expressions for the fluxes $S_j$ and $\Pi_j$, we find the functions

$S^{\text{ext}}(x)$ and $\Pi_j^{\text{ext}}(x)$ and then, using relationships (4) and (5), determine the particle and heat sources for which the solutions derived are possible *if they ever exist for the chosen profiles of the plasma density and plasma temperatures.* It is clear that, in this way, the functions $S^{\text{ext}}$ and $\Pi_j^{\text{ext}}$ in different solutions $V(x)$ will be different.

The second way is, in the author's opinion, more reasonable, but it requires the solving of differential equations for $\rho(x)$ and $t_j(x)$. In this way, we have to specify the particle and heat sources, i.e., the functions $S^{\text{ext}}(x)$ and $\Pi_j^{\text{ext}}(x)$, and to simultaneously solve the second and third of Eqs. (14). We thus arrive at a quadratic equation for the function $V(x)$, the coefficients of this equation being dependent on $\rho$ and $t_j$, and at a set of nonlinear first-order differential equations for $\rho$ and $t_j$.

In the next sections, we will consider both of these approaches in more detail.

## 3. SOLUTIONS TO THE AMBIPOLARITY EQUATION FOR PRESCRIBED PROFILES OF THE DENSITY AND TEMPERATURES

We first consider the solutions to ambipolarity equation (1) assuming that the plasma density $\rho(x)$ and plasma temperatures $t_j(x)$ are given functions of the radius $x$. Taking into account expressions (8) and (9) for the diffusion coefficients $D_j(x, V)$, we can rewrite Eq. (1) as

$$\frac{\partial V}{\partial \tau} = -G(x, V)F(x, V);$$
$$F(x, V) = V^3 + B(x)V^2 + C(x)V + D(x). \tag{15}$$

Here,

$$G(x, V) = \frac{D_e D_i}{t_e t_i^{0.5} \rho^3 x^{2-3l} D_0} \tag{16}$$

is a strictly positive function and the coefficients $B(x)$, $C(x)$, and $D(x)$ are given by the relationships

$$B(x) = \frac{\mu t_i^{0.5} t_e L_e - t_e^{0.5} t_i L_i + 2(\mu t_i^{0.5} \nu_i - t_e^{0.5} \nu_e)}{\mu t_i^{0.5} + t_e^{0.5}}, \tag{17}$$

$$C(x) = \frac{\mu u^2 \rho^2 x^{2-2l}(0.9\mu t_e^{-2.5} + t_i^{-2.5}) + 2(\mu t_i^{0.5} \nu_i t_e L_e + t_e^{0.5} \nu_e t_i L_i) + \mu t_i^{0.5} \nu_i^2 + t_e^{0.5} \nu_e^2}{\mu t_i^{0.5} + t_e^{0.5}}, \tag{18}$$

$$D(x) = \frac{-\mu u^2 \rho^2 x^{2-2l}(0.9\mu t_e^{-2.5} t_i L_i - t_i^{-2.5} t_e L_e) + \mu t_i^{0.5} \nu_i^2 t_e L_e - t_e^{0.5} \nu_e^2 t_i L_i}{\mu t_i^{0.5} + t_e^{0.5}}, \tag{19}$$

where

$$L_j = \frac{\partial \ln \rho}{\partial x} + b_j^{(1)} \frac{\partial \ln t_j}{\partial x}; \quad \nu_j = l\varepsilon t_j x^{l-1}. \tag{20}$$

The steady solutions to the ambipolarity equation coincides with the solutions to the equation

$$F(x, V) = 0, \tag{21}$$

which, depending on the values of the coefficients $B(x)$, $C(x)$, and $D(x)$ may have three real roots, $V_1(x) \geq V_2(x) \geq V_3(x)$, or one real root, $V_3(x)$. The smallest and the largest roots, which satisfy the condition

$$\frac{\partial F}{\partial V} > 0 \quad \text{for} \quad V = V_{1,3} \tag{22}$$

are obviously stable and the intermediate root $V_2(x)$, for which we have $\partial F/\partial V < 0$, corresponds to an unstable solution. The solution to cubic equation (21) is well known, so we do not present it here in general form. As an illustration, we write it out for a particular case of an $l = 2$ stellarator and of an isothermal plasma in which the density and temperature profiles are shaped as

$$\rho(x) = 50(1.02 - x^6),$$
$$t_e(x) = t_i(x) = \exp[4(1 - x^2)]. \tag{23}$$

In this case, the character of the solution to Eq. (21) is determined by a single parameter $u$, which depends on the boundary values of the density and temperature, $N_0$ and $T_0$, and also on the magnetic field $B_0$ and plasma radius $r_0$ (see formula (12)).

Calculations show that, for $u > 35.6$, Eq. (21) has one real solution for all $x$ values, namely, the solution $V_3(x)$, such that $V_3(x) \longrightarrow t_i(x)L_i(x)$ as $u \longrightarrow \infty$ (see Fig. 1). For small values $u < 0.32$, it has two stable solutions, $V_1(x)$ and $V_3(x)$, which are real for all $x$ values (see Fig. 2). For $u \longrightarrow 0$, the solution $V_3(x)$ approaches $-\nu_i(x)$ and the solution $V_1(x)$ approaches $-t_e(x)L_e(x)$. In the intermediate range $0.32 < u < 35.6$, the equation also has two stable solutions, $V_1(x)$ and $V_3(x)$. In this

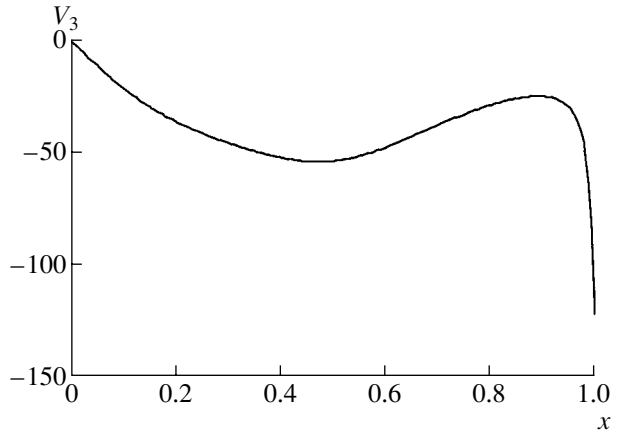


**Fig. 1.** Solution $V_3(x)$ to ambipolarity equation (21) for profiles (23) and for $u = 40$.

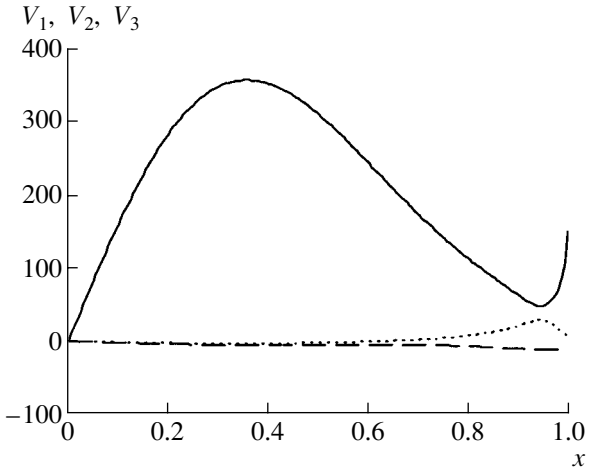


**Fig. 2.** Three solutions $V_1(x)$ (solid curve), $V_2(x)$ (dotted curve), and $V_3(x)$ (dashed curve) to ambipolarity equation (21) for profiles (23) and for $u = 0.3$.

case, however, the solution $V_1(x)$, as well as $V_2(x)$, is real not over the entire range of $x$ values but over the range $x < x_1$, where $x_1$ is the point at which the solutions $V_1(x)$ and $V_2(x)$ coincide and which exhibits the following behavior: $x_1 \longrightarrow 1$ as $u \longrightarrow 0.32$ and $x_1 \longrightarrow 0$ as $u \longrightarrow 35.6$ (see Fig. 3). Hence, in the intermediate range $0.32 < u < 35.6$, the solution at the point $x = x_1$ can undergo a jump from $V_1(x)$ to $V_3(x)$ and vice versa. The property of the solution to take on two different values at the point $x = x_1$ might be called bifurcation (i.e., the bifurcation of the corresponding equilibrium plasma state), but such is not the case, as will be clear later. However, before proceeding to a discussion of this issue, we consider the conditions for the existence of either a continuous solution, $V_3(x)$, or a discontinuous solution that jumps from $V_1(x)$ to $V_3(x)$ at the point $x = x_1$. To do this, we turn to Eq. (15), which accounts for the time dependence of the ambipolar electric field, and find its steady solutions for different initial conditions. We can assume that the plasma density and temperature are time-independent because, by virtue of the smallness of the quantity $D_0$ (see formula (12) and Eq. (15)), the electric field relaxes to its steady-state value in a time much shorter than the relaxation times of the density and temperature.

Since the solution $V_2(x)$ is unstable, it is obvious that, if the initial value of the electric field, $V_0(x)$, in the region $0 < x < x_1$ is less than $V_2(x)$, then, as $\tau \longrightarrow \infty$, the solution to Eq. (15) approaches $V_3(x)$ over the entire range of $x$ values (see Fig. 4).

For $V_0(x) > V_2(x)$, the solution in the region $x < x_1$ approaches $V_1(x)$ and, in the region $x > x_1$, in which $V_1(x)$ is complex, the solution approaches $V_3(x)$ (Fig. 5). If the curve $V_0(x)$ intersects the curve $V_2(x)$ at a number of points, then the steady solution has the same number of discontinuities; moreover, in the regions where $V_0(x) > V_2(x)$, it coincides with $V_1(x)$, and, in the regions where $V_0(x) < V_2(x)$, it coincides with $V_3(x)$. In other words, by appropriately choosing the initial conditions $V_0(x)$, we can obtain a steady solution having a discontinuity at any arbitrary number of prechosen points. This is illustrated in Figs. 4–6, which display the steady solutions to Eq. (15) for $u = 4$ and for three different initial profiles of the electric field: $V_0(x) = -100x(1 - x)$, $V_0(x) = 200x(1 - x)$, and $V_0(x) = 100\sin(60x)$. By $V_M(x)$ we denote the function $V(\tau_M, x)$, where $\tau_M$ is the $\tau$ value at which the solution becomes essentially time-independent (i.e., reaches its steady-state value).

Hence, we arrive at the conclusion that ambipolarity equation (15) can have an infinite number of steady solutions. This seemingly strange result is explained by each of these solutions having their own source functions $S^{\text{ext}}(x)$ and $\Pi_j^{\text{ext}}(x)$. As for the discontinuous solu-

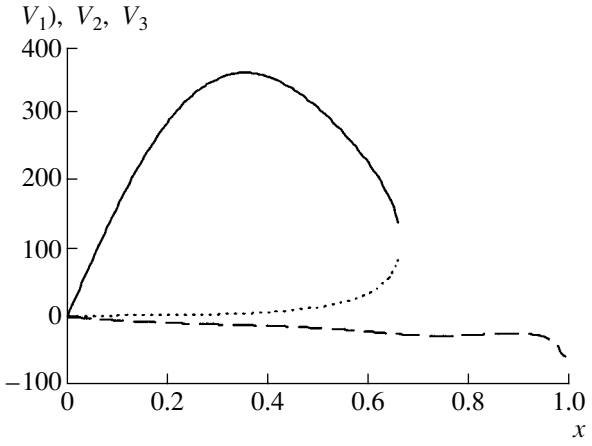


**Fig. 3.** The same as in Fig. 2, but for $u = 4$.

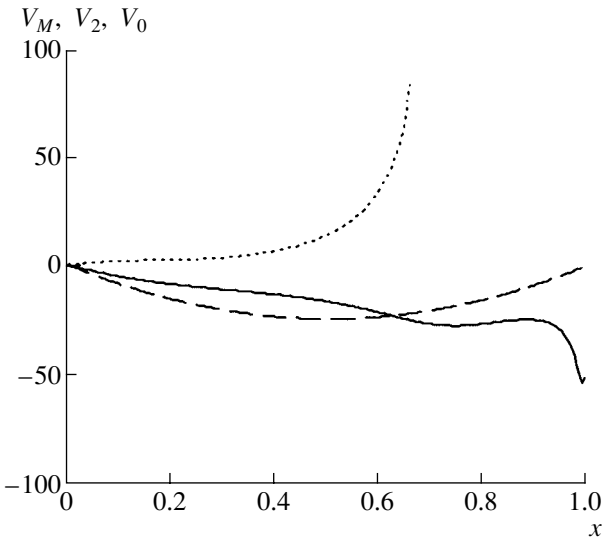


**Fig. 4.** Steady solution to Eq. (21) and unsteady solution to Eq. (15) for the initial electric field profile $V_0(x) = -100x(1-x)$ and for $u = 4$. The solid curve is for the established solution $V_M(x)$ to Eq. (15), the dotted curve is for the solution $V_2(x)$ to Eq. (21), and the dashed curve is for the initial electric field $V_0(x)$.

tions, they are physically implausible, because the presence of discontinuities in the function $V(x)$ leads to discontinuities in the functions $S^{\text{ext}}(x)$ and $\Pi_j^{\text{ext}}(x)$, which in turn leads to singularities of the δ-function type in the particle and heat sources. Figures 7–9 show the steady-state fluxes $S_e(x) = S_i(x) = S^{\text{ext}}$ that correspond to the solutions $V_M(x)$ obtained for the above three initial profiles of the ambipolar electric field.

The situation with a nonisothermal plasma such that $t_e > t_i$ can be more complicated. As an example, Figs. 10–14 depicts the steady solutions to ambipolarity equation (21) for different values of the parameter $u$ in the case in which the plasma density and ion temperature profiles are given by relationships (23) and the electron temperature is higher than the ion temperature by a factor of $e$,

$$t_e(x) = \exp(5 - 4x^2).$$

Thus, over a certain parameter range ($u < 1$), the solutions $V_2$ and $V_3$ are real not for every value of $x$ and the only solution that is continuous over the entire range of $x$ values is $V_1(x)$ (see Fig. 10). For larger $u$ values, it is plausible that the time-independent ambipolarity equation has no solutions that are real at every radius $x$ (Figs. 11, 12). In this case, the equation has only discontinuous solutions, which are physically implausible because they lead to singularities of the δ-function type in the particle and heat sources. Consequently, for these values of $u$, steady solutions *with the chosen profiles of the density and temperatures* do not exist. For even larger $u$ values, there is only one solution, $V_3$, which is real for all $x$ values (Fig. 14). Hence, for small $u$ values, the solution is $V_1(x)$ (the electron root) and, for large $u$ values, the solution is $V_3(x)$; these solutions are real for all $x$ values. However, it will be shown in Section 5 that the solution $V_1(x)$ is unstable against slow variations in the density and temperature, as in the case of an isothermal plasma. This result calls into question the

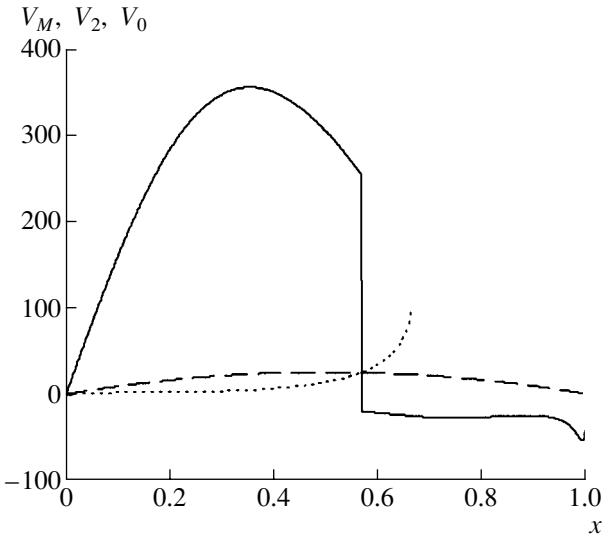


**Fig. 5.** The same as in Fig. 4, but for $V_0(x) = 200x(1-x)$.

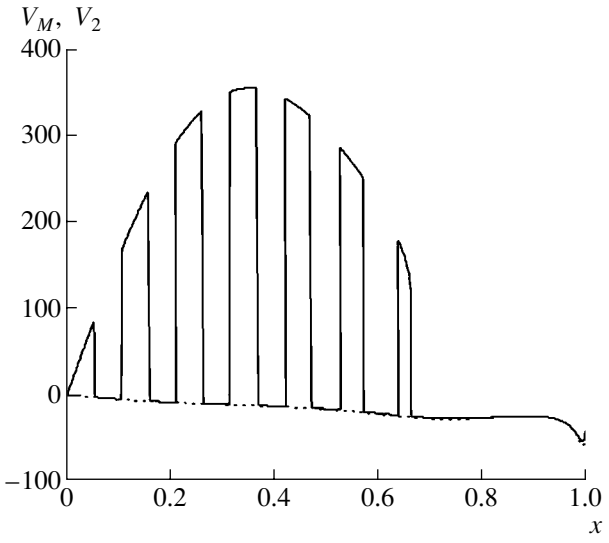


**Fig. 6.** The same as in Fig. 4, but for $V_0(x) = 100\sin 60x$ (the initial electric field is not shown).

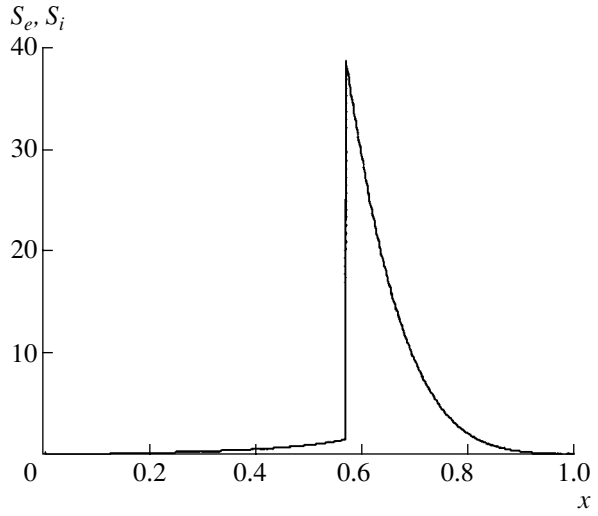


**Fig. 7.** Steady-state fluxes $S_e = S^{\text{ext}}$ as functions of $x$ for $u = 4$ and for the initial ambipolar electric field profile $V_0(x) = 200x(1 - x)$.

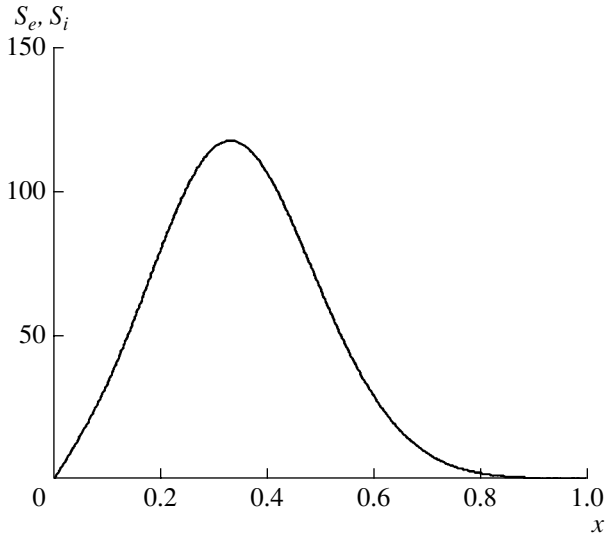


**Fig. 8.** The same as in Fig. 7, but for $V_0(x) = -100x(1 - x)$.

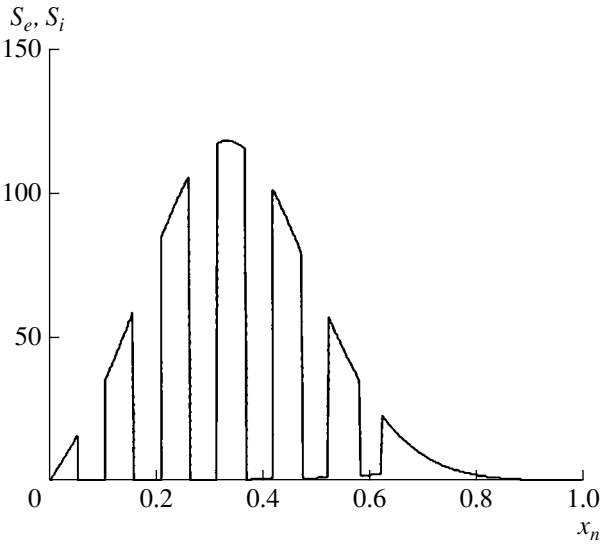


**Fig. 9.** The same as in Fig. 7, but for $V_0(x) = 100\sin 60x$.

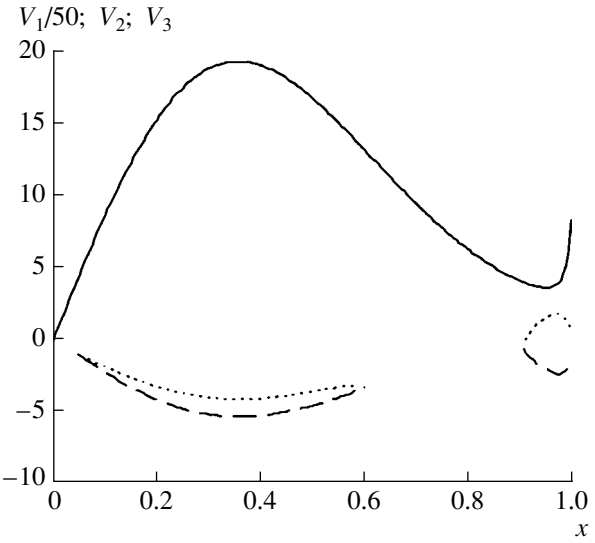


**Fig. 10.** Solutions $V_1(x)$ (solid curve), $V_2(x)$ (dotted curve), and $V_3(x)$ (dashed curve) to Eq. (21) for $u = 0.4$ in the case of a nonisothermal plasma with $t_e(x) = 2.71t_i(x)$.

possible existence of an equilibrium plasma state with the electron root $V_1 \cong -t_e L_e$.

We thus arrive at the following conclusion: for given profiles of the plasma density and plasma temperatures, the ambipolarity equation admits only one stable steady solution, which can exist only if the solution $V_3(x)$ is real for all values of the radial variable $x$.

## 4. STEADY SOLUTIONS TO TRANSPORT EQUATIONS FOR PRESCRIBED PARTICLE AND ENERGY SOURCES

We now analyze the solutions to Eqs. (14) assuming that the particle and energy source functions $S^{\text{ext}}(x)$ and $\Pi_j^{\text{ext}}(x)$ (rather than the plasma density $\rho(x)$ and plasma temperatures $t_j(x)$) are prescribed. In what follows, we

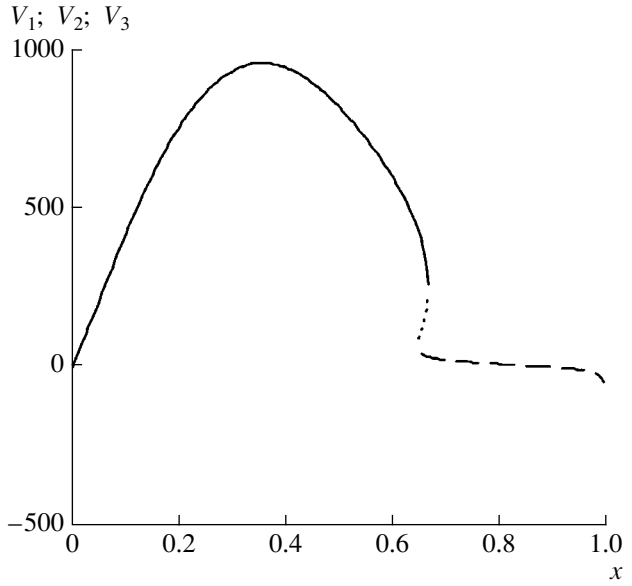


**Fig. 11.** The same as in Fig. 10, but for $u = 40$.

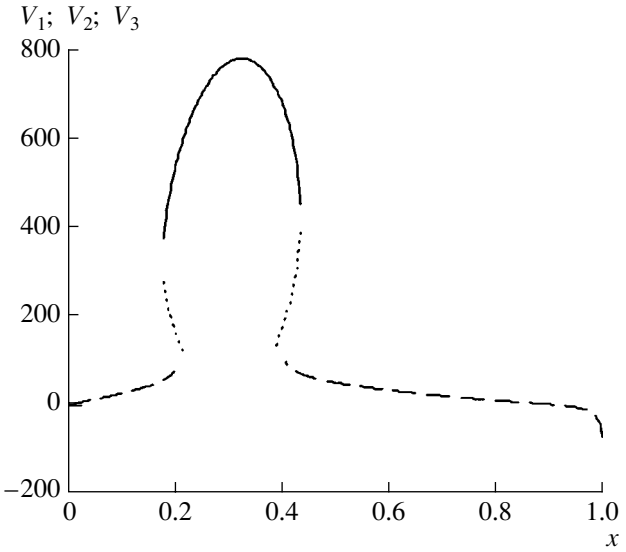


**Fig. 12.** The same as in Fig. 10, but for $u = 200$.

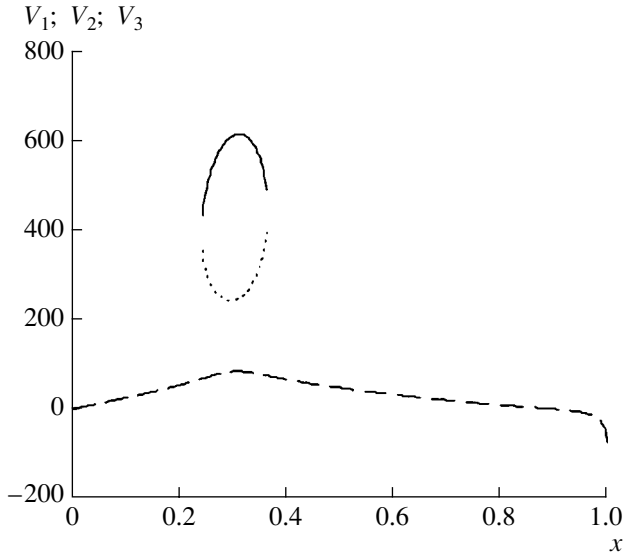


**Fig. 13.** The same as in Fig. 10, but for $u = 250$.

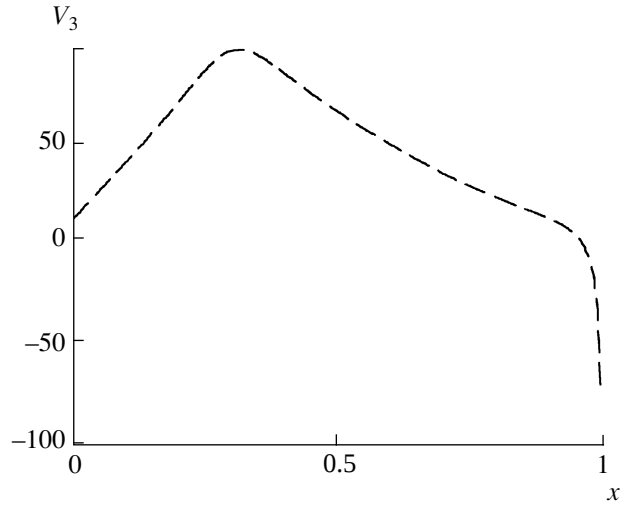


**Fig. 14.** The same as in Fig. 10, but for $u = 270$: there is only a single real solution $V_3(x)$.

will assume that there are no external charge sources (i.e., $S_e^{\text{ext}} = S_i^{\text{ext}} = S^{\text{ext}}$). Under this assumption, the first of Eqs. (14), i.e., the ambipolarity equation, is a consequence of the second and third equations, $S_j = S^{\text{ext}}$, and thereby can be excluded from consideration. The remaining four equations are sufficient to determine the four unknown functions $\rho(x)$, $t_j(x)$, and $V(x)$. The equations have the form

$$\frac{\rho'}{\rho} + b_i^{(1)}\frac{t_i'}{t_i} - \frac{V}{t_i} = -\frac{S^{\text{ext}}}{D_i}; \quad \frac{\rho'}{\rho} + b_e^{(1)}\frac{t_e'}{t_e} + \frac{V}{t_e} = -\frac{S^{\text{ext}}}{D_e}; \quad (24)$$

$$\frac{\rho'}{\rho} + b_i^{(2)}\frac{t_i'}{t_i} - \frac{V}{t_i} = -\frac{\Pi_i^{\text{ext}}}{K_i}; \quad \frac{\rho'}{\rho} + b_e^{(2)}\frac{t_e'}{t_e} + \frac{V}{t_e} = -\frac{\Pi_e^{\text{ext}}}{K_e}. \quad (25)$$

Subtracting Eqs. (24) from Eqs. (25), we obtain the equations for determining the plasma temperatures:

$$(b_j^{(2)} - b_j^{(1)})\frac{t_j'}{t_j} = \frac{S^{\text{ext}}}{D_j} - \frac{\Pi_j^{\text{ext}}}{K_j}. \quad (26)$$

Eliminating the quantities $t_j'/t_j$ in Eqs. (24) with the help of Eqs. (26), we arrive at the following set of two equations for the ambipolar electric field $V(x)$ and plasma density $\rho(x)$:

$$\frac{\rho'}{\rho} - \frac{V}{t_i} = -A_i\frac{S^{\text{ext}}}{D_i}, \quad \frac{\rho'}{\rho} + \frac{V}{t_e} = -A_e\frac{S^{\text{ext}}}{D_e}, \quad (27)$$

where

$$A_j = 1 + \frac{b_j^{(1)}}{b_j^{(2)} - b_j^{(1)}}\left(1 - \frac{\Pi_j^{\text{ext}} D_j}{S^{\text{ext}} K_j}\right). \quad (28)$$

Taking the difference between the second and first of Eqs. (27) yields a second-order algebraic equation for determining the steady-state electric field $V$:

$$\left(\frac{1}{t_e} + \frac{1}{t_i}\right)V = S^{\text{ext}}\left(\frac{A_i}{D_i} - \frac{A_e}{D_e}\right). \quad (29)$$

Performing some manipulations, we can reduce this equation to the form

$$V^2 - 2aV - b = 0, \quad (30)$$

where

$$a = \frac{(t_e + t_i)(t_e t_i)^{-0.5}\rho^2 x^{2-0.5l}}{2S^{\text{ext}}(t_e^{0.5}A_i - \mu^{-1}t_i^{0.5}A_e)} - \frac{\varepsilon l x^{l-1}(t_i^{0.5}A_i + \mu^{-1}t_e^{0.5}A_e)}{(t_e t_i)^{-0.5}(t_e^{0.5}A_i - \mu^{-1}t_i^{0.5}A_e)}, \quad (31)$$

$$b = \frac{\rho^2 u^2 x^{2-2l}(0.9\mu t_e^{-3}t_i^{0.5}A_e - t_i^{-3}t_e^{0.5}A_i)}{(t_e^{0.5}A_i - \mu^{-1}t_i^{0.5}A_e)} - \frac{(\varepsilon l x^{l-1})^2(t_i^{1.5}A_i - \mu^{-1}t_e^{1.5}A_e)}{(t_e t_i)^{-0.5}(t_e^{0.5}A_i - \mu^{-1}t_i^{0.5}A_e)}. \quad (32)$$

Strictly speaking, Eq. (30) is not a second-order equation in $V$ because the ratio $D_j/K_j$ is decidedly, although weakly, dependent on $V$. It can be shown, however, that, for electrons, the term $V_e^2$ in the denominators in expressions (9) and (11) for $D_e$ and $K_e$ is unimportant, while, for the ion plasma component, it plays a governing role. Therefore, the ratios

$$\frac{D_j}{K_j} = \frac{k_j}{t_j}, \quad k_e \cong 0.2, \quad k_i \cong 0.44, \quad (33)$$

and, accordingly, the quantities $A_j$, can be treated as being explicitly independent of the field $V$.

Equation (30) has two roots,

$$V_1 = a + (a^2 + b)^{0.5}, \quad V_2 = a - (a^2 + b)^{0.5}, \quad (34)$$

i.e., there are two different solutions for a steady-state electric field. We insert these two solutions into the expressions for the diffusion coefficients to obtain the final equations for the plasma temperatures:

$$b_j^{(1)}\frac{t_j'}{t_j} = (A_j - 1)\frac{S^{\text{ext}}}{D_j}, \quad A_j = 1 + \frac{b_j^{(1)}}{b_j^{(2)} - b_j^{(1)}}\left(1 - \frac{k_j\Pi_j^{\text{ext}}}{t_j S^{\text{ext}}}\right). \quad (35)$$

Equations (35) should be supplemented with the equation for the plasma density, for example, with either of Eqs. (27), say,

$$\frac{\rho'}{\rho} = -\frac{V}{t_e} - A_e\frac{S^{\text{ext}}}{D_e}. \quad (36)$$

Solving the resulting set of three differential equations, we determine the sought-for functions $\rho(x)$ and $t_j(x)$. Substituting these functions into expressions (31) and (32) for the quantities $a$ and $b$ and using expressions (34), we find the solutions $V_1$ and $V_2$ as functions of the $x$ coordinate. Hence, specifying the continuous functions $S^{\text{ext}}(x)$ and $\Pi_j^{\text{ext}}(x)$, we arrive at the two solutions $V_1(x)$ and $V_2(x)$ for the ambipolar electric field. However, in order to decide which of the two plasma states corresponding to these two solutions can actually occur, it is necessary to check whether the solutions are stable. The stability of the solutions against small deviations from equilibrium will be analyzed in the next section.

## 5. STABILITY ANALYSIS OF THE STEADY SOLUTIONS

In the previous section, it was shown that the time-independent transport equations admit two different solutions $V_1(x)$ and $V_2(x)$ for the ambipolar electric field and, moreover, that these solutions *correspond to the same particle and heat sources.* In order to establish which of the two solutions corresponds to an actual plasma state, it is necessary to investigate their stability. To do this, we must begin with the complete set of transport equations (1)–(3) and must vary all four quantities entering them. We analyze the stability of the solutions in the standard way, by considering small deviations of the quantities from their equilibrium values:

$$\rho = \rho_0 + \tilde{\rho}, \quad t_j = t_{0j} + \tilde{t}_j, \quad V = V_0 + \tilde{V}, \quad (37)$$

where $\rho_0$, $t_{0j}$, and $V_0$ are the equilibrium values and the deviations are represented by the formulas

$$\tilde{\rho}, \tilde{t}_j, \tilde{V} \propto e^{(\gamma t + ikx)}. \tag{38}$$

To prevent misunderstanding, it should be stressed that Eq. (1) differs from the *steady-state* ambipolarity condition because the expressions for the fluxes $S_e$ and $S_i$ account, in particular, for the convective fluxes that are associated with the polarization currents and are proportional to *the time derivative of the electric field* (see expressions (6) and (7)).

We substitute relationships (37) into Eqs. (1)–(3) and linearize the resulting equations in the small deviations $\tilde{\rho}$, $\tilde{t}_j$, and $\tilde{V}$ to obtain a set of four homogeneous equations, which are solvable if they have a zero determinant:

$$\begin{vmatrix} D_0\Gamma + Q_i - Q_e & ik(D_e - D_i) & ikb_e^{(1)}D_e t_e^{-1} & -ikb_i^{(1)}D_i t_i^{-1} \\ ikQ_e & \Gamma + k^2 D_e & k^2 b_e^{(1)} D_e t_e^{-1} & 0 \\ ikP_e & 1.5\Gamma t_e + k^2 K_e & 1.5\Gamma + b_e^{(2)} k^2 K_e t_e^{-1} & 0 \\ ikP_i & 1.5\Gamma t_i + k^2 K_i & 0 & 1.5\Gamma + b_i^{(2)} k^2 K_i t_i^{-1} \end{vmatrix}, \tag{39}$$

where $\Gamma = \gamma\rho$ and

$$\begin{aligned} Q_e &= S^{\text{ext}}\frac{\partial \ln D_e}{\partial V} - \frac{D_e}{t_e}; \quad Q_i = S^{\text{ext}}\frac{\partial \ln D_i}{\partial V} + \frac{D_i}{t_i}, \\ P_e &= \Pi_e^{\text{ext}}\frac{\partial \ln K_e}{\partial V} - \frac{K_e}{t_e}; \quad P_i = \Pi_i^{\text{ext}}\frac{\partial \ln K_i}{\partial V} + \frac{K_i}{t_i}. \end{aligned} \tag{40}$$

Since, for arbitrary wavenumbers $k$, the expression for the determinant is very involved, we do not write it out here and present only expression (39), which refers to the short-wavelength limit $k \gg 1$. Also, the equation for $\Gamma$ was derived with allowance for the inequality $D_0 = (\rho_L/r_0)^2 \ll 1$ and for the fact that, in accordance with the diffusion approximation, the product $k^2 D_0$ is much less than unity.

Evaluating determinant (39), we obtain the following fourth-order equation for $\Gamma$:

$$\frac{9}{4}D_0\Gamma^4 + \frac{9}{4}(Q_i - Q_e)\Gamma^3 + k^2 X\Gamma^2 + k^4 Y\Gamma + k^6 Z = 0, \tag{41}$$

where

$$\begin{aligned} X &= \frac{9}{4}[Q_i D_e(1 - b_e^{(1)}) - Q_e D_i(1 - b_i^{(1)})] \\ &+ \frac{3}{2}(Q_i - Q_e)(b_e^{(2)} K_e t_e^{-1} + b_i^{(2)} K_i t_i^{-1}) \\ &- \frac{3}{2}D_e D_i t_e^{-1} t_i^{-1}[P_i K_e b_i^{(1)}(b_e^{(2)} - b_e^{(1)}) \\ &- P_e K_i b_e^{(1)}(b_i^{(2)} - b_i^{(1)})], \end{aligned} \tag{42}$$

$$\begin{aligned} Y &= Q_i\Big[K_e K_i t_e^{-1} t_i^{-1} b_i^{(2)} b_e^{(2)} + \frac{3}{2}D_e K_e t_e^{-1}(b_e^{(2)} - b_e^{(1)}) \\ &+ \frac{3}{2}D_e K_i t_i^{-1} b_i^{(2)}(1 - b_e^{(1)})\Big] - Q_e\Big[K_e K_i t_e^{-1} t_i^{-1} b_i^{(2)} b_e^{(2)} \\ &+ \frac{3}{2}D_i K_i t_i^{-1}(b_i^{(2)} - b_i^{(1)}) + \frac{3}{2}D_i K_e t_e^{-1} b_e^{(2)}(1 - b_i^{(1)})\Big] \\ &- \frac{3}{2}D_i D_e[P_e t_e^{-1} b_e^{(1)}(1 - b_i^{(1)}) - P_i t_i^{-1} b_i^{(1)}(1 - b_e^{(1)})] \\ &+ b_i^{(1)} b_e^{(2)} D_i K_e P_i t_e^{-1} t_i^{-1} - b_e^{(1)} b_i^{(2)} D_e K_i P_e t_i^{-1} t_e^{-1}, \end{aligned} \tag{43}$$

$$\begin{aligned} Z &= K_e K_i t_e^{-1} t_i^{-1}[Q_i D_e b_i^{(2)}(b_e^{(2)} - b_e^{(1)}) \\ &- Q_e D_i b_e^{(2)}(b_i^{(2)} - b_i^{(1)})] - D_e D_i t_e^{-1} t_i^{-1} \\ &\times [P_i K_e b_i^{(1)}(b_e^{(2)} - b_e^{(1)}) - P_e K_i b_e^{(1)}(b_i^{(2)} - b_i^{(1)})]. \end{aligned} \tag{44}$$

Since the first term in Eq. (41) contains the small parameter $D_0$ and since $k^2 D_0 \ll 1$, the largest root of this equation, $\Gamma_1$, is equal to

$$\Gamma_1 \cong -D_0^{-1}(Q_i - Q_e). \tag{45}$$

This root describes the rapid relaxation of the ambipolar electric field, during which the plasma density and plasma temperatures remain essentially unchanged. It is also easily seen that the stability condition $\Gamma_1 < 0$ coincides with condition (22), which is equivalent to the inequality

$$\frac{\partial}{\partial V}(S_i - S_e) = Q_i - Q_e > 0. \tag{46}$$

The remaining three roots, which describe slow variations of all the quantities, $\rho$, $t_j$, and $V$, on time scales on

the order of the diffusion times, are determined from the equation

$$\frac{9}{4}(Q_i - Q_e)\Gamma^3 + k^2 X\Gamma^2 + k^4 Y\Gamma + k^6 Z = 0. \quad (47)$$

Hence, in order for equilibrium solutions (34) to be stable against fast variations in the ambipolar electric field, it is necessary that condition (46) be satisfied, i.e., that the difference $Q_i - Q_e$ be positive. Assuming that this condition holds at least for one of the two equilibrium solutions (34), we consider whether either of them can be unstable against the slow perturbations associated with variations in the plasma density and plasma temperatures. To do this, we rewrite expression (44) for $Z$ in a form that is more convenient for our analysis. Taking into account relationships (28) and Eqs. (35) and carrying out simple manipulations yields

$$Z = H(t_e^{0.5}A_i - \mu^{-1}t_i^{0.5}A_e)(a - V), \quad (48)$$

where

$$H = \frac{2S^{\text{ext}}K_eK_iD_eD_i(b_i^{(2)} - b_i^{(1)})(b_e^{(2)} - b_e^{(1)})}{(t_et_i)^{1.5}\rho^2 x^{2-0.5l}} > 0 \quad (49)$$

is a strictly positive quantity and the function $a(x, \rho, t_e, t_i)$ is given by relationship (31).

Since the roots $\Gamma_1$, $\Gamma_2$, $\Gamma_3$, and $\Gamma_4$ of Eq. (41) should satisfy the relationship

$$\Gamma_1\Gamma_2\Gamma_3\Gamma_4 = \frac{4}{9}D_0^{-1}Zk^6 \quad (50)$$

and since the first root is negative, $\Gamma_1 < 0$, the product of the remaining three roots $\Gamma_2\Gamma_3\Gamma_4$ in the case $Z < 0$ should be positive, i.e., at least one of them is positive, which indicates that the equilibrium state is unstable.

Substituting expressions (34) for $V_{1,2}$ into expression (48), we find that, under the condition

$$t_e^{0.5}A_i - \mu^{-1}t_i^{0.5}A_e > 0, \quad (51)$$

the solution $V_1$ is unstable, and, under the opposite condition

$$t_e^{0.5}A_i - \mu^{-1}t_i^{0.5}A_e < 0, \quad (52)$$

the unstable solution is $V_2$.

Hence, necessary stability conditions are given by inequality (46) and the inequality

$$Z > 0, \quad (53)$$

and a sufficient instability condition is given by the opposite inequality

$$Z < 0. \quad (54)$$

Taking into account expression (31) for $a$ and relationship (48), the unstable and stable solutions, $V_{\text{unst}}$ and $V_{\text{st}}$, can be written as

$$V_{\text{unst}} = a + |q|q^{-1}(a^2 + b)^{0.5}; \quad V_{\text{st}} = a - |q|q^{-1}(a^2 + b)^{0.5}, \quad (55)$$

where

$$q = t_e^{0.5}A_i - \mu^{-1}t_i^{0.5}A_e. \quad (56)$$

Note that the unstable solution $V_{\text{unst}}(x)$ is discontinuous and equals $\pm\infty$ at the point where $q(x)$ is equal to zero, whereas the stable solution is a continuous function of the $x$ coordinate.

Hence, if Eqs. (34)–(36) have a stable steady solution for prescribed continuous functions $S^{\text{ext}}(x)$ and $\Pi_j^{\text{ext}}(x)$, then this solution is unique and is a continuous function of radius.

At the end of this section, we return to Section 3. Having derived instability criterion (54), we can now show that the steady state characterized by the electron root $V_1$ is unstable against slow variations in the electric field, plasma density, and plasma temperatures. In this way, we are to show that the following product is negative,

$$q(a - V_1) < 0.$$

Taking into account the inequality $\mu \gg 1$ and the fact that the solution $V_1$, which is real over the entire range of $x$ values, exists only for $u \ll 1$, we obtain from Eq. (15) the relationship

$$V_1 = -t_eL_e + \mu^{-1}t_e^{0.5}t^{-0.5}(t_eL_e + t_iL_i), \quad (57)$$

where the quantities $L_j$ are defined in relationships (20). To determine $q$, we must know the expressions for the quantities $A_j$. These expressions can be found from formulas (27) with allowance for the relationships

$$S^{\text{ext}} = S_i = -(t_eL_e - V_1)t_i^{-1}D_i. \quad (58)$$

Inserting expression (57) for the field $V_1$ into the expressions for $A_j$ so obtained, we then arrive at the following formula for $q$:

$$q = (t_e + t_i)L_et_e^{0.5}(t_eL_e + t_iL_i)^{-1}. \quad (59)$$

Finally, inserting relationships (58) into expression (31) for $a$ and taking into account relationship (57), we find that the product in question is less than zero,

$$q(a - V_1) = 0.5(t_e + t_i)(t_eL_e)^2t_e^{-0.5}(t_eL_e + t_iL_i)^{-1} < 0, \quad (60)$$

because the sum $t_eL_e + t_iL_i$ is obviously negative (at least for a certain region of the plasma column). This

proves the assertion made at the end of Section 3, namely, that the equilibrium state with the electron root $V_1$ is unstable.

With regard to the solution $V_3$, it can be said that, although attempts to prove the stability of the equilibrium state with this root generally do not succeed (for arbitrary profiles of the density and temperatures), numerical simulations show that necessary condition (53) for the stability of the equilibrium state with the root $V_3$ is satisfied for all the examples considered in Section 3.

## 6. CONCLUSIONS

Hence, we have considered two methods for finding steady solutions. In the first method (see Section 3), the profiles of the plasma density and plasma temperatures are specified in advance and then are used to determine the ambipolar electric field. In this way, however, the particle and heat source functions, i.e., the fluxes $S^{\text{ext}}(x)$ and $\Pi_j^{\text{ext}}(x)$, are uniquely expressed in terms of the chosen functions $\rho(x)$ and $t_j(x)$ and the field $V(x)$. In addition, the solutions so derived should be tested by their agreement with criterion (53) for stability against slow variations in the density and temperatures.

Note also that, in principle, a situation is possible in which the set of equations (14) has no steady solutions *for given profiles of the density and temperatures.*

In the second method (which, in the author's opinion, provides a more systematic analysis), the particle and heat sources are specified in advance and the self-consistent stable solution for the plasma density $\rho(x)$, plasma temperatures $t_j(x)$, and ambipolar electric field $V(x)$ is then obtained by solving the set of differential equations (35) and (36) with allowance for expression (55) for the field $V$. In both methods, however, the steady solution (if it exists) is single-valued and is expressed in terms of continuous functions of the coordinate, i.e., the steady state is nonbifurcating.

Finally, it is pertinent to make one more remark. Since the above analysis was carried out using purely neoclassical transport theory, without allowance for possible anomalous losses, it seems to be somewhat unsatisfactory. This is not only because neoclassical theory fails to adequately describe real experiments, but also because of the following: expressions (8)–(11) for the diffusion coefficients and thermal conductivity (as well as Fig. 8) show that, for actual profiles of the density and temperatures, the fluxes $S^{\text{ext}}(x)$ and $\Pi_j^{\text{ext}}(x)$ decrease very sharply toward the boundary of the plasma at its edge, and, as a result, the particle and heat sources at the plasma periphery turn out to be negative, which seems rather strange from the physical standpoint. In addition, numerical analysis shows that the solutions are fairly sensitive to the shape of the profiles of the particle and heat sources; this result, too, does not agree quite well with the experimental data. The drawbacks outlined above can possibly be overcome by taking into account anomalous losses, which increase toward the plasma boundary. The nature of these losses is not as yet quite clear and they are difficult to account for analytically. From general considerations, however, it might be anticipated that, even when anomalous losses are taken into account in the diffusion approximation, the steady state will again be nonbifurcating, i.e., the solution will be a single-valued function of the coordinates.

## ACKNOWLEDGMENTS

This work was supported in part by the Russian Federal Program for State Support of Leading Scientific Schools, project no. NSh-1965.2003.2.

## REFERENCES

1. A. A. Galeev and R. Z. Sagdeev, in *Reviews of Plasma Physics*, Ed. by M. A. Leontovich (Atomizdat, Moscow, 1973; Consultants Bureau, New York, 1979), Vol. 7.
2. L. M. Kovrizhnykh, Nucl. Fusion **24**, 851 (1984).
3. L. M. Kovrizhnykh, Zh. Éksp. Teor. Fiz. **56**, 877 (1969) [Sov. Phys. JETP **29**, 475 (1969)].
4. A. Fujisawa, Plasma Phys. Controlled Fusion **45**, R1 (2003).
5. L. M. Kovrizhnykh, Fiz. Plazmy **25**, 827 (1999) [Plasma Phys. Rep. **25**, 760 (1999)].

*Translated by I.A. Kalabalyk*

*Plasma Physics Reports, Vol. 31, No. 1, 2005, pp. 26–45. Translated from Fizika Plazmy, Vol. 31, No. 1, 2005, pp. 30–51.*


**PLASMA DYNAMICS**

# Localization of Magnetized Electrons in Current Filaments as a Fundamental Cause of Coulomb Explosion

**A. V. Gordeev* and T. V. Losseva****

**Russian Research Centre Kurchatov Institute, pl. Kurchatova 1, Moscow, 123182 Russia*

***Institute of Geosphere Dynamics, Russian Academy of Sciences, Leninskiĭ pr. 38-1, Moscow, 119334 Russia*

Received June 17, 2004

**Abstract**—Mechanisms for generating current filaments in a dense plasma under the action of focused laser pulses and in a Z-pinch configuration are discussed. The main properties of current filaments with a zero and nonzero electron vorticity $\mathbf{\Omega}_e = \mathbf{B} - (c/e)\nabla \times \mathbf{p}_e$ that originate at magnetic fields in the range $4\pi n_e m_e c^2 \ll \mathbf{B}^2 \ll 4\pi n_i m_i c^2$ are investigated under the conditions of Coulomb explosion at currents below the ion Alfvén current. A study is made of the equilibrium configurations of nonquasineutral current filaments in a purely longitudinal ($B_z$) and a purely azimuthal ($B_\theta$) magnetic field and also in a more general case of a helical magnetic field, having two components, under conditions such that the charge separation occurs on a spatial scale on the order of the magnetic Debye radius $r_B \simeq |\mathbf{B}|/(4\pi e n_e)$. It is shown that strong electric fields generated in the current filaments are comparable in magnitude to the atomic field and are capable of accelerating ions to energies of several tens of megaelectronvolts. The ion dynamics in strong electric fields of the filaments is calculated numerically and is shown to lead to the formation of collisionless shock waves on time scales on the order of several inverse ion plasma frequencies $\omega_{pi}^{-1}$. The possible formation of current filaments on different spatiotemporal scales is considered. © *2005 Pleiades Publishing, Inc.*

## 1. INTRODUCTION

Generation of high-energy ions by means of focused laser pulses [1–3] and Z-pinches [4–6] is an important branch of present-day inertial confinement fusion research. Laser pulses and Z-pinches seem at first sight to be completely different entities, yet they are manifestations of the same phenomenon: the conversion of electromagnetic energy—a high-intensity electromagnetic wave or an applied electric field—into the particle energy (Fig. 1). In both cases, the objective is to optimize the acceleration process. A distinctive feature of acceleration under the action of laser pulses and in Z-pinch configurations is the small dimensions of the region where the energy is transferred from the one or another type of electromagnetic field to charged particles. It might sometimes seem that, in contrast to laser-related phenomena in question, which occur on micron scales within a characteristic time of about $10^{-12}$ s, the physical processes in a Z-pinch develop on spatial scales of 0.1–1 cm over times on the order of $10^{-8}$ s [5, 6]. Accordingly, the processes occurring in these two acceleration methods might seem to be entirely different in nature. However, a more careful analysis of the processes in the two acceleration methods reveals a striking similarity between them. This is well illustrated by the experimental results that have recently been obtained in studying X-pinches with the help of diagnostic techniques with extremely high spatial and temporal resolution [7–12]; in fact, the X-pinches under investigation were Z-pinches organized in a standard fashion. High-precision measurements carried out in those experiments showed that the reproducible processes in Z-pinches occurred on spatial scales of about $10^{-4}$ cm over times as short as $3 \times 10^{-12}$ s [8–10]. This indicates that, in actual pinches, electrodynamic processes occur on the same spatiotemporal scales as those in laser acceleration schemes. That the spatiotemporal scales were essentially the same and that the energy deposited on these scales, too, was found to be approximately the same [9, 13, 14] suggests there is a certain unique mechanism responsible for generating fast charged particles in laser-related processes and in Z-pinches. It should also be noted that the first results have recently been obtained on the direct generation of Z-pinches with currents higher than 100 kA in experiments on the interaction of focused laser radiation with targets containing fine wires [15]. As the matter of fact, the last circumstance most clearly illustrates how close the laser- and Z-pinch-based acceleration schemes are to one another.

The above provides a new insight into the processes that occur during the formation of a Z-pinch when an electric field is applied to the interelectrode gap. At present, most theoretical investigations of the phenomena in Z-pinches involve laborious numerical simulations in which, along with electrodynamic processes, account is taken of radiation and of different dissipative effects in plasmas [11, 12]. At the same time, in order to provide insights into the processes occurring on very

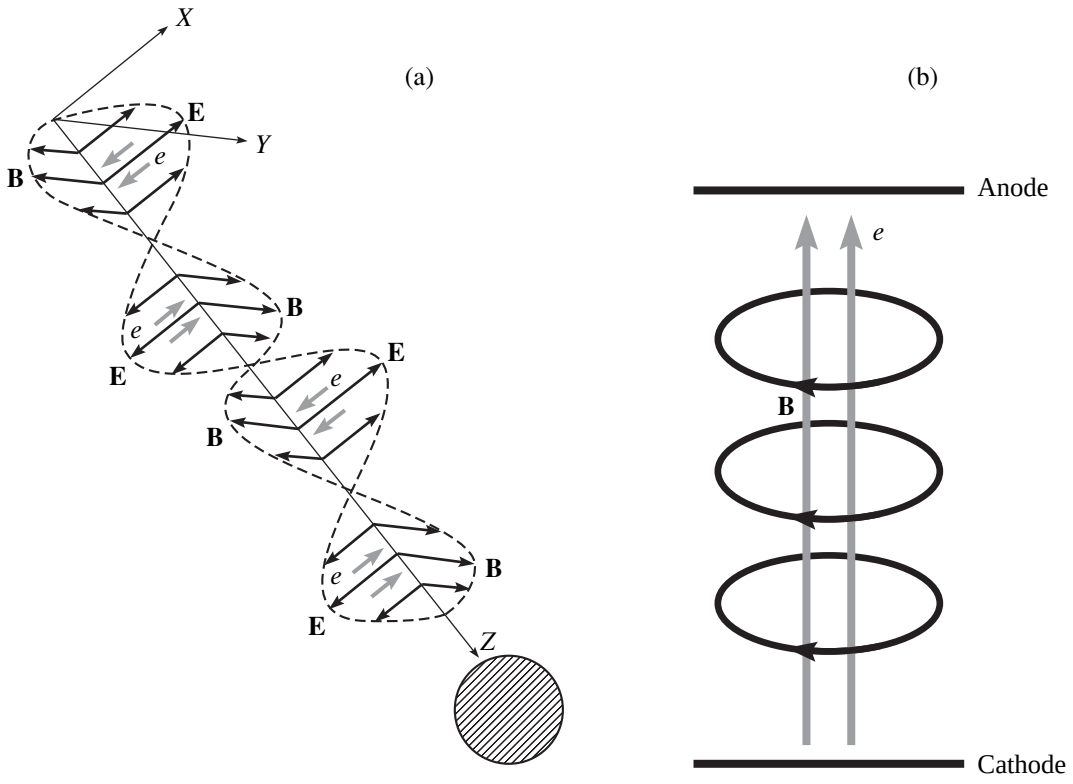


**Fig. 1.** Generation of a vortex structure in (a) a laser plasma and (b) a Z-pinch.

small spatial and temporal scales, on which the majority of the dissipative processes are of the same importance, it is necessary, first of all, to have a clear understanding of the electrodynamic processes accompanying the motion of electrons and ions in strong electric and magnetic fields [14, 16]. In the initial stage of gas breakdown, a major role is played by the electric field $E_z$, which generates and maintains the ohmic current $j_z = \sigma E_z$. However, as the magnetic field $B_\theta$ grows at large values of the dimensionless Hall parameter, $\sigma B_\theta/(en_e c) \gg 1$, the role of the dissipative processes decreases. Moreover, in this stage, the electrons can form current-carrying filaments on time scales on the order of $\omega_{pe}^{-1}$ by the Weibel mechanism for generating a quasistatic magnetic field due to the anisotropy of the electron motion [17]. The physical processes governing the formation and subsequent evolution of current filaments were investigated by state-of-the-art computational means in a recent paper by Sakai *et al.* [18]. The characteristic radius of the electron current filaments calculated in that paper is on the order of the magnetic Debye radius $r_B$, which provides direct confirmation for the possibility of the existence of electron current structures during the evolution of a pulsed current-carrying plasma. A distinctive feature of such current structures is the violation of plasma quasineutrality and the generation of a strong Hall electric field $E_r$ on a spatial scale of about the magnetic Debye radius $r_B \sim B_\theta/(4\pi en_e)$ (see [19–21]), on which the electrons within the filament drift along the $z$ axis in crossed electric ($E_r$) and magnetic ($B_\theta$) fields, thereby producing the filament current in the absence of dissipation. In this case, the radial drop in the electric potential across such an effective "capacitor" is substantially higher than the potential difference between the electrodes. It is of interest to note that, as early as 1977, Young *et al.* [22] reported that they had detected ions that were radially accelerated in Z-pinches to energies of up to 8 MeV. Measurements show that the Z-pinch starts to emit electromagnetic radiation and neutrons in the stage in which the electrode voltage decreases considerably; moreover, the characteristic electron energy in the experimentally observed electron beams can be higher than the applied voltage [5]. In such a nonquasineutral electron filament, the compression of the ion plasma component on a time scale of about $\omega_{pi}^{-1}$ by the inwardly directed radial electric field gives rise to a nonlinear unloading wave that propagates away from the axis and in which the radial ion velocity decreases to zero due to the accumulation of hot ions in the core of the Z-pinch. The corresponding calculations were carried out in the hydrodynamic approximation assuming that the process is adiabatic with an adiabatic index equal to 2.

The creation of ultraintense lasers in the last several years has led to their numerous possible applications [1, 2]. Here, the term ultraintense laser means that the laser radiation intensities are $I_{\text{laser}} > 10^{18}$ W/cm$^2$, the laser wavelengths are $\lambda \leq 1$ μm, and the laser pulse duration is shorter than $10^{-12}$ s. In the context of the applications of such lasers, a standard object of investigation is a filament with an initial radius of $r_0 \sim c/\omega_{pe}$, whose electrons are pushed away from it by the passing laser pulse. The discussion of the processes that occur during the evolution of such a filament has lead to the notion of Coulomb explosion—the expansion of the ion plasma component at a rather high velocity. In the literature on laser plasma, several different mechanisms for the onset of such filaments are now being discussed [1]. In the present paper, it will be assumed that an electron filament originates during the focusing of a laser pulse and leads to the ion acceleration (which will be considered below) and also that, in the initial stage of the process, the ions are accelerated by the electrostatic field arising under the action of the laser-field ponderomotive force [23].

The main conclusion of the nonquasineutral vortex model [19] is that the plasma quasineutrality may be violated near the vortex axis as a result of the vorticity generation in a laser plasma. This occurs when the radius $r_0$ of the axial region in which vorticity is generated is comparable to the magnetic Debye radius $r_B \sim B/(4\pi e n_e)$ and, as a result, the electron density $n_e$ in this region is substantially reduced. Such cavities in the electron density can arise in a laser plasma as a result of a peculiar kind of electron diamagnetism in a configuration in which the magnetic field is strongest at the axis. When the longitudinal magnetic field $B_z$ is maximum at the filament axis, the electrons are expelled from the axial electron vortex region of radius $r_0 \sim c/\omega_{pe} \leq r_B$ in quasi-steady-state magnetic fields with a strength of $eB/(m_e\omega_{pe}c) \geq 1$, which can be produced by the Weibel instability at relativistic laser intensities $a \equiv eE_{\text{laser}}/(m_e\omega_0 c) > 1$, where $\omega_0$ is the laser frequency and $E_{\text{laser}}$ is the amplitude of the electric field of the laser radiation. The characteristic strength of such quasi-steady magnetic fields can be estimated by using the results obtained in [24, 25] in studying the magnetic field generation during the passage of an ultrashort laser pulse through a plasma. Order-of-magnitude estimates made in accordance with [24, 25] show that the quasi-steady magnetic fields are as strong as $B \simeq 4\pi e n_e a c/\omega_{pe}$. For the parameter values $a \simeq 2$ and $n_e \simeq 10^{19}$ cm$^{-3}$, which were used in [23], the characteristic magnetic field strength is $B \simeq 10^7$ G.

It is natural to expect that, because of the same spatiotemporal scales and essentially the same energy deposited at the final stage of the evolution of the object, the filaments produced during the focusing of a high-power laser pulse in a plasma should be identical to the filaments in Z-pinches. The main objective of the present review is to explain the generation of current filaments in Z-pinches and in laser plasmas by the same universal mechanism.

Among the physical processes in laser plasmas and in Z-pinches, the most important effect is that associated with the presence of accelerated ions. In this case, because of the large mass of the ions, the characteristic times of electromagnetic processes occurring on the spatial scales under consideration are significantly shorter than the characteristic ion acceleration time. Consequently, in order for the ion acceleration efficiency to be high, it is necessary to achieve a certain quasi-equilibrium state in which the balance of electromagnetic forces allows the accelerating structure to exist for a sufficiently long time. Such a structure, existing on a time scale of about several ion times $\omega_{pi}^{-1}$, will surely be observed in experiments and captured by numerical simulations. Based on a great deal of experimental and numerical information about laser and pinch phenomena in the present-day literature, it is natural to suppose that the role of this quasi-equilibrium state can be played by the long-known current filaments observed in laser experiments [2, 24–28] and in experiments on current-carrying plasmas with charged particle beams [18, 29, 30]. That the characteristic transverse scales of filaments in laser plasmas are on the order of several units of $c/\omega_{pe}$ was already pointed out in the early studies on this subject [1]. In order for such filaments to be capable of efficiently accelerating ions on these scales, it is necessary that there be a strong radial electric field within them. For a sufficiently cold plasma, this implies that the filament radius should be less than or on the order of the magnetic Debye radius, $r_B \simeq B/(4\pi e n_e) \gg c/\omega_{pe}$. This inequality represents the condition for the existence of a strong charge-separation electric field, in the presence of which the filament operates as an efficient direct-action accelerator. With allowance for the fact that the ions in a magnetic field usually move with Alfvén velocity $v_{Ai} = B/\sqrt{4\pi n_i m_i}$ and the characteristic spatial scale is equal to $r_B$, the characteristic acceleration time scale turns out to be $\omega_{pi}^{-1}$. (Note that a proportional decrease in the characteristic values of the velocity and spatial scale does not change the characteristic acceleration time.) It should be noted that electron current vortices are generated on a characteristic time scale of $\omega_{pe}^{-1}$ [18, 25, 28–30]. Consequently, the time scales on the order of several characteristic acceleration times $\omega_{pi}^{-1}$ are long enough for the vortices to develop and to gradually decay. The electron current filaments can of course be observed only when they are stable and keep their structure unchanged in the course of various processes. An appropriate object of this kind may be a vortex current filament, which is stable because of the conservation of the vorticity $\mathbf{\Omega}_e = \mathbf{B} - (c/e)\nabla \times \mathbf{p}_e$, where $\mathbf{B}$ is the magnetic field and $\mathbf{p}_e = \gamma m_e \mathbf{v}_e$ is the momentum of the elec-

trons moving in the filament [31, 14, 19, 20]. On the short time scales on which collisions play a very minor role, the greater stability of such a filament can be attributed to the conservation of vorticity. Yatsuyanagi *et al.* [26] showed, however, that the stability of the filaments is fairly high even when collisions are taken into account. Hence, a vortex current filament can in principle be treated as a structure that is capable of efficiently accelerating ions, provided that there are strong electric fields within it. This possible role of the filaments was pointed out by Burnett and Enright [1], who considered the Coulomb explosion mechanism at a qualitative level and gave an essentially correct estimate for the ion energy, $\varepsilon_i \sim m_e c^2$. Further investigations carried out in [19–21, 32, 33] showed that, in any medium with free electrons, the current filaments in question are considerably nonquasineutral in magnetic fields as high as $B^2 \gg 4\pi n_e m_e c^2$, which corresponds to the onset of strong electric fields. Note that, for electron velocities of about the speed of light, $|\mathbf{v}_e| \sim c$, this inequality indicates that the current in the filament exceeds the limiting Alfvén current [34]

$$J > \frac{m_e c^3}{e}. \quad (1)$$

It might seem that such a high current is impossible without the generation of a reverse current of the electrons that are deflected by the current's self-magnetic field. Further investigation shows, however, that the electrons in such filaments execute drift motion, during which the role of their inertia in quasi-steady processes is insignificant. For instance, this is the case in a filament with the azimuthal magnetic field. (It should be emphasized that the mechanisms underlying the electron drift motion in steady-state crossed electric and magnetic fields and in the oscillating fields of an electromagnetic wave are essentially the same [35].) In the case of a longitudinal magnetic field and azimuthal electron currents, the electron inertia plays an important role, resulting in a substantial reduction of the magnetic field in the filament (see Section 4).

Hence, further investigation of the current filaments will be carried out by considering the quasi-steady equilibrium state of a nonquasineutral current filament in a high-density plasma in which the electrons execute drift motion in crossed electric and magnetic fields. In this situation, the magnetic field is itself maintained by the electron drift current and the presence of the strong electric field is related to violation of the plasma quasineutrality on spatial scales on the order of the magnetic Debye radius $r_B \simeq B/(4\pi e n_e)$ [19–21, 32, 33]. This corresponds to a situation in which the magnetized electrons are localized and the ions are unmagnetized and are freely accelerated by the electric fields; as a result, the usually mobile electrons fail to neutralize the spatial electric charge in the plasma.

At this point, it is expedient to discuss the phenomenon of Coulomb explosion, which has long been known in laser plasma physics, in the light of the Earnshaw theorem [36], according to which a neutral (on the whole) system of charged particles cannot be in equilibrium under the action of Coulomb forces alone. It is known that stable equilibrium of a wholly neutral system of charged particles can be provided by the presence of additional forces, such as those associated with the quantum-mechanical exchange effects and with the induced dipole moments, magnetic forces (e.g., those caused by the diamagnetic effect), etc. It is also known that it is the electric forces that ensure the rigidity of the solids. In turn, the Coulomb explosion is related to the gross violation of electrical neutrality, which cannot be restored sufficiently rapidly. During the focusing of a laser pulse in a plasma, a high-power electromagnetic wave strips light electrons from neutral particles and blow them off, thus producing a unneutralized ion space charge. The blown-off electrons expand, and the cold electrons that are always present in the system then restore the electric neutrality of the plasma.

During the generation of electron vortex structures because of the expelling of electrons from the region of the strong magnetic field due to the diamagnetic effect, the electrical neutrality is violated on a spatial scale of $r_B$; as a result, unmagnetized ions are accelerated by the arising strong electric field. In this case, the electrical neutrality cannot be restored by the motion of the electrons because their mobility is suppressed in a certain direction and they fail to make the plasma electrically neutral. Even when there are some other forces in addition to Coulomb forces, the quasineutrality, which is violated so abruptly, cannot be restored on a time scale shorter than several inverse ion plasma frequencies $\omega_{pi}^{-1}$. It is only on time scales longer than this characteristic time that, in accordance with the Earnshaw theorem, the stable equilibrium state can be restored in a system of charged particles in the presence of additional forces. Such a violation of electrical neutrality has catastrophic consequences for the plasma of a current filament: strong electric fields accelerate unmagnetized ions to substantial energies, thereby destroying the initial structure of a dense plasma.

The above is valid only for magnetic fields lying in the range

$$4\pi n_e m_e c^2 \ll B^2 \ll 4\pi n_i m_i c^2. \quad (2)$$

In this case, the electrons are magnetized and the ions are not. The left-hand inequality is just the condition for violating the plasma quasineutrality and for the onset of strong electric fields. The right-hand inequality determines the maximum magnetic field for which the effects mentioned above are still important. At magnetic fields stronger than that given by the right-hand inequality, the plasma is fully magnetized; moreover, when such a plasma is nondissipative and the kinetic pressure in it is sufficiently low, its evolution is governed completely by the dynamics of the strong charge-

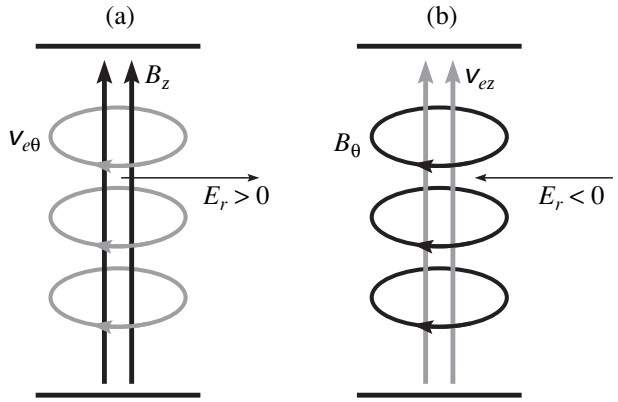


**Fig. 2.** Two types of current filaments: (a) with the longitudinal magnetic field and (b) with the azimuthal magnetic field.

separation electric field and the associated magnetic field [37]. It should be noted that, in the limit of relativistic particle motion, the above range of magnetic fields implies a certain range of currents,

$$\frac{m_e c^3}{e} \ll J \ll \frac{m_i c^3}{z_i e}, \tag{3}$$

where $z_i$ is the ion charge number.

Note that inequalities (2) can be rewritten in the following form:

$$\frac{c}{\omega_{pe}} \ll r_B \ll \frac{c}{\omega_{pi}}. \tag{4}$$

These inequalities imply that the transverse dimensions of the filaments that can be considered under the above assumptions are restricted to $c/\omega_{pi}$. Thus, for a hydrogen plasma with a characteristic electron density of $n_e \sim 10^{20}$ cm$^{-3}$, the limiting transverse dimension of a filament turns out to be $10^{-3}$ cm. In this case, by virtue of inequality $r_B \ll c/\omega_{pi}$, such filaments are ineffective in accelerating the ions because of the plasma quasineutrality on such transverse scales.

The above analysis shows that, for the onset of quasi-steady filaments, it is first of all necessary that there be a quasistatic magnetic field on a spatial scale on the order of $r_B$; moreover, the main mechanism for generating such a field is Weibel instability, which is driven by anisotropy of the motion of charged particles in a plasma [17]. There are many papers devoted to the generation of magnetic fields in laser plasmas (see, e.g., [38] and the literature cited therein). Although the case $\mathbf{\Omega}_e = 0$ is in principle possible from the fundamental point of view, situations with nonzero electron vorticity, $\mathbf{\Omega}_e \neq 0$, driven by Weibel instability are far more important for laser plasma physics. Weibel instability results in generating a quasistatic magnetic field on a time scale on the order of $\omega_{pe}^{-1}$ at the expense of the anisotropy of the distribution of electrons moving in an electromagnetic wave [24, 39–41]. In this case, the characteristic transverse dimensions of the filaments are on the order of several units of $c/\omega_{pe}$. Hence, the initial basis for subsequent acceleration of the fast ions is provided by the formation of a quasistatic plasma configuration with a magnetic field that generates a strong electric field.

In the case of nonrelativistic electrons with a nonzero temperature, the quasistatic magnetic field can be produced at the expense of the noncollinear character of the plasma pressure and plasma density gradients. In the nonrelativistic limit, the hydrodynamic equation of electron motion in a nondissipative plasma at a nonzero pressure can be written as

$$m_e \frac{d\mathbf{v}_e}{dt} = -e\mathbf{E} - \frac{e}{c}\mathbf{v}_e \times \mathbf{B} - \frac{1}{n_e}\nabla p_e. \tag{5}$$

Taking the curl of this equation and using the induction equation, we obtain

$$\frac{\partial \mathbf{\Omega}_e}{\partial t} - \nabla \times (\mathbf{v}_e \times \mathbf{\Omega}_e) = \nabla \times \frac{\nabla p_e}{n_e}. \tag{6}$$

Hence, if $p_e$ depends not only on $n_e$ but also on some other parameters, then, according to Eq. (6), the vorticity is generated and vortex structures may arise (this mechanism differs from the Weibel instability mechanism, in which the quasistatic magnetic field is generated at the expense of the pressure anisotropy). It should be noted that the vorticity generation mechanism just described, which is associated with thermal effects, usually corresponds to moderately strong magnetic fields. This limiting case of magnetic field generation was observed experimentally [42] and was interpreted theoretically by Krushelnick *et al.* [43].

For further analysis, it is important to stress that there are two essentially different types of vortex structures: (i) structures with azimuthal electron currents $j_\theta$, in which the magnetic field is aligned with the $z$ axis ($\mathbf{B} = B_z\mathbf{e}_z$) and (ii) structures with longitudinal electron currents $j_z$, which produce an azimuthal magnetic field $B_\theta$ (Fig. 2). Our investigations show that the electron density profiles in these two types of vortex structures are radically different. In vortex structures with azimuthal electron currents, the electron density near the axis is low, so the axial plasma region of the structure is charged positively. As a result, the plasma ions fly apart in the radial direction toward the periphery of the structure [20]. In contrast, in a vortex structure with a longitudinal electron current and an azimuthal magnetic field $B_\theta$, the electron density at the axis is maximum and the axial plasma region is charged negatively, so the plasma ions collapse toward the axis, giving rise to a Z-pinch [14].

## 2. MECHANISMS FOR THE GENERATION OF FAST CHARGED PARTICLES BY ELECTROMAGNETIC FIELDS

Numerous mechanisms for particle acceleration under the action of high-power focused laser pulses have been known for a long time [1, 2, 44]. The simplest situation is that in which the electrons can be accelerated by the field of an electromagnetic wave in the absence of plasma and of an external magnetic field [2, 35]. The cyclotron acceleration mechanism in the presence of a quasistatic magnetic field was investigated in a recent paper by Belyaev *et al.* [45]. These schemes allow the electrons to be accelerated to energies of several hundred MeV; for the ions, however, they are inefficient for state-of-the-art laser intensities because the ions have very large masses. This is why ion acceleration requires the presence of a high-density plasma in which a quasistatic electric field can be generated. In this case, the most widely used (and long-known) scheme for ion acceleration during the focusing of a high-power laser pulse in a plasma can be described as follows: As a high-power laser pulse propagates in plasma, the electrons are pushed away from its path by the ponderomotive force $\mathbf{F} = -m_e c^2 \nabla \sqrt{1 + a^2}$, where $a = eE/(m_e \omega c)$, with $E$ and $\omega$ being, respectively, the electric field of the electromagnetic wave and its frequency. The motion of the ejected electrons gives rise to a magnetic field. Since there are no electrons near the axis of the produced channel, the ions remaining there generate a strong radial electric field, which forces them to expand in the radial direction. It should be noted that, in considering the propagation of an electromagnetic wave in a channel, additional resonant acceleration of the electrons by the wake wave is sometimes taken into account. A distinctive feature of such filaments with rapidly oscillating fields is that they are subject to various possible instabilities that destroy them, so they exist over a relatively short time [46]. It should be emphasized that, according to [14, 20, 23, 47], the ponderomotive mechanism and the mechanism for electron acceleration in the electric field of a current vortex structure result in comparable values of the ion expansion velocity (which was measured in [23]). Recent numerical calculations for ion acceleration by high-power laser pulses clearly indicate that the magnetic field does indeed play a role in these acceleration processes [48]. In recent years, computer simulations have also demonstrated the existence of another possible acceleration mechanism, specifically the acceleration of ions at the front of a nonlinear wave propagating in the direction of the laser pulse. In this case, the highest energies of the accelerated ions are reached when a laser pulse is focused on a thin plasma slab [48].

It is also necessary to mention the large number of studies in which ion acceleration was calculated under the assumption that the electron vorticity $\mathbf{\Omega}_e$ is zero and with allowance for strong nonlinearities in the equations describing the interaction of the oscillating fields of a laser pulse with a plasma [38]. A time-averaged version of these equations for nonlinear laser–plasma interaction can include a quasistatic magnetic field, which may be strong when $a \gg 1$. By virtue of the condition $\mathbf{\Omega}_e = 0$, this approach is valid for a peculiar London medium such that

$$\mathbf{B} = \frac{c}{e}\nabla \times \mathbf{p}_e. \tag{7}$$

In this case, the resulting quasi-steady equilibrium can be explained as follows: Taking into account the fact that, in accordance with equality (7), the electron vorticity is zero, we reduce Eq. (11) from Section 3 of this paper to the form

$$\frac{\partial \mathbf{p}_e}{\partial t} + \nabla \gamma m_e c^2 = -e\mathbf{E}, \tag{8}$$

where $\gamma$ is the relativistic factor. In a quasi-steady state such that the electrons move only in the direction of the azimuthal coordinate $\theta$, the radial component of this equation becomes

$$\frac{\partial}{\partial r}\gamma m_e c^2 = -eE_r. \tag{8'}$$

For a configuration whose parameters depend only on the radius, we obtain from Eq. (7) the following expression for the magnetic field along the filament:

$$B_z = \frac{m_e c^2}{e}\frac{1}{r}\frac{\partial}{\partial r}(r\sqrt{\gamma^2 - 1}), \tag{9}$$

where $\gamma = (1 - v_\theta^2/c^2)^{-1/2}$ and $v_\theta$ is the azimuthal electron velocity within the filament. Resolving Eq. (9) in terms of the variable $\gamma$ and substituting the resulting expression into Eq. (8') yields

$$-eE_r = m_e c^2 \frac{\partial}{\partial r}\sqrt{1 + \frac{1}{r^2}\left(\int_0^r r dr \frac{eB_z}{m_e c^2}\right)^2}. \tag{10}$$

When the magnetic field flux is concentrated predominantly in the region $r < r_0$, expression (10) implies that $E_r > 0$ at $r \geq r_0$; therefore, the ions at the periphery of the filament are accelerated outward from its axis. On the other hand, near the axis ($r \ll r_0$), we have $E_r < 0$; as a result, the electrons are expelled from the axial region. In the model based on the time-averaged nonlinear equations, all the electrons are pushed away from an axial region of a certain radius—a phenomenon called "electron cavitation" (see [38]).

## 3. BASIC EQUATIONS

The basic set of equations consists of hydrodynamic equations for describing the electron and ion plasma components separately. The electron plasma component is described by relativistic hydrodynamic equations for cold electrons. The reason for this is that the

time scales on which the electron vortex structures are generated are too short for the electrons to be heated to any significant extent.

As initial equations for a nonquasineutral electron current structure, we use the hydrodynamic equation of electron motion converted into the form (see [14])

$$\frac{\partial \mathbf{p}_e}{\partial t} + \nabla \gamma m_e c^2 = -e\mathbf{E} - \frac{e}{c}\mathbf{v}_e \times \boldsymbol{\Omega}_e,$$
$$\boldsymbol{\Omega}_e = \mathbf{B} - \frac{c}{e}\nabla \times \mathbf{p}_e, \quad (11)$$

the electron continuity equation

$$\frac{\partial n_e}{\partial t} + \nabla \cdot (n_e \mathbf{v}_e) = 0, \quad (12)$$

and Maxwell's equations

$$\nabla \times \mathbf{B} = \frac{4\pi e}{c}(z_i n_i \mathbf{v}_i - n_e \mathbf{v}_e) + \frac{1}{c}\frac{\partial \mathbf{E}}{\partial t} \quad (13)$$

and

$$-\frac{1}{c}\frac{\partial \mathbf{B}}{\partial t} = \nabla \times \mathbf{E}. \quad (14)$$

We also write out Poisson's equation, which plays an especially important role in further analysis:

$$\nabla \cdot \mathbf{E} = 4\pi e(z_i n_i - n_e). \quad (15)$$

Here, $m_e$ and $\mathbf{p}_e = \gamma m_e \mathbf{v}_e$ are the mass of an electron and its momentum, $\gamma = 1/\sqrt{1 - \mathbf{v}_e^2/c^2}$ is the relativistic factor, $\mathbf{v}_e$ and $n_e$ are the electron velocity and electron density, and $\mathbf{E}$ and $\mathbf{B}$ are the electric and magnetic fields.

Taking the curl of Eq. (11) and using induction equation (14), we can obtain the following vector equation for the conservation of vorticity $\boldsymbol{\Omega}_e$:

$$\frac{\partial \boldsymbol{\Omega}_e}{\partial t} = \nabla \times (\mathbf{v}_e \times \boldsymbol{\Omega}_e). \quad (16)$$

In what follows, all quantities will be assumed to depend only on the radial coordinate $r$. Consequently, the magnetic field can vary only at the expense of variations of the electric fields $E_\theta$ and/or $E_z$. With the use of Eq. (16), there is no need to explicitly incorporate these electric field components in describing the filament dynamics.

Below, in different particular cases, we introduce the Lagrangian invariants $I_1 = \Omega_{e\theta}/(rn_e)$ and $I_2 = \Omega_{ez}/n_e$, which completely determine the structure of the current filaments at a fixed ion density.

The ion dynamics is described by the hydrodynamic equations

$$\frac{\partial n_i}{\partial t} + \nabla \cdot (n_i \mathbf{v}_i) = 0,$$
$$m_i \frac{d\mathbf{v}_i}{dt} = z_i e\mathbf{E} + \frac{z_i e}{c}\mathbf{v}_i \times \mathbf{B} - \frac{1}{n_i}\nabla p_i, \quad (17)$$

where $n_i$ and $\mathbf{v}_i$ are, respectively, the density and velocity of the ions and $p_i$ is their pressure.

Of course, the question arises of whether the hydrodynamic approach is applicable to such extreme conditions. Estimates show that the ions are decelerated primarily because they lose their energy in collisions with electrons; consequently, the ion mean free path $l_i \sim \tau^{i/e}|\mathbf{v}_i|$ serves as a characteristic spatial scale in related physical problems. In our calculations, we ignore collisions; however, Sagdeev [49] has already pointed out that, under conditions like those in the highly nonquasineutral plasma under consideration, a collisionless shock wave can form on the spatial scale $r_B$, which, in the problem as formulated, turns out to be on the order of $l_i$ [14]. In this case, in our numerical simulations, the formation of steep fronts of the ion density and velocity in a collisionless shock wave is associated with the violation of plasma quasineutrality at the wave front.

For convenience of further calculations, we switch to dimensionless variables; this also allows us to determine the characteristic scales on which the physical quantities vary in space and time.

First of all, we introduce the main spatiotemporal scales—the characteristic time scale $t_0 = \omega_{pi}^{-1}$ and spatial scale $c/\omega_{pe}$—and switch to the dimensionless time $\tau$ and radius $\rho$:

$$t = \tau\sqrt{\frac{m_i}{4\pi e^2 z_i n_{e\infty}}}, \quad r = \rho\sqrt{\frac{m_e c^2}{4\pi e^2 n_{e\infty}}}. \quad (18)$$

We also introduce the dimensionless magnetic and electric fields,

$$B_{\theta,z} = b_{1,2}\sqrt{4\pi m_e c^2 n_{e\infty}}, \quad E_r = e_r\sqrt{4\pi m_e c^2 n_{e\infty}}, \quad (19)$$

and the dimensionless ion and electron velocities,

$$v_{ir} = uc\sqrt{\frac{z_i m_e}{m_i}}, \quad v_{ez,\theta} = cv_{1,2}. \quad (20)$$

Note that the radial electron velocity $v_{er}$ is small in terms of the parameter $\varepsilon = r_B/(ct_0) \ll 1$; it is normalized in the same way as the radial ion velocity.

For a filament with a helical magnetic field, the two different components of the dimensionless magnetic field and of the dimensionless electron velocity in relationships (19) and (20) are distinguished by subscripts 1 and 2. For filaments with a single (longitudinal or azimuthal) component of the magnetic field, the subscripts are omitted.

We note that, since the ions are insignificantly deflected the magnetic field on the spatial scale $r_B$, one can set, in accordance with inequalities (4), $r_\infty \sim c/\omega_{pi}$, which corresponds to the above-introduced densities $n_{e\infty}$ and $n_{i\infty}$.

It should be stressed that the Lagrangian invariants $I_1 = \Omega_{e\theta}/(rn_e)$ and $I_2 = \Omega_{ez}/n_e$, which are used in further

analysis, have different dimensions and thereby are normalized in different ways:

$$i_1 = I_1/(4\pi e), \quad i_2 = I_2\sqrt{n_{e\infty}/(4\pi m_e c^2)}. \tag{21}$$

The dimensionless ion pressure $p$ is introduced through the relationship

$$p_i = p n_{e\infty} m_e c^2, \tag{22}$$

which also determines the characteristic scale on which the ion energy varies (this scale was already mentioned in [1]).

Finally, the dimensional ion and electron densities at infinity are assumed to be related by the natural relationship $n_{e\infty} = z_i n_{i\infty}$, according to which the densities are normalized as follows:

$$n_e = n_{e\infty}\nu, \quad n_i = \frac{n_{e\infty}}{z_i} n. \tag{23}$$

The above normalization enables us to introduce the following dimensionless ion equations, which will be used in further calculations:

$$\frac{\partial n}{\partial \tau} + \frac{1}{\rho}\frac{\partial}{\partial \rho}(\rho n u) = 0, \tag{24}$$

$$\frac{\partial u}{\partial \tau} + u\frac{\partial u}{\partial \rho} = e_r - \frac{1}{n}\frac{\partial p}{\partial \rho}. \tag{25}$$

In the approximation adopted here, these equations are valid for filaments of any type. In this case, the particular expression of the dimensionless radial electric field $e_r$ is governed by the type of the filament in question.

With the equations introduced above, the plasma dynamics can only be studied for magnetic fields lying in the range

$$4\pi n_e m_e c^2 \ll B^2 \ll 4\pi n_i m_i c^2.$$

The left-hand inequality corresponds to the main assumption that the electron current structure is nonquasineutral on a spatial scale on the order of the magnetic Debye radius $r_B \sim B/(4\pi e n_e)$. According to the above normalization, the characteristic time scale is the inverse ion plasma frequency, $t_0 = \omega_{pi}^{-1}$. In this case, the right-hand inequality introduces the small parameter $\varepsilon = r_B/ct_0 \ll 1$, which indicates the quasistatic approximation for electrons and makes it possible to ignore the time-dependent term in Eq. (11) and to remove from consideration the ion motion on a scale of $r \sim r_B$ along the $z$ axis.

As will be seen below, in the $r$ component of the ion hydrodynamic equation

$$m_i\frac{d\mathbf{v}_i}{dt} = z_i e\mathbf{E} + \frac{z_i e}{c}\mathbf{v}_i \times \mathbf{B} - \frac{1}{n_i}\nabla p_i$$

we will ignore the term that describes the deflection of the ions by the magnetic field. The reason is that, in accordance with the right-hand inequality in conditions (4), this term is small for the radial scales of the Z-pinches under consideration. Using induction equation (14), we can reduce the $z$ component of the equation of ion motion to the following equation for the longitudinal ion velocity $v_{iz}$:

$$v_{iz} = \frac{z_i e}{m_i c}\int_\infty^r dr B_\theta. \tag{26}$$

Here, the symbol $\infty$ refers to the far periphery of the filament, $r(\infty) \sim c/\omega_{pi}$. The dimensionless equation for the $r$ component of the equation of ion motion takes the form

$$\frac{du}{d\tau} = e_r - \frac{1}{n}\frac{\partial p}{\partial \rho} - \frac{z_i m_e}{m_i} b\int_\infty^\rho d\rho b, \tag{27}$$

where $e_r$ is the dimensionless electric field. Conditions (2) make it easy to verify that

$$b^2 \ll \frac{m_i}{z_i m_e} n, \tag{28}$$

so the last term in Eq. (27) can be discarded. This indicates that, even for the maximum possible magnetic-field strengths, which correspond to the right-hand side inequality in conditions (2), the deflection of the ions by the magnetic field can be ignored, provided that their density $n$ is moderate and that the dimensionless radius $\rho$ is about several units (in the numerical calculations described here, the maximum value of $\rho$ was $\rho_0 = 3$).

The above considerations make it possible to formulate the problem about the possible mechanism for ion acceleration in a situation in which the current flowing through a plasma filament produces a magnetic field that magnetizes the electrons but has a minor effect on the ion motion. In a plasma with an initially uniform ion density, the electrons are magnetized by the magnetic field. Being diamagnetic, they are localized predominantly in the region where the field is weak. This process gives rise to charge separation on a spatial scale of $r_B \sim B/(4\pi e n_e)$ and generates a strong electric field that accelerates ions to high energies. The strength of this electric field can be estimated from Poisson's equation (15),

$$E_r \sim 4\pi e n_e r_B, \tag{29}$$

which allows us to estimate the ion energy $\varepsilon_i$ by

$$\varepsilon_i \sim z_i e\Phi \sim z_i \frac{B^2}{4\pi n_e}. \tag{30}$$

As a result, using conditions (2), we arrive at the following range of energies to which the ions can be accelerated by the mechanism under consideration:

$$z_i m_e c^2 \ll \varepsilon_i \ll m_i c^2. \tag{31}$$

## 4. VORTEX STRUCTURES WITH A LONGITUDINAL MAGNETIC FIELD $B_z$

In accordance with the above, a current filament produced as a result of the Weibel instability of a high-power laser electromagnetic wave propagating in plasma can serve as an efficient ion accelerator based on Coulomb explosion. The main difference between the model of an electron vortex proposed in [19] and Abrikosov's model of vortices is that the former model, along with the basic equation for the electron vorticity,

$$\mathbf{\Omega}_e = \mathbf{B} - \frac{c}{e}\nabla \times \mathbf{p}_e$$

also deals with Poisson's equation because of the violation of plasma quasineutrality on a spatial scale of about $\sim r_B$ [14].

Since the quasineutrality at the axis of an electron vortex is violated, the electron density decreases and the arising electric field begins to accelerate the ions, thereby leading to the formation of a collisionless shock wave on a time scale of about $\sim \omega_{pi}^{-1}$. During this acceleration process, the structure of the electron vortex becomes sensitive to the ion density profile, which results in a redistribution of the magnetic field and the destruction of the vortex structure. A key element in the process under analysis is the cavity that forms in the electron density and in which the vorticity is nonzero. The way by which the cavity is produced is unimportant: thus, the role of the driving mechanism can be played by the ejection of the electron plasma component by the laser pulse; in this case, a decrease in the plasma density facilitates the onset of a plasma state with a nonzero vorticity and the cavity so created may initiate Coulomb explosion. At this point, it is necessary to emphasize the difference between, on the one hand, the plane geometry in the traditional problem about the propagation of a laser pulse and, on the other, the cylindrical geometry in the problem that will be formulated below. In our model, the direction of the azimuthal coordinate $\theta$ in the vortex corresponds to the propagation direction of the laser pulse along the $y$ axis and the ion motion along the radial coordinate $r$ corresponds to the transverse plasma expansion along the $x$ coordinate. Note that, in both cases, the quasistatic magnetic field is directed along the $z$ axis.

The approach proposed here implies that the Coulomb explosion proceeds in two stages independent of one another. In the first stage, the structure is rearranged on a time scale of about $\sim \omega_{pe}^{-1}$. This is accompanied by the generation of electron vorticity and the violation of plasma quasineutrality, the plasma ions being immobile. In the second stage, the nonquasineutrality-related electric field sets the ions into motion, thereby destroying the vortex "quasi-particle" on a time scale of about a few $\omega_{pi}^{-1}$.

We can readily verify that, in an axisymmetric case, the radial expansion of the ions under the action of the radial electric field $E_r$ is accompanied by their motion in the direction along the azimuthal coordinate $\theta$. Although the azimuthal velocity of the ions is low in comparison to their radial velocity, $v_{i\theta} \sim (r_B/ct_0)v_{ir}$ (where $t_0$ is the characteristic ion time), the ion motion along the azimuthal coordinate $\theta$ is of fundamental importance because only this motion is capable of maintaining the azimuthal electric field $E_\theta$, which, at $\partial/\partial\theta \equiv 0$, leads to variations in the longitudinal magnetic field $B_z$.

In what follows, in describing the dynamics of an electron vortex structure, we will use the notion of the Lagrangian invariant, whose main property is that it is conserved along the electron trajectories, provided that collisions are ignored [50].

The equation for the Lagrangian invariant $I \equiv \Omega_{ez}/n_e$ can be derived from Eq. (16) with the use of electron continuity equation (12) in a way analogous to that in [19]:

$$\frac{\partial I}{\partial t} + v_{er}\frac{\partial I}{\partial r} = 0. \tag{32}$$

Here, the expression for the radial component $v_{er}$ of the electron velocity can be obtained from Eq. (13):

$$v_{er} = \frac{z_i n_i}{n_e} v_{ir} + \frac{1}{4\pi e n_e}\frac{\partial E_r}{\partial t}. \tag{33}$$

By virtue of the assumption of axisymmetry, expression (33) does not contain the term that accounts for the magnetic field. In the initial stage of the filament evolution, the displacement current can play an important role because the radial electric field in the filament is strong. The dimensionless equation (33) implies that the rate of the radial variations in the Lagrangian invariant $I$ is determined by the characteristic ion velocity.

Because of the smallness of the azimuthal electric field $E_\theta$, the ions in an electron vortex move predominantly in the radial direction, which results in a rearrangement of the magnetic field and all the remaining vortex parameters. We stress that, in the non-steady-state case, the symmetry properties of the problem are responsible for the appearance of the induction electric field $E_\theta$, which changes the magnetic field $B_z$. However, our equations do not explicitly include the field component $E_\theta$ and we can show that the induction equation turns out to be equivalent to Eq. (3) for the electron Lagrangian invariant $I$. Hence, Eq. (32) for the Lagrangian invariant $I$ provides a convenient tool for describing the electron cavity. The azimuthal ion velocity $v_{i\theta}$, which also does not enter into the equations, can be calculated from the conservation law for the ion vorticity $\Omega_{iz}$ (see Section 3).

The dynamics of the ion plasma component is described by the hydrodynamic equations with a zero pressure. This indicates that, in the limiting case of strong magnetic fields, which will be analyzed below,

the ion acoustic effects will not be taken into account (see [20, 43]).

Hence, in investigating Coulomb explosion, we calculate the ion motion under the action of the electric field of a nonquasineutral electron vortex. The calculations are performed using hydrodynamic equations without allowance for the kinetic pressure. Note that, unlike in [19], the electron vortex structure is now essentially governed by the shape of the ion density profile but is independent of the ion velocity [51].

The above normalization procedure yields the following dimensionless equations for the parameters $v$, $\gamma = 1/\sqrt{1-v^2}$, $b$, and $\nu$, which characterize the structure of the electron filament [19, 20]:

$$\frac{\partial g}{\partial \rho} = \frac{\nu i - g}{\rho} - \frac{\gamma f}{\rho} - \nu \rho f, \tag{34}$$

$$\frac{\partial f}{\partial \rho} = \frac{\nu i - g}{\rho \gamma^3} - \frac{f}{\rho}, \tag{35}$$

$$\nu = \frac{\gamma^3 n + g^2 + \gamma^4 f^2}{\gamma + i(g + \gamma^3 f)}, \tag{36}$$

where $g = b + \gamma f$ and $v = -\rho f$.

These equations should be supplemented with the time-dependent equations describing the ion dynamics and the evolution of the Lagrangian invariant. Omitting the terms with the pressure in Eqs. (24) and (25) and switching to dimensionless variables in Eq. (33), we arrive at the following time-dependent equations describing the filament dynamics:

$$\frac{\partial u}{\partial \tau} + u\frac{\partial u}{\partial \rho} = e_r, \quad \frac{\partial u}{\partial \tau} + \frac{1}{\rho}\frac{\partial}{\partial \rho}(\rho n u) = 0, \tag{37}$$

$$\frac{\partial i}{\partial \tau} + \left(\frac{n}{\nu}u + \frac{1}{\nu}\frac{\partial e_r}{\partial \tau}\right)\frac{\partial i}{\partial \rho} = 0, \tag{38}$$

where the dimensionless radial electric field is given by the expression $e_r = -vg$.

In Eq. (36) for $\nu$, we take into account the change in the ion density, $n = n_i/n_{i\infty}$, which leads to a rearrangement of the structure of the electron filament. We can say that Eqs. (34)–(36) define an effective adiabatic functional $b \equiv b[n(\rho)]$ for the ions, which makes it possible to close the set of equations describing the ion dynamics. An approach to describing the current filament on the basis of Eqs. (34)–(36) is valid for electrons treated in the quasistatic approximation $r_B/ct_0 < 1$, which corresponds to magnetic fields lying in the range $B^2 < 4\pi n_i m_i c^2$.

Numerical integration of Eqs. (34)–(38) shows the formation of a collisionless shock wave on a characteristic spatial scale of about $\delta \sim r_B$ (such waves were first considered by Sagdeev [49, 52, 53]). Figure 3 presents initial radial profiles of the dimensionless Lagrangian invariant $i$, magnetic field $b$, and electron velocity $v$ in an electron vortex structure. Figure 4 displays the profiles of the same physical quantities at a time when the shock wave has already been formed. We can see that, as the shock wave propagates toward the filament periphery, the energy of the electron filament is converted into the energy of the ions, and the electron

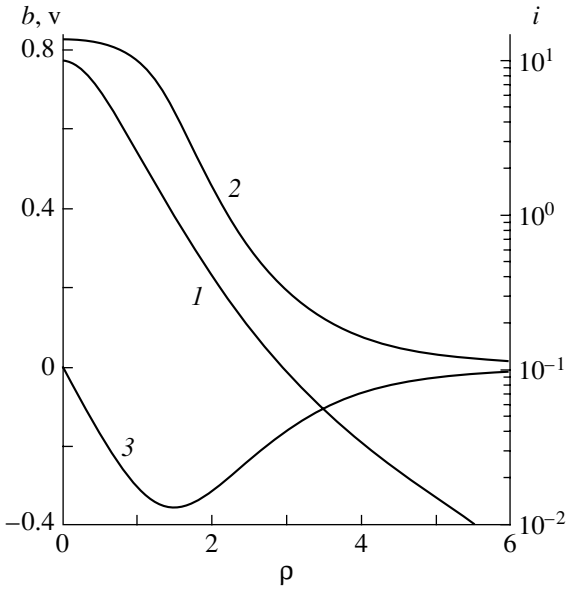


**Fig. 3.** Initial radial profiles of (*1*) the Lagrangian invariant, (*2*) magnetic field, and (*3*) electron velocity in a filament with a longitudinal magnetic field.

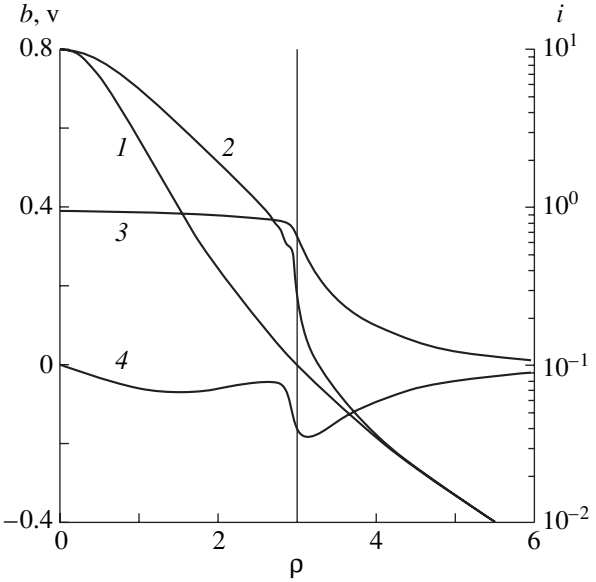


**Fig. 4.** (*1*) The initial radial profile of the Lagrangian invariant and the profiles of the (*2*) Lagrangian invariant, (*3*) magnetic field, and (*4*) electron velocity at the time $t = 3.5\,\omega_{pi}^{-1}$ in a filament with a longitudinal magnetic field. The vertical line corresponds to the front of the collisionless shock wave.

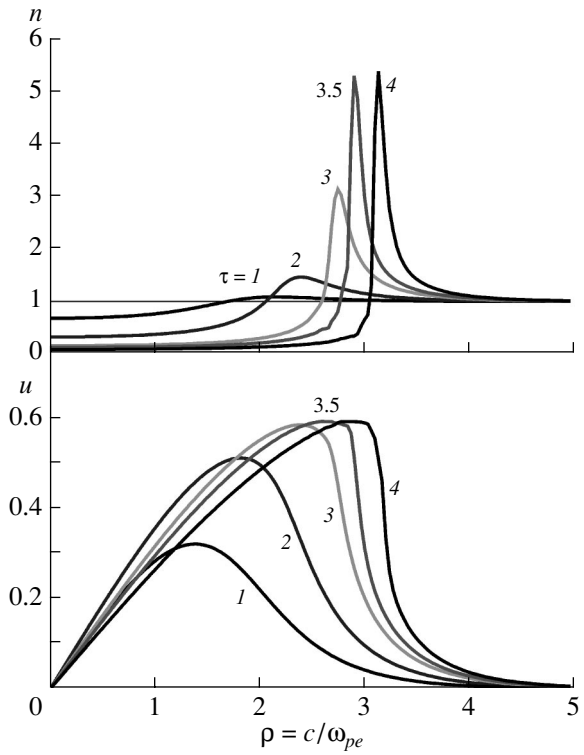


**Fig. 5.** Time evolution of the ion density $n$ and ion velocity $u$ during the ion expansion in the course of the formation of a shock wave in a filament with a longitudinal magnetic field.

velocity decreases very rapidly. In this case, the magnetic field $b$ behind the wave front equalizes and decreases during the propagation of the wave; thus, at large distances, the velocity of the shock wave decreases and the ions begin to expand inertially.

Numerical simulations show that the highly nonquasineutral plasma that was initially near the filament axis becomes quasineutral after the passage of a nonlinear wave. It follows from these simulations that, behind the wave front, the electron and ion densities are essentially the same (so, the plasma is quasineutral there) and that the characteristic length of the front agrees with the estimate $\delta \sim r_B$ obtained from the maximum electron density in the shock wave (see Fig. 5). We can also see that, as the ions are accelerated by the electric field, the wave front steepens progressively. In our earlier paper [20], we found that, for the characteristic values $b_0 \sim 1$, which correspond to the measurements carried out in [23], the magnetic field and electron density are about $B \simeq 10^7$ G and $n_e \simeq 10^{19}$ cm$^{-3}$, respectively, the maximum dimensionless radial velocity being about $u_{\max} \sim 0.7$. This allows us to estimate the maximum radial ion velocity by $v_{ir} \sim 3.5 \times 10^8$ cm/s, which correlates well with the experimentally recorded plasma expansion velocity after the passage of a laser pulse [23].

The main parameters that determine the structure of the electron filament are the Lagrangian invariant $I$ and the characteristic filament radius $r_0$. Calculations show that the ion energy depends weakly on the value of the Lagrangian invariant: when the invariant $i$ was varied within the range from 5 to 130 at $r_0 = c/\omega_{pe}$, the initial magnetic field $b_0$ at the axis changed by a factor of less than three and the dimensionless wave velocity $w$ changed from 0.41 to 0.95 [20]. The comparatively weak values of the dimensionless magnetic field at the filament axis ($b_0 \sim 1$) are governed by the above limiting effect of the electron inertia on the azimuthal currents (see the Introduction). In this case, the ion energy is estimated to be $\varepsilon_i \simeq z_i m_e c^2 u_{\max}^2/2$; in contrast to [1], this estimate takes into account the laser pulse intensity $I_{\text{laser}}$. The larger the value of the parameter $r_B/ct_0$, the more important the role of the azimuthal ion motion driven by the induction effects. For the above conditions of the laser pulse propagation along the $y$ axis, Krushelnick *et al.* [54] established experimentally that the plasma expands with the maximum velocity a right angle (90°) to the propagation direction of the laser pulse (the $x$ axis); this agrees well with the radial ion acceleration in an electron vortex. In this case, the generation of the fast ions that are accelerated in the direction opposite to the propagation direction of the laser pulse (i.e., in the negative direction of the $y$ axis) just corresponds to the ion acceleration by the induction electric field along the negative direction of the azimuthal coordinate $\theta$ ($v_{i\theta} < 0$).

In order to gain insight into the mechanisms for the formation of a collisional shock wave, we turn to the known theoretical results [49, 52, 53]. The most important aspect of our approach is that we have introduced the Lagrangian invariant as a physical quantity. In view of the steepening of the profile of the Lagrangian invariant $I$ at the wave front, we can also introduce a certain quantity $I_0$ in order to characterize the invariant on a small scale within the front. This provides an analytic description in the case of plane geometry at strong magnetic fields such that $B^2 > 4\pi n_e m_e c^2$, which, for the parameter values adopted here, is equivalent to the condition $a > 1$. In particular, one can obtain the following equation for the magnetic field profile $B(x)$:

$$\frac{\partial}{\partial x}\left(\frac{1}{B}\frac{\partial B}{\partial x}\right) = \left(\frac{4\pi e}{I_0}\right)^2 \frac{B(W - v_{ix}) - n_{e\infty} I_0 W}{B(W - v_{ix})}, \qquad (39)$$

where $W$ is the velocity of a nonlinear wave propagating in the $x$ direction and the ion velocity $v_{ix}$ can be expressed in terms of the magnetic field strength $B$. It can be seen that the characteristic spatial scale of the wave is $\delta \sim r_B$.

## 5. CURRENT FILAMENTS WITH AN AZIMUTHAL MAGNETIC FIELD $B_\theta$

We now consider the structure and dynamics of a filament with an azimuthal magnetic field. The equations for an electron filament will be derived with the use of

the small parameter $\varepsilon = r_B/ct_0 \ll 1$; this way guarantees that the electron structure will be quasistatic. In order to arrive at the desired equation we turn to Eq. (11) and also to the drift equation

$$\mathbf{E} + \frac{1}{c}\mathbf{v}_e \times \mathbf{B} = 0, \tag{40}$$

which is valid for $\varepsilon = r_B/ct_0 \ll 1$. Estimating the displacement current in Eq. (13) with the help of Eq. (40) and using the condition that the electric field is quasistatic, we obtain from Eq. (13) the following equation:

$$v_{ez} = -\frac{c}{4\pi e n_e r}\frac{\partial}{\partial r}(rB_\theta). \tag{41}$$

The definition of the electron vorticity component $\Omega_{e\theta}$ yields

$$\gamma^3\frac{\partial v_{ez}}{\partial r} = \frac{e}{m_e c}(\Omega_{e\theta} - B_\theta). \tag{42}$$

Finally, we extract the expression for $E_r$ from Eq. (40), substitute it into Eq. (15), perform differentiation, and make use of Eqs. (41) and (42) and of the definition of the Lagrangian invariant $I$:

$$I = \frac{\Omega_{e\theta}}{rn_e}. \tag{43}$$

As a result, we arrive at the following expression for the electron density $n_e$:

$$n_e\left(\gamma + \frac{rB_\theta I}{4\pi m_e c^2}\right) = \gamma^3 z_i n_i + \frac{B_\theta^2}{4\pi m_e c^2}. \tag{44}$$

Switching in the above equation to dimensionless variables just as was done in Section 3, we obtain the set of equations describing the quasistatic electron current structure (see also [14]):

$$\frac{1}{\rho}\frac{\partial}{\partial\rho}(\rho b) = -\nu v, \quad \gamma^3\frac{\partial v}{\partial\rho} = \rho\nu i - b, \qquad \nu = \frac{n\gamma^3 + b^2}{\gamma + \rho i b}. \tag{45}$$

We can see that, for a given ion density $n$, the structure of the filament is completely determined by the radial profile of the Lagrangian invariant $i$. In Eqs. (45), describing the filament structure, the time plays the role of a parameter because the electron equilibrium state in question is quasistatic.

In this formulation of the problem, the dynamics of an electron current structure is governed by the relatively slow ion motion in an electric field. In the present paper, in ion hydrodynamic equations (17), we take into account only the longitudinal motion of the ions because, in view of inequality (2), their motion in the $z$ direction can be ignored in accordance with the estimates made in Section 3. In addition, all the parameters of the problem are assumed to depend only on the radial coordinate $r$, so the kink instabilities and sausage-type instabilities, which are typical of Z-pinches, cannot be considered here.

Using Eq. (16) and electron continuity equation (12), we can obtain the equation for the Lagrangian invariant $I = \Omega_{e\theta}/(rn_e)$ that coincides formally with Eq. (32) for a filament with the longitudinal magnetic field. Switching to the corresponding dimensionless variables, we arrive at the following time-dependent dimensionless equations, which enable us to close the set of equations (45) and to determine the time-dependent ion density $n$ and the Lagrangian invariant $i$:

$$\frac{\partial n}{\partial\tau} + \frac{1}{\rho}\frac{\partial}{\partial\rho}(\rho n u) = 0, \quad \frac{\partial u}{\partial\tau} + u\frac{\partial u}{\partial\rho} = e_r - \frac{1}{n}\frac{\partial p}{\partial\rho}, \tag{46}$$

$$\frac{\partial i}{\partial\tau} + \left(\frac{n}{\nu}u + \frac{1}{\nu}\frac{\partial e_r}{\partial\tau}\right)\frac{\partial i}{\partial\rho} = 0, \tag{47}$$

where the dimensionless radial electric field is given by the expression $e_r = vb$. The ion pressure is described by the adiabatic equation of state with an adiabatic index equal to 2,

$$p = \lambda\frac{n^2}{2}. \tag{48}$$

We use the initial conditions $n(\tau = 0) = 1$ and $u(\tau = 0) = 0$ and the boundary conditions $n(\rho = \infty) = 1$ and $u(\rho = 0) = u(\rho = \infty) = 0$. With the chosen adiabatic index, we have carried out numerical simulations for several values of $\lambda$ or, equivalently, for several different ion pressures. Note that the choice of the adiabatic law in the form (48) is somewhat incorrect because the pressure at infinity is certainly equal to zero. However, in the case at hand, this choice does not lead to contradictions, because the formulas contain the derivatives of the pressure $p$ and because, for the region where $n \gg 1$, the form of the adiabatic law is quite unimportant.

Equations (45)–(47) can be divided into two sets: (i) time-independent equations (45) for calculating a steady-state electron vortex in an azimuthal magnetic field (these are ordinary differential equations, from which the functions $b$, $v$, and $\nu$ are determined for given values of $n$ and $i$) and (ii) time-dependent equations (46) and (47) for calculating the ion dynamics and the evolution of the Lagrangian invariant $i$ (these are partial differential equations describing the transport of the quantities $n$, $u$, and $i$ with the corresponding rates). Equations (45) were integrated by the Gear method [55]. Among the integral curves that originate from the singular point $r = 0$, which is a removable singularity, the curves that satisfy the boundary conditions at $r \longrightarrow \infty$ were chosen by adjusting the value of $\nu$ at $r = 0$. Equations (46) and (47) were integrated by a modified version of the Boris–Book method (specifically, the LCPFCT version [56]), which is the nonlinear flux-corrected transport (FCT) algorithm, ensuring that the solution will always be monotonic and positive. In the numerical integration of the equations of ion motion by

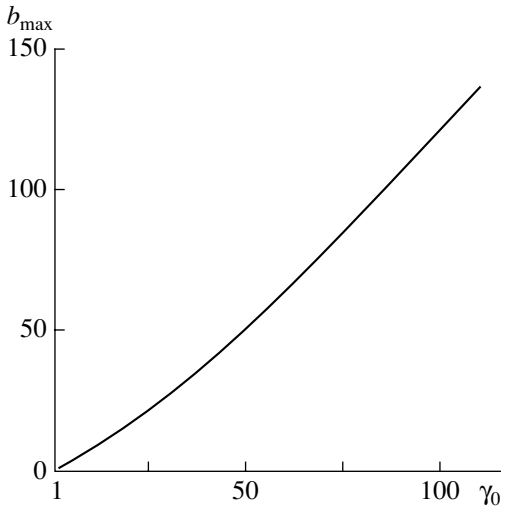


**Fig. 6.** Maximum dimensionless magnetic field $b_{max}$ as a function the electron relativistic factor $\gamma_0$ at the axis of a filament with an azimuthal magnetic field.

the LCPFCT algorithm, artificial viscosity resulted implicitly from the use of a controlled antidiffusive correction.

It is obvious that, on time scales much shorter than the characteristic time $\omega_{pi}^{-1}$ of the evolution of the ion plasma component, an electron filament can be considered to be a quasisteady structure. From the electron equations, the potential of an electron current filament can be estimated as $U \sim J/c$ (where $J$ is the current flowing on the spatial scale $r_B$ within the filament) [21]. Even for currents of about $J \sim 100$ kA, this yields a potential in excess of one megavolt.

By using dimensionless equations (45) describing electron equilibrium, we can obtain the following expression for the absolute value of the dimensionless potential $\varphi_0$ at the axis of a current filament:

$$|\varphi_0| = 1 - \gamma_0 + \frac{2i_0}{\rho_0^2}\int_0^\infty \frac{b\rho^2 d\rho}{\left(1 + \dfrac{\rho^2}{\rho_0^2}\right)^2}. \qquad (49)$$

Here, the potential at infinity is assumed to be zero, the ions are assumed to be immobile, and the dimensionless Lagrangian invariant $i$ at the initial instant has the form

$$i = \frac{i_0}{1 + \dfrac{\rho^2}{\rho_0^2}},$$

where $\rho_0$ is the characteristic spatial scale of the current filament structure. For numerical simulations, we chose the value $\rho_0 = 3$. In expression (49), the relativistic factor of the electrons at the axis, $\gamma_0$, determines the height of the peak in the electron density in the axial region, $\nu_0 = \gamma_0^2$.

Calculations performed on the basis of expression (49) for two initially equilibrium filaments with the currents $J_1 = 153$ kA and $J_2 = 191$ kA yielded the following two values of the potential at the axis: $U_1 = -6.0$ MV and $U_2 = -9.1$ MV. That the values of the potential are so high is confirmed to some degree by the experimental results of [8], where, at a total current of $J \sim 400$ kA, ions with an energy of about 1 MeV were recorded by measuring the Doppler shift of their spectral lines. These high values of the potential in the filament also correlate with the numerical results obtained in [18], where the ions were found to be accelerated to energies of several MeV.

It is also instructive to present the maximum magnetic field strengths $b_{max}$ in electron filaments at different values of $\gamma_0$. Figure 6 shows the dependence $b_{max}(\gamma_0)$ calculated for a wide range of $\gamma_0$ values. We can see that the relativistic factor of the electrons at the axis increases with the magnetic field in the filament. As a result, the electron–ion collisions in the system are in fact "switched off."

It is important to stress here that the model structure of the electron current filaments under discussion differs substantially from the fine structure of filaments that was calculated numerically by Sakai *et al.* [18]. In that paper, the total current in the filaments produced by an electron beam propagating in a plasma is zero because, on very short time scales, the current of fast beam electrons generates a return current, which is able to flow in the absence of dissipation over a fairly long time. In the approach developed here, it is assumed that, although the return current is initially generated by the current flowing in a filament (at the expense of the applied electric field $E_z$), it dissipates on comparatively short time scales. As a result, only the current flowing in the direction of the applied field remains within the filament. Estimates show that, under conditions where the initial electric conductivity is fairly low, the return current on micron scales is dissipated sufficiently rapidly. It is because of the absence of the return current that, in our model, the filament does not expand and the ions are not accelerated toward the filament periphery, in contrast to the numerical results presented in [18]. However, despite the above differences between the two approaches, the characteristic radius of the electron filaments calculated in [18] turns out to be approximately equal to the magnetic Debye radius, which can be estimated by $r_B \simeq c/\omega_{pe}\sqrt{\varepsilon_i/(m_e c^2)}$, where $\varepsilon_i$ is the calculated energy of the accelerated ions.

Figure 7 illustrates the initial equilibrium of an electron current structure with unperturbed ions. We can see that the electron density in the initial state is peaked near the axis of the structure. The peak produces a radial electric field directed toward the axis. The rela-

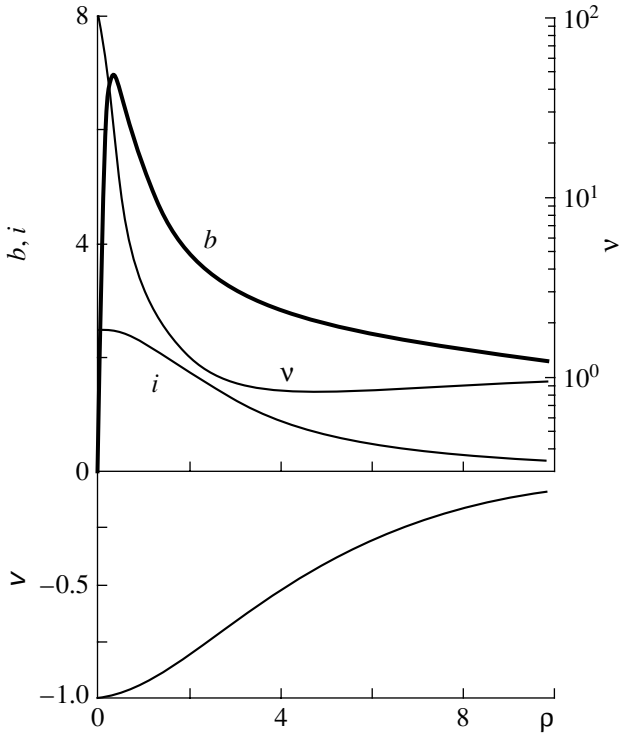


**Fig. 7.** Radial profile of the Lagrangian invariant $i$ in a filament with an azimuthal magnetic field and with a current of $J_2$ = 191 kA and the calculated initial radial profiles of the magnetic field $b$, electron density ν, and electron velocity $v$.

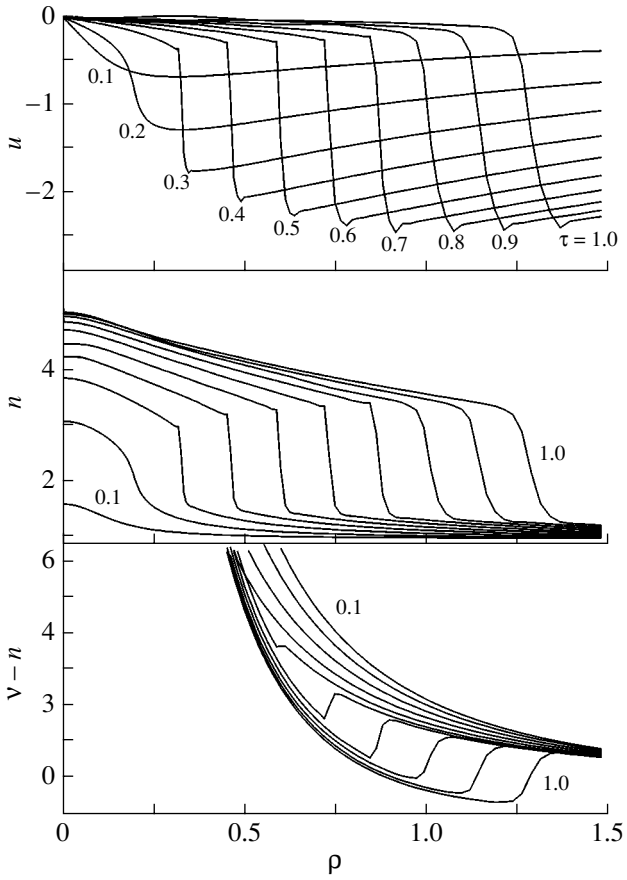


**Fig. 8.** Formation of a collisionless unloading shock wave within a current filament in the initial stage of deceleration of the inwardly accelerated ions by the pressure gradient in the dense core of a Z-pinch: $u$ is the ion velocity, $n$ is the ion density, and ν–$n$ is the charge density at the shock front.

tivistic electron motion in the $z$ direction generates an azimuthal magnetic field; in this case, the electrons themselves drift in crossed electric and magnetic fields. Such a filament is a universally encountered formation, the structure of which changes due to the slow motion of unmagnetized ions in its electric field [14, 16]. The numerical results obtained in [18] confirm fairly well the validity of the model used in our simulations. The characteristic radius of the filaments was calculated to be on the order of $r_B$, which agrees with the estimates obtained for the parameters adopted in that paper.

Figure 8 shows time evolutions of the density $n$ and velocity $u$ of the ions moving in a radial electric field in the initial stage of development of the current filament. We can see that accelerated ions moving from the periphery are decelerated in the axial region by the pressure gradient of the ions that have been accumulated in the dense hot core near the axis. It follows from Fig. 8 that, at the beginning of the process (on time scales τ from about 0.2 to 0.5), the profiles of the ion density and velocity have already steepened and a discontinuity has appeared. As a result, after the time τ = 0.3, the forming unloading wave in which the radial ion velocity vanishes has a steep front, at which the accelerating electric field and decelerating pressure gradient cancel one another. This front, which has already become flatter on time scales τ ≃ 0.7–1, propagates toward the periphery of the current structure of the filament, leaving behind an essentially immobile, dense hot core. A comparison of the profile of the dimensionless electric field, $e_r(\rho)$, with a narrow peak in the profile of the decelerating force, $(1/n)\partial p/\partial\rho$, shows that the front of the unloading wave occurs between the two surfaces whose radii are determined by the intersections of the profiles, $e_r(\rho) = (1/n)\partial p/\partial\rho$. Figure 8 shows that, at a time of about τ ~ 0.5, positive ion charge starts to be accumulated within the wave front, thereby weakening the electric field therein. It is presumably because of the weakening of the electric field (and, accordingly, the decrease in the electron drift velocity) that the front of the unloading wave propagating toward the periphery divides the electron-drift region into two parts and forms an advancing "cloud" of drifting electrons (Fig. 9). In this case, the front of the increasing ion density profile and the front of the velocity profile of the decelerated ions in the wave propagating away from the axis occur just at the minimum (which falls to zero on longer time scales) of the absolute value of the electron velocity.

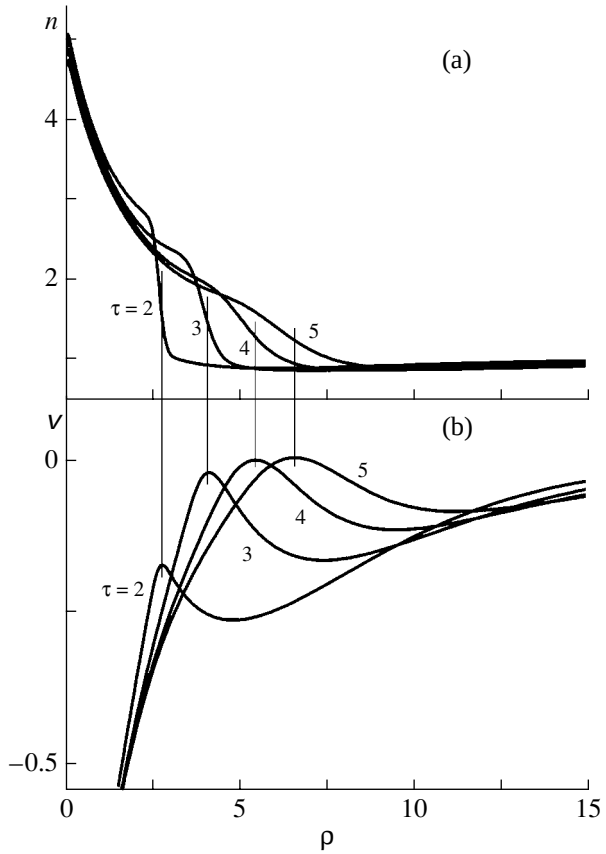


**Fig. 9.** Evolution of a cloud of drifting electrons ahead of the front of a nonlinear unloading wave propagating away from the axis of the filament: (a) the radial profiles of the ion density $n$ indicating the shock front and (b) the profiles of the electron velocity $v$.

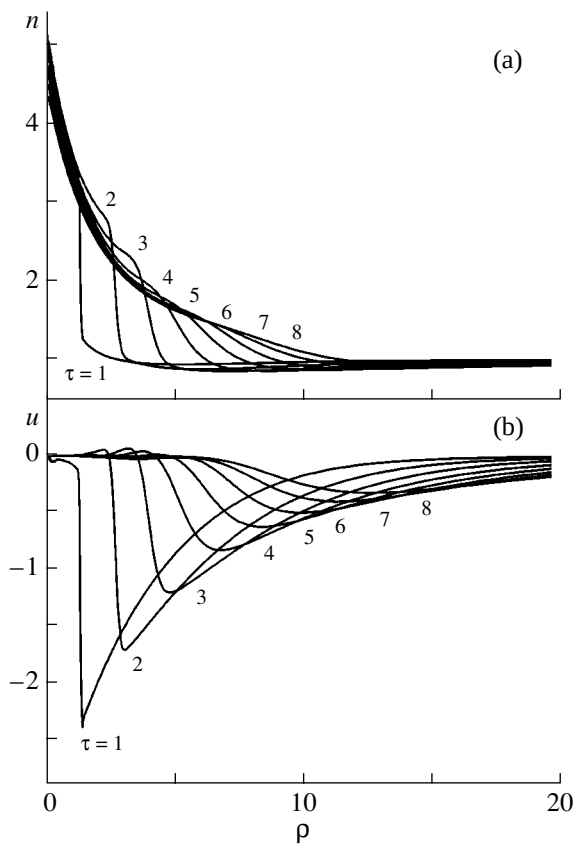


**Fig. 10.** Calculated profiles of the (a) ion density $n$ and (b) ion velocity $u$ within an unloading wave at successive times $\tau$ (in units of $\omega_{pi}^{-1}$) for the current $J_2$ = 191 kA.

Recall that, as a nonlinear unloading wave propagates toward the periphery, the profiles of all the quantities in the wave become flatter on time scales of $\tau > 1$. Consequently, the fact that the profiles of the quantities do not steepen within the wave allows us to interpret the wave in this propagation stage merely as a nonlinear unloading wave. The ion density and ion velocity profiles in this nonlinear wave on long time scales are shown in Fig. 10.

Note that, as the current $J$ increases and the initial temperature, which is described by the dimensionless parameter $\lambda$ (see adiabatic equation of state (48)), decreases, the ion density near the axis becomes higher. An increase in the steady-state ion density at the axis with decreasing $\lambda$ agrees with the experimental results of [9]. Calculations also show that, for a low initial ion temperature, the ion density at the filament axis can increase by several orders of magnitude as compared to its initial value.

As time progresses, the nonlinear unloading wave propagating toward the periphery becomes less intense and an equilibrium plasma structure with hot ions is formed. The ions in this structure are kept at equilibrium by magnetic and electric fields on a spatial scale on the order of $r_B$.

The Z-pinch configuration obtained above results from electrodynamic compression of the ion plasma component. The equilibrium state in which the configuration is maintained is described by the integral relationship

$$r^2(B_\theta^2 - E_r^2) + 8\pi\int_0^r dr r^2 \frac{\partial p_i}{\partial r} = 0, \qquad (50)$$

which implies that not only the magnetic but also the electric field plays an important role.

Our numerical calculations show that, e.g., for a Z-pinch of length $L$ = 1 cm, carrying the current $J_2$ = 191 kA, the energy transferred to the ions (primarily from the magnetic field) does not exceed 2–3 J (see also [8]). Thus, the characteristic energy deposition and the spatial and time scales of the processes in a micropinch with a current of about several hundred kiloamperes are found to be very close to those in a laser plasma produced by a focused laser pulse with an intensity on the order of $10^{19}$ W/cm$^2$ [23]. However, it should be kept in

mind that, in the problem of ion acceleration by the focused laser radiation, nonquasineutral plasma dynamics in a quasistatic magnetic field [14, 18] is as important as the direct action of the ponderomotive pressure force [23].

On longer time scales, the plasma structure is expected to evolve to an almost quasineutral equilibrium state. The experimentally observed destruction of the pinch structure on even longer time scales can be attributed to ion–ion collisions. Analytic estimates show that taking ion–ion collisions into account results in a self-similar expansion of the hot core of the Z-pinch on picosecond time scales [14, 57].

## 6. CURRENT FILAMENTS WITH A HELICAL MAGNETIC FIELD

In this section, we will extend the approaches that were used earlier to calculate the structure of filaments with a single magnetic-field component to the case of filaments with a field having two components, $B_z$ and $B_\theta$.

From the equation of electron motion and electron continuity equation, we can readily obtain the following three equations for the three components of the electron vorticity in the presence of an arbitrary magnetic field:

$$\frac{d}{dt}\left(\frac{\Omega_{er}}{n_e}\right) = \frac{\mathbf{\Omega}_e}{n_e}\cdot\nabla v_r, \quad (51)$$

$$\frac{d}{dt}\left(\frac{\Omega_{e\theta}}{rn_e}\right) = \frac{\mathbf{\Omega}_e}{n_e}\cdot\nabla\frac{v_\theta}{r}, \quad (52)$$

$$\frac{d}{dt}\left(\frac{\Omega_{ez}}{n_e}\right) = \frac{\mathbf{\Omega}_e}{n_e}\cdot\nabla v_z. \quad (53)$$

Since $B_r = 0$, it is quite natural to assume that $\Omega_{er} = 0$. In this case, the equilibrium configurations such that

$$\partial/\partial\theta \equiv \partial/\partial z \equiv 0 \quad (54)$$

are described by two time-dependent equations for the Lagrangian invariants in which only the derivative with respect to $r$ is taken into account in the total time derivative. Note that the question of how a filament evolves into such a configuration remains open. If a filament will still evolve in one way or another to a structure whose parameters depend only on $r$, then this structure will be described by the following equations for the two Lagrangian invariants $I_1 = \Omega_{e\theta}/(rn_e)$ and $I_2 = \Omega_{ez}/n_e$:

$$\left(\frac{\partial}{\partial t} + v_{er}\frac{\partial}{\partial r}\right)I_{1,2} = 0. \quad (55)$$

In terms of the corresponding dimensionless quantities, the main equations describing a filament with a helical magnetic field take the form

$$\gamma\frac{\partial v_1}{\partial\rho} = (1 - v_1^2)(\rho\nu i_1 - b_1) + v_1 v_2(\nu i_2 - g_2), \quad (56)$$

$$\gamma\frac{\partial v_2}{\partial\rho} = -(1 - v_2^2)(\nu i_2 - g_2) - v_1 v_2(\rho\nu i_1 - b_1), \quad (57)$$

$$\nu v_2 = \frac{\partial b_2}{\partial\rho}, \quad -\nu v_1 = \frac{1}{\rho}\frac{\partial}{\partial\rho}(\rho b_1), \quad (58)$$

where

$$g_2 = b_2 - \frac{\gamma v_2}{\rho} > 0, \quad v_1 v_2 > 0,$$
$$\nu = \frac{\gamma n + 2v_1 v_2 b_1 g_2 + \gamma^2 v_2^2/\rho^2 + (1 - v_1^2)b_1^2 + (1 - v_2^2)g_2^2}{1/\gamma + \rho i_1[v_1 v_2 g_2 + (1 - v_1^2)b_1] + i_2[v_1 v_2 b_1 - \gamma v_2/\rho + (1 - v_2^2)g_2]}. \quad (59)$$

Note that, for a filament with a helical magnetic field, the dimensionless radial electric field is given by the expression $e_r = v_1 b_1 - v_2 g_2$.

A steady-state configuration calculated from these equations is shown in Fig. 11. A distinctive feature of this equilibrium state is that the electric field changes its sign at a certain radius. As a consequence, the ion dynamics in this case should be more complicated than that in the above cases of filaments with a single magnetic field component.

## 7. CURRENT FILAMENTS ON DIFFERENT SPATIOTEMPORAL SCALES

In this review, we have analyzed the results of experiments with laser plasmas and with Z-pinch plasmas in terms of the concept of filaments in which the presence of a quasistatic magnetic field plays a key role in the evolution of a dense plasma with a characteristic density of $n_e \sim 10^{20}$ cm$^{-3}$ to a quasi-steady force equilibrium state on time scales on the order of several inverse ion plasma frequencies $\omega_{pi}^{-1}$. If the interpretation developed

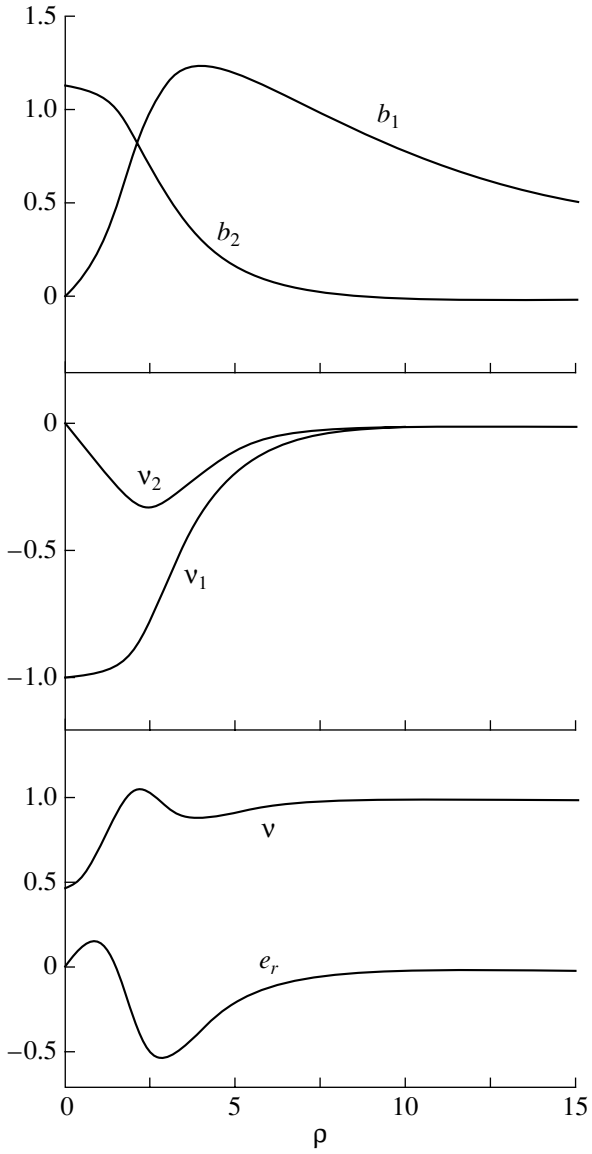


**Fig. 11.** Initial radial profiles of the dimensionless azimuthal magnetic field $b_1$, longitudinal electron velocity $v_1$, longitudinal magnetic field $b_2$, azimuthal electron velocity $v_2$, electron density ν, and radial electric field $e_r$ in a filament with a helical magnetic field.

here to describe the vortex structures is valid, then similar structures should occur on spatial scales other than those considered above. Up to this point, we have been interested in plasmas with a characteristic density of $n_e \sim 10^{20}$ cm$^{-3}$, the characteristic transverse dimensions of the objects under investigation being about 1 μm. It is obvious, however, that, if the proposed approach correctly describes the plasma processes in question, then analogous vortex structures occurring on other spatial scales should also be revealed. Substantially shorter spatial scales refer to clusters (with sizes in the range of $l \sim 10^{-6}$ cm) [58] and to the objects of quantum theory; in this case, the approach used here to study the above effects should be substantially modified. At the same time, for larger scale filaments, the approach can be used without any significant modification (even with allowance for ion–neutral collisions [59]).

In this context, we first illustrate the possible parameters of filaments with an arbitrary magnetic field in the Earth's ionosphere. Such filaments can occur under the action of, e.g., the solar wind during periods of high solar activity.

In order to systematically extend our approach to larger scale structures, we introduce several dimensionless coefficients that determine scaling from current filaments in high-density laboratory plasmas (the relevant physical quantities will be denoted by the subscript 0) to low-density structures in the Earth's ionosphere (for which the subscript 1 will be used). We assume that, in both cases, all of the processes proceed in precisely the same way, which allows us to utilize the same dimensionless equations. In order to describe scaling relationships between the dimensional quantities, we introduce the dimensionless coefficients mentioned above and assume that the physical parameters of the ionospheric plasma structures under consideration satisfy inequalities (2), which are the main conditions of our model.

We introduce three dimensionless coefficients and write out the following three basic relationships between the physical quantities:

$$B_0 = \lambda_1 B_1, \quad n_0 = \lambda_2 n_1, \quad E_0 = \lambda_3 E_1. \tag{60}$$

In this way, we can easily verify that the parameters of the structures in high-density laboratory plasmas and in a low-density ionospheric plasma satisfy the following relationships:

$$r_1 = \frac{\lambda_2}{\lambda_1} r_0, \quad v_1 = \frac{\lambda_1}{\lambda_3} v_0, \quad I_1 = I_0, \quad U_1 = \frac{\lambda_2}{\lambda_1 \lambda_3} U_0. \tag{61}$$

If we also introduce the dimensionless parameter $\Lambda_0$,

$$\Lambda_0 = \frac{B_0^2}{4\pi n_0 m_e c^2} \gg 1, \tag{62}$$

then, in order to satisfy the condition $\Lambda_1 \gg 1$ (which corresponds to the ionospheric plasma), it is necessary that

$$\lambda_1^2 \simeq \lambda_2. \tag{63}$$

We assume that the electrons in both situations are relativistic; in this case, we have $\lambda_1 \simeq \lambda_3$. Assuming also that condition (63) holds, we obtain the following relationships between the physical parameters of a micropinch in the laboratory plasma and a current structure in the ionospheric plasma:

$$r_1 \simeq \lambda_1 r_0, \quad n_1 \simeq \frac{n_0}{\lambda_1^2}, \quad U_1 \simeq U_0. \tag{64}$$

Let us determine the characteristic spatiotemporal scales of current structures in the ionospheric plasma, assuming that the magnetic field and plasma density in the Earth's ionosphere are about $B_1 \simeq 1$ G and $n_1 \simeq 10^5$ cm$^{-3}$, respectively [60]. In this case, from the relationship $B_0 \simeq \sqrt{4\pi n_0 m_e c^2} \simeq 3 \times 10^7$ G, we find

$$\lambda_1 \simeq 3 \times 10^7, \quad \lambda_2 \simeq 10^{15}. \tag{65}$$

This indicates that the characteristic transverse dimension of a current structure in the ionosphere is about $r_1 \simeq 30$ m. In this case, the time scale on which the structure evolves should be about $t_1 \simeq 3 \times 10^{-5}$ s and the electron and ion energies in an ionospheric structure should coincide with those of the charged particles in a micropinch.

Let us present analogous estimates for the interstellar medium [61], in which the mean magnetic field is on the order of

$$B \simeq 3 \times 10^{-6} \text{ G}, \tag{66}$$

and the mean electron density is about

$$n_e \simeq 10^{-7} \text{ cm}^{-3}. \tag{67}$$

Performing the relevant calculations, we find

$$\lambda_1 \simeq 10^{13}, \quad \lambda_2 \simeq 10^{27}. \tag{68}$$

With these relationships, the characteristic transverse dimension of a filament in the interstellar medium is estimated by $r_1 \simeq 10^5$–$10^6$ km, the characteristic evolution time being about $t_1 \simeq 1$ s.

Interestingly, when a similar approach is applied to the dart leader of lightning, where the electron density is on the order of $n_e \simeq 10^{14}$ cm$^{-3}$, we have $\lambda_2 \simeq \lambda_1^2 \simeq 10^6$ and the characteristic radius of the current channel is equal to $10^{-1}$ cm, which corresponds to a magnetic field of $B_1 \simeq 10^4$–$3 \times 10^4$ G. In this case, the ion dynamics in the current filament is strongly affected by ion–neutral collisions because of the very low degree of ionization in the current channel [59].

## 8. CONCLUSIONS

The above analysis shows that, in laser experiments with high-density plasmas created by focused laser pulses and in high-precision experiments with X-pinches, the fundamental object is a filament in which the quasistatic magnetic field is as strong as about $B \sim 10^7$–$3 \times 10^7$ G and which develops on a time scale on the order of the inverse electron plasma frequency $\omega_{pe}^{-1}$. Because of the nonquasineutrality of such a filament, the strong electric field accelerates ions to megaelectronvolt energies [62, 63].

We have demonstrated the existence of a universal nonquasineutral electron current structure—a filament with a strong quasistatic magnetic field that is maintained by the self-consistent electron drift current produced by the strong charge-separation radial electric field.

In filaments with a longitudinal magnetic field, a cavity in the electron density is produced and a strong radial electric field directed toward the filament periphery is generated. The ions expanding in this field away from the filament axis form a collisionless shock wave. Behind the wave front, the magnetic field equalizes and the energy of the electrons rotating within the filament is converted into the energy of the accelerated ions.

A filament with a nonzero ion pressure can evolve into a steady state in which the electromagnetic field pressure is balanced by the ion pressure [33]. In contrast, in filaments with an azimuthal magnetic field, the electron density becomes peaked, which leads to the collapse of the ion plasma component toward the filament axis and to the formation of the dense hot core of the Z-pinch. The characteristic time scales on which such filaments evolve are on the order of the inverse ion plasma frequency $\omega_{pi}^{-1}$.

The larger the radius $r_0$ of the vortex, the higher the ion energy in it. For $r_0 \sim c/\omega_{pi}$, the quasistatic approximation for electrons is violated and it is also necessary to take into account the ion motion along the $z$ axis [32].

The generation of high-energy ions by filaments in a deuterium-containing plasma gives rise to a neutron pulse [64, 65]. The possibility of neutron generation in laser–plasma interaction is confirmed by the corresponding calculations [47, 66]. Further calculations yielded the laser pulse intensities that are required to produce pions [67]. The generation of neutrons at the shock front within a filament with a longitudinal magnetic field was calculated in our earlier paper [68].

Sholin and Baronova [69] pointed out that, because of the Stark effect, the spectrum of the helium-like lines of multicharged ions in strong radial electric fields ($E_r \sim 10^{10}$ V/cm) in a Z-pinch should contain a forbidden line, which, in the authors' opinion, was experimentally revealed by X-ray diagnostic technique.

It should be noted that the final stage of the X-pinch evolution, which was investigated experimentally by Pikuz *et al.* [9], is presumably dominated by collisions. Estimates show that collisions should destroy the filament on picosecond time scales. [14]. The process of this collisional destruction of the structure of the filaments can be regarded as an explosion of the "hot spots." Strictly speaking, the hot spot, by its definition, is a localized formation and its description should involve two-dimensional localized filaments in which the current forms a closed ringlike structure. This generalization of the above theoretical approach to investigating the equilibrium of the filaments requires the calculation of two-dimensional non-steady-state configurations. We must emphasize that ringlike current

structures were captured in particle-in-cell simulations in a number of papers [70–72].

Hence, in this review, we have considered a scenario of the acceleration of charged particles under the conditions of strong charge separation and have found that the quasistatic magnetic field plays a decisive role in the acceleration mechanism. Note that the experimental results obtained by Pikuz *et al.* [73] provide evidence that, in an X-pinch, there is a strong quasistatic magnetic field. The distortion of the emission spectra of Al that can be seen in the lower plot of Fig. 6 from that paper corresponds to a quasistatic magnetic field with a strength of about 30 MG. In this context, it is of interest to mention a review paper by Maksimchuk *et al.* [74], who presented experimental results on and described theoretical models of the acceleration of charged particles under the action of a focused laser pulse. That paper contains the data of numerous experiments on ion acceleration to energies above about 1 MeV; moreover, the data were interpreted under the assumption that the plasma is quasineutral, but nothing was said about the magnetic field. At the same time, in [13, 15, 42, 75], results were presented from measurements of megagauss (and even stronger) magnetic fields in laser experiments. In [76], it was shown that, in the limit $\mathbf{\Omega}_e = 0$, a filament with a magnetic field of several megagaus can arise in plasma under the action of a laser pulse. The fact that there is disagreement among physicists about the interpretation of the experimental results indicates that there is still no common opinion on particle acceleration in laser plasma. According to the above analysis, the ion acceleration is directly attributed to the generation of quasistatic magnetic fields. The theoretical and numerical results presented here can bring about a deeper understanding of the mechanisms for accelerating charged particles in laser plasmas and Z-pinches.

## ACKNOWLEDGMENTS

This work was supported in part by the Russian Research Centre Kurchatov Institute Program for the Support of Initiative Projects.

## REFERENCES

1. N. H. Burnett and G. D. Enright, IEEE J. Quantum Electron. **26**, 1797 (1990).
2. A. Pukhov, Rep. Prog. Phys. **66**, 47 (2003).
3. D. Umstadter, J. Phys. D **36**, 151 (2003).
4. D. D. Ryutov, M. S. Derzon, and M. K. Matzen, Rev. Mod. Phys. **72**, 167 (2000).
5. Yu. L. Bakshaev, P. I. Blinov, A. S. Chernenko, *et al.*, in *Proceedings of the International Conference on Research Application of Plasmas, Warsaw, 2001*, Paper PS-22.
6. Yu. L. Bakshaev, P. I. Blinov, V. V. Vikhrev, *et al.*, Fiz. Plazmy **27**, 1101 (2001) [Plasma Phys. Rep. **27**, 1039 (2001)].
7. G. V. Ivanenkov, S. A. Pikuz, D. B. Sinars, *et al.*, Fiz. Plazmy **26**, 927 (2000) [Plasma Phys. Rep. **26**, 868 (2000)].
8. T. A. Shelkovenko, D. B. Sinars, S. A. Pikuz, and D. A. Hammer, Phys. Plasmas **8**, 1305 (2001).
9. S. A. Pikuz, D. B. Sinars, T. A. Shelkovenko, *et al.*, Phys. Rev. Lett. **89**, 035003 (2002).
10. T. A. Shelkovenko, S. A. Pikuz, D. B. Sinars, *et al.*, Phys. Plasmas **9**, 2165 (2002).
11. S. A. Pikuz, D. B. Sinars, T. A. Shelkovenko, *et al.*, Pis'ma Zh. Éksp. Teor. Fiz. **76**, 571 (2002) [JETP Lett. **76**, 490 (2002)].
12. G. V. Ivanenkov and V. Stepniewski, Fiz. Plazmy **28**, 499 (2002) [Plasma Phys. Rep. **28**, 457 (2002)].
13. J. Stamper, Science **281**, 1469 (1998).
14. A. V. Gordeev and T. V. Losseva, Fiz. Plazmy **29**, 809 (2003) [Plasma Phys. Rep. **29**, 748 (2003)].
15. F. N. Beg, E. L. Clark, M. S. Wei, *et al.*, Phys. Rev. Lett. **92**, 095001 (2004).
16. A. V. Gordeev and T. V. Losseva, in *Proceedings of the 14th International Conference on High-Power Particle Beams and the 5th International Conference on Dense Z-Pinches, Albuquerque, NM, 2002*, Book of Abstracts, p. 259; AIP Conf. Proc. **651**, 420 (2002).
17. E. W. Weibel, Phys. Rev. Lett. **2**, 83 (1959).
18. J. Sakai, S. Saito, H. Mae, *et al.*, Phys. Plasmas **9**, 2959 (2002).
19. A. V. Gordeev and S. V. Levchenko, Pis'ma Zh. Éksp. Teor. Fiz. **67**, 461 (1998) [JETP Lett. **67**, 482 (1998)].
20. A. V. Gordeev and T. V. Losseva, Pis'ma Zh. Éksp. Teor. Fiz. **70**, 669 (1999) [JETP Lett. **70**, 684 (1999)].
21. A. V. Gordeev, Fiz. Plazmy **27**, 251 (2001) [Plasma Phys. Rep. **27**, 235 (2001)].
22. F. C. Young, S. J. Stephanakis, and G. Mosher, J. Appl. Phys. **48**, 3642 (1977).
23. G. S. Sarkisov, V. Yu. Bychenkov, V. T. Tikhonchuk, *et al.*, Pis'ma Zh. Éksp. Teor. Fiz. **66**, 787 (1997) [JETP Lett. **66**, 828 (1997)].
24. G. A. Askar'yan, S. V. Bulanov, F. Pegoraro, and A. M. Pukhov, Pis'ma Zh. Éksp. Teor. Fiz. **60**, 240 (1994) [JETP Lett. **60**, 251 (1994)].
25. S. V. Bulanov, M. Lontano, T. Zh. Esirkepov, *et al.*, Phys. Rev. Lett. **76**, 3562 (1996).
26. Y. Yatsuyanagi, T. Ebisuzaki, T. Hatori, and T. Kato, Phys. Plasmas **9**, 446 (2002).
27. Y. Kazimura, J.-I. Sakai, and S. V. Bulanov, Fiz. Plazmy **27**, 350 (2001) [Plasma Phys. Rep. **27**, 330 (2001)].
28. F. Califano, F. Praudi, F. Pegoraro, and S. V. Bulanov, Phys. Rev. E **58**, 7837 (1998).
29. F. Califano, F. Pegoraro, and S. V. Bulanov, Phys. Rev. Lett. **84**, 3602 (2000).
30. F. Califano, N. Attico, F. Pegoraro, *et al.*, Phys. Rev. Lett. **86**, 5293 (2001).
31. O. Buneman, Proc. R. Soc. London, Ser. A **215**, 346 (1952).
32. A. V. Gordeev and S. V. Levchenko, Electromagn. Waves Electron. Syst. **3** (2–3), 25 (1998).
33. A. V. Gordeev and T. V. Losseva, Fiz. Plazmy **26**, 1030 (2000) [Plasma Phys. Rep. **26**, 965 (2000)].
34. H. Alfven, Phys. Rev. **55**, 425 (1939).

35. L. D. Landau and E. M. Lifshitz, *The Classical Theory of Fields* (Nauka, Moscow, 1973; Pergamon, Oxford, 1975).
36. I. E. Tamm, *The Principles of Electricity Theory* (GITTL, Moscow, 1976).
37. A. V. Gordeev, Fiz. Plazmy **27**, 815 (2001) [Plasma Phys. Rep. **27**, 769 (2001)].
38. V. I. Berezhiani, S. M. Mahajan, and N. L. Shatashvili, Phys. Rev. E **55**, 995 (1997).
39. V. P. Krainov, J. Phys. B **36**, 3187 (2003).
40. V. P. Kraĭnov, Zh. Éksp. Teor. Fiz. **123**, 487 (2003) [JETP **96**, 430 (2003)].
41. A. V. Gordeev and S. V. Levchenko, in *Proceedings of the 18th Symposium on Plasma Physics Technology, Prague, 1997*, p. 74.
42. M. Borghesi, A. J. Mackinnon, A. R. Bell, *et al.*, Phys. Rev. Lett. **81**, 112 (1998).
43. K. Krushelnick, A. Ting, C. I. Moore, *et al.*, Phys. Rev. Lett. **78**, 4047 (1997).
44. E. Esarey, P. Sprangle, J. Krall, and A. Ting, IEEE Trans. Plasma Sci. **24**, 252 (1996).
45. V. S. Belyaev, O. F. Kostenko, and V. S. Lisitsa, Pis'ma Zh. Éksp. Teor. Fiz. **77**, 784 (2003) [JETP Lett. **77**, 653 (2003)].
46. D. Pesme, W. Rozmus, V. T. Tikhonchuk, *et al.*, Phys. Rev. Lett. **84**, 278 (2000).
47. G. S. Sarkisov, V. Yu. Bychenkov, and V. T. Tikhonchuk, Pis'ma Zh. Éksp. Teor. Fiz. **69**, 20 (1999) [JETP Lett. **69**, 20 (1999)].
48. S. V. Bulanov, F. Kalifano, G. I. Dudnikova, *et al.*, in *Review of Plasma Physics*, Ed. by V. D. Shafranov (Kluwer Academic, New York, 2001), Vol. 22, p. 227.
49. R. Z. Sagdeev, in *Plasma Physics and the Problem of Controlled Thermonuclear Reactions*, Ed. by M. A. Leontovich (Izd. Akad. Nauk SSSR, Moscow, 1958; Pergamon, New York, 1960), Vol. 4.
50. A. V. Gordeev, Fiz. Plazmy **23**, 108 (1997) [Plasma Phys. Rep. **23**, 92 (1997)].
51. A. V. Gordeev, A. S. Kingsep, and L. I. Rudakov, Phys. Rep. **243**, 215 (1994).
52. R. Z. Sagdeev, in *Reviews of Plasma Physics*, Ed. by M. A. Leontovich (Atomizdat, Moscow, 1964; Consultants Bureau, New York, 1968), Vol. 4.
53. V. V. Krasnosel'skikh, Zh. Éksp. Teor. Fiz. **89**, 498 (1985) [Sov. Phys. JETP **62**, 282 (1985)].
54. K. Krushelnick, E. L. Clark, Z. Najmudin, *et al.*, Phys. Rev. Lett. **83**, 737 (1999).
55. C. W. Gear, *Numerical Initial Value Problem in Ordinary Differential Equations* (Prentice-Hall, Englewood Cliffs, NJ, 1971).
56. E. S. Oran and J. P. Boris, *Numerical Simulation of Reactive Flows* (Elsevier, New York, 1987; Mir, Moscow, 1990).
57. A. V. Gordeev, Fiz. Plazmy **27**, 700 (2001) [Plasma Phys. Rep. **27**, 659 (2001)].
58. Y. Sentoku, T. V. Liseikina, T. Zh. Esirkepov, *et al.*, Phys. Rev. E **62**, 7271 (2000).
59. A. V. Gordeev and T. V. Losseva, in *Book of Abstracts of 10th International Conference and School on Plasma Physics and Controlled Fusion, Alushta, 2004*, p. 102.
60. P. M. Banks and G. Kockarts, *Aeronomy* (Academic, New York, 1973).
61. *Handbook of Physical Quantities*, Ed. by I. S. Grigoriev and E. Z. Meilikhov (Énergoizdat, Moscow, 1991; CRC, Boca Raton, 1997).
62. T. Z. Esirkepov, Y. Sentoku, K. Mima, *et al.*, Pis'ma Zh. Éksp. Teor. Fiz. **70**, 80 (1999) [JETP Lett. **70**, 82 (1999)].
63. G. S. Sarkisov, V. Yu. Bychenkov, V. N. Novikov, *et al.*, Phys. Rev. E **59**, 7042 (1999).
64. G. Pretzler, A. Saeman, A. Pukhov, *et al.*, Phys. Rev. E **58**, 1165 (1998).
65. J. Zweiback, R. A. Smith, T. E. Cowan, *et al.*, Phys. Rev. Lett. **84**, 2634 (2000).
66. V. Yu. Bychenkov, V. T. Tikhonchuk, and S. V. Tolokonnikov, Zh. Éksp. Teor. Fiz. **115**, 2080 (1999) [JETP **88**, 1137 (1999)].
67. V. Yu. Bychenkov, Y. Sentoku, S. V. Bulanov, *et al.*, Pis'ma Zh. Éksp. Teor. Fiz. **74**, 664 (2001) [JETP Lett. **74**, 586 (2001)].
68. A. V. Gordeev and T. V. Losseva, in *Proceedings of the 13th International Conference on High-Power Particle Beams, Nagaoka, 2000*, Vol. II, p. 968.
69. G. V. Sholin and E. O. Baronova, in *Book of Abstracts of 1st All-Russia Seminar on Z-Pinches, Moscow, 2004*, p. 40.
70. Y. Kazimura, J.-I. Sakai, and S. V. Bulanov, J. Phys. Soc. Jpn. **68**, 3271 (1999).
71. M. Honda, J. Meyer-ter-Vehn, and A. M. Pukhov, Phys. Plasmas **7**, 1302 (2000).
72. M. Honda, J. Meyer-ter-Vehn, and A. M. Pukhov, Phys. Rev. Lett. **85**, 2128 (2000).
73. S. A. Pikuz, T. A. Shelkovenko, D. B. Sinars, *et al.*, J. Quant. Spectrosc. Radiat. Transf. **71**, 581 (2001).
74. A. Maksimchuk, K. Flippo, H. Krause, *et al.*, Fiz. Plazmy **30**, 514 (2004) [Plasma Phys. Rep. **30**, 473 (2004)].
75. U. Wagner, M. Tatarakis, A. Gopal, *et al.*, Phys. Rev. E **70**, 026401 (2004).
76. A. A. Frolov, Fiz. Plazmy **30**, 750 (2004) [Plasma Phys. Rep. **30**, 698 (2004)].

*Translated by G.V. Shepekina*

*Plasma Physics Reports, Vol. 31, No. 1, 2005, pp. 3–13. Translated from Fizika Plazmy, Vol. 31, No. 1, 2005, pp. 6–16.*


**MAGNETIC CONFINEMENT SYSTEMS**

# Stabilization of Ballooning Modes by Nonparaxial Cells

**V. V. Arsenin, A. V. Zvonkov, and A. A. Skovoroda**

*Institute of Nuclear Fusion, Russian Research Centre Kurchatov Institute, pl. Kurchatova 1, Moscow, 123182 Russia*

Received June 2, 2004; in final form, July 13, 2004

**Abstract**—An analysis is made of the effect of high-curvature stabilizing nonparaxial elements (cells) on the MHD plasma stability in open confinement systems and in confinement systems with closed magnetic field lines. It is shown that the population of particles trapped in such cells has a stabilizing effect not only on convective (flute) modes but also on ballooning modes, which govern the maximum possible β value. In the kinetic approach, which distinguishes between the effects of trapped and passing particles, the maximum possible β values consistent with stability can be much higher than those predicted by the MHD model. *© 2005 Pleiades Publishing, Inc.*

## 1. INTRODUCTION

In confinement systems with closed magnetic field lines, as well as in open systems, the strong nonuniformity of the magnetic field (such that the characteristic spatial scale on which it varies is comparable to the plasma radius) can have a stabilizing effect on convective (flute) MHD perturbations. It is by means of a strongly nonuniform (i.e., highly nonparaxial) magnetic field that plasmas with a moderately decreasing pressure profile can be stably confined in several types of systems without a magnetic well, specifically, in "compact" systems, in which the plasma length $L$ along the magnetic field is comparable to its dimension $a$ across the field (such as configurations in the Earth's magnetosphere, Z-pinches, and configurations with levitated current-carrying coils; for a general approach, see [1], and, for applications to particular systems with internal conductors, see [2–5]), and in long systems, $L \gg a$, equipped with such internal nonparaxial elements as "fat" mirror cells [6], semicusps [7], and divertors [8, 9]. Stabilization by nonparaxial elements has already been attained and is to be achieved in some future experiments [10–15].

In describing the stability of a plasma with isotropic pressure in ideal magnetohydrodynamics (in what follows, such description will be referred to as the MHD model), strong nonuniformity of the magnetic field shows itself as the plasma compressibility effect. In this case, for a confinement system with closed magnetic field lines, the condition for convective (flute) stability has the form [16]

$$w_{\mathrm{MHD}} = \nabla p \cdot \nabla U + \gamma p \frac{|\nabla U|^2}{U} \geq 0, \qquad (1)$$

Here, $p$ is the plasma pressure, $U = \oint \frac{dl}{B}$ (the integration is carried out along a magnetic field line), and $\gamma = 5/3$ is the adiabatic index. In equilibrium, the constant pressure surfaces (or, equivalently, the magnetic surfaces) coincide with the surfaces $U = \mathrm{const}$. It is assumed that $\nabla p \cdot \nabla U < 0$ (i.e., there is no average magnetic well). According to condition (1), the pressure profile that is marginally stable against convective modes ($w_{\mathrm{MHD}} = 0$) is given by the formula

$$p^* = p_0 \left(\frac{U}{U_0}\right)^{-\gamma}, \qquad (2)$$

where $p_0$ and $U_0$ are the values of $p$ and $U$ at the axis. If the magnetic surfaces $U = \mathrm{const}$ are labeled by a magnetic flux ψ enclosed in them (at the axis, we have $\psi = 0$ and $|\nabla\psi| = 0$), then condition (1) and formula (2) give the profiles $p(\psi)$.

In a confinement system with a divertor (a toroidal divertor in the case of a closed configuration with a toroidal magnetic field), there is a separatrix surface $\psi = \psi_s$, which contains a magnetic null line and in the immediate vicinity of which $U \longrightarrow \infty$. A system of this kind exhibits convectively stable pressure profiles $p(\psi)$ such that the pressure vanishes at the separatrix surface, $p(\psi_s) = 0$; thereby, the separatrix of finite radius serves as a natural plasma boundary [9]. This, as well as the possibility of placing the required number of divertors at the proper positions along the system, is drawing increased attention to divertor stabilization schemes.[1]

[1] A nonparaxial mirror cell like that considered in [6], in which the plasma terminates at a finite distance from the separatrix, also can be built into the system at the desired position along the system, but it provides convective (and ballooning) stability only over a certain portion of the plasma cross section (it is this portion to which the results obtained below are applicable) and is incapable of stabilizing the layer near the outer plasma boundary. Stability over the entire plasma cross section can only be achieved by means of an array of nonparaxial mirror cells with positive and negative field-line curvature when the pressures in them are in proper ratios to each other [17, 18].

1063-780X/05/3101-0003$26.00 

Condition (1) for stability against convective perturbations does not restrict the value of $\beta = 2p/B^2$ because it can also be satisfied for a finite pressure, when the integral $U$ contained in it is calculated from the actual equilibrium magnetic field **B** (in this case, the shape of the neutrally stable pressure profile $p^*(\psi)$ can generally depend on $\beta$). The maximum $\beta$ values are limited by non-flute (ballooning) perturbations. For a long system, the maximum possible $\beta$ values for which the MHD model reliably predicts stability in this case can be low (see Section 2).

For a collisionless plasma, the stability conditions derived from the MHD model are sufficient ones since the actual potential energy $W$ of the perturbation is not less than that in the MHD model. Because of the strong nonuniformity of the magnetic field, the particles trapped in nonparaxial cells make a large contribution to the energy $W$. Consequently, such cells have a greater stabilizing effect on oscillations than that predicted by the MHD model. As regards axisymmetric open confinement systems, this circumstance was taken into account in [6, 17–20] in studying the conditions for stability against flute perturbations. In the present paper, which concerns open confinement systems and confinement systems with closed magnetic field lines, we will consider how the populations of particles trapped in nonparaxial cells affects not only the flute perturbations but also the ballooning modes.[2] We will show that the limiting $\beta$ values set by the ballooning instability can be substantially higher than those predicted by the MHD model.

## 2. LIMITATIONS ON $\beta$ VALUES IN THE MHD STABILITY MODEL

In confinement systems with closed magnetic field lines, the set of equations that describe ideal ballooning modes localized near a magnetic field line in an arbitrary toroidal geometry (see [23], Eqs. (6.137), (6.138)) at the stability boundary $\omega^2 = 0$ reduces to a single equation for the radial component $\xi$ of the plasma displacement $\boldsymbol{\xi} = \xi\frac{\nabla\psi}{|\nabla\psi|^2} + \eta\frac{\mathbf{B}\times\nabla\psi}{B^2} + \tau\frac{\mathbf{B}}{B^2}$ (see, e.g., [24]):

$$\mathbf{B}\cdot\nabla\left(\frac{k_\perp^2}{B^2k_b^2}\mathbf{B}\cdot\nabla\xi\right) + \frac{2\kappa^* p'}{|\nabla\psi|}\xi = \frac{\dfrac{2\kappa^*}{|\nabla\psi|}\oint\dfrac{2\kappa^*\xi}{|\nabla\psi|}\dfrac{dl}{B}}{\oint\dfrac{\gamma p + B^2}{\gamma p B^2}\dfrac{dl}{B}}. \quad (3)$$

Here, $k_\perp = |\mathbf{k}_\perp|$, $\mathbf{k}_\perp$ is the transverse component of the wave vector ($\mathbf{k}_\perp\cdot\mathbf{B} = 0$; $k_\perp \gg a^{-1}, k_\parallel$), $k_b = (\mathbf{B}\times\nabla\psi)\cdot\mathbf{k}_\perp/B^2$,

$$\frac{\kappa^*}{|\nabla\psi|} = \frac{(\mathbf{B}\times\boldsymbol{\kappa})\cdot\mathbf{k}_\perp}{(\mathbf{B}\times\nabla\psi)\cdot\mathbf{k}_\perp}, \quad (4)$$

$\boldsymbol{\kappa} = \left(\frac{\mathbf{B}}{B}\cdot\nabla\right)\frac{\mathbf{B}}{B}$ is the curvature of the magnetic field line, and the prime denotes the derivative with respect to $\psi$.[3]

We integrate Eq. (3) with a weighting factor of $B^{-1}$ along a closed magnetic field line; assume that $I = \oint\frac{\kappa^*\xi}{|\nabla\psi|}\frac{dl}{B} \neq 0$; and account for the relationship $\oint\left(\frac{2\kappa^*}{|\nabla\psi|} - \frac{p'}{B^2}\right)\frac{dl}{B} = -U'$, which is a consequence of the equilibrium equation (for the transformation of the integral $\oint\frac{\kappa^* dl}{B|\nabla\psi|}$, see Appendix 1). As a result, we arrive at the equality

$$p' + \gamma p\frac{U'}{U} = 0, \quad (5)$$

which coincides with marginal stability condition (1). Under condition (5), Eq. (3) has the solution $\xi = \text{const}$, which describes a flute mode and for which the quantity $I/\xi = -U' + p'\oint B^{-3}dl$ is actually nonzero in the situation of interest, i.e., when there is no magnetic well ($p' < 0$, $U' > 0$).

The analyses carried out in [26] for configurations with an axisymmetric poloidal magnetic field and in [24] for systems such that the magnetic field lines in them are closed and the axisymmetry is not necessarily required both showed that, in the MHD model, the maximum possible $\beta$ values under condition (1) are set by the instability of ballooning perturbations whose wavenumber along the magnetic field is nonzero and for which

$$\oint\frac{\kappa^*\xi}{|\nabla\psi|}\frac{dl}{B} = 0. \quad (6)$$

For such perturbations, the integral term in Eq. (3) vanishes. A solution of this kind, which implies that there is a threshold in $\beta$ for instability, corresponds to the zero second eigenvalue $\Lambda = \Lambda_2$ of the problem

$$\frac{\partial}{\partial l}\left(\frac{k_\perp^2}{Bk_b^2}\frac{\partial}{\partial l}\xi\right) + \left(\Lambda\rho + \frac{2\kappa^* p'}{B|\nabla\psi|}\right)\xi = 0, \quad (7)$$

$$\xi(l + L) = \xi(l) \quad (8)$$

[2] In [21, 22], it was noted that trapped particles have a stabilizing effect on MHD oscillations in a tokamak.

[3] In [25], Eq. (3) was used to analyze plasma stability against perturbations in which the transverse component of the wave vector, $\mathbf{k}_\perp$, is much less than the azimuthal component in the low local shear approximation (this approximation, however, was not explicitly mentioned there).

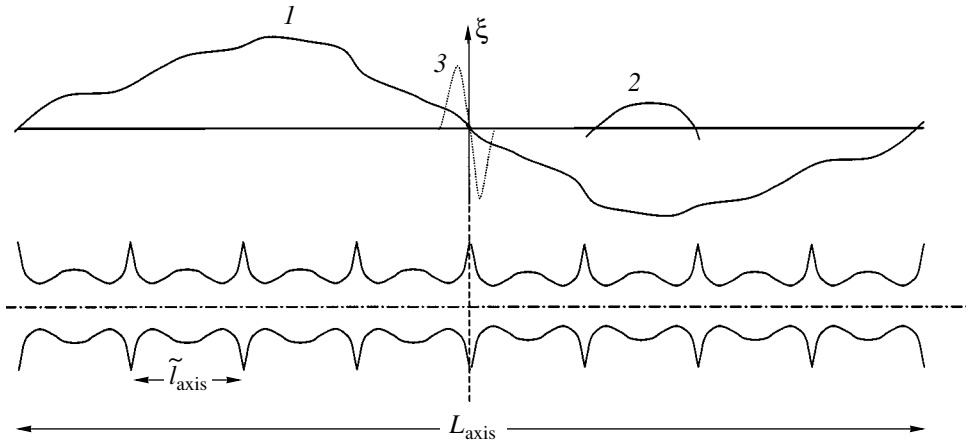


Sketch of a periodic confinement system with closed magnetic field lines and dependence of the plasma displacement ξ in a ballooning perturbation on the longitudinal coordinate: (*1*) a long-wavelength perturbation in which the displacement has two zeros and which sets the limiting β value in the MHD model, (*2*) a perturbation in which the displacement has zeros in every nonparaxial cell and which governs the maximum possible β value in the kinetic approach with allowance for the effect of trapped particles, and (*3*) an antisymmetric perturbation mode localized in the divertor. Here, $L_{\text{axis}}$ and $\tilde{l}_{\text{axis}}$ denote the system length and the period length, respectively, both measured along the system axis.

where $\rho(l)$ is a positive function and $L$ is the length of the magnetic field line. In this case, the corresponding eigenfunction has two zeros within the interval $[0, L)$. Since Eq. (7) does not contain the plasma compressibility, the ballooning stability boundary is governed by a competition between the stabilizing effect of the field line bending in the perturbation (the first term) and the destabilizing effect of convective charge separation in an unperturbed curved magnetic field (the term containing $p'$ and the curvature). In this case, nonparaxial elements (in particular, divertors) have a destabilizing effect on the ballooning modes because of the great unfavorable magnetic field curvature in them.

For illustrative purposes, we will restrict ourselves to the case in which the magnetic field coils are symmetric with respect to a certain plane intersecting the toroidal plasma column (such a symmetry ensures that the magnetic field lines are closed). To be specific, we assume that the system has $2N$ field periods. If the distance $l$ along the magnetic field line is measured from the plane just mentioned, the coefficients of Eq. (4) are even functions of $l$. Condition (6) is certainly satisfied for odd perturbations,

$$\xi(-l) = \xi(l) \tag{9}$$

(which are also odd with respect to $l = L/2$). The lowest critical β value at which the instability occurs corresponds to the mode with the longest wavelength, namely, that in which the plasma displacement has two zeros (see figure, curve *1*):

$$\beta_1 \sim \pi^2 \frac{a}{|\overline{\kappa^*}| L^2}, \tag{10}$$

where $a$ the plasma minor radius, $\overline{\kappa^*}$ is the characteristic value of $\kappa^*$ at the magnetic field line, and the retained numerical coefficient $\pi^2$ stems from the fact that the longitudinal wavenumber of the lowest mode of the perturbation is equal to $2\pi/L$. The estimate has been obtained under the assumption that the relative variation of the magnetic field along $l$ is on the order of unity. The permissible beta values are much lower than unity, $\beta \ll 1$; moreover, the longer the system (and the larger the parameter $N$), the lower the permissible beta values. The destabilizing effect of the nonparaxial cells manifests itself in an increase in the effective value $|\overline{\kappa^*}|$ in relationship (10).

For a confinement system having $2N \gg 1$ field periods, we can obtain, instead of the above approximate estimate, a rather precise (with a relative accuracy of about $\sim 1/N$) critical β value by taking into account the fact that the plasma displacement in long-wavelength perturbations varies insignificantly over one period $\tilde{l}$. To do this, we represent the plasma displacement in the form $\xi = \xi_0(z) + \varepsilon\xi_1(l, z)$ with $\varepsilon \ll 1$, where the quantity $\xi_0$ varies on a "long" spatial scale $L$ and the variations on small scales (of about $\sim\tilde{l}$) are accounted for by the quantity $\xi_1$. Using the method of averaging over the small scales [27], we obtain from Eq. (7) with $\Lambda = 0$ the following equation for $\xi_0$:

$$\frac{d^2\xi_0}{dz^2} + A^2\xi_0 = 0,$$

$$A^2 = \frac{p'\int_{\tilde{l}} \frac{2\kappa^* dl}{|\nabla\psi| B} \int_{\tilde{l}} \frac{B k_b^2 dl}{k_\perp^2}}{\tilde{l}^2}. \tag{11}$$

where the symbol $\tilde{l}$ stands for the interval of integration along the magnetic field line. The first of the two integrals in the numerator of the expression for $A^2$ reduces to $\int_{\tilde{l}} \frac{2\kappa_\psi dl}{B}$, where $\kappa_\psi$ is the component of the curvature vector in its expansion in the basis vectors $\nabla\psi$ and $\nabla\theta$, defined through the relationship $\mathbf{B} = \nabla\psi \times \nabla\theta$ (see Appendix 1). The second of the integrals in Eq. (11) depends on the relationship between the components of the wave vector $\mathbf{k}_\perp$: the integral is the largest (this is the most dangerous for stability because the increase in the integral produces the same effect as the increase in $|p'|$) when the azimuthal component of the wave vector is much larger than its radial component (a situation quite different from that considered in the Mercier stability analysis), so we have $Bk_b^2/k_\perp^2 \approx B/|\nabla\theta|^2$. Replacing $B/|\nabla\theta|^2$ with a larger (or equal) quantity $|\nabla\psi|^2/B$, we find the $\beta$ value below which condition (8) cannot be satisfied ($A < 2\pi/L$) for the odd solution $\xi_0 \propto \sin(Az)$ with two zeros (for which condition (6) holds under the assumption of mirror-image symmetry), i.e., the instability is impossible:

$$\langle\beta\rangle = 8\pi^2 \frac{\langle B^{-2}\rangle}{U^2}\left\langle \frac{-\nabla p \cdot \nabla U}{pU}\right\rangle^{-1}. \quad (12)$$

Here, we have introduced the notation $\langle f\rangle = \oint \frac{f dl}{B} / \oint \frac{dl}{B}$. For $U' = -\oint \frac{2\kappa_\psi dl}{|\nabla\psi| B}$, we have used the relationship $U = \oint \frac{dl}{B} = 2N\int_{\tilde{l}} \frac{dl}{B}$, which is valid for low $\beta$ values. In accordance with estimate (10), formula (12) yields the scaling $\langle\beta\rangle \propto 1/N^2$.

The permissible plasma pressure in a confinement system is determined by the lowest of the limiting $\beta$ values set by ballooning instabilities at individual magnetic field lines; in this case, the most "dangerous" lines are considered to be those at which the magnetic field is weak along the portions of unfavorable curvature.

We also present an estimate obtained from the MHD model for the limiting $\beta$ values set by the ballooning instability in the case of a straight chain of $N$ axisymmetric open mirror cells. We assume that such a system is symmetric about the equatorial plane. The natural boundary conditions for the plasma displacement at the ends of the system follow from the fact that the longitudinal plasma permittivity within the system is much higher than that beyond it:

$$\left.\frac{\partial\xi}{\partial l}\right|_{l = \pm L/2} = 0. \quad (13)$$

We take into account the fact that, in a straight system, the curvature is on the order of $r/l_M^2$, where $r$ is the distance from the axis and $l_M$ is the characteristic scale length on which the magnetic field varies. As a result, for the lowest odd (with respect to $l$) mode (with one zero at the equatorial plane), we obtain

$$\beta_1 \sim \pi^2 \frac{l_M^2}{L^2}. \quad (14)$$

For an open system consisting of a single mirror cell ($N = 1$) with a mirror ratio of about two, we have $l_M \sim L$, so the stability is achieved at $\beta \sim 1$. For a long ($N \gg 1$) strongly rippled (the scale length $l_M$ is comparable to the cell length $L/N$) mirror system, estimate (14) gives $\beta_1 \sim (\pi/N)^2$; this indicates that the instability occurs even at low $\beta$ values.

In what follows, we will show that, because of the influence of the population of particles trapped in nonparaxial elements, the limiting $\beta$ values set by the ballooning instability can be substantially higher than those predicted by estimates (10) and (14).

## 3. SUFFICIENT STABILITY CONDITIONS IN THE CASE OF LARGE RELATIVE POPULATION OF PARTICLES TRAPPED IN NONPARAXIAL CELLS

In the kinetic approach, the unperturbed plasma state in a system is described by the distribution function $f(\varepsilon, \mu, \psi)$, with $\varepsilon = mv^2/2$ and $\mu = mv_\perp^2/2B$; this function refers to the cross section in which the absolute value of the magnetic field as a function of the coordinate along the magnetic field **B** has minima and through which all the particles pass (so that all of them are taken into account). The description of a system consisting of several mirror cells separated by magnetic mirrors is more complicated. To illustrate, let confinement system *1* be equipped with identical mirror cells *2*, which are arranged on both sides of the equatorial plane and in which the magnetic field is weakened (i.e., the main part of the system and the mirror cells are separated by the magnetic mirrors). In such a system, there are three populations of particles: those confined in the main volume *1*, those trapped in mirror cells *2*, and common (passing) particles. In this case, the distribution function $f_1$ at the equatorial plane of confinement system *1* takes into account only the first and third populations of the particles and does not account for the second population, which is described individually by the distribution function $f_2$ referring to the equatorial plane of mirror cell *2*. For a closed system, it is natural to require that the distribution be Maxwellian (to within errors associated with the transverse nonuniformity of the plasma). In this case, the distribution function $f_2$ should be chosen to complement the distribution created by the passing particles in mirror cells *2* to a Maxwellian one. An important point for further analysis is that the motion of the particles of population *2* is

affected by the curvature of the magnetic field only in mirror cells *2*.

In this section, whose subject is to analyze a confinement system with closed magnetic field lines, we assume that the plasma pressure is isotropic (an open system with an anisotropic pressure will be considered in Section 5). We also assume that each of the $2N$ periods of the system can include a paraxial subsystem (subsystems) within which the curvature of the magnetic field line is much less than the reciprocal of the plasma minor radius $a$ and also a nonparaxial subsystem (subsystems). The potential energy $W$ of the perturbation mode localized in the plasma and characterized by the displacement $\xi_\perp$ is equal to

$$W = W^{(u)} + W^{(k)}, \tag{15}$$

Here,

$$W^{(u)} = \frac{1}{2}\int\{\mathbf{Q}^2 - \mathbf{Q}\cdot[\boldsymbol{\xi}_\perp\times(\nabla\times\mathbf{B})] + (\boldsymbol{\xi}_\perp\cdot\nabla p)\nabla\cdot\boldsymbol{\xi}_\perp\}dV, \tag{16}$$

where $\mathbf{Q} = \nabla\times(\boldsymbol{\xi}_\perp\times\mathbf{B})$, $dV = d\Phi dl/B$, $d\Phi$ is the magnetic flux in the magnetic tube, and the integration is carried out over the plasma volume. The so-called kinetic term $W^{(k)}$ contains integrals along the bounce orbits of the particles, and the averaging over the pitch angles is carried out (see, e.g., [28]). The contribution from the particles of the $\nu$th population to the kinetic term (per magnetic tube $d\Phi$) is equal in order of magnitude to $p_\nu l_\nu \kappa_\nu^2 B^{-1}\xi_\perp^2$, where $p_\nu$ is the partial pressure, $l_\nu$ is the length of the region in which these particles execute bounce oscillations, and $\kappa_\nu$ is the curvature of the magnetic field line in this region. The contribution from the particles trapped in the low-curvature paraxial region of the system (the quantities referring to this region will be indicated by the subscript $\mathcal{P}$) and from the passing particles, which move predominantly within this region, is small in comparison to the convective term ($\propto p'$) in the expression for $W^{(u)}$ and thus can be ignored. As for the population of particles trapped in nonparaxial elements (the quantities referring to these elements will be indicated by the subscript $\mathcal{N}$), its contribution to the expression for $W^{(k)}$ is comparable to the convective term (because of the high curvature, which is on the order of $\sim a^{-1}$) and thus should be retained.

To simplify matters, we assume that the mirror ratio in the nonparaxial cell is large (just as it is in a divertor near the separatrix surface). In this case, the distribution of the particles trapped in such a cell is close to an isotropic Maxwellian distribution and the population of passing particles is small (although these are the particles that ensure electric coupling between different parts of the system). In Appendix 2, the resulting equation (22) will be generalized to the case of a finite mirror ratio.

According to the comparison theorem [29, 30], the potential energy $W_\mathcal{N}^{(k)}$ for one nonparaxial element of length $l_\mathcal{N}$ is no lower than

$$\overline{W}_\mathcal{N}^{(k)} = \frac{5}{6}\int p\,d\Phi\left\{\frac{\left[\int_{l_\mathcal{N}}(\nabla\cdot\boldsymbol{\xi}_\perp)\frac{dl}{B}\right]^2}{\int_{l_\mathcal{N}}\frac{dl}{B}}\right\}, \tag{17}$$

where $l_\mathcal{N}$ is the length of the portion of the magnetic field line within a nonparaxial cell. Replacing $W_\mathcal{N}^{(k)}$ with $\overline{W}_\mathcal{N}^{(k)}$, we obtain the sufficient stability condition

$$\sum_n (W_{\mathcal{P}n}^{(u)} + W_{\mathcal{N}n}^{(u)} + \overline{W}_{\mathcal{N}n}^{(k)}) \geq 0, \tag{18}$$

where the summation over $n$ indicates summation over all $2N$ components of the system.

In what follows (as in Section 2), we will be interested in ballooning perturbations localized inside a thin magnetic tube whose transverse dimension is much less than the plasma radius. The short nonparaxial elements under consideration will be assumed to be axisymmetric.

## 4. LONG CONFINEMENT SYSTEM WITH CLOSED MAGNETIC FIELD LINES

Let us consider a long toroidal confinement system with closed magnetic field lines. It will be seen later that the limiting $\beta$ values consistent with stability are low, $\beta \ll 1$ (but are nevertheless higher than those given by estimate (10)). For low $\beta$ values (such that the perturbation electric field has the form $\mathbf{E}_\perp = -\nabla_\perp\phi$), the plasma displacement $\xi$ in nonparaxial elements, in which, in view of their axisymmetry, the magnetic field line curvature has only a normal component, satisfies the equation

$$\nabla\cdot\boldsymbol{\xi}_\perp \approx -2\kappa\frac{\xi}{|\nabla\psi|}, \tag{19}$$

(where $\kappa = \boldsymbol{\kappa}\cdot\frac{\nabla\psi}{|\nabla\psi|}$), so we have

$$\overline{W}_\mathcal{N}^{(k)} = \frac{5}{6}\int p\,d\Phi\frac{\left[\int_{l_\mathcal{N}}\frac{2\kappa\xi}{|\nabla\psi|}\frac{dl}{B}\right]^2}{\int_{l_\mathcal{N}}\frac{dl}{B}}. \tag{20}$$

A sufficient condition for the stability (i.e., for the functional $W/(\oint \rho \xi^2 dl)$ to nonnegative) is given by the condition for the Euler equation

$$\frac{\partial}{\partial l}\left(\frac{k_\perp^2}{Bk_b^2}\frac{\partial}{\partial l}\xi\right) + \left(\Lambda\rho + \frac{2\kappa^* p'}{B|\nabla\psi|}\right)\xi - \frac{5}{3}Hp\frac{2\kappa}{B|\nabla\psi|}\frac{\int_{l_\mathcal{N}} \frac{2\kappa\xi}{|\nabla\psi|}\frac{dl}{B}}{\int_{l_\mathcal{N}} \frac{dl}{B}} = 0 \quad (21)$$

complemented with condition (8), to have no negative eigenvalues $\Lambda$. Here, $H(l)$ is a function that is equal to unity in nonparaxial cells and to zero along the remaining portions of the magnetic field line.

Assuming that the displacement $\xi$ varies insignificantly along the magnetic field lines over the length of the nonparaxial cell (as will be clear later, this is the case for long-wavelength modes such that $\partial \ln\xi/\partial l \ll a^{-1}$ except when the displacement $\xi$ has a zero within the cell), we can factor $\xi$ out of the integral sign in the integral terms in Eq. (21). The equation then reduces to

$$\frac{\partial}{\partial l}\left(\frac{k_\perp^2}{Bk_b^2}\frac{\partial}{\partial l}\xi\right) + \left(\Lambda\rho + \frac{2\kappa^* p'}{B|\nabla\psi|} - \frac{5}{3}Hp\frac{2\kappa}{B|\nabla\psi|}\frac{\int_{l_\mathcal{N}} \frac{2\kappa}{|\nabla\psi|}\frac{dl}{B}}{\int_{l_\mathcal{N}} \frac{dl}{B}}\right)\xi = 0. \quad (22)$$

In the MHD model, we would have Eq. (21) with the last term replaced by $\frac{5}{3}p\left[\frac{2\kappa^*}{B|\nabla\psi|}\int_L \frac{2\kappa^*\xi}{|\nabla\psi|}\frac{dl}{B}\right]/\int_L \frac{dl}{B}$ (see [24]). Two circumstances are important here: first, in contrast to the MHD model, the integral $\int \frac{dl}{B}$ in the terms in Eqs. (21) and (22) that are quadratic in the curvature is taken over the length of the nonparaxial cell rather than along the entire length $L$ of the magnetic field line and, second, the integration in the numerators in these equations is also carried out over the length of the cell. One of the consequences of this first circumstance is that the requirement $\xi$ = const for stability against flute perturbations admits pressure profiles such that the relative pressure gradient $d\ln p/d\psi$ is greater that that in the MHD model. For flute perturbations, the condition $W \geq 0$ can be written in the form [cf. condition (1)]

$$\nabla p \cdot \nabla(U_\mathcal{P} + U_\mathcal{N}) + \gamma p\frac{(\nabla U_\mathcal{N})^2}{U_\mathcal{N}} \geq 0, \quad (23)$$

where the integral $U_\mathcal{P} = \int_{l_\mathcal{P}} \frac{dl}{B}$ is taken over the length of the paraxial portion of the period of the system and the integral $U_\mathcal{N} = \int_{l_\mathcal{N}} \frac{dl}{B}$ is taken over the length of the nonparaxial cell. For a neutrally stable pressure profile, the relative pressure gradient is

$$\left|\frac{p'}{p}\right| = \left|\frac{p'}{p}\right|_* \equiv \gamma\frac{|U_\mathcal{N}'|}{U_\mathcal{N}\left(1 + \frac{U_\mathcal{P}'}{U_\mathcal{N}'}\right)}, \quad (24)$$

where the prime denotes differentiation with respect to $\psi$. For a low-curvature paraxial portion of the period of the system ($\kappa_\mathcal{P} l_\mathcal{P} \ll 1$, so that $|U_\mathcal{P}'/U_\mathcal{N}'| \ll 1$), expression (24) passes over to the expression

$$\left|\frac{p'}{p}\right| = \gamma\frac{|U_\mathcal{N}'|}{U_\mathcal{N}}, \quad (25)$$

and the marginally stable pressure profile coincides with that for a single nonparaxial cell (with $U = U_\mathcal{N}$ in formula (2)). In the corresponding case in the MHD model, we would arrive, instead of expression (25), at the expression

$$\left|\frac{p'}{p}\right| = \gamma\frac{|U_\mathcal{N}'|}{U_\mathcal{N} + U_\mathcal{P}}, \quad (26)$$

so, for a long paraxial portion, the denominator on the right-hand side of this expression is much larger than $U_\mathcal{N}$.

The fact that the integration in the integral term in Eq. (21) is carried out along the magnetic field lines only within the nonparaxial cells implies that, unlike in the MHD model, the quadratic (in the curvature) terms (which give rise to the integral term in Eq. (21)) that account for the contribution from the particles trapped in nonparaxial cells to the expression for the potential energy $W$ have a stabilizing effect on both even, $\xi(-l) = \xi(l)$, and odd, $\xi(-l) = -\xi(l)$, modes, provided that the total sum of the potential energies over all the cells is nonzero,

$$\sum_n W_{\mathcal{N}n}^{(k)} \neq 0. \quad (27)$$

We assume that condition (23) is satisfied with a sufficiently large margin (see the Introduction): $|p'/p| = \alpha|p'/p|_*$, where $\alpha < 1$. Under this assumption, if the plasma displacement $\xi$ in the $n$th nonparaxial element

of the chain is not close to zero, then the potential energy $W_{\mathcal{N}n}^{(k)}$ and the contribution of this element to the total potential energy $W$ are larger than the destabilizing contribution from the adjacent $n$th paraxial portion of the period of the system. If this is the case for all (or almost all) of the nonparaxial elements, then the perturbation on the whole is stable. The contribution from a particular nonparaxial element to the sum $\sum_n W_{\mathcal{N}n}^{(k)}$ is small when the displacement $\xi$ has a zero within it. (In particular, the potential energy $W_{\mathcal{N}}^{(k)}$ of an odd mode is equal to zero when the equatorial plane of such an element coincides with the plane $l = 0$.) For a periodic chain of open mirror cells with a stabilizer at each of the $2N$ periods, we have $\sum_n W_{\mathcal{N}n}^{(k)} = 0$ for a perturbation with the wavelength $L/N$ that has a zero within each of the stabilizers (see figure, curve *2*). The positive energy of the field line bending in such a perturbation is $N^2$ times higher than that in the longest wavelength ballooning mode with the same amplitude and with $k_\parallel \approx 2\pi/L$, for which, under condition (6), the MHD model yields estimate (10). Therefore, the plasma is stabile up to beta values of

$$\beta \sim \pi^2 N^2 \frac{a}{|\overline{\kappa^*}| L^2}, \tag{28}$$

or

$$\beta \sim \pi^2 \frac{a}{|\overline{\kappa^*}| \tilde{l}^2}, \tag{29}$$

where $\tilde{l}$ is the length of the period and $\overline{\kappa^*}$ is the characteristic value of $\kappa^*$ over the paraxial portion of the period. It can be said that, for $\alpha < 1$, the nonparaxial cells function as anchors (such that, for each cell, we have $W_{\mathcal{N}}^{(u)} + W_{\mathcal{N}}^{(k)} > 0$, although $W_{\mathcal{N}}^{(u)} < 0$) that force the perturbation structure to have a longitudinal wavelength of $\approx L/N$. Long-wavelength ballooning modes are suppressed even when condition (23) is satisfied with a far smaller margin: the only unstable modes are those in which the plasma displacement $\xi$ is small in some stabilizers; in this case, the corresponding wavenumber $k_\parallel$ ($>2\pi/L$) determines the critical $\beta$ value, which is intermediate between those given by estimates (10) and (29).

Let us now consider another possible situation with ballooning instability in a confinement system with divertors. As the magnetic null line $\mathbf{B} = 0$ is approached, the unfavorable magnetic field curvature increases; so, for a magnetic flux above a certain critical value, $\psi_{cr} < \psi_s$, there may occur an unstable mode that is odd with respect to the equatorial plane of the divertor (such that $W_{\mathcal{N}}^{(k)} = 0$) and is localized along a magnetic field line near this plane in the region where the magnetic field line curvature $|\kappa|$ is large (see figure 1, curve *3*). In this case, we are again dealing with the problem given by Eq. (7) and condition (8). For such a perturbation mode, the eigenvalue is negative, $\Lambda < 0$, under the condition

$$(2p/B^2)\left|\kappa \frac{\partial \ln p}{\partial r}\right| (\delta r)^2 \lesssim 1, \tag{30}$$

where the quantities are taken at the point (in the equatorial plane) that is closest to the circumference at which the magnetic field vanishes and $\delta r$ is the distance from this point to the null line $\mathbf{B} = 0$. If we have $\beta \ll 1$ at the axis, then condition (30) is satisfied only in a certain radial peripheral layer $\psi_{cr} < \psi < \psi_s$ adjacent to the separatrix. The instability can be avoided by filling the vicinity of the magnetic null line with a plasma such that the pressure gradient within the layer is nonnegative, $p' \geq 0$ [14].

## 5. AXISYMMETRIC POLOIDAL MAGNETIC FIELD CONFIGURATION

An axisymmetric poloidal magnetic field configuration (in particular, in a straight system) can readily be analyzed analytically without assuming that the parameter $\beta$ is low. Using the relevant lower estimate for the kinetic term $W$ that was obtained in [31, 32] and minimizing $W$ in the azimuthal component $\eta$ of the displacement $\boldsymbol{\xi}_\perp$, we arrive at the following sufficient condition for the stability against perturbations with the azimuthal mode number $m \longrightarrow \infty$ (see [33]):

$$\int_{-L/2}^{L/2} \frac{dl}{B}\left\{\frac{B^2\sigma}{|\nabla\psi|^2}\left(\frac{\partial\xi}{\partial l}\right)^2 - \frac{\kappa}{|\nabla\psi|}\left(\frac{\partial p_\parallel}{\partial\psi} + \frac{\sigma}{\tau}\frac{\partial p_\perp}{\partial\psi}\right)\xi^2\right\} + \sum_n w_n^{(k)} \geq 0. \tag{31}$$

Here, $p_{\perp,\parallel} = p_{\perp,\parallel}(\psi, B)$ are the transverse and longitudinal pressures (which are related by the longitudinal equilibrium condition), $\sigma = 1 + (p_\perp - p_\parallel)/B^2$, $\tau = 1 + B^{-1}\partial p_\perp/\partial B$, $\frac{\partial p_{\parallel,\perp}}{\partial\psi} = |\nabla\psi|^{-1}\left(\frac{\partial p_{\parallel,\perp}}{\partial\nu} - \frac{\partial p_{\parallel,\perp}}{\partial B}\frac{\partial B}{\partial\nu}\right)$, $\frac{\partial}{\partial\nu} \equiv \frac{\nabla\psi}{|\nabla\psi|}\cdot\nabla$,

$$w_n^{(k)} = \frac{5}{3}\left[\int_{l_{\mathcal{N}n}} P\frac{\kappa\xi}{|\nabla\psi|}\frac{dl}{B}\right]^2 \Big/ \int_{l_{\mathcal{N}n}} \Pi\frac{dl}{B}, \tag{32}$$

$P = \hat{p}_{\parallel t} + \frac{\sigma}{\tau}\hat{p}_{\perp t}$, $\Pi = \hat{p}_t + \frac{3}{5}\frac{\hat{p}_{\perp t}^2}{\tau B^2}$, $p_t = (2p_{\perp t} + p_{\parallel t})/3$, $\hat{a} = a - \frac{2}{5}B\frac{\partial a}{\partial B}$, the summation is over all the nonparaxial cells, the integrals in $w_n^{(k)}$ are taken along the mag-

netic field line in the *n*th cell, the subscript $\mathcal{N}$ again stands for nonparaxial cells of the system, and the subscript *t* denotes the populations of particles trapped in the cells.[4]

Condition (31) is satisfied if the Euler equation

$$\frac{\partial}{\partial l}\left(\frac{\sigma B}{|\nabla\psi|^2}\frac{\partial\xi}{\partial l}\right)+\left(\Lambda\rho+\frac{\kappa}{B|\nabla\psi|}\left(\frac{\partial p_\parallel}{\partial\psi}+\frac{\sigma}{\tau}\frac{\partial p_\perp}{\partial\psi}\right)\right)\xi - \frac{5}{3}HP\frac{\kappa}{B|\nabla\psi|}\frac{\int_{l_\mathcal{N}} P\frac{\kappa\xi}{|\nabla\psi|}\frac{dl}{B}}{\int_{l_\mathcal{N}}\Pi\frac{dl}{B}} = 0 \quad (33)$$

supplemented with condition (8) (in the case of closed magnetic field lines, e.g., in a confinement system with internal current-carrying conductors) or with boundary conditions (13) (in the case of a straight open confinement system) does not have negative eigenvalues ($\Lambda < 0$). In a somewhat different form, Eq. (33) was also used by Simakov *et al.* [35] in considering a single mirror cell.

For perturbations whose wavelengths in the magnetic field direction are long and in which the plasma displacement $\xi$ varies insignificantly along the nonparaxial element, Eq. (33) can be rewritten in the form [cf. Eq. (22)]

$$\frac{\partial}{\partial l}\left(\frac{\sigma B}{|\nabla\psi|^2}\frac{\partial\xi}{\partial l}\right)+\left(\Lambda\rho+\frac{\kappa}{B|\nabla\psi|}\left(\frac{\partial p_\parallel}{\partial\psi}+\frac{\sigma}{\tau}\frac{\partial p_\perp}{\partial\psi}\right)\right)\xi - \frac{5}{3}HP\frac{\kappa}{B|\nabla\psi|}\frac{\int_{l_\mathcal{N}} P\frac{\kappa}{|\nabla\psi|}\frac{dl}{B}}{\int_{l_\mathcal{N}}\Pi\frac{dl}{B}}\xi = 0. \quad (34)$$

For an isotropic perturbed plasma pressure, $p_\perp = p_\parallel$, and for $\beta \ll 1$, Eqs. (33) and (34) pass over to Eqs. (21) and (22), respectively.

[4] The plasma stability in a "simple mirror + end cusps" system was analyzed by Drozdov and Martynov [34] by using relationships (31) and (32) and by taking into account the ballooning effect. They assumed that $\partial p_{\perp,\parallel}/\partial\psi \neq$ only in a radial peripheral layer of the mirror. In this case, the layer is stabilized by the favorable magnetic field curvature in the cusps (according to the average min-*B* principle) and the stabilizing (for an appropriate pressure profile in the inner region of the confined plasma, i.e., the region that is on the side of the magnetic field null) effect of the nonparaxial nature of the cusp on the oscillations in the axial region of the mirror cell does not manifest itself.

The plasma pressure profile is stable against flute perturbations ($\xi$ = const) under the condition

$$\int_L \frac{\kappa}{|\nabla\psi|}\left(\frac{\partial p_\parallel}{\partial\psi}+\frac{\sigma}{\tau}\frac{\partial p_\perp}{\partial\psi}\right)\frac{dl}{B} \le \frac{5}{3}\sum\frac{\left[\int_{l_{\mathcal{N}n}} P\frac{\kappa}{|\nabla\psi|}\frac{dl}{B}\right]^2}{\int_{l_{\mathcal{N}n}}\Pi\frac{dl}{B}}. \quad (35)$$

Let a straight confinement system with a rippled magnetic field be equipped with nonparaxial cells (stabilizers) placed between every *S* ripples of total length *D*, and let the convective stability condition for such a system be satisfied with a sufficient margin (i.e., for a chosen plasma pressure profile, inequality (35) is assumed to be strong). In this case, the maximum possible $\beta$ values consistent with stability are set by the perturbations for which the plasma displacement $\xi$ in the stabilizing cells is close to zero, so that $k_\parallel \approx \pi/D$. As a result, we have

$$\beta_{cr} \sim \pi^2\left(\frac{l_M}{D}\right)^2 = \frac{\pi^2}{S^2}\left(\frac{l_M}{l_b}\right)^2, \quad (36)$$

where $l_M$ is the scale length on which the magnetic field varies in the ripple and $l_b = D/S$ is the length of the ripple.

Note that a long main straight confinement system can be stabilized, up to $\beta_\mathcal{P} \sim 1$, by nonparaxial cells with $\beta_\mathcal{N} \ll 1$. If, in this case, nonparaxial cells are divertors, then the instability within them can be suppressed by the method mentioned in the previous section; i.e., by filling the vicinity of the magnetic null line with a plasma at a certain pressure (see condition (30)).

## 6. CONCLUSIONS

In the bulk volume of a nonparaxial element, the magnetic field is far weaker than in the mirrors through which this element is coupled to the system. Consequently, the overwhelming majority of the particles are trapped in the nonparaxial element and thereby are subject to the large field-line curvature. Because of this, such elements have a far greater stabilizing effect, which is accounted for by the quadratic (in the curvature) kinetic term in the expression for the potential energy of the perturbation, on the MHD plasma oscillations than might be expected from the simple MHD model. We have demonstrated that, on the one hand, a decreasing pressure profile at which the convective instability can be stabilized is steeper than that predicted by the MHD model and, on the other hand, the limitations imposed by the ballooning modes on the maximum possible $\beta$ values are less stringent.

In the expression for the potential energy *W* of the perturbation, we have used lower estimates (17) and (32) of the kinetic term. In actuality, however, this term

can be substantially larger and, accordingly, the nonparaxial elements can have even stronger stabilizing effect (for a divertor, this is demonstrated by the calculations of the Kruskal–Oberman criterion that were carried out in [36]).

## ACKNOWLEDGMENTS

We are grateful to M.I. Mikhaĭlov for valuable remarks. This work was supported in part by the RF Program for State Support of Leading Scientific Schools (project no. NSh-2024.2003.2), the Russian Foundation for Basic Research (project no. 03-02-16768), and the Department of Atomic Science and Technology of the RF Ministry of Atomic Industry.

## *APPENDIX 1*

### *Transformation of the Integral* $\oint \frac{\kappa^* dl}{|\nabla\psi| B}$

We switch to the coordinates with straightened field lines by introducing the azimuthal variable $\theta$ and represent the magnetic field in the form $\mathbf{B} = (\nabla\psi \times \nabla\theta)$. We expand the vectors $\mathbf{k}_\perp$ and $\boldsymbol{\kappa}$, which are normal to the magnetic field, in the vectors $\nabla\psi$ and $\nabla\theta$: $\mathbf{k}_\perp = k_\psi \nabla\psi + k_\theta \nabla\theta$, and $\boldsymbol{\kappa} = \kappa_\psi \nabla\psi + \kappa_\theta \nabla\theta$ (note that the component $k_\theta$ coincides with the quantity $k_b$ used in the body of the paper). As a result, we obtain

$$\oint \frac{(\mathbf{B}\times\boldsymbol{\kappa})\cdot\mathbf{k}_\perp dl}{(\mathbf{B}\times\nabla\psi)\cdot\mathbf{k}_\perp B} = \oint \frac{k_\psi (\mathbf{B}\times\boldsymbol{\kappa})\cdot\nabla\psi dl}{k_\theta (\mathbf{B}\times\nabla\psi)\cdot\nabla\theta B} + \oint \frac{\kappa_\psi dl}{B}. \quad \text{(A1.1)}$$

Using formulas (6.129) and (6.134) from [23],

$$\frac{d}{dl}\left(\frac{k_\theta(\mathbf{B}\times\nabla\psi)\cdot\nabla\theta}{B^2}\right) = 0,$$
$$\frac{2p'(\mathbf{B}\times\boldsymbol{\kappa})\cdot\nabla\psi}{B^3} = \frac{d}{dl}\left(\frac{j_\parallel}{B}\right) \quad \text{(A1.2)}$$

and the fact that the component $k_\psi$ is independent of $l$ (which is a consequence of relationship (6.130) from [23]), we verify that the first integral on the right-hand side of relationship (A1.1) vanishes. Consequently, we have

$$\oint \frac{\kappa^* dl}{|\nabla\psi| B} = \oint \frac{\kappa_\psi dl}{B}, \quad \text{(A1.3)}$$

and the equilibrium equation yields (for details, see, e.g., [37], which made use of the equality $\kappa_\psi = ((\mathbf{B}\times\boldsymbol{\kappa})\cdot\nabla\theta)/B^2$)

$$\oint \frac{\kappa_\psi dl}{B} = \frac{1}{2}\left(\oint \frac{p' dl}{B^3} - U'\right). \quad \text{(A1.4)}$$

Relationship (A1.3) is valid not only for the integral along the entire closed magnetic field line but also for the integral $\int_{\tilde{l}} \frac{\kappa^* dl}{|\nabla\psi| B}$ over one magnetic field period (if the system is periodic) and for an analogous integral over a portion (if it exists) of the magnetic field line at whose ends we have $j_\parallel = 0$.

## *APPENDIX 2*

### *Case of a Finite Mirror Ratio in the Low* $\beta$ *Approximation*

We begin with a general expression for the perturbation $f_1$ of the Maxwellian distribution function $f_M$ due to the plasma displacement $\boldsymbol{\xi}_\perp$ in a "short" system (see, e.g., [28]):

$$f_1 = -\boldsymbol{\xi}_\perp\cdot\nabla f_M + \frac{1}{\tau}\frac{df_M}{d\varepsilon}\oint\left[\left(\frac{V_\perp^2}{2} - V_\parallel^2\right)(\boldsymbol{\xi}_\perp\cdot\boldsymbol{\kappa}) + \frac{V_\perp^2}{2}\nabla\cdot\boldsymbol{\xi}_\perp\right]\frac{dl}{V_\parallel}, \quad \text{(A2.1)}$$

where $\tau = \oint dl/V_\parallel$ is the bounce period. For trapped particles, the integration is carried out along the portion of the magnetic field line between two points where the longitudinal particle velocity vanishes ($V_\parallel = 0$), and, for passing particles, the integral is taken along the entire magnetic field line. For an axisymmetric nonparaxial cell, we take into account relationship (19) to rewrite expression (A2.1) as

$$f_1 = -\boldsymbol{\xi}_\perp\cdot\nabla f_M - \frac{1}{\tau}\frac{df_M}{d\varepsilon}\oint\left(\frac{V_\perp^2}{2} + V_\parallel^2\right)\frac{\kappa\xi dl}{|\nabla\psi| V_\parallel}. \quad \text{(A2.2)}$$

Using expression (A2.2), we can calculate the perturbation $\tilde{p}$ of the total plasma pressure $p = (p_\perp + p_\parallel)/2$:

$$\tilde{p} = -\xi p' + \tilde{p}_2, \quad \tilde{p}_2 = p\left\langle\frac{\xi}{R}\right\rangle,$$
$$\left\langle\frac{\xi}{R}\right\rangle = \frac{15}{16}\int_0^{1/B}\left[\frac{B(2-\lambda B)}{\sqrt{1-\lambda B}}\frac{\oint\frac{(2-\lambda B)\kappa\xi dl}{|\nabla\psi|\sqrt{1-\lambda B}}}{\oint\frac{dl}{\sqrt{1-\lambda B}}}\right]d\lambda. \quad \text{(A2.3)}$$

For long-wavelength perturbations, we can factor $\xi$ out of the integral over the trajectory of a trapped particle. As for passing particles, their contribution to expression (A2.3) is insignificant (provided that mirror ratio is not too small) because of the large value of the integral in the denominator. Therefore, we have

$$\left\langle\frac{1}{R}\right\rangle \approx \frac{15}{16}\int_{1/B_{\max}}^{1/B}\left[\frac{B(2-\lambda B)}{\sqrt{1-\lambda B}}\frac{\oint\frac{(2-\lambda B)\kappa dl}{|\nabla\psi|\sqrt{1-\lambda B}}}{\oint\frac{dl}{\sqrt{1-\lambda B}}}\right]d\lambda. \quad \text{(A2.4)}$$

Hence, the term $\tilde{p}_2$ in the expression for the pressure perturbation is associated only with the trapped particles. In order to incorporate the term $\tilde{p}_2$ into the equation for the oscillations that derives from the condition $\nabla \cdot \tilde{\mathbf{j}} = 0$, where $\tilde{\mathbf{j}} = \tilde{\alpha}\mathbf{B} + \tilde{\mathbf{j}}_\perp$ with $\tilde{\alpha} = \tilde{\mathbf{j}} \cdot \mathbf{B}/B^2$ is the perturbed current (see, e.g., [22]), we take into account the fact that the perturbed pressure enters into $\tilde{\mathbf{j}}_\perp$ through the expression $(\mathbf{B} \times \nabla \tilde{p})/B^2$. In this case, the additional term that arises in Eq. (7) and is associated with $\tilde{p}_2$ turns out to be proportional to $\nabla \cdot ((\mathbf{B} \times \nabla \tilde{p}_2)/B^2)$ and has the form $p\left\langle \frac{1}{R} \right\rangle \frac{2\kappa^*\xi}{|\nabla\psi|B}$. As a result, we arrive at the equation

$$\frac{\partial}{\partial l}\left(\frac{k_\perp^2}{Bk_b^2}\frac{\partial}{\partial l}\xi\right) + \left[\frac{2\kappa^*}{B|\nabla\psi|}\left(p' - p\left\langle\frac{1}{R}\right\rangle_b\right) + \Lambda\rho\right]\xi = 0. \quad \text{(A2.5)}$$

Here, the term with $\left\langle \frac{1}{R} \right\rangle$ is nonzero only along those portions of the magnetic field line where there are trapped particles; in this case, in a nonparaxial cell, we have $\kappa^* = \kappa$.

The stabilization condition for perturbations whose wavelength is much longer than the period length $\tilde{l}$ can be written as

$$\int_{\tilde{l}} \left(p' - p\left\langle\frac{1}{R}\right\rangle\right)\frac{2\kappa^* dl}{|\nabla\psi|B} \le 0. \quad \text{(A2.6)}$$

The lower estimate of the second integral on the left-hand side of condition (A2.6) can be obtained using the Schwarz inequality:

$$\oint \left\langle\frac{1}{R}\right\rangle \frac{2\kappa^* dl}{|\nabla\psi|B} = \frac{15}{8}\int_{1/B_{\max}}^{1/B}\left[\frac{\left(\oint \frac{(2-\lambda B)\kappa dl}{|\nabla\psi|\sqrt{1-\lambda B}}\right)^2}{\oint \frac{dl}{\sqrt{1-\lambda B}}}\right]d\lambda$$
$$\ge \frac{15}{8}\frac{\left(\int_{1/B_{\max}}^{1/B}\oint \frac{(2-\lambda B)\kappa dl}{|\nabla\psi|\sqrt{1-\lambda B}}d\lambda\right)^2}{\int_{1/B_{\max}}^{1/B}\oint \frac{dl}{\sqrt{1-\lambda B}}d\lambda} \quad \text{(A2.7)}$$
$$= \frac{5}{3}\frac{\left(\oint \frac{2\sqrt{1-B/B_{\max}}(1-B/4B_{\max})\kappa dl}{|\nabla\psi|B}\right)^2}{\oint \frac{\sqrt{1-B/B_{\max}}dl}{B}}.$$

Conditions (A2.6) and (A2.7) yield the following sufficient stability condition:

$$p'U' + \frac{5}{3}p\frac{\left(\oint \frac{2\sqrt{1-B/B_{\max}}(1-B/4B_{\max})\kappa dl}{|\nabla\psi|B}\right)^2}{\oint \frac{\sqrt{1-B/B_{\max}}dl}{B}} \ge 0. \quad \text{(A2.8)}$$

In the case of a large mirror ratio, which was considered in the body of the paper, condition (A2.8) passes over to condition (23).

## REFERENCES


1. B. B. Kadomtsev, in *Reviews of Plasma Physics*, Ed. by M. A. Leontovich (Gosatomizdat, Moscow, 1963; Consultants Bureau, New York, 1966), Vol. 2.
2. A. Hasegava, L. Chen, and M. E. Mauel, Nucl. Fusion **30**, 2405 (1990).
3. M. E. Mauel and D. T. Garnier, T. Sunn Pedersen, *et al.*, in *Proceedings of the 18th IAEA Fusion Energy Conference, Sorrento, 2000*, Paper IAEA-CN-77/THP2/05.
4. A. I. Morozov, V. P. Pastukhov, and A. Yu. Sokolov, in *Proceedings of the Workshop on D–$^3$He Based Reactor Studies, Moscow, 1991*, Paper 1C1; in *Proceedings of the International Sherwood Fusion Energy Conference, Santa Fe, 1992*, Paper 2C44.
5. P. A. Popovich and V. D. Shafranov, Fiz. Plazmy **26**, 519 (2000) [Plasma Phys. Rep. **26**, 484 (2000)].
6. D. D. Ryutov and G. V. Stupakov, Fiz. Plazmy **12**, 1411 (1986) [Sov. J. Plasma Phys. **12**, 815 (1986)].
7. G. I. Dimov, Preprint No. 82-150 (Institute of Nuclear Physics, Siberian Division, USSR Acad. Sci., Novosibirsk, 1982); G. I. Dimov and P. B. Lysyanskiĭ, Preprint No. 86-102 (Institute of Nuclear Physics, Siberian Division, USSR Acad. Sci., Novosibirsk, 1986).
8. B. Lane, R. S. Post, and J. Kesner, Nucl. Fusion **27**, 227 (1987).
9. V. P. Pastukhov and A. Yu. Sokolov, Fiz. Plazmy **17**, 1043 (1991) [Sov. J. Plasma Phys. **17**, 603 (1991)].
10. J. A. Casey, B. G. Lane, J. H. Irby, *et al.*, Phys. Fluids **31**, 2009 (1988).
11. Y. Yasaka, N. Takano, and H. Takeno, Trans. Fusion Technol. **39** (1T), 350 (2001).
12. T. D. Akhmetov, V. S. Belkin, E. D. Bender, *et al.*, Fiz. Plazmy **23**, 988 (1997) [Plasma Phys. Rep. **23**, 911 (1997)].
13. J. Kesner, L. Bromberg, M. Mauel, *et al.*, in *Proceedings of the 17th IAEA Fusion Energy Conference, Yokohama, Japan, 1998* (IAEA, Vienna, 1999), Vol. 3, p. 1165.
14. V. V. Arsenin, E. D. Dlougach, V. M. Kulygin, *et al.*, Nucl. Fusion **41**, 945 (2001).
15. M. M. Berdnikova, S. V. Vaĭtonis, A. M. Vaĭtonene, *et al.*, Vopr. At. Nauki Tekh., Ser. Termoyad. Sintez, No. 1, 22 (2003).
16. B. B. Kadomtsev, in *Plasma Physics and the Problem of Controlled Thermonuclear Reactions*, Ed. by M. A. Leontovich (Pergamon Press, New York, 1960), Vol. 4.
17. V. V. Arsenin and L. V. Mikhaĭlovskaya, Fiz. Plazmy **14**, 1015 (1988) [Sov. J. Plasma Phys. **14**, 596 (1988)].

18. V. V. Arsenin, Itogi Nauki Tekh. Ser.: Fiz. Plazmy **8**, 49 (1988).
19. S. V. Kuz'min, Fiz. Plazmy **16**, 992 (1990) [Sov. J. Plasma Phys. **16**, 576 (1990)].
20. S. V. Kuz'min and P. B. Lysyanskiĭ, Fiz. Plazmy **16**, 1001 (1990) [Sov. J. Plasma Phys. **16**, 581 (1990)].
21. J. W. Connor and R. J. Hastie, Phys. Rev. Lett. **33**, 202 (1974).
22. A. B. Mikhailovskii, *Instabilities in a Confined Plasma* (IOP, Philadelphia, 1998), Chap. 18.
23. V. D. Pustovitov and V. D. Shafranov, in *Reviews of Plasma Physics*, Ed. by B. B. Kadomtsev (Énergoatomizdat, Moscow, 1987; Consultants Bureau, New York, 1990), Vol. 15.
24. V. V. Arsenin, E. D. Dlougach, V. M. Kulygin, *et al.*, Trans. Fusion Sci. Technol. **43** (1T), 147 (2003).
25. V. V. Arsenin, Fiz. Plazmy **28**, 843 (2002) [Plasma Phys. Rep. **28**, 776 (2002)].
26. A. B. Bernstein, E. A. Frieman, M. D. Kruskal, and R. M. Kulsrud, Proc. R. Soc. London **A244**, 17 (1958).
27. N. N. Bogolyubov and Yu. A. Mitropol'skii, *Asymptotic Methods in the Theory of Nonlinear Oscillations* (Nauka, Moscow, 1974; Gordon & Breach, New York, 1962).
28. A. B. Mikhailovskii, *Theory of Plasma Instabilities* (Atomizdat, Moscow, 1971; Consultants Bureau, New York, 1974)., Vol. 2.
29. M. D. Kruskal and C. R. Oberman, Phys. Fluids **1**, 275 (1958).
30. M. N. Rosenbluth and N. Rostoker, Phys. Fluids **2**, 23 (1959).
31. L. S. Hall and B. McNamara, Phys. Fluids **18**, 552 (1975).
32. A. F. Walstead, Phys. Fluids **25**, 1358 (1982).
33. V. V. Drozdov and A. A. Martynov, Fiz. Plazmy **12**, 1429 (1986) [Sov. J. Plasma Phys. **12**, 826 (1986)].
34. V. V. Drozdov and A. A. Martynov, Fiz. Plazmy **14**, 1308 (1988) [Sov. J. Plasma Phys. **14**, 765 (1988)].
35. A. N. Simakov, R. J. Hastie, and P. J. Catto, Phys. Plasmas **7**, 3309 (2000).
36. V. V. Arsenin and A. Yu. Kuyanov, Fiz. Plazmy **27**, 675 (2001) [Plasma Phys. Rep. **27**, 635 (2001)].
37. A. A. Skovoroda, Fiz. Plazmy **31** (2005) (in press).

*Translated by O.E. Khadin*

*Plasma Physics Reports, Vol. 31, No. 1, 2005, pp. 46–56. Translated from Fizika Plazmy, Vol. 31, No. 1, 2005, pp. 52–63.*


**DUSTY PLASMA**

# Basics of Dusty Plasma

**A. M. Ignatov**

*Prokhorov Institute of General Physics, Russian Academy of Sciences, ul. Vavilova 38, Moscow, 119991 Russia*

Received June 30, 2004

**Abstract**—The paper presents an introductory review of the basic physical processes in dusty plasmas. The topics to be addressed are dust charging, forces acting on dust grains, interaction between dust grains, and dust–plasma structures. © *2005 Pleiades Publishing, Inc.*

## 1. INTRODUCTION

Dusty plasma (also called complex, colloidal, or aerosol plasma) is an ordinary plasma contaminated with a certain amount of condensed (solid or liquid) particulates (grains). To start with, such a definition is quite sufficient because there is currently no exact definition of plasma in general. The main objective of the present review is to provide a clearer insight to some aspects of the problem.

Aerosols in gas discharges were observed under laboratory conditions as early as the beginning of the twentieth century. In 1912, A. F. Joffe measured the elementary charge with the help of metallic grains that were synthesized in a gas discharge and acquired an electric charge. The grains then fell down into a capacitor with a dc electric field counterbalancing gravity so that each grain steadily held its position over a long period. This experimental setup anticipated many modern installations.

Astronomical observations of various objects such as nebulae or Saturn's rings had began much earlier. We now realize that these are also examples of dusty plasma. However, dusty plasma physics is a very young science. When the first issue of *Plasma Physics Reports* was published, the term "dusty plasma" had not yet come into use. Although astrophysicists always understood the importance of dust grains in space, only a few papers on this subject were published annually.

About thirty years ago, the first experiments on plasma with a condensed disperse phase (CDP) were performed. Such a plasma is actually a hot flame with an admixture of aerosol particles emitting electrons. In addition, water solutions of charged colloids have been investigated for a long time. Many phenomena in CDP plasmas and in colloidal solutions have analogues in gas-discharge dusty plasma, so it is sometimes proposed that a single term to unify all these physical systems be used. For example, the terms "colloidal" or "complex" are applied. However, there are important distinctions between all these systems; therefore, in what follows, the term "dusty plasma" will be used in its narrow sense to designate a low-temperature plasma containing aerosols. A medium composed of electrons, ions, and neutral atoms is called, for simplicity, a pure plasma. The more formal term "complex plasma" is regarded as a synonym for dusty plasma. Aerosol particulates are commonly called dust grains. When speaking about colloidal plasma, we imply just water colloidal solutions, which are not addressed here.

Tremendous advances in dusty plasma physics were made in the late 1980s and were triggered mainly by the needs of plasma surface treatment, where the formation of dust plays a major and, as a rule, harmful role. On the other hand, synthetic dust grains produced in plasma allow one to create new materials with numerous beneficial properties. From the physical standpoint, the most stimulating discovery was the theoretical prediction of dust condensation and, in particular, the formation of Coulomb crystals composed of dust grains. Experimental observations of dust–plasma crystals have given impetus to thorough investigations on this subject.

Since the early 1990s, the number of papers on dusty plasma has grown exponentially without any tendency to saturation. A few thousand papers on this subject are now published annually. It seems that it is time to strike a balance. This is why many review papers have been written during the last few years. *Plasma Physics Reports* has recently published an encompassing series of articles on dusty plasmas [1–4]. The basic physical processes are discussed in the reviews [5, 6] and in the monograph [7]. Processes in chemically active dusty plasmas are addressed in [8–11]. Astrophysical aspects are discussed in [12], and the state of the art in colloidal plasma physics is described in [13, 14].

In the present paper, I try to briefly describe a few physical processes occurring in dusty plasmas that are most important in my opinion. Considerations of space preclude a comprehensive account of the problem. The list of references is minimal; a much more complete bibliography may be found in the above reviews.

1063-780X/05/3101-0046$26.00 

## 2. TYPICAL EXPERIMENT

Most of the dusty plasma experiments have been performed with a discharge chamber like that sketched in Fig. 1. The plasma is produced by applying a voltage to electrodes *1* and *2*. With an rf discharge, there may be only one (lower) electrode. Various gases with pressures varying over a very wide range are used. In estimating the characteristic plasma parameters, we will imply that the buffer gas is argon at a relatively low (<1 torr) pressure. There are also a lot of other means to produce plasma; the details may be found in the reviews cited above.

Dust grains may form spontaneously from the gaseous or plasma phase or appear due to sputtering of the electrodes. The grains thus produced are polydisperse and have very different dimensions and properties. Artificial grains with well-controlled dimensions are also often injected into plasma. The total number of grains, in this case, may vary from one to a few tens of thousands.

Grains with a size larger than a few microns can easily be observed by optical methods. The relatively slow grain motion may be recorded with a video camera. By processing the video record, one can determine the velocity and position of each grain. This yields unique information about the dust component as a whole. For example, one may observe various structures formed by dust grains, study phase transitions, etc. However, measuring the plasma parameters in the region occupied by dust is a much more difficult task; therefore, many experimental works deal only with estimated values of these parameters.

A distinctive feature of dusty plasma is that various nonelectric forces can play a very important role in it. In ground-based experiments, gravity dominates for grains with a size larger than a few microns, so these grains fall. Near the lower electrode, the weight of relatively light grains is counterbalanced by the electric field and they gather in the electrode sheath (see Fig. 1).

There are various ways to confine grains in the bulk of the plasma. First, Brownian motion is capable of suspending submicron-size grains; however, it is rather difficult to observe the motion of such grains by optical means. The second way is to use thermophoresis in a neutral gas. Cooling the upper electrode (or/and heating the lower one) creates a heat flux in a neutral gas, which supports grains in the bulk of the plasma. In a stratified dc discharge, potential wells in the central part of the plasma column are formed; this also results in the trapping of grains. Finally, the most radical way to get rid of the gravity force is to place the experimental chamber on a ballistic missile or on an aircraft flying over a parabolic trajectory or to perform the experiments onboard the orbital space station. All these ways of embedding grains in the main plasma have been successfully used (in particular, in experiments performed onboard the International Space Station).

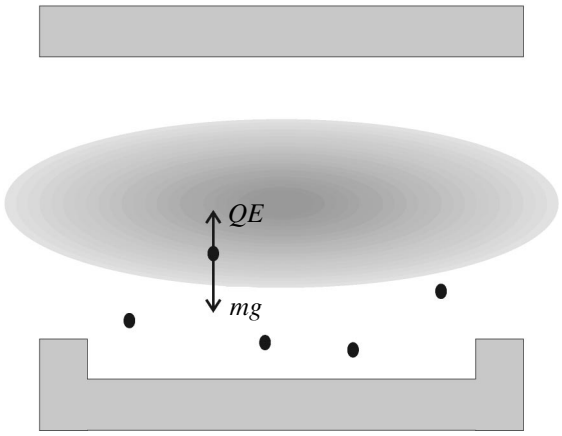


**Fig. 1.** Sketch of the discharge chamber in which most of ground-based dusty plasma experiments have been performed.

Obviously, the physical conditions in the plasma bulk and in the sheath region are quite different and, accordingly, different processes may dominate in them. As a result, dust structures formed in the plasma bulk differ from those formed in the sheath. This issue will discussed below in more detail.

## 3. DUST CHARGING

The main difference between dusty plasmas and aerosols in a neutral gas lies in the huge charges of the dust grains. A neutral grain placed in plasma acquires a negative charge since the electron flux onto its surface exceeds the ion flux due to the higher electron mobility. The negative charge reduces the electron flux and increases the flux of positive ions. The steady state is achieved when the net electric current at the grain surface becomes zero,

$$I = I_e(Q) + I_i(Q) + \ldots = 0, \quad (1)$$

where $I_{e,i}$ are the electron and ion currents, which depend on the grain charge $Q$, and the ellipsis stands for other currents (e.g., those of negative ions), which sometimes are also of importance. This process is similar to the charging of a floating probe; however, the charge of the probe is of little interest for plasma diagnostics, while in dusty plasmas, the grain charge plays the major role.

In order to evaluate the equilibrium grain charge, we have to solve Eq. (1); i.e., it is necessary to know the explicit dependence of the currents on the grain charge. As applied to probes, this problem has been discussed for a number of decades; nevertheless, comprehensive analytical theory of charging is still lacking. To estimate the equilibrium grain charge in an isotropic plasma, the so-called orbital motion limited (OML) model is often used. This approximation is based on the following assumptions: First, collisions between electrons, ions, and neutral atoms are ignored. Second, it is

supposed that a charged plasma particle hitting the grain is either absorbed by the grain or recombines on its surface, thus producing a neutral atom. Finally, it is assumed that, if the laws of conservation of energy and angular momentum allow a particle to reach the grain surface, then it does reach this surface. This is enough to evaluate the currents at the grain surface:

$$I_e = -4\pi e a^2 n_e \sqrt{\frac{T_e}{2\pi m_e}} e^{e\varphi_0/T_e}, \quad (2)$$

$$I_i = 4\pi e a^2 n_i \sqrt{\frac{T_i}{2\pi m_i}} \left(1 - \frac{e\varphi_0}{T_i}\right). \quad (3)$$

Here, it is assumed that the plasma consists of electrons and one ion species; $m_{e,i}$, $T_{e,i}$, and $n_{e,i}$ are the electron and ion masses, temperatures, and densities, respectively; and $\varphi_0$ is the surface electric potential of a spherical grain of radius $a$. Substituting these expressions into Eq. (1), one may calculate the equilibrium surface potential $\varphi_0$. However, knowing currents (2) and (3) is yet insufficient to evaluate the grain charge or, equivalently, the electric field on its surface; it is also necessary to know the self-consistent distribution of the electric potential around the grain. It was found that the capacitance of a sufficiently small grain ($a \ll \lambda_{De} \equiv \sqrt{T_e/4\pi e^2 n_e}$) in plasma is close to its vacuum value; i.e., $Q = a\varphi_0$. Moreover, a rigorous analysis shows that the basic assumptions of the OML model are satisfied in this limit only. In evaluating currents (see expressions (2), (3)), it was supposed that the grain charge is negative; i.e., it repels electrons and attracts ions. The difference between expressions (2) and (3) is due to the additional assumption that there are no trapped ions (i.e., ions with a negative total energy), which follow finite orbits around the grain. If, for some reason, the grain charge becomes positive, then expressions (2) and (3) should be interchanged. It should also be stressed that for the OML model of charging to be applicable, the grain size should not be too small. We may regard a grain as a solid body and plasma as a continuous medium only if $a \gg n_{e,i}^{-1/3}$. Otherwise, the dust should be treated as an additional microparticle species.

It follows from balance equation (1) and expressions (2) and (3) for the currents that the equilibrium charge may be represented in the form $Q = -zaT_e/e$, where the dimensionless coefficient $z$ depends weakly on the plasma parameters and usually ranges from 2 to 5. For typical plasma parameters and micron-size grains, the normalized grain charge $Z_d = |Q|/e$ may be as large as $Z_d \approx 10^4$–$10^5$. It could be even larger; however, at $Z_d \approx 10^5$–$10^6$, the negative electric field pressure at the grain surface becomes comparable to the ultimate strength of the grain material and the grain is destroyed.

As was noted above, a negatively charged grain forms a potential well for positive ions. In the idealized collisionless model, the potential well is empty. However, even at an arbitrarily low collision frequency, the well is gradually filled with ions and the resulting potential distribution may substantially differ from that given by the OML model. In particular, numerical simulations show that the equilibrium charge may be halved as compared to the OML model.

Plasma absorption by the grain surface leads to a specific distribution of the electric field around the grain. Since electrons and ions are absorbed, there exists a converging plasma flow in the vicinity of the grain and the plasma density perturbation $\delta n_{e,i}$ at large distances from the grain behaves as $\delta n_{e,i} \sim 1/r^2$. Accordingly, the electric potential also decreases in inverse proportion to the distance squared, $\varphi(r) \sim 1/r^2$. Therefore, due to plasma absorption, the grain electric field penetrates into the ambient plasma to a depth much exceeding the Debye length.

In order to evaluate the currents at the grain surface, the effective charging (or absorption) cross section is often introduced. In the OML model, this cross section can be easily calculated for an arbitrary spherically symmetric distribution of the electric potential, assuming that all the plasma particles approaching the grain center a distance smaller then $a$ are absorbed:

$$\sigma_\alpha(q, v) = \pi a^2 \left(1 - \frac{2Qe_\alpha}{am_\alpha v^2}\right) \theta(am_\alpha v^2 - 2Qe_\alpha). \quad (4)$$

Here, $\alpha = e, i$; $v$ is the particle velocity at infinity; and $e_\alpha = \pm e$ is the charge of a plasma particle. The Heaviside step function $\theta$ applies here to the repulsive potential only, i.e., to the plasma species some particles of which cannot reach the grain surface. The current density of the particles absorbed by the grain surface is given by the integral

$$j_\alpha = e_\alpha \int d\mathbf{v}\, v \sigma_\alpha(q, v) f_\alpha(\mathbf{v}, \mathbf{r}), \quad (5)$$

where $f_\alpha(\mathbf{v}, \mathbf{r})$ is the distribution function of the particles of the $\alpha$ species at the grain location. Evaluating integral (5) with a Maxwellian distribution, one obtains expressions (2) and (3). Absorption cross section (4) is also often used to evaluate the grain charge in more complicated anisotropic situations, e.g., when the plasma drifts relative to the grain. It should be stressed that such an approach is groundless. In anisotropic plasmas, we cannot assume that the potential distribution around the grain is spherically symmetric, and the analysis of the conservation laws underlying the OML model fails. The influence of the deviations from spherical symmetry on the dust charge has not yet been estimated even in the case of weakly anisotropic plasmas. Thus, we may accept as a reasonable estimate that the grain charge is equal to $Z_d = zaT_e/e^2$, where the factor $z$ is on the order of unity and depends on the properties of the ambient plasma; however, the accuracy with which this factor is evaluated in various theoretical models should not be exaggerated.

It follows from the above estimates that a single grain absorbs nearly all the electrons from a plasma region with a characteristic size of $L_0$, defined by $L_0^3 n_e \sim Z_d$, i.e, $L_0 \sim (a\lambda_{De}^2)^{1/3}$. If $a \ll \lambda_{De}$, then the size of this region is much larger than the grain radius. Strictly speaking, it is only to this case that the dusty plasma concept is applicable. Otherwise, we are dealing with an absorbing body that changes the density of the surrounding plasma only near its surface.

For a sufficiently high dust concentration, when the average distance between grains is about $L_0$, a considerable part of plasma electrons is absorbed by the dust. Since, on average, plasma is quasineutral, the condition of the zero net charge, $Z_d n_d + n_e = n_i$, where $n_d$ is the dust density, is satisfied. The relative dust concentration is conveniently characterized by the dimensionless parameter $P = Z_d n_d/n_i$, which indicates what fraction of electrons is absorbed by the dust. Under experimental conditions, $P$ may be close to unity. The average electron density and the grain charge are then considerably reduced. This happens at a relatively small dust concentration, $n_d/n_i \sim 10^{-6}$–$10^{-5}$. The difference between the electron and ion densities influences the dispersion of some plasma oscillations (e.g., Alfvén waves) whose frequency is much higher than the characteristic frequency of dust motion.

The grain charge also varies over time. The rate of charge relaxation toward its equilibrium value is determined by the derivative of current (1) with respect to the charge. If the charge is close to its equilibrium value, $Q = Q_0 + \delta Q$, where $I(Q_0) = 0$, then we have $d\delta Q/dt = -\nu_{ch}\delta Q$, where the charging frequency is $\nu_{ch} = -I'(Q_0)$. In the OML model, from Eqs. (2) and (3) we obtain

$$\nu_{ch} = \omega_{pi}\frac{a}{\lambda_{Di}}\frac{z+1+\tau}{\sqrt{2\pi}}, \qquad (6)$$

where $\tau = T_i/T_e$ (as a rule, $\tau \ll 1$) and $\omega_{pi}$ is the ion plasma frequency. Under typical laboratory conditions, the charging frequency substantially exceeds the characteristic frequency of dust motion, which is usually about a few hertz. For this reason, the charge of a dust grain moving through an inhomogeneous plasma is permanently changing. This results, e.g., in the specific damping of dust waves. The character of the electric interaction between dust grains may also change [15].

Fluctuations of the grain charge are of great importance. Since the charging is a discrete Markovian process, the charge fluctuations are proportional to the square root of the grain charge, i.e., $\langle \delta Z_d \rangle^2 \sim Z_d$. For sufficiently small grains with $Z_d \sim 10$, this leads to a random change in the sign of the grain charge; this effect plays an important role in the coagulation and synthesis of dust grains from the plasma phase. At larger values of $Z_d$, the charge fluctuations correlate with the fluctuations of the ambient plasma and the grain velocity. Therefore, the grain charge must be considered as an additional inner degree of freedom.

Besides the charging due to plasma absorption, there are also other mechanisms for dust charging. This is, e.g., photoemission, which is often dominant under space conditions and results in a positive grain charge. If the temperature of the grain surface is sufficiently high (as is the case with grains in flame), the thermal electron emission becomes efficient. The surface heating may also be caused by plasma recombination; in this case, the equilibrium charge is determined by both the current and heat balance [16].

For comparison, we also mention the charging in colloidal suspensions. Colloidal particles in water acquire an electric charge due to electrochemical reactions at their surface. Although the charge of colloidal particles ($Z_d \sim 100$) is smaller than the grain charge in a gas-discharge plasma, colloidal plasma is a more nonlinear medium. The ratio $e\varphi_0/T_e$ in a dusty plasma is on the order of unity, while in a colloidal plasma at room temperature, the characteristic surface potential of a particulate is about one volt, i.e., $e\varphi_0/T \gg 1$. Another important distinction that does not allow one to consider dusty and colloidal plasmas from a common viewpoint is that colloidal systems are in thermodynamic equilibrium, while dusty plasmas are always far from equilibrium.

## 4. FORCES ACTING ON A GRAIN IN PLASMA

Unlike pure plasmas, there are many different forces acting on a grain in dusty plasma. A characteristic effect is the so-called ion drag. In low-pressure gas-discharge plasmas, surface recombination occurs predominantly at the chamber wall; as a result, there are always directed plasma flows that drag dust grains. Evidently, interaction with ions plays the governing role. In the central part of the discharge, the flow velocity may be much smaller than the thermal velocity, while near the wall or the electrodes, it can exceed the ion sound velocity.

Ion drag arises due to both the ion absorption by a grain and the ion scattering in its electric field. Accordingly, the ion wind force is a sum of two parts, the first of which is related to the momentum flux of the ions absorbed by the grain and the second is related to the momentum flux of the scattered ions. The net force acting on the grain may be written as

$$\mathbf{F}_d = m_i \int d\mathbf{v}\, v\mathbf{v} f_i(\mathbf{v})[\sigma_i(v) + \sigma_s(v)], \qquad (7)$$

where $\sigma_i(v)$ is the ion absorption (or collection) cross section given, e.g., by Eq. (4) and $\sigma_s(v)$ is the scattering cross section. The latter may be evaluated analytically only for a Coulomb potential by cutting off the divergent integrals at large and small scales. Since the cutoff parameters are somewhat arbitrary, the resulting

drag force may vary by many times [17]. When the flow velocity $u$ is much smaller than the thermal velocity, the drag force is written as

$$F_d = a^2 m_i n_i v_{Ti} u (K_a + K_s), \quad (8)$$

where $K_a$ and $K_s$ are dimensionless coefficients corresponding to absorbed and scattered ions, respectively. Under the conditions typical of a gas-discharge plasma, both coefficients in Eq. (8) are large, $K_{a,s} \gg 1$. By using different approximations, different authors obtain dissimilar results. For example, when the ion scattering with impact parameters exceeding the Debye length is taken into account, it turns out that the scattering dominates, $K_s \gg K_a$ [17], while ignoring such scattering yields $K_s \sim K_a$. Although there are experimental indications in favor of the second alternative [18], the question about the drag force still remains open even for low drift velocities. The situation with drift velocities exceeding the ion thermal velocity is much more indeterminate. Thus, the possibility of a negative friction force directed opposite to the ion flow was discussed in [19] and was recently confirmed by numerical simulations [20].

In this context, it is worth returning to the discussion of the grain charge. As was already pointed out, dust grains in a low-temperature plasma acquire a negative charge. It is sometimes reasonable to regard the grain and the accompanying perturbation of the ambient plasma as a whole, i.e., as a quasi-atom. Due to quasineutrality, the net charge of a quasi-atom is nearly zero. When an external electric field is applied to the plasma, two forces act on the grain: the electric field force, directed against the field, and the ion drag force, directed along the field. It follows from the above estimates that the ion drag force is much larger than the electric field force. In other words, the net force acting on a quasi-atom, i.e., the electrophoretic force, is directed along the external electric field. In physics, the charge is usually defined as a force-to-field ratio; if we accept this definition, then we should consider dust grains as positively charged objects.

In low-temperature plasmas, the degree of ionization is small and the interaction of dust grains with a neutral gas influences their motion. Two processes are most important here. First, the friction on the neutral buffer gas affects the grain motion. The friction force may be approximately found from Eq. (8) by substituting $K_a = K_s = 1$ and replacing the ion density and the ion thermal velocity with the corresponding parameters of the neutral gas. Under typical laboratory conditions, the friction force is comparable to the grain weight; as a result, after several centimeters of free fall, the grain moves uniformly.

The thermophoretic force produced by the neutral gas also can play an important role. In the free-molecular regime, thermophoresis is caused by the heat flux that distorts the atom velocity distribution. The thermophoretic force is $\mathbf{F}_{th} = -8a^2 n_n \lambda \nabla T_n$, where $n_n$ and $T_n$ are the density and temperature of the neutral gas, respectively, and $\lambda$ is the mean free path. This force pushes the grains toward a colder gas regions. Producing the proper temperature gradient in the neutral gas, one may easily counterbalance the grain weight and hold the grains in the plasma bulk.

Experimentalists often use laser radiation to control the motion of individual grains [21]. Using a laser beam, one can push a grain in an ordered structure (e.g., in a crystal), thus exciting a sound wave. The light may influence the grain motion via two mechanisms. First, the grain may drift toward the maximum of the electromagnetic field due to the ponderomotive force that acts across the laser beam. Second, when the grain is illuminated by a laser, a force acting along the laser beam appears. Although this force is usually attributed to the light pressure, in most cases the photophoresis provided by the radiometric force dominates. The latter arises because the grain surface is headed nonuniformly by the laser and the neutral gas pressure at the hotter side is larger than at the colder one.

Since both thermophoresis and photophoresis are provided by the heat exchange between the grain surface and the ambient medium, the presence of plasma may drastically influence these processes. In an anisotropic medium, the heat flux $\Phi$ at the grain surface can be represented as $\Phi = \langle\Phi\rangle + \delta\Phi$, where $\langle\Phi\rangle$ is the heat flux averaged over the grain surface. In a steady state, the condition of the zero net flux, $\langle\Phi\rangle = 0$, determines the average equilibrium temperature of the grain, while the anisotropic part $\delta\Phi$ is responsible for nonuniform heating. A dust grain exchanges its energy with both the plasma and the neutral gas. With reasonable accuracy, we may suppose that, when a neutral atom hits the grain surface, its energy is completely accommodated, i.e., the atom wastes its energy on the grain heating and leaves the grain with the energy corresponding to the local surface temperature. An ion hitting the grain surface recombines, and a considerable amount of energy that is on the order of the ionization potential (10–20 eV) is transferred to heat. Moreover, due to the large grain charge, the ions falling on the grain surface gain additional kinetic energy. All this increases the energy flux from the ion component by two or even four orders of magnitude. As a result, the average grain temperature may achieve a few hundred degrees. The anisotropic plasma heat flux may also result in the nonuniformity of the surface temperature. For example, when the plasma anisotropy is caused by the ion heat flux, the plasma thermophoretic force is directed along the ion temperature gradient and a grain drifts to the hotter plasma region [22]. Seemingly, the presence of plasma may also influence the photophoresis but, so far, this problem has not been investigated.

## 5. INTERACTION BETWEEN GRAINS

Above, we discussed various macroscopic forces acting on a single grain. Analogous forces also result in the interaction between grains. Two ultimate cases should be distinguished. At a sufficiently low dust concentration, the dust has little effect on the parameters of the ambient plasma. In this case, one can talk about pairwise interactions between grains. In contrast, at a high dust concentration, the dust determines the discharge structure and the plasma parameters, thereby resulting in collective interactions.

We start with pairwise interactions. Evidently, the electrostatic interaction between grains is of great importance. In an isotropic plasma, the electric field of an external charge is screened on the spatial scale on the order of the Debye length. This leads to the repulsion interaction between grains at intermediate distances between them. As was already mentioned above, plasma absorption at the grain surfaces results in a power-law radial profile of the grain potential. However, this effect yields a rather weak interaction force, so other (nonelectric) forces dominate at large intergrain distances.

At intergrain distances smaller than the Debye length and comparable to the grain size, the interaction is more complicated. In this case, the grains can no longer be considered as point charges and their electric field is described by essentially nonlinear equations that cannot be solved analytically. Moreover, the grain charge depends on the distance to the neighboring grain. It should be noted that there have been many attempts to derive the attraction between like charges due to the nonlinear electrostatic interaction. However, a rigorous analysis of the momentum balance in collisionless plasmas shows that this is impossible [23]. Attraction may arise due to some other nonelectric forces, e.g., those caused by plasma absorption by grains.

In an anisotropic plasma, the situation is quite different. Supersonic ion flows are always present near the electrodes and the chamber wall. The dielectric permittivity of a homogeneous plasma under these conditions has the form $\epsilon(\omega, \mathbf{k}) = 1 - \omega_{Li}^2/(\omega + k_z u - i0)^2 + 1/k^2\lambda_{De}^2$, where it assumed that the ions move along the $u$ axis and their directed velocity $u$ points downward. Since the static dielectric function $\epsilon(0, \mathbf{k})$ may change its sign, a point charge at rest produces an ion sound wake with a spatially alternating electric potential. Figure 2 shows a typical potential distribution around a unit charge located at $z = 0$ and $x = 0$; here, the darker regions correspond to the lower electric potential. The potential oscillates in the region located below the charge and confined by the Mach cone. Outside the Mach cone the electric potential decays exponentially with increasing distance from the charge.

Downstream from a negatively charged grain a local maximum of the ion density is formed. This effect, which is often called ion focusing, results in interesting features of the grain interaction. A bounded pair forms when the second grain is placed in the wake excited by the first grain [24]. This interaction is asymmetric: if one push the upper grain with the help of a laser pulse, the lower grain will follows the upper one. However, the lower grain acts on the upper one through a screened Coulomb potential; therefore, when the lower grain is shifted, the position of the upper grain remains unchanged. This elegant experiment demonstrates that the pairwise interaction provided by the ion focusing is essentially nonpotential and, moreover, Newton's third law is violated in this case.

In a homogeneous plasmas, grains situated at the same altitude repel one another. However, if they are placed near a conducting wall, the electrostatic images of their Mach cones may provide attractive interaction

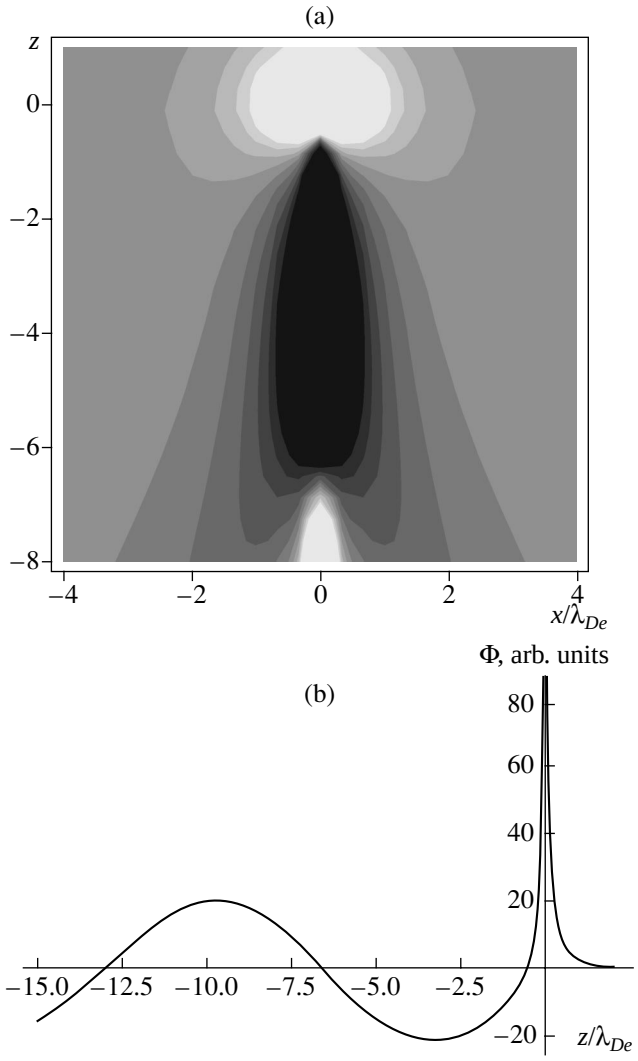


**Fig. 2.** (a) Two-dimensional distribution of the electric potential around a unit charge in the presence of an ion flow with $u/v_s = 2$ and (b) the $z$ profile of the potential at $x = 0$.

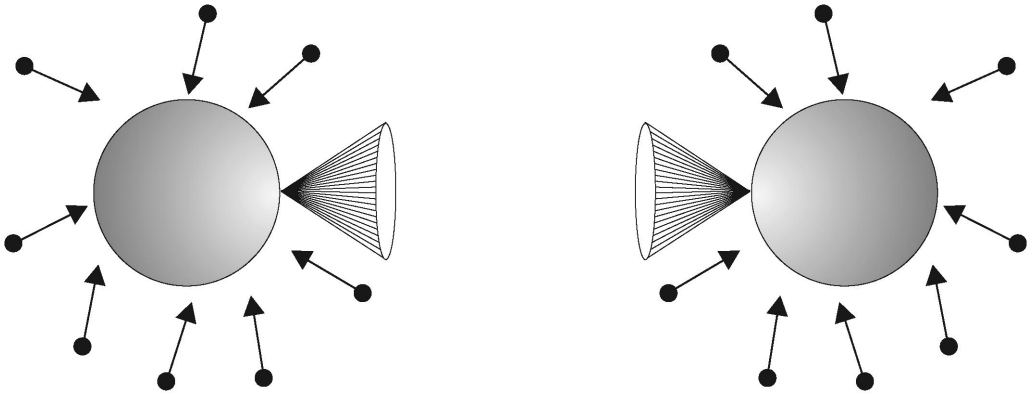

**Fig. 3.** Shadow interaction between two dust grains. The ions with velocities lying within the shadow cones do not reach the grains.

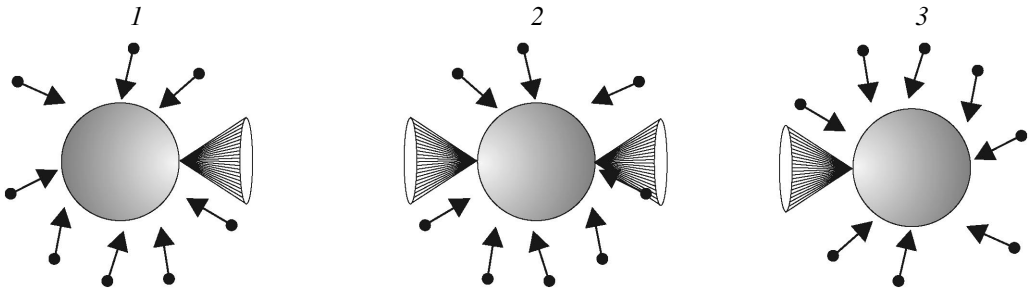


**Fig. 4.** Shadow interaction among three dust grains.

[25, 26]. In this case, the interaction force between the grains is an oscillating function of distance.

In addition to the electric forces, the forces caused by the ion wind also affects the grain interaction. As was mentioned above, the plasma is absorbed by a grain and there is a converging plasma flow around it. Using Eq. (3), one can readily estimate the flow velocity far from the grain ($r \gg \lambda_{De}$): $v_r \sim v_s z a^2/r^2$, where $v_s = \sqrt{T_e/m_i}$ is the ion sound velocity. If another grain is placed a certain distance $r$ from the first one, then it is dragged by the ion wind force (8). This drag force is estimated as $F \sim zT_e n_i K a^4/r^2$, where $K = K_a + K_s$ is the net dimensionless coefficient in Eq. (8). Such an interaction results in attraction between grains. The origin of this attraction is sketched schematically in Fig. 3. Since grains absorb the plasma, part of the ions moving toward, e.g., the left grain are trapped by the right one. As a result, the ion velocity distribution function at the grain surface is zero inside a certain cone. This, in turn, reduces the plasma pressure in the gap between grains.

Attraction provided by plasma absorption is called the shadow force or the LeSage gravity, after the French scientist who proposed a similar explanation of universal gravitation in the 18th century [27]. Although the shadow force is caused by the redistribution of the ion momentum flux, its magnitude is proportional to the electron temperature. The reason is that the electron temperature determines the grain charge and, accordingly, the net current of the absorbed ions. As was mentioned above, the electric potential of the grain behaves asymptotically as $1/r^2$ (i.e., the electric field decreases with radius as $E \sim 1/r^3$); hence, at large distances, the electric repulsion changes with the shadow attraction.

To the best of my knowledge, the attraction between two isolated grains has not yet been observed experimentally; however, experiments demonstrated the attraction of grains toward more massive bodies. Thus, in [28], a negatively biased wire was placed in a dusty plasma. The grains placed near the wire were repelled, while the grains situated at larger distances were attracted. This effect was interpreted as an attraction caused by the ion wind, i.e., as the LeSage force.

The shadow force exemplifies nonpairwise interaction. Let us suppose that there are three neighboring grains (Fig. 4). The force acting on grain *1* is then independent of the position of grain *3*. The change in the plasma momentum flux that results in the shadow force is provided by the second grain only, while the third grain is invisible from the surface of the first grain. This example shows that the LeSage force may be screened by other grains.

At a sufficiently high dust concentration, the shadow forces become collective. In the absence of dust, the transport processes in a discharge plasma are mainly governed by the collisions of charged particles

with neutral atoms. The cross section for ion–dust collisions is very large. Under typical experimental conditions, cross section (4) for thermal ions is $\sigma_i \sim 10^{-5}$–$10^{-4}$ cm$^2$, which exceeds characteristic collisional cross sections in pure plasmas by approximately ten orders of magnitude. Therefore, even a moderate dust concentration is sufficient for the gas-discharge structure to be governed by the ion–dust collisions, rather than ion–neutral or ion–ion collisions; in this case, the plasma mainly recombines in the bulk of the discharge rather than on the discharge chamber wall. The theory of grain interaction [4] under these conditions takes into account the plasma production by an external source, the bulk recombination, and the electric forces. According to the theory, the characteristic spatial scale (analogous to the Debye length in pure plasmas) above which collective processes become important is $L_{\rm cr} = \lambda_{Di}^2/aP$.

A number of other mechanisms of grain interaction have been discussed in the literature: the thermophoresis provided by the heat exchange between dust grains and the neutral gas, the polarization forces analogous to van der Waals forces acting between neutral atoms, and others. Under typical laboratory conditions, all these forces are much smaller than the electric or shadow forces, but one cannot exclude that they may manifest themselves somewhere.

## 6. STRUCTURES IN DUSTY PLASMAS

As is well known, the degree to which a pure plasma is nonideal is characterized by the so-called coupling parameter $\Gamma = U(n^{-1/3})/T$, which is the ratio of the average interparticle potential energy to the average kinetic energy. For charge particles (with the charge $eZ$) interacting via the Coulomb potential, the coupling parameter is equal to $\Gamma = e^2Z^2n^{1/3}/T$. A pure plasma is regarded as nonideal if $\Gamma > 1$; as a rule, the coupling parameter for pure plasmas does not substantially exceed unity.

The main difference between dusty and pure plasmas is the large variety of the interaction processes in the former. As was already pointed out, the interaction between dust grains is often nonpotential and nonpairwise and, strictly speaking, there is no exact analogue of the coupling parameter for dust. Nevertheless, the coupling parameter is often used to characterize dusty plasma. It is usually introduced by assuming that the interaction between grains is described by the Debye–Hückel or Yukawa potential, $U(r) = e^2Z_d^2\exp(-r/\lambda_D)/r$. For the dust grains in the plasma bulk, the predictions of this model are in qualitative agreement with experimental data. Dusty plasmas are characterized by very large values of $\Gamma$ (up to tens of thousands). For this reason, the dust is often strongly correlated and the grains form various ordered structures.

The grain ordering depends the plasma parameters and the method for the gain trapping. Three-dimensional crystalline dust structures were observed in standing striations of a dc discharge in [5]. As the discharge current grows, the crystal melts and a phase transition to a short-range order fluid state occurs. As the current grows further, a transition to a gaseous state is observed. An interesting feature of the gaseous state is the anomalous heating of dust. The dust temperature defined as the average kinetic energy of grains may exceed the electron plasma temperature. The reasons for this are not quite understood, and a number of theories has been proposed to explain this phenomenon. Anyway, the temperature difference between the dust and the ambient plasma shows that the traditional concepts of Brownian motion are inapplicable to dusty plasmas.

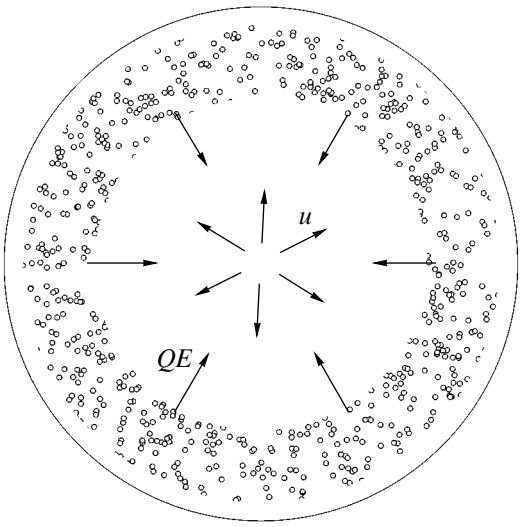


**Fig. 5.** Formation of a dust void.

Another interesting feature is the structural instability of dust in a gaseous state, as is depicted in Fig. 5. Let us suppose that the gravity force is insignificant, the plasma is produced by an external ionizer, and the dust homogeneously fills a spherical chamber. At a sufficiently high dust concentration, the plasma density is determined by the balance between ionization and bulk recombination on dust grains. Let there accidentally appear a region with a reduced dust concentration. The plasma density in this region then increases, and the ion flows extruding the dust arise. This leads to a further reduction in the dust concentration. However, the dust cannot settle down at the chamber wall since the latter is negatively charged. As a result, a peculiar plasma bubble (void) forms (see Fig. 5). The void is characterized by a sharp interface between the pure plasma and the region occupied by the dust. When a grain is at the void boundary, the electric field force pushing it toward the center is counterbalanced by the ion drag force and by the excess plasma pressure. The thickness of the transition layer is determined by the dust temperature, which should be small, otherwise no void blows up. The void formation is related to the universal instability

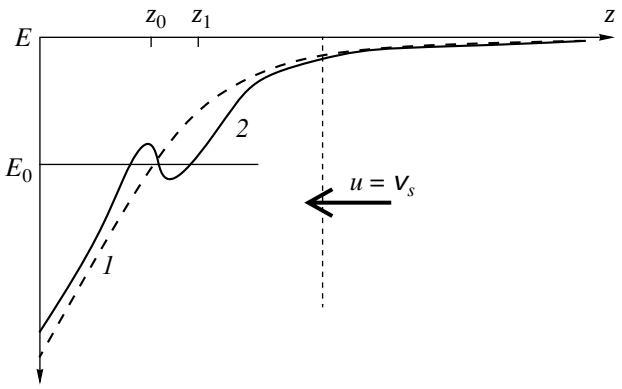


**Fig. 6.** Electric field profile near a floating electrode (*1*) in the absence of dust and (*2*) in the presence of a dust layer with a sufficiently high dust concentration. Here, $E_0 = -m_d g/Q_d$ and the vertical dashed line shows the Bohm boundary of the electrode sheath, where the directed ion velocity is $u = v_s$.

of dusty plasma [4] and is eventually provided by the above collective shadow force.

Under the action of the Earth's gravity, heavy grains settle down near the lower electrode. Curve *1* in Fig. 6 schematically shows the spatial distribution of the electric field at a distance of a few Debye lengths from the floating electrode. Qualitatively, electrons in the electrode sheath obey a Boltzmann distribution; i.e., the electron density is inhomogeneous. Hence, the grain charge also depends on the distance to the electrode. If the mass $m_d$ of a grain is not too large, there is an equilibrium height at which the electric field compensates for the grain weight, $m_d g + Q_d(z_0)E(z_0) = 0$.

As the number of grains of equal masses increases, they gather at the same height. Ions drift toward the electrode at a velocity that is larger or comparable to the ion sound velocity. Under these conditions, the electrostatic forces repel the grains from one another in the horizontal direction (Fig. 2). Apparently, in most experiments, there are no intergrain forces that might confine grains in a horizontal plane. In order to prevent grains from pushing out from the electrode, the latter is made a little concave or, as is shown in Fig. 1, a conducting ring is placed along the electrode perimeter. This forms a potential well that prevents grains from flying away.

By investigating the horizontal motion of a single grain, one can measure the parameters of the potential well and the friction force acting on the grain. With one grain placed at the bottom of the well, one can throw another grain and follow the process of scattering. This allows one to find in the dependence of the intergrain force on the distance. Evidently, such experiments require extremely proficient technique.

A small number of grains ($N \le 5$) in equilibrium form a regular polygon in a horizontal plane. When $N$ = 6, 7, or 8, one grain settles in the center and others arrange in an $(N-1)$-sided polygon. As the number of grains increases, more complex clusters consisting of a set of concentric polygons are formed. This resembles the filling of the electron shells in an atom and there exist an analogue of the periodic table for dust clusters [29]. Investigating oscillations of dust clusters, one can get more precise information on the grain interaction.

A large number of grains ($N \gg 1$) arrange in a layer with a hexagonal ordering; i.e., a two-dimensional plasma crystal appears. Such a crystal has all the attributes of a solid. For example, waves of different polarization (and, accordingly, different dispersion) may propagate through the crystal. When the number of grains reaches a certain critical value and the average distance between grains becomes small enough, the crystal melts. The second layer situated above the first one then starts to grow. Curve 2 in Fig. 6 shows the field distribution near the electrode at a sufficiently large surface charge density of the dust layer. It can be seen that, near the dust layer, there are two additional equilibrium positions for a single grain. Only the upper position ($z = z_1$) is stable; it is this position where the second layer starts to grow. By adding grains to the discharge chamber, it is possible to grow a multilayer dust crystal consisting of more than ten layers. Due to the above discussed anisotropy of the electric forces in the sheath, the grains arrange in vertical chains, while in the horizontal plane, hexagonal symmetry is conserved.

In most models implemented so far to describe two-dimensional dust crystals, grains situated at the same height were assumed to interact via the Debye–Hückel potential. This assumption usually agrees with experimental data. However, there have been experiments indicating that some other forces may play an important role in the sheath. In [30], a void in a two-dimensional dust layer was observed. The origin of this phenomenon is still unclear: it may be attributed to some external influence or to an alternating interaction potential.

Until now, we have discussed various structures in dusty plasmas under the Earth's gravity conditions. Under microgravity conditions, a much more fascinating picture is observed that has not yet been studied in detail. The PKE-Nefedov facility (named in honor of A.P. Nefedov, one of the pioneers and developers of the project) has been operating onboard the International Space Station since 2001. Although most of the results obtained are still being processed, the first papers have already appeared (see, e.g., [5, 31, 32]). As in ground-based experiments, the central part of the plasma turned out to be free of dust. The dust boundary sometimes performs periodic anharmonic oscillations resembling the heartbeats of the central void. Closer to the electrodes, the dust may be in various phase states. Unlike conditions on Earth, three different crystalline phases with pronounced interfaces between them have been observed. Moreover, there are regions filled with dust in a liquid state. Finally, dust vortices are formed in spite

of the absence of considerable plasma flows. Although several theories have already been proposed to explain the latter phenomenon, there is still no complete understanding of the vortex generation.

## 7. CONCLUSIONS

So, what is dusty plasma? The answer depends on the level of description and on the kind of phenomena with which we are dealing. In the simplest definition, it is a customary plasma with an additional ion species carrying a huge mass and charge. Although this approach allows one to describe some effects, many important phenomena are omitted.

In studying the processes evolving on electron or ion time scales, the presence of dust results in unequal electron and ion densities, which may lead to observable phenomena. In this case, it may be assumed that dusty plasma is a customary plasma with an admixture of a heavy electronegative gas.

The distinctive features of dusty plasmas are most clearly pronounced in the processes evolving on the characteristic time scale of an individual grain's motion. In this case, a dusty plasma should be regarded as a complex open system with an energy flux supplied from an external ionizer and dissipated on the grains. In order to properly describe these processes, it is insufficient to consider grains as huge ions, because the inner degrees of freedom also must be taken into account. The most important degree of freedom is the grain charge, which varies as a grain moves. Besides the charge, other quantities may be of significance. For example, the average surface temperature (i.e., the grain's thermal energy) and the temperature gradients can play a decisive role when there are heat fluxes in the plasma. The rotational degrees of freedom are important for nonspherical grains. In the kinetic description of the dust, all these quantities act as additional coordinates in phase space. As any other open system, dusty plasma exhibits self-organization. Bearing in mind the experiments performed onboard the ISS, the idea of the self-organization of a dust cloud to the stage of a rational being [4] does not seem so fantastic.

The present paper has excluded from consideration many interesting and important issues that can only be briefly outlined here. In the physics of dusty plasma, considerable attention is devoted to the investigation of waves and oscillations. We have described the phenomena occurring with spherical grains. In many experiments that deal with rodlike grains, structures analogous to liquid crystals emerge. Sometimes the orientation oscillations of the rods become unstable. Applying an external magnetic field leads to very rich physics. Also, nothing has been said about the synthesis of grains from a gaseous plasma and about dusty plasmas in space. The quoted reviews address these and many others issues.

## ACKNOWLEDGMENTS

This work was supported in part by the Russian Foundation for Basic Research (project no. 02-02-16439), the Netherlands Organization for Scientific Research (NWO) (grant no. 047.016.020), and the RF Presidential Program for State Support of Leading Scientific Schools (project no. 1962.2003.2).

## REFERENCES

1. V. N. Tsytovich, G. E. Morfill, and H. Thomas, Fiz. Plazmy **28**, 675 (2002) [Plasma Phys. Rep. **28**, 623 (2002)].
2. G. E. Morfill, V. N. Tsytovich, and H. Thomas, Fiz. Plazmy **29**, 3 (2003) [Plasma Phys. Rep. **29**, 1 (2003)].
3. H. Thomas, G. E. Morfill, and V. N. Tsytovich, Fiz. Plazmy **29**, 963 (2003) [Plasma Phys. Rep. **29**, 895 (2003)].
4. V. N. Tsytovich, G. E. Morfill, and H. Tomas, Fiz. Plazmy **30**, 877 (2004) [Plasma Phys. Rep. **30**, 816 (2004)].
5. V. E. Fortov, A. G. Khrapak, S. A. Khrapak, *et al.*, Usp. Fiz. Nauk **174**, 495 (2004) [Phys. Usp. **47**, 447 (2004)].
6. A. Piel and A. Melzer, Plasma Phys. Controlled Fusion **44**, R1 (2002).
7. P. K. Shukla and A. Mamun, *Introduction to Dusty Plasma Physics* (IOP, Bristol, 2002).
8. H. Kersten, H. Deutsch, E. Stoffels, *et al.*, Int. J. Mass Spectrom. **223–224**, 313 (2003).
9. Ch. Hollenstein, Plasma Phys. Controlled Fusion **42**, R93 (2000).
10. S. V. Vladimirov and K. Ostrikov, Plasmas Polymers **8**, 135 (2003).
11. S. V. Vladimirov and K. Ostrikov, Phys. Rep. **393**, 175 (2004).
12. D. A. Mendis, Plasma Sources Sci. Technol. **11**, A219 (2002).
13. H. Löwen, E. Allahyarov, C. N. Likos, *et al.*, J. Phys. A **36**, 5827 (2003).
14. A. Yu. Grosberg, T. T. Nguyen, and B. I. Shklovskii, Rev. Mod. Phys. **74**, 329 (2002).
15. O. M. Belotserkovskiĭ, I. E. Zakharov, A. P. Nefedov, *et al.*, Zh. Éksp. Teor. Fiz. **115**, 819 (1999) [JETP **88**, 449 (1999)].
16. A. V. Kozyrev and A. N. Shishkov, Pis'ma Zh. Tekh. Fiz. **28** (12), 33 (2002) [Tech. Phys. Lett. **28**, 504 (2002)].
17. S. A. Khrapak, A. V. Ivlev, G. E. Morfill, and H. Thomas, Phys. Rev. E **66**, 046414 (2002).
18. C. Zafiu, A. Melzer, and A. Piel, Phys. Plasmas **10**, 1278 (2003); S. A. Khrapak, A. I. Ivlev, G. E. Morfill, *et al.*, Phys. Plasmas **10**, 4579 (2003); C. Zafiu, A. Melzer, and A. Piel, Phys. Plasmas **10**, 4582 (2003).
19. S. A. Trigger, Phys. Rev. E **67**, 046403 (2003).
20. S. A. Maĭorov, Fiz. Plazmy **30** (2005) (in press).
21. A. Melzer, Plasma Sources Sci. Technol. **10**, 303 (2001).

22. A. M. Ignatov, Fiz. Plazmy **28**, 919 (2002) [Plasma Phys. Rep. **28**, 847 (2002)].
23. A. M. Ignatov, Usp. Fiz. Nauk **171**, 213 (2001) [Phys. Usp. **44**, 199 (2001)].
24. A. Melzer, V. A. Schweigert, and A. Piel, Phys. Rev. Lett. **83**, 3194 (1999).
25. A. M. Ignatov, Fiz. Plazmy **29**, 325 (2003) [Plasma Phys. Rep. **29**, 296 (2003)].
26. I. Kourakis and P. K. Shukla, Phys. Lett. A **317**, 156 (2003).
27. A. M. Ignatov, Fiz. Plazmy **22**, 648 (1996) [Plasma Phys. Rep. **22**, 585 (1996)].
28. D. Samsonov, A. V. Ivlev, G. E. Morfill, and J. Goree, Phys. Rev. E **63**, 025401 (2001).
29. Minghui Kong, B. Partoens, and F. M. Peeters, New J. Phys. **5**, 231 (2003).
30. R. P. Dahiya, G. V. Paeva, and W. W. Stoffels, Phys. Rev. Lett. **89**, 125001 (2002).
31. A. P. Nefedov, G. E. Morfill, V. E. Fortov, *et al.*, New J. Phys. **5**, 33 (2003).
32. V. V. Yaroshenko, B. M. Annaratone, S. A. Khrapak, *et al.*, Phys. Rev. E **69**, 066401 (2004).

*Translated by the author*

*Plasma Physics Reports, Vol. 31, No. 1, 2005, pp. 57–74. Translated from Fizika Plazmy, Vol. 31, No. 1, 2005, pp. 64–83.*


**TURBULENCE AND CHAOS**

# New Possibilities for the Mathematical Modeling of Turbulent Transport Processes in Plasma

**N. N. Skvortsova*, V. Yu. Korolev**, T. A. Maravina**, G. M. Batanov*, A. E. Petrov*, A. A. Pshenichnikov*, K. A. Sarksyan*, N. K. Kharchev*, J. Sanchez***, and S. Kubo******

**Prokhorov Institute of General Physics, Russian Academy of Sciences, ul. Vavilova 38, Moscow, 119991 Russia*

***Moscow State University, Vorob'evy Gory, Moscow, 119899 Russia*

****EUROATOM-CIEMAT, Madrid, Spain*

*****National Institute of Fusion Research, Toki, Japan*

Received May 20, 2004; in final form, June 17, 2004

**Abstract**—A new mathematical model is proposed for the probability distributions of the characteristics of the processes observed in turbulent plasmas. The model is based on formal theoretical considerations related to probabilistic limit theorems for a nonhomogeneous random walk and has the form of a finite mixture of Gaussian distributions. The reliability of the model is confirmed by the results of a statistical analysis of the experimental data on density fluctuations in high-temperature plasmas of the L-2M, LHD, and TJ-II stellarators and the local fluctuating flux in the TAU-1 linear device and in the edge plasma of the L-2M stellarator with the use of the estimation–maximization algorithm. It is shown that low-frequency structural turbulence in a magnetized plasma is related to non-Brownian transport, which is determined by the characteristic temporal and spatial scales of the ensembles of stochastic plasma structures. Mechanisms that could be responsible for the random nature of time samples of the local turbulent flux in TAU-1 are indicated. A new physical concept of the intermittence of plasma turbulent pulsations is developed on the basis of the statistical separation of mixtures in terms of the model proposed. The intermittence of plasma pulsations is shown to be associated with the generation of plasma structures (solitons and vortices) and their nonlinear interaction, as well as with their damping and drift. © *2005 Pleiades Publishing, Inc.*

## 1. INTRODUCTION. STRONG STRUCTURAL PLASMA TURBULENCE

One of the fundamental problems in creating a controlled fusion reactor is plasma instability resulting in anomalous particle and energy losses. For this reason, much effort has been devoted to studying plasma instabilities and searching for methods of their suppression. Low-frequency (LF) plasma turbulence caused by these instabilities is an important loss channel.

Studies of LF turbulence in closed magnetic confinement systems have become very common in recent years. The 30th EPS Conference on Plasma Physics and Controlled Fusion (St. Petersburg, 2003) [1] showed that such experimental studies are presently being carried out in all of the existing tokamaks and stellarators, such as T-10, LHD, TJ-II, DIII-D, JET, CASTOR, and FT-2 (see, e.g., report nos. P-2.56, P-3.121, P-4.5, O-2.1A, and P-179). The same trend was also noted at the XXXI Zvenigorod Conference on Plasma Physics and Controlled Fusion (Zvenigorod, 2004) [2], where studies on LF turbulence in toroidal devices were supplemented with reports on experiments in linear devices and gas discharges. It is not surprising that almost one-half of the papers presented at the last Toki Conference dedicated to progress in plasma theory [3] were devoted to various turbulent phenomena of this kind: blobs, streamers, zonal flows, solitons, vortices, etc. (see, e.g., report nos. PL-1, I-01, I-02, I-04, I-06, O-6, and O-7). It should be noted that not all of these theoretical concepts have been confirmed experimentally. The studies of this plasma state attract particular attention because there are many experimental facts pointing to the influence of LF turbulence on the macroscopic plasma characteristic in closed magnetic confinement systems. For example, LF turbulence governs anomalous transport in the edge plasma [4, 5], the changes in its parameters correlate with observations of internal and external transport barriers in plasma [6–8], and the statistical parameters of the turbulent particle flux in the edge plasma correlate with the gas influx from the chamber wall [9]. Note that the question of the frequency at which large-amplitude random events of "catastrophic" type occur in long-term and steady-state discharges still remains open [10]. An important factor is that the computerization of experiments has made it possible to accumulate large arrays of statistical data (temporal and spatial samples) and then calculate steady-state and transient characteristics (spectral, correlational, probabilistic, dimensional, etc.) of LF plasma turbulence. This stimulated experimental studies on LF turbulence and provided a great body of new information requited for its theoretical description and analysis.

1063-780X/05/3101-0057$26.00 © 2005 Pleiades Publishing, Inc.

In many toroidal and linear devices, LF turbulence in the plasma core and at the plasma periphery has the form of strong structural (SS) turbulence [11–13]. The term *strong structural turbulence* means that there are ensembles of stochastic, nonlinearly interacting plasma structures against the background of well-developed steady-state plasma turbulence. SS plasma turbulence was first discovered in the TAU-1 linear device with a longitudinal magnetic field [14] and was then observed in the L-2M, LHD, and TJ-II stellarators [15]. Measurements of the fluctuation parameters in most toroidal devices indicate that LF SS turbulence may be present in these devices. Let us consider the characteristic features of this phenomenon using as an example the L-2M stellarator, in which turbulence has been studied over the entire plasma volume [9].

Time samples of any fluctuating plasma parameter are bursty in character. Such time samples are more adequately described by finite-duration oscillating wavelets rapidly decaying in time. The observed wavelet spectra contain quasi-harmonics, and their correlation functions have oscillating tails. The LF SS turbulence has been observed over the entire plasma volume in L-2M, although, in different plasma regions, different instabilities are responsible for its excitation: drift-dissipative instability, MHD resistive ballooning instability [9], and trapped-electron-driven instability [3]. Nonlinear structures comprise a considerable fraction (from 10 to 30% in different plasma regions) of the turbulence energy. Turbulent fluctuations in LF SS turbulence are correlated over the entire plasma volume via ensembles of stochastic plasma structures. The main characteristic feature of LF SS turbulence is that the probability density functions (PDFs) of the fluctuating parameters differ from a normal distribution: the observed PDFs are leptokurtic and are characterized by heavier tails. Non-Gaussian PDFs of stochastic plasma processes point to the non-Brownian (anomalous) motion of particles in stochastic fields [16]. In a plasma with LF SS turbulence, the role of rare events with magnitudes far exceeding the average values substantially increases and needs to be estimated.

Thus, the fundamental problem of describing the nature (state) of LF SS turbulence leads us to the applied problem of describing anomalous plasma transport in closed magnetic configurations.

So far, the methods for modeling particle diffusion in a plasma with LF SS turbulence described by non-Gaussian statistics have been poorly developed. Such a modeling is closely related to the problem of describing non-Brownian particle motion in the probability theory. The key question is whether the classical Fokker–Planck–Kolmogorov (FPK) equation can be used to analyze the motion of ensembles of plasma particles in stochastic plasma fields. It is well known [17] that the FPK equation was derived from the stochastic differential equation only for the stochastic term representing a random Gaussian process. The diffusion coefficient in this approximation has a form familiar to plasma physicists [18]. A general analytic solution to the stochastic differential equation for the stochastic non-Gaussian term is still lacking. Therefore, no universal prescription has been devised for making corrections in the FPK equation and determining the terms and factors into which they are to be introduced.

In this paper, we propose a new mathematical model for probability distributions of the characteristics of the processes observed in turbulent plasmas. The model is based on formal theoretical considerations related to probabilistic limit theorems for a nonhomogeneous random walk and has the form of a finite mixture of Gaussian distributions. The reliability of the model is confirmed by the results of a statistical analysis of the experimental data on plasma density fluctuations in high-temperature plasmas of the L-2M, LHD, and TJ-II stellarators and the local fluctuating flux in the TAU-1 linear device and in the edge plasma of the L-2M stellarator with the use of the estimation–maximization (EM) algorithm. It is shown that LF SS turbulence is related to anomalous transport in a magnetized plasma. A new physical concept of the intermittence of plasma turbulent pulsations is developed on the basis of the statistical separation of mixtures in terms of the model proposed. The intermittence of plasma pulsations is shown to be associated with the generation of plasma structures and their nonlinear interaction, as well as with their damping and drift.

## 2. MATHEMATICAL MODEL

### *2.1. Nonhomogeneous Continuous-Time Random Walk*

There have been many attempts to explain the observed leptokurtic PDFs. The most progress in solving this problem has been achieved with the use of the limit theorems for a homogeneous random walk with discrete or continuous time. According to these theorems, the so-called *stable* or *fractionally stable* PDFs characterized by power-law tails can be used as an alternative to a Gaussian distribution [19–21]. As applied to plasma turbulence, such models were considered in [22–25]. However, stable or fractionally stable models sometimes fail to provide an adequate description of plasma turbulence. First, a basic assumption underlying these models is the absence of the second moment (variance) of the distribution of random particle jumps and/or the absence of the first moment (mathematical expectation) of the distribution of time intervals between the jumps. For this assumption to be valid, it is necessary that, at the least, these random variables with positive probabilities could take arbitrary large values. It is evident that this assumption fails to be valid in practice, because the recorded processes are always limited in space and time, so the above random variables possess all the moments. Second, a statistical analysis of experimental data shows that, although the tails of the observed PDFs are heavier than

those described by a Gaussian law, they are much lighter than the tails of stable or fractionally stable non-Gaussian PDFs, which decrease as $O(x^{-\alpha})$ with $0 < \alpha < 2$ at $x \longrightarrow \infty$ [16].

In contrast to traditional models, our mathematical models are based on limit theorems for a *nonhomogeneous* continuous-time random walk. This walk differs from a homogeneous walk in that the distributions of the random time intervals between successive jumps of a walking particle are, in general, different. The assumption of the nonhomogeneity (different distributions of the time intervals between successive jumps) of a random walk is consistent with a concept that the *rate of the coordinate increment* of a particle that undergoes Brownian motion in a turbulent medium is essentially nonhomogeneous.

Let $N(t)$ be the number of jumps of a walking particle over the time interval $[0, t]$, where $t \geq 0$. The instants of jumps form a chaotic point random process on the time axis. However, by virtue of the above concept, this chaotic random process is nonhomogeneous. As is well known [26], the most reasonable stochastic models of nonhomogeneous chaotic point processes are *doubly stochastic Poisson processes*, which are also referred to as *Cox processes*. They are defined as follows:

Let $N_1(t)$ $(t \geq 0)$ be a homogeneous Poisson process with a unit intensity, whereas $\Lambda(t)$ $(t \geq 0)$ is a stochastic process that is independent of $N_1(t)$ and possesses the following properties: $\Lambda(0) = 0$ and $P(\Lambda(t) < \infty) = 1$ for any time $t \geq 0$ and the trajectories $\Lambda(t)$ do not decrease and are continuous from the right. A doubly stochastic Poisson process (a Cox process) is defined as a superposition of $N_1(t)$ and $\Lambda(t)$:

$$N(t) = N_1(\Lambda(t)), \quad t \geq 0.$$

In this case, we will say that the Cox process $N(t)$ is controlled by the process $\Lambda(t)$. In particular, if the process $\Lambda(t)$ admits the representation

$$\Lambda(t) = \int_0^t \lambda(\tau) d\tau, \quad t \geq 0,$$

in which $\lambda(t)$ is a positive stochastic process with integrable trajectories, then $\lambda(t)$ can be interpreted as an instantaneous stochastic intensity of the process $N(t)$. For this reason, the process $\Lambda(t)$ controlling the Cox process $N(t)$ is called the *accumulated intensity* of the process $N(t)$.

The properties of Cox processes are described in detail in [27, 28].

The objective of this section is to formulate the problem of the modeling of nonhomogeneous chaotic flows of events in a turbulent plasma with the use of compound Cox processes and to demonstrate that the departure of the observed distributions of the processes from normal can be attributed to substantial variations in the intensity of nonhomogeneous chaotic flows of events described by Cox processes.

Let $X_1, X_2, \ldots$ be identically distributed random variables. We assume that, for any $t \geq 0$, the random variables $N(t)$, $X_1, X_2, \ldots$ are independent of one another. The process

$$S(t) = \sum_{j=1}^{N(t)} X_j, \quad t \geq 0 \tag{1}$$

describes the coordinate of a particle that undergoes a nonhomogeneous random walk at a time $t$; this process will further be referred to as a compound Cox process (for definiteness, we assume that $\sum_{j=1}^{0} = 0$).

As was noted above, general processes $S(t)$ of form (1) with a random intensity $d\lambda(t) = \dfrac{\Lambda(t)}{dt}$ are adequate models of real random walks (in particular, those governed by plasma turbulence), for which the property of homogeneity is rather an exception than a rule. The parameters of turbulent plasma fluctuations observed in tokamaks and stellarators are nonhomogeneous in both space and time.

Hereinafter, we will assume that the random quantities $\{X_j\}_{j \geq 1}$ have at least first two moments. We denote $EX_1 = a$ and $DX_1 = \sigma^2$, where $0 < \sigma^2 < \infty$. It will be shown below that, even under these assumptions, the limit distributions of compound Cox processes can have arbitrary heavy tails. In this section, as an illustrative example, we will consider a situation in which $a = 0$. The reasons for this are as follows: First, our object here is to describe the *principles* of constructing adequate stochastic models of plasma turbulence, without going into details. Second, as will be demonstrated in the subsequent sections, the actual values of the parameter $a$ turn out to be close to zero.

We will formulate the necessary and sufficient conditions for the convergence of the one-dimensional distributions of compound Cox processes with jumps that possess the above properties, without imposing any moment restrictions on the control process. We will demonstrate that the asymptotic behavior of the process $S(t)$ is completely determined by the asymptotic behavior of the accumulated intensity $\Lambda(t)$. Furthermore, we will see that the heavy (e.g., Pareto-type) tails of distributions that are limit for sums (1) can be caused by an extremely wide spread in the values of the control process $\Lambda(t)$ rather than by the "misbehavior" of summands (e.g., by the absence of their moments).

In what follows, the symbol $\Rightarrow$ designates the convergence in distribution. The standard normal (Gauss-

ian) distribution function will be denoted as $\Phi(x)$:

$$\Phi(x) = \frac{1}{\sqrt{2\pi}}\int_{-\infty}^{x} e^{-u^2/2}du, \quad -\infty < x < \infty.$$

The symbol $E$ denotes the mathematical expectation with respect to the probabilistic measure $P$.

Let $d(t) > 0$ be an auxiliary normalization (scaling) function increasing without bound at $t \longrightarrow \infty$.

*Theorem 1.* Let $\Lambda(t)$ increase without bound at $t \longrightarrow \infty$. Then, for a one-dimensional distribution of a normalized compound Cox process to converge to a distribution of some random variable $Z$,

$$\frac{S(t)}{\sigma\sqrt{d(t)}} \Rightarrow Z \quad (t \longrightarrow \infty),$$

it is necessary and sufficient that there exist a nonnegative random variable $U$ such that

$$\text{(i)}\ \ P(Z < x) = \int_0^\infty \Phi\left(\frac{x}{\sqrt{u}}\right)dP \quad (U < y)$$

$$\left(\equiv E\Phi\left(\frac{x}{\sqrt{U}}\right)\right), \quad -\infty < x < \infty;$$

$$\text{(ii)}\ \ \frac{\Lambda(t)}{d(t)} \Rightarrow U \quad (t \longrightarrow \infty).$$

See the proof in [29, 30].

Note that condition (ii) of Theorem 1 can be interpreted as the requirement for the accumulated intensity to be statistically regular: the limit of the ratio $\Lambda(t)/d(t)$ at $t \longrightarrow \infty$ can be random, but it must exist. Another interpretation of this condition is that, at large $t$, the distribution of the random variable $\Lambda(t)/d(t)$ depends only slightly on $t$. In this case, condition (i) implies that the limit distribution of a compound Cox process is a scale mixture of normal distributions that has heavier (in general, arbitrarily heavier) tails in comparison to a normal distribution (see below).

From Theorem 1 and the identifiability of a family of scale mixtures of normal distributions, the following corollary immediately follows:

*Corollary 1.* Under the conditions of Theorem 1, we have

$$P\left(\frac{S(t)}{\sigma\sqrt{d(t)}} < x\right) \Rightarrow \Phi(x) \quad (t \longrightarrow \infty)$$

if and only if

$$\frac{\Lambda(t)}{d(t)} \Rightarrow 1 \quad (t \longrightarrow \infty).$$

In other words, the limit distribution of a compound Cox process can be normal if and only if the random variable $\Lambda(t)/d(t)$ is asymptotically (at $t \longrightarrow \infty$) nonrandom.

Another corollary of Theorem 1 is a criterion for the convergence of one-dimensional distributions of compound Cox processes with a zero average and *finite dispersions* to stable distributions. We will show that one-dimensional distributions of compound Cox processes with the properties described above are asymptotically stable if and only if their control processes are asymptotically stable.

Let $G_{\alpha,\theta}(x)$ be a stable distribution function with an index $\alpha$ and a parameter $\theta$. As is well known, such a distribution function is defined by its characteristic function

$$g_{\alpha,\theta}(t) = \exp\left\{-|t|^\alpha \exp\left\{-i\frac{\pi\theta\alpha}{2}\operatorname{sgn} t\right\}\right\},$$

where $-\infty < t < \infty$, $0 < \alpha \le 2$, and $|\theta| \le \theta_\alpha = \min(1, 2/\alpha - 1)$ (see, e.g., [22]).

*Theorem 2.* Let $\Lambda(t) \longrightarrow \infty$ $(t \longrightarrow \infty)$ in probability. Then, for

$$\lim_{t\to\infty} P\left(\frac{S(t)}{\sigma\sqrt{d(t)}} < x\right) = G_{\alpha,0}(x), \quad -\infty < x < \infty,$$

it is necessary and sufficient that

$$\lim_{t\to\infty} P\left(\frac{\Lambda(t)}{d(t)} < x\right) = G_{\alpha/2,1}(x), \quad -\infty < x < \infty$$

(see the proof in [29]).

Let us now consider a situation with a discrete time $t = n = 1, 2, \ldots$ and assume that the control process $\Lambda(n)$ has the form

$$\Lambda(n) = Z_1 + \ldots + Z_n, \tag{2}$$

where $\{Z_i\}$ are independent and uniformly distributed random quantities: $Z_i \ge 0$, $i \ge 1$. Such a representation is possible when $\Lambda(t)$ is a homogeneous process with independent increments and a compound Cox process is observed at equidistant instants of time, i.e., $Z_i$ are increments of the control process $\Lambda(t)$ on time intervals between observations. In accordance with definition (1), we assume that

$$S(n) = \sum_{j=1}^{N_1(\Lambda(n))} X_j. \tag{3}$$

In this situation, in view of Theorem 2 of this paper and Theorem 2 of Section 35 from [31], we arrive at the following theorem:

*Theorem 3.* One-dimensional distributions of a normalized compound Cox discrete-time process $S(n)/\delta_n$ are weakly converging to a strictly stable distribution $G_{\alpha,0}$ at a certain choice of constants $\delta_n$ if and only if

$$\lim_{x\to\infty} \frac{P(Z_1 \ge x)}{P(Z_1 \ge kx)} = k^{\alpha/2}$$

for any $k > 0$.

In other words, heavy tails often observed in stable distributions that are limiting for compound Cox processes as the intensity increases can arise not only in situations where the distributions of jumps are characterized by heavy tails. As is seen from Theorem 3, even at arbitrary light tails of the distributions of jumps, heavy tails of the limiting laws may arise due to heavy (Pareto) tails of the distributions of increments of the control process.

### *2.2. Leptokurtocity of Scale Mixtures of Normal Distributions*

Mixtures $E\Phi(x/\sqrt{U})$ are always more leptokurtic and, consequently, possess heavier tails in comparison to a normal distribution. Indeed, scale mixtures of normal distributions correspond to the product of a stochastically independent normal random variable $X$ and nonnegative random variable $Y = \sqrt{U}$. As a numerical characteristic of leptokurtocity, we consider the excess factor $\kappa(Z)$, which, for a random variable $Z$ with $EZ^4 < \infty$, is defined as

$$\kappa(Z) = E\left(\frac{Z - EZ}{\sqrt{DZ}}\right)^4.$$

If $P(X < x) = \Phi(x)$, then we have $\kappa(X) = 3$. For densities that are more leptokurtic (and, accordingly, possess heavier tails) in comparison to normal densities, we have $\kappa > 3$, whereas for densities that are less leptokurtic, we have $\kappa < 3$. From the statements formulated below, it follows that scale mixtures of normal distributions are more leptokurtic in comparison to a normal distribution.

*Lemma 1*. Let $X$ and $Y$ be independent random quantities with finite fourth moments. If $EX = 0$ and $P(Y \geq 0) = 1$, then we have $\kappa(XY) \geq \kappa(X)$. Furthermore, $\kappa(XY) = \kappa(X)$ if and only if $P(Y = \text{const}) = 1$.

Therefore, if $X$ is a standard normal random variable and $U$ is a nonnegative random variable independent of $X$, with $EU^2 < \infty$, then we have $\kappa(X\sqrt{U}) \geq 3$; $\kappa(X\sqrt{U}) = 3$ if and only if $U$ is nonrandom.

Using Jensen's inequality, we obtain another inequality that directly relates the tails of scale mixtures of normal distributions to the tails of the normal distributions themselves.

*Lemma 2*. Let a nonnegative random variable $U$ satisfy the normalization condition $EU^{-1/2} = 1$. We then have

$$1 - E\Phi\left(\frac{x}{\sqrt{U}}\right) \geq 1 - \Phi(x), \quad x > 0. \tag{4}$$

It follows from Lemma 2 that, if $X$ is a standard normal random variable and $U$ is a nonnegative random variable independent of $X$, with $EU^{-1/2} = 1$, then, for any $x \geq 0$, we have

$$P(|X\sqrt{U}| \geq x) \geq P(|X| \geq x) \quad (=2[1 - \Phi(x)]), \tag{5}$$

i.e., scale mixtures of normal distributions are always more leptokurtic than a normal distribution and, consequently, possess heavier tails. For more details on the properties of mixtures of normal distributions, see [32, 33].

### *2.3. Specific Features of the Statistical Analysis of Scale Mixtures of Normal Distributions*

The class of scale mixtures of normal distributions with a zero average is very extensive. In particular, it includes Cauchy, Student, and symmetric strictly stable distributions (see, e.g., [32, 33]).

It follows from the above considerations that the statistical analysis of the distribution of the increments of turbulent plasma processes reduces to the separation of mixtures, i.e., to the statistical determination of the mixing distribution of the control process, which is an unknown parameter of the statistical problem under consideration. Without any additional assumptions, the parametric set of mixing distributions coincides with the set of all the distributions concentrated on the nonnegative semiaxis. The choice of an appropriate distribution is a very laborious statistical problem. Therefore, it is desirable to reduce the parametric set (i.e., the class of admissible mixing distributions) by adopting some additional assumptions.

In this section, we propose one possible approach to solving this problem. According to this approach, a *discrete distribution with a finite number of jumps* can be used a mixing distribution. The approach is based on the following considerations:

(i) Any probability distribution concentrated at the nonnegative semiaxis can be approximated *arbitrarily closely* by a discrete distribution with a finite number of jumps. Therefore, there are reasons to believe that, considering a *finite* mixture of normal distributions, we are dealing with a convenient approximation of an actual distribution.

(ii) It follows from Theorem 1 that, when compound Cox processes are used as models of a nonhomogeneous random walk describing the observed turbulent plasma process, the form of the mixing distribution in the limiting law is completely determined by the character of the accumulated intensities and, hence, by the statistical features of changes in the instantaneous intensities of elementary processes. The instantaneous intensities of continuous-time random walks are naturally related to the diffusion coefficients. In turn, the diffusion coefficients characterize the types of dynamic structures formed in a turbulent plasma (in other words,

**Table 1**

| Device | L-2M | LHD | TJ-1I | TAU-1 |
|---|---|---|---|---|
| Major radius $R$, cm | 100 | 800 | 150 | |
| Average minor radius $r$, cm | 11.5 | 60 | 10–22 | 2 |
| Magnetic field $B$, T | 1.3–1.4 | <3 | <1.2 | <0.06 |
| Input microwave power $P_0$, kW | 150–200 | 600 | 200–400 | |
| Average density $\langle n \rangle$, $10^{13}$ cm$^{-3}$ | 1.0–1.3 | ~1.0 | <1.0 | 0.001 |
| Central electron temperature $T_e(0)$, eV | 400–800 | ≥1000 | 500–800 | 4–7 |
| Relative fluctuation level in the edge plasma $(\delta n/n)_{\text{edge}}$ | 0.2–0.25 | | 0.2–0.25 | 0.2–0.3 |

each type of structure is characterized by its own rate of change). In mixtures of the form

$$E\Phi\left(\frac{x}{\sqrt{U}}\right) = \int_0^\infty \Phi\left(\frac{x}{\sigma}\right) dP(\sqrt{U} < \sigma)$$

the scale parameter $\sigma$ also has the meaning of the diffusion coefficient, whereas $dP(\sqrt{U} < \sigma)$ signifies a fraction of structures characterized by diffusion from a small interval $[\sigma, \sigma + d\sigma)$ in the general picture of plasma turbulence. Hence, replacing the mixture $E\Phi\left(\frac{x}{\sqrt{U}}\right)$ with its finite discrete approximation

$$E\Phi\left(\frac{x}{\sqrt{U}}\right) \approx \sum_{j=1}^{k} p_j \Phi\left(\frac{x}{\sigma_j}\right)$$

and statistically estimating the parameters $\sigma_1, \sigma_2, \ldots, \sigma_k$ and $p_1, p_2, \ldots, p_k$, we can distinguish *typical* structures and describe their contributions to the general picture.

Without going into analytical details, we note that, using the general limit theorems for compound Cox processes (see, e.g., [27, 30]), it is possible to theoretically justify models for the distributions of the increments of turbulent plasma processes in the form of more general finite *shift-scale* (drift-diffusion) mixtures of normal distributions as

$$\sum_{j=1}^{k} p_j \Phi\left(\frac{x - a_j}{\sigma_j}\right)$$

where $a_j$ is the drift coefficient and $\sigma_j$ is the diffusion coefficient of the $j$th component. It is this approach that we used in statistically analyzing the processes observed.

## 3. EXPERIMENTAL DEVICES AND METHODS FOR INVESTIGATING TURBULENCE

### *3.1. Experimental Devices*

Studies and modeling of LF SS plasma turbulence were performed for four devices: the L-2M, TJ-II, and LHD stellarators and the TAU-1 linear device. The main parameters of these devices are listed in Table 1. The densities, temperatures, and diameters of the plasmas vary from $n \sim 10^{10}$ cm$^{-3}$, $T_e \sim 5$ eV, and $D \sim 4$ cm for a low-temperature plasma of the TAU-1 linear device to $n \sim 10^{13}$–$10^{14}$ cm$^{-3}$, $T_e \sim 10^3$–$10^4$ eV, and $D \sim 150$ cm for the high-temperature plasma of the most advanced LHD superconducting stellarator. Irrespective of the type of plasma device and even the kind of plasma instability, LF turbulence in a magnetized plasma exhibits general features that allow one to compare the results obtained under so different conditions. It is well known that, to describe the probability parameters of turbulence in any medium, it is of primary importance to study steady turbulent states, since only in this case one might expect that ergodic condition would be satisfied and the results obtained would be statistically consistent. The typical duration of the steady-state phase of a discharge is 10 ms in L-2M, 300 ms in TJ-II, 1 s in LHD (at present, the maximum discharge duration of a few minutes has been achieved in this device), and three to five hours in TAU-1.

The L-2M device is an $l = 2$ stellarator, its parameters are described in detail in [34]. In the edge plasma, at a radius of $r/a = 0.9$ (here, $a$ is the separatrix radius), the plasma density is $n = (1–2) \times 10^{12}$ cm$^{-3}$ and the electron temperature is $T_e = 30$–$40$ eV. The plasma is produced and heated by a 75-GHz gyrotron under the electron cyclotron resonance (ECR) conditions at the second harmonic of the electron gyrofrequency.

The TJ-II device is an $l = 4$ stellarator [35]. The average plasma radius varies along the torus from 10 to 22 cm. In the experiments under consideration, the plasma was produced and heated by a single 53.2-GHz gyrotron at the second harmonic of the electron gyrofrequency.

The LHD device is the largest superconducting heliac with a divertor [36]. In the experiments under consideration, the plasma was produced and heated by several 168-GHz and 84-GHz gyrotrons under the ECR conditions at the fundamental and second harmonics of the electron gyrofrequency.

The TAU-1 device was specially designed for studying and modeling nonlinear processes in a low-temperature plasma [37]. In TAU-1, a cylindrical argon plasma

**Table 2**

| Device | L-2M | LHD | TJ-1I | TAU-1 |
|---|---|---|---|---|
| Measurements in the edge plasma | Probes | | | Probes |
| Measurements near the mid-radius of the plasma column | 2-mm scattering | | 2-mm scattering | Probes |
| Measurements near the center of the plasma column | Gyrotron radiation scattering | | | Probes |

column of diameter 4 cm and length 100 cm was produced in a uniform magnetic field of strength ≤0.06 T by a steady low-energy ($E_b$ = 60–150 eV) electron beam at an argon pressure of $p = (2–4) \times 10^{-4}$ torr. The plasma density was maintained at a level of $n = (0.9–1.2) \times 10^{10}$ cm$^{-3}$. The electron temperature was $T_e$ = 4–7 eV, and the ion temperature was $T_i \approx 0.1T_e$.

### *3.2. Measurements of Plasma Fluctuations*

Plasma fluctuations were measured by probe diagnostics [38] and microwave scattering diagnostics [39, 40]. Depending on the type of radiation source, the microwave diagnostics used were subdivided into the diagnostics measuring the scattered radiation of the heating gyrotron and the 2-mm scattering diagnostics. Table 2 describes the types of diagnostics used to measure plasma fluctuations in different plasma regions of the above devices.

Fluctuations on the plasma density, floating potential, and particle flux in the edge plasma of L-2M and the low-temperature plasma of TAU-1 were measured by Langmuir probes of different type [38]. Plasma density fluctuations were measured by correlation probes, the local turbulent particle flux was measured by three-pin probes, and electric-field fluctuations were measured by double probes.

Fluctuations at the edge of the high-temperature plasma (at the mid-radius of the plasma column) in L-2M and TJ-II were measured by 2-mm microwave scattering diagnostics [39, 41]. These measurements allowed us to determine the parameters of turbulent fluctuations with specified spatial scales corresponding to given components of the wave vector **k**. In TJ-II, we measured turbulent fluctuations with wavenumbers of $k$ = 3 and 6 cm$^{-1}$.

Fluctuations in the microwave heating region (at the axis of the plasma column) in L-2M and LHD were measured from the scattering of the heating gyrotron radiation. In these devices, the heating radiation was launched into the vacuum chamber as a linearly polarized Gaussian beam. The linearly polarized wave was split at the plasma boundary into an extraordinary and an ordinary waves. At densities typical of modern toroidal devices, the plasma is transparent for the ordinary wave but is optically thick for the extraordinary wave. The fact that the incident radiation excites two waves in the plasma is unfavorable for ECR plasma heating, because this leads to a reduction of the single-pass absorption of the heating extraordinary microwave [40–42]. However, the ordinary wave can serve as a probing wave in scattering diagnostics. Measurements of this kind allowed us to determine the parameters of turbulent fluctuations with narrow $k$ spectra: $k \approx 20$ and 40 cm$^{-1}$ in L-2M and $k \approx$ 25–34 cm$^{-1}$ in LHD.

### *3.3. Processing of the Experimental Results*

Experimental data were acquired in the same way for all of the above diagnostics. After amplification and filtering, signals from detectors (probes and microwave detectors) were fed to the inputs of analog-to-digital converters (ADCs) and then into the local computer network. For example, in the L-2M and TJ-II experiments, CAMAC ADCs with 512-KB buffers were used to record signals with a sampling rate of up to 1 MHz. In the L-2M and TAU-1 experiments, we used OS-2 direct-access ADCs to record signals with a length of up to 256 KB with a sampling rate of up to 40 MHz. In all of the above stellarators, the ADCs were incorporated into data acquisition systems.

The results of measurement in all of the experiments were digital files of the magnitudes of fluctuations of the plasma parameters in the form of time samples. The time samples comprised up to a few hundred thousands of data points. To preliminarily examine the signal characteristics, in all of the devices, we used a common software devised for analyzing random time sequences (see [12, 43] for details). The data processing included spectral Fourier analysis, correlation analysis, spectral wavelet analysis, construction of histograms, and the computation of the moments of random variables and the Herst parameter (R/S analysis). We also used auxiliary programs for smoothing, filtering, and averaging of signals.

Statistical models in the form of mixtures of normal distributions were used for the first time to analyze the data obtained (see Section 2). In these models, the PDF of a random process has the form

$$f(x) = \sum_{j=1}^{k} p_j \frac{1}{\sqrt{2\pi}\sigma_j} \exp\left(-\frac{(x-\mu_j)^2}{2\sigma_j^2}\right) = \sum_{j=1}^{k} p_j \phi(x, \mu_j, \sigma_j) \quad (6)$$

being a finite mixture of $k$ normal components. Here, the probabilities $p_j$, which are referred to as weights,

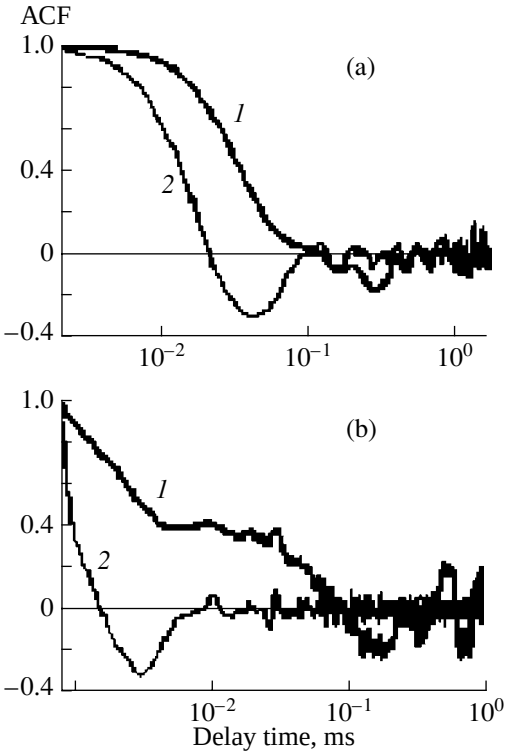


**Fig. 1.** Autocorrelation coefficients of (*1*) the magnitudes and (*2*) the increments of magnitudes of plasma density fluctuations in the heating region of the plasma column in (a) LHD (shot no. 22016) and (b) L-2M (shot no. 54468).

satisfy the condition $\sum_{j=1}^{k} p_j = 1$ and the function $\phi(x, \mu, \sigma)$ is the PDF of a normal distribution with a mathematical expectation $\mu$ and dispersion $\sigma^2$.

To fit a mixture of normal distributions to a data sample, we must solve the problem of separating the mixture of distributions. This problem consists in finding statistical estimates for the number $k$ of the mixture components, their specific weights $p_1, \ldots, p_{k-1}$ ($p_k = 1 - \sum_{i=1}^{k-1} p_i$), and the parameters of the components themselves ($\theta_1 = (\mu_1, \sigma_1), \ldots, \theta_k = (\mu_k, \sigma_k)$). When the number $k$ of the mixture components is fixed, the parameters of the model can be efficiently estimated by the EM algorithm (see, e.g., [44]).

The application of the EM algorithm to analyzing the time samples of the magnitudes of plasma density fluctuations in L-2M, LHD, and TJ-II and the particle flux in TAU-1 and in the edge plasma of L-2M allowed us to model the increments of the fluctuation magnitudes by three- and four-component mixtures of normal distributions. Taking the first-order differences (i.e., passing to the samples of increments $\Delta X_t = X(t) - X(t-1)$) is necessary to remove the intrinsic nonhomogeneity of the original sample $X(t)$.

## 4. MODELING OF LF SS TURBULENCE IN HIGH-TEMPERATURE STELLARATOR PLASMAS

Let us consider time samples of plasma density fluctuations obtained from the central high-temperature plasma regions of the three stellarators. We studied LF plasma turbulence in the microwave heating regions of L-2M and LHD and in the high-temperature plasma outside the heating region of TJ-II. Previous experiments revealed the SS nature of turbulence in these devices [40–42, 46]. Note that, although we performed PDF modeling for all the above devices, the plots of autocorrelation coefficients and the histograms of LF SS turbulent processes will be presented only for some of these devices, because these plots are similar for different devices.

Figure 1 shows the autocorrelation functions (ACFs) of the magnitudes and the increments of magnitudes of plasma density fluctuations in L-2M ($k$ = 40 cm$^{-1}$) and LHD ($k \approx 30$ cm$^{-1}$). Original time samples of the signal magnitudes are not homogeneous and independent.[1] The ACFs of magnitudes demonstrate long-lived tails (Fig. 1a). In contrast, the increment processes in LF SS turbulence turn out to be independent, which is confirmed by the absence of long-term correlation of the ACFs of increments (Fig. 1b).

Figure 2a shows non-Gaussian PDFs of the magnitudes of plasma density fluctuations measured in successive time intervals 130–140 ms (curve *1*) and 140–150 ms (curve *2*) during the steady-state phase of an LHD discharge. Note that the non-Gaussian PDFs of magnitudes vary appreciably within the same stationary sample. Unlike the PDFs of magnitudes, the PDFs of increments within the same successive time intervals vary insignificantly (Fig. 2b) but remain non-Gaussian.

The independence and homogeneity (the invariability of the probability densities) of the samples of increments of the fluctuation magnitudes allows us to use conventional statistical procedures for their analysis.

The longest stationary sample of plasma density fluctuations with a duration of up to 200 ms ($2 \times 10^5$ data points acquired at a sampling rate of 1 MHz) was obtained in TJ-II. Figure 3 presents the first four statistical moments of a sample of magnitudes and the time behavior of the average density in a discharge with a boronized chamber wall. The boronization of the chamber wall improves the reproducibility of the discharge parameters (including the parameters of turbulence) from shot to shot.

Plasma fluctuations in TJ-II were measured in the most quiescent plasma region: far from the microwave

[1] This fact is closely related to the presence of ensembles of stochastic plasma structures in LF SS turbulence.

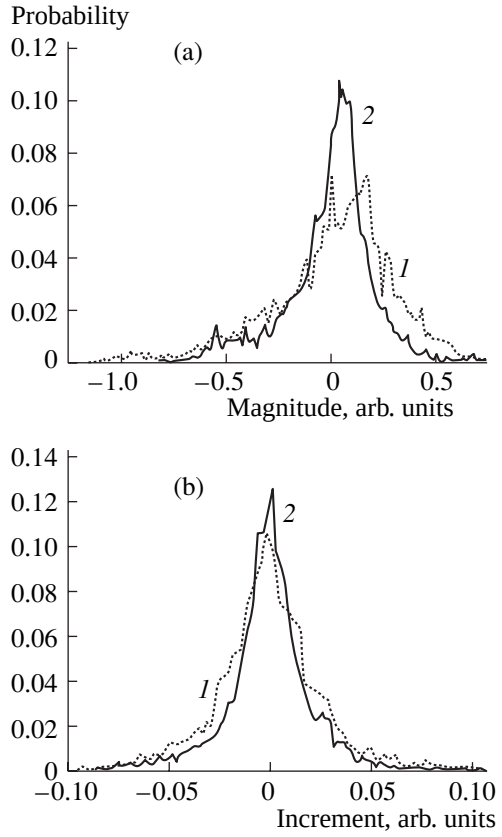


**Fig. 2.** Probability densities of (a) the fluctuation magnitudes and (b) their increments in two successive time intervals in the steady-state phase of an LHD discharge (shot no. 22016): (*1*) 130–140 ms and (*2*) 140–150 ms.

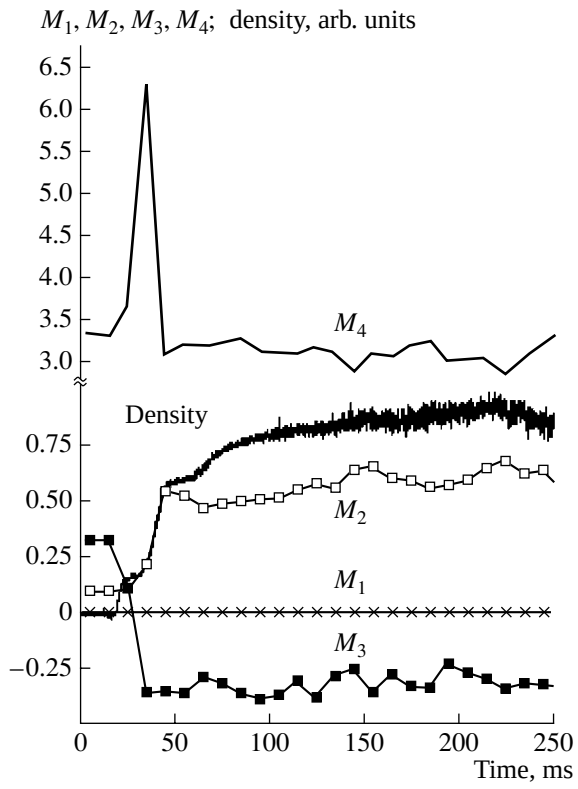


**Fig. 3.** Time behavior of the plasma density and four statistical moments (mathematical expectation $M_1$, dispersion $M_2$, skewness $M_3$, and excess $M_4$) of a time sample of the magnitudes of density fluctuations with $k = 6$ cm$^{-1}$ in TJ-II (shot no. 8192).

heating region (where energy is deposited in the plasma) and also far from the chamber wall and the edge plasma (where energy is dissipated). This region may be considered as an inertial interval for the nonlinear turbulent state of the entire plasma column. It is primarily in this region that energy is redistributed among different nonlinear states under steady-state conditions. Figure 4 shows time samples of the magnitudes of plasma density fluctuations with $k = 6$ cm$^{-1}$ and their increments in the steady-state phase of a discharge (the sample consists of $6 \times 10^5$ data points). In this region of the TJ-II plasma (i.e., far from energy sources and sinks), the probability densities of the increments of the fluctuation magnitudes seem to be closest to a normal distribution (Figs. 5, 6). However, even in this case, the hypothesis of the normal distribution of the increments of the magnitudes of plasma density fluctuations is discarded for the number of observations more than $10^4$ because the P value in the Kolmogorov–Smirnov goodness-of-fit test is less than 0.05. As is well known, the P value shows the degree of assurance that the adopted model is realistic. The hypothesis of the form of a distribution is not discarded if the P value computed for statistical packages is higher than a given confidence level $\alpha$ (which is usually taken to be 0.05).

The increments of the fluctuation magnitudes in TJ-II were analyzed using time samples of different length. A short sample consisting of 5000 data points, even though its histogram looks normal, is best fitted by a three-component mixture of normal distributions with a PDF of form

$$f(x;\ p, \mu_1, \mu_2, \mu_3, \sigma_1, \sigma_2, \sigma_3) = \sum_{k=1}^{3} \frac{p_k}{\sqrt{2\pi}\sigma_k} \exp\left\{-\frac{(x-\mu_k)^2}{2\sigma_k^2}\right\}, \quad (7)$$

where $p_k > 0$ and $p_1 + p_2 + p_3 = 1$. The parameters of this mixture are $p_1 = 0.0987$, $\mu_1 = -0.0413$, $\sigma_1 = 0.5206$; $p_2 = 0.6523$, $\mu_2 = -0.07$, $\sigma_2 = 0.3426$, $p_3 = 0.2490$, $\mu_3 = 0.1999$, and $\sigma_3 = 0.2983$, and the P value is 0.99. Note that the P value for the hypothesis of a normal distribution of the same sample is 0.44. Figure 5 shows a histogram of the increments of the magnitudes of plasma density fluctuations for this sample and the PDFs of the normal distributions for each of the component of the mixture (with account for the weights $p_k$), and for the mixture itself (its PDF is the sum of PDFs *1*, *2*, and *3*).

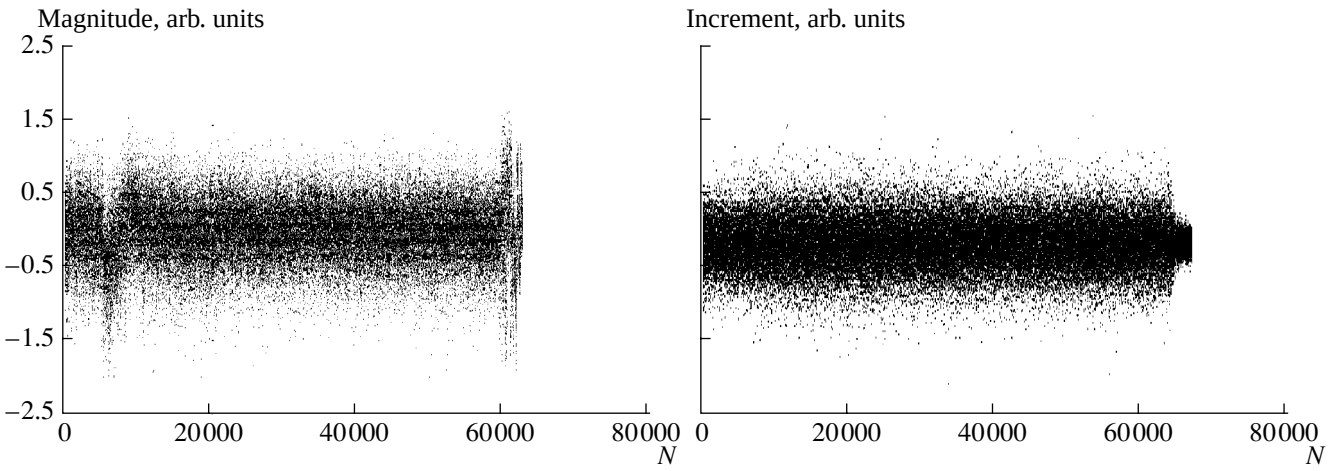


**Fig. 4.** Time samples of the magnitudes of plasma density fluctuations ($k$ = 6 cm$^{-1}$) and their increments in the steady-state phase of a TJ-II discharge (shot no. 8227).

For a long sample of $3 \times 10^4$ data points acquired over 60 ms (i.e., over almost the entire discharge), the histogram of increments is fitted with a good accuracy by a mixture of four Gaussian distributions (Fig. 6):

$$f(x;\ p, \mu_1, \mu_2, \mu_3, \mu_4, \sigma_1, \sigma_2, \sigma_3, \sigma_4) = \sum_{k=1}^{4} \frac{p_k}{\sqrt{2\pi}\sigma_k} \exp\left\{-\frac{(x-\mu_k)^2}{2\sigma_k^2}\right\}, \quad (8)$$

where $p_k > 0$ and $p_1 + p_2 + p_3 + p_4 = 1$. The parameters of this mixture are $p_1$ = 0.0007, $\mu_1$ = 0.0759, $\sigma_1$ = 0.0205, $p_2$ = 0.0729, $\mu_2$ = –0.0934, $\sigma_2$ = 0.2970, $p_3$ = 0.4362, $\mu_3$ = 0.0172, $\sigma_3$ = 0.3082, $p_4$ = 0.4902, $\mu_4$ = –0.0015, $\sigma_4$ = 0.4288, and the P value is 0.8385. It can be seen from Fig. 6 that the contribution of the fourth component is insignificant. Note that the positive (negative) values of the mathematical expectations may be related to the growth (decay) rates of LF instabilities. This matter requires further investigation.

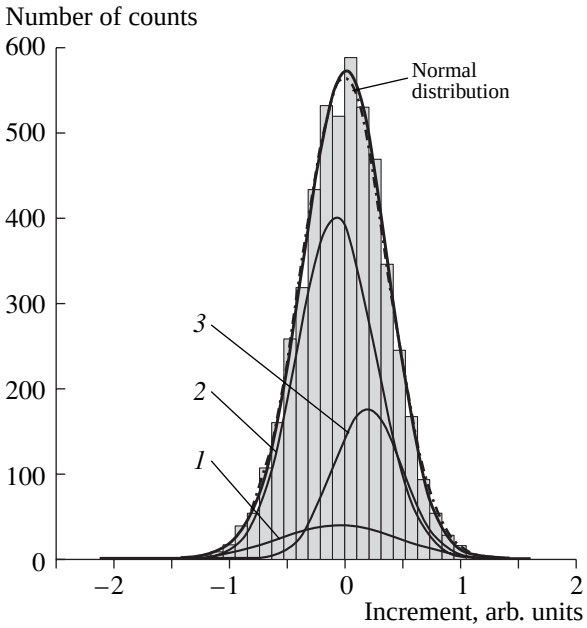


**Fig. 5.** Modeling of the PDF of a time sample of the increments of plasma density fluctuations in TJ-II (shot no. 8227) by a scale mixture of three Gaussian distributions marked by *1*, *2*, and *3*.

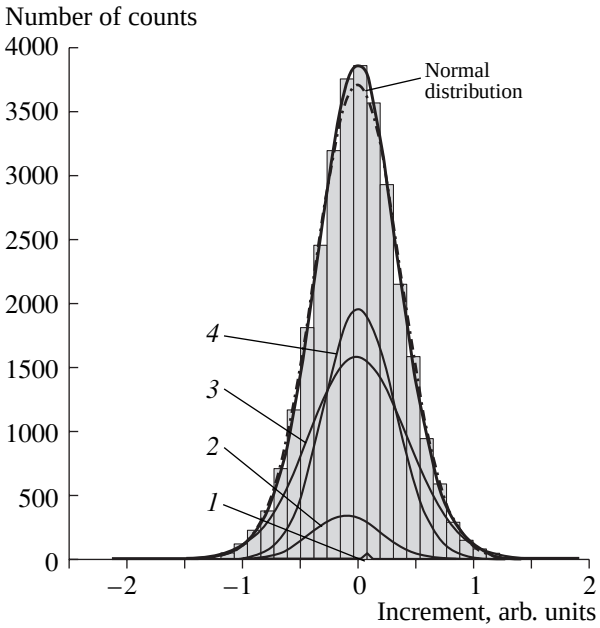


**Fig. 6.** Modeling of the PDF of a time sample of the increments of plasma density fluctuations in TJ-II (shot no. 8227) by a scale mixture of four Gaussian distributions marked by *1*, *2*, *3*, and *4*.

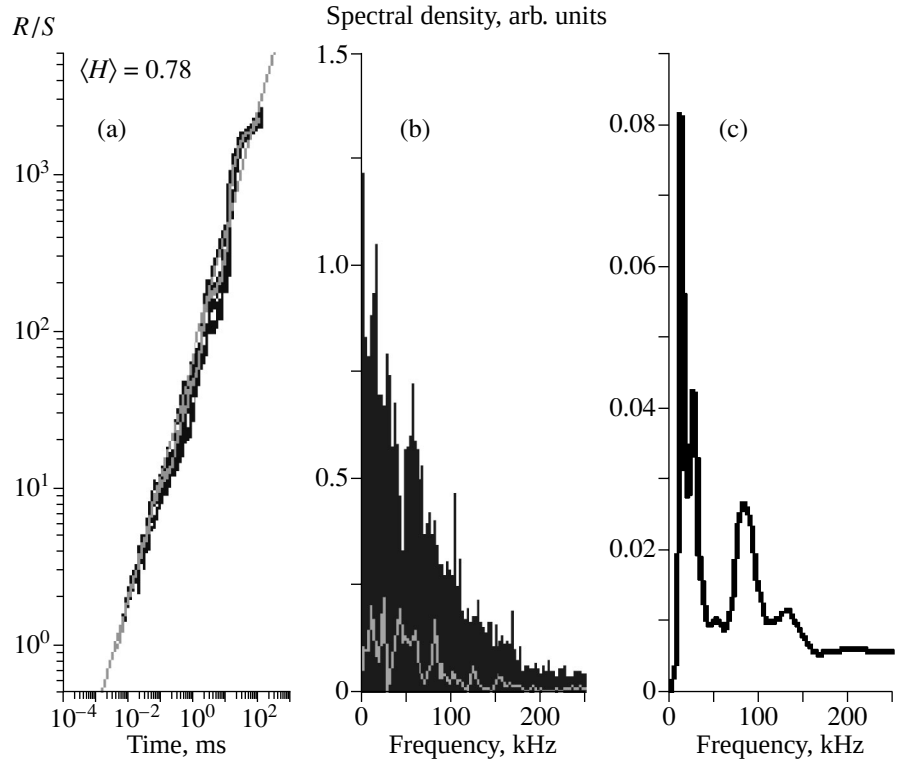


**Fig. 7.** (a) R/S dependence, (b) Fourier spectrum, and (c) wavelet spectrum for the magnitudes of LF fluctuations with $k = 6$ cm$^{-1}$ in TJ-II. The plots are averaged (summed) over seven successive discharges (shot nos. 8227–8233).

The R/S analysis of long time samples (with the number of data points more than $10^5$) in TJ-II is more sensitive to long-lived components than to the analysis of the tails in histograms and ACFs. This method allows one to estimate the Herst parameter $H$, which characterizes the dependence between events occurring with a long time delay.[2] The following criteria in terms of the Herst parameter are usually used: $H = 1$ for regular processes, $H = 0.5$ for Gaussian processes, $H > 0.5$ for self-similar processes with a positive correlation, and $H < 0.5$ for self-similar processes with a negative correlation. Figure 7 shows (a) the R/S dependence (increments of the fluctuation magnitudes versus delay time, plotted on a log–log scale), (b) Fourier spectrum, and (c) wavelet spectrum of plasma density fluctuations; the plots are averaged (summed) over seven successive discharges with the same macroscopic plasma parameters.

For LF SS turbulence under consideration, the Herst parameter is equal to 0.78. This unambiguously indicates that the time samples of the magnitudes of plasma density fluctuations at the mid-radius of the plasma column are described by a self-similar process with a positive correlation. This self-similar process corresponds to LF SS turbulence in which memory is determined by the stochastic generation of plasma structures and the nonlinear interaction between them. It should be noted that the Herst parameter is the most stable (robust) characteristic of LF SS turbulence because it varies only slightly from shot to shot. The averaged spectra clearly exhibit the presence of quasi-harmonics that are typical of LF SS turbulence.

Thus, LF SS turbulence in the high-temperature plasma of TJ-II is a random self-similar process with memory and the PDF of the increments of this process is adequately modeled by three-component mixtures of Gaussian distributions.

The scattered signal from the microwave heating region (the region of energy deposition in plasma, including the deposition of energy in LF plasma turbulence) in LHD seems to be less homogeneous than the time sample of fluctuations from TJ-II. Figure 8 shows time samples of the magnitudes of plasma density fluctuations and their increments in the heating region. The data acquired over two time intervals were modeled by mixtures of normal distributions. For the sample of increments from the 9400th to 11000th data point (i.e., for an intermediate time interval corresponding to 2000 data points), the hypothesis of the normal distri-

[2] Stationary probability processes for which the dispersion of the average decreases as $n^{-\alpha}$ at any $\alpha$ between 0 and 2 were discovered by A.N. Kolmogorov in 1941. These processes are known as self-similar processes. In the mid 1960s, A. Mandelbrot applied the concept of self-similar processes to some fields of statistical analysis and justified their application in hydrology and geophysics. The self-similarity parameter $H = 1 - \alpha/2$, or the parameter of long-range dependence, was called by Mandelbrot the Herst parameter.

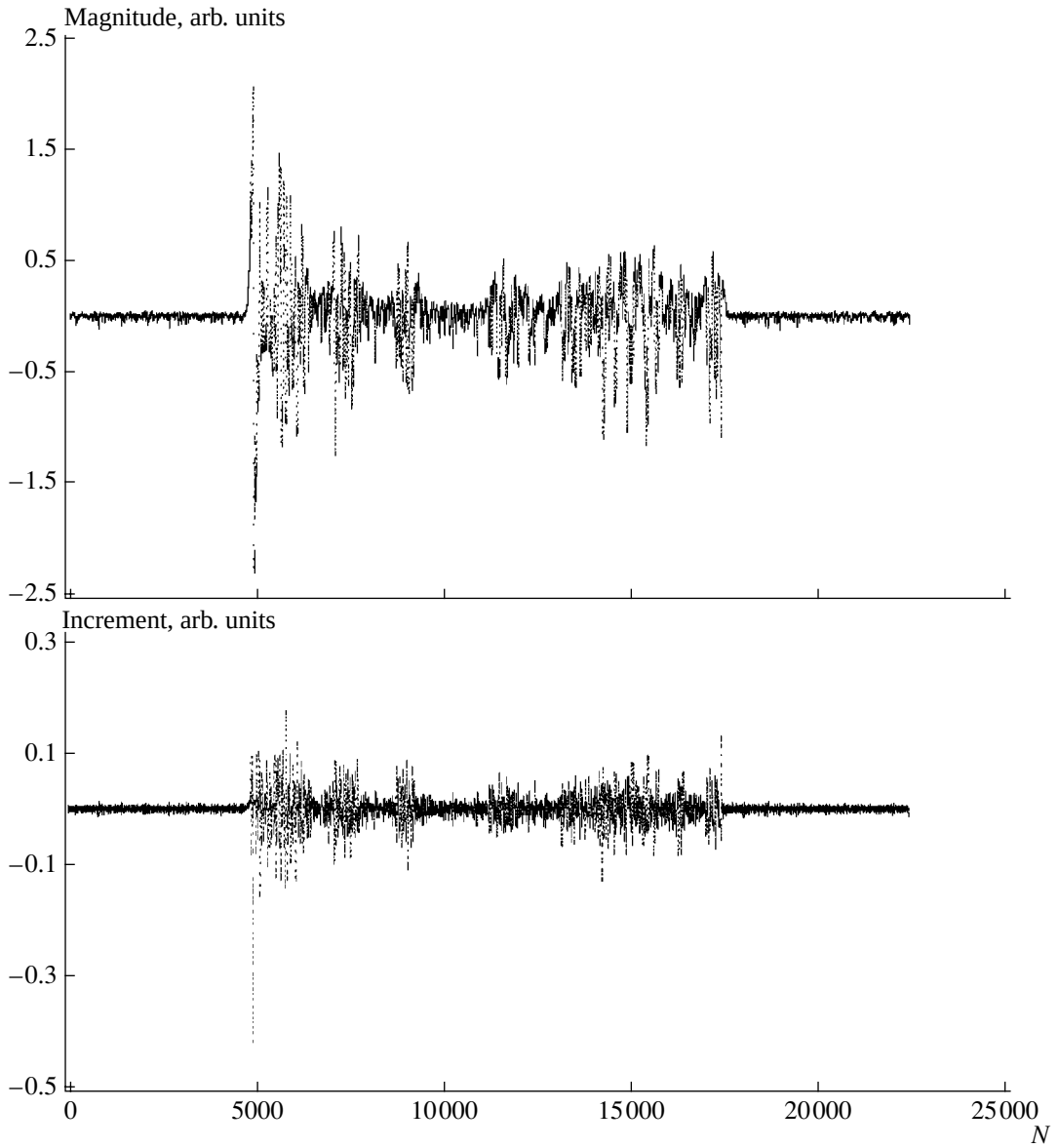


**Fig. 8.** Time samples of the magnitudes of plasma density fluctuations and their increments in the heating region in the steady-state phase of an LHD discharge (shot no. 22016).

bution of the sample was no discarded (the P value is 0.1412, and the parameters of the normal distribution are $\mu = -0.000049$ and $\sigma = 0.009742$). A good fit can be achieved by separating the distribution into two components with $p_1 = 0.4147$, $\mu_1 = 0.0003$, $\sigma_1 = 0.0061$, $p_2 = 0.5853$, $\mu_2 = -0.0003$, and $\sigma_2 = 0.0116$, the P value being 0.9935. The sample of increments from 14000th to 16000th data point (which corresponds to a time interval with a large spread in the data) is not described by a normal distribution (the P value is 0.0017, $\mu = 0.00014$, and $\sigma = 0.02943$). However, this sample is modeled with a probability of 98% by a three-component mixture of normal distributions with the parameters $p_1 = 0.5731$, $\mu_1 = -0.0006$, $\sigma_1 = 0.0352$; $p_2 = 0.3072$, $\mu_2 = 0.0006$, $\sigma_2 = 0.0134$; $p_3 = 0.1197$, $\mu_3 = 0.0003$, and $\sigma_3 = 0.0291$. Figure 9 shows the histogram of increments for this time interval.

Fluctuations in the microwave heating region were also measured in L-2M. The modeling of the increments of the fluctuation magnitudes in this device gives almost the same result as in LHD. We studied the increments of density fluctuations with $k = 40$ cm$^{-1}$ (second-harmonic gyrotron scattering with a 1-MHz sampling rate) in the steady-state phase of a discharge (2000 data points). These data also do not obey a normal distribution. However, even a three-component mixture of normal distributions (see Eq. (7)) with the parameters $p_1 = 0.1521$, $\mu_1 = -0.0037$, $\sigma_1 = 0.0013$; $p_2 = 0.6497$, $\mu_2 =$

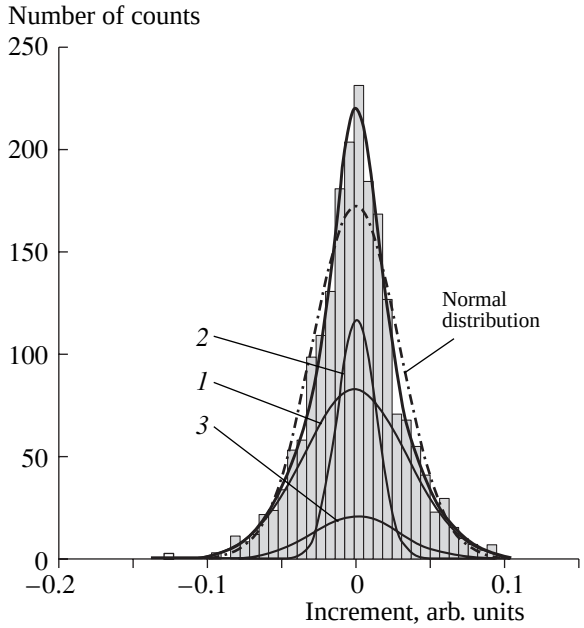


**Fig. 9.** Modeling of the PDF of a time sample of the increments of plasma density fluctuations in LHD (shot no. 22016) by a scale mixture of three Gaussian distributions marked by *1*, *2*, and *3*.

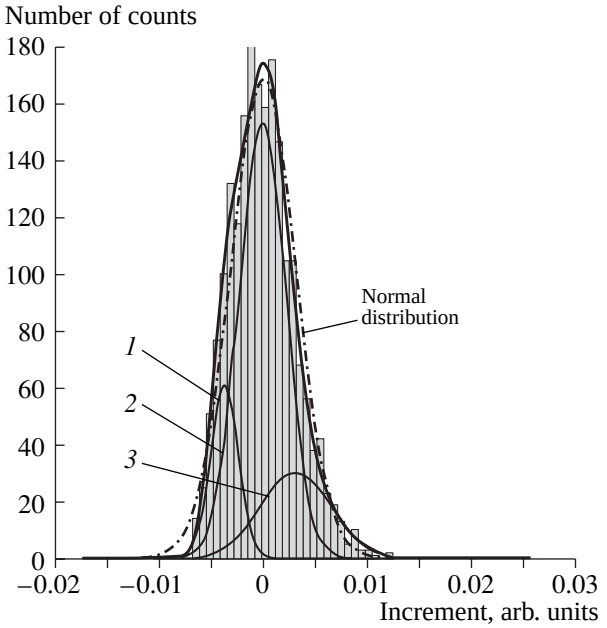


**Fig. 10.** Modeling of the PDF of a time sample of the increments of plasma density fluctuations in L-2M (shot no. 54215) by a scale mixture of three Gaussian distributions marked by *1*, *2*, and *3*.

$-0.0001$, $\sigma_2 = 0.0023$; $p_3 = 0.1982$, $\mu_3 = 0.0031$, and $\sigma_3 = 0.0034$ fairly well describes this time sample: the P value is 0.9688. Figure 10 presents a histogram of the increments for a time sample of plasma density fluctuations in L-2M and the corresponding model distributions.

Time samples of the increments of the fluctuation magnitudes in high-temperature plasmas of L-2M, LHD, and TJ-II are adequately modeled by finite mixtures of normal distributions. Variances and mathematical expectations of the normal distributions of these samples are proportional to the characteristic autocorrelational and incremental times in LF SS plasma turbulence.[3] Such a presentation of LF SS turbulent fluctuations allows us to estimate the contribution of different diffusion mechanisms to anomalous transport in stellarators.

## 5. SS PLASMA TURBULENCE AND ANOMALOUS NON-BROWNIAN DIFFUSION: ANALYSIS OF TURBULENT FLUXES

Plasma experiments provide a unique possibility of studying the diffusion of ensembles of particles by directly measuring turbulent plasma fluxes. Such measurements can be carried out in low-temperature plasma. In experiments, the local fluctuating particle flux across the magnetic field is measured using a set of Langmuir probes. This flux is defined as [47]

$$\Gamma = c\frac{n_{\sim}\mathbf{E}\times\mathbf{B}}{B^2}, \qquad (9)$$

where $\mathbf{B}$ is the longitudinal magnetic field, $n_{\sim}$ is the density fluctuation, $\mathbf{E}$ is the fluctuation of the poloidal electric fields, and $c$ is the speed of light. Local fluxes in the edge plasma have been measured in many tokamaks and stellarators. In the FT-2 tokamak, the total (through the entire closed magnetic surface) particle flux caused by plasma fluctuations was measured [48].

Local fluxes were measured in the edge plasma of the L-2M stellarator and in the low-temperature plasma of the TAU-1 linear device. The local particle flux was determined from the formula $\tilde{\Gamma} = (\delta n_e \cdot \delta v_r)$ [47], where $\delta n_e$ is the plasma density fluctuation and $\delta v_r = c\delta E_\Theta/B$ is the fluctuation of the radial drift velocity (here, $\delta E_\Theta = (\delta\varphi_1 - \delta\varphi_2)/\Delta\Theta r$ is the fluctuation of the poloidal electric field, $\delta\varphi$ is the fluctuation of the floating potential, $\Theta$ is the poloidal angular coordinate, and $r$ is the mean radius of the magnetic surface). Local fluxes were measured by probe systems consisting of three single cylindrical probes measuring plasma density fluctuations $\delta n$ and fluctuations of the floating potential $\delta\varphi$.

The values of the local particle flux measured in successive instants constitute a time sample of a stochastic diffusion process, which can be studied by the same methods of spectral, correlation, and probability analy-

[3] Signals from 2-mm scattering in TJ-II are proportional to density-fluctuation signals. For the scattering signals of the gyrotron radiation in other devices, this dependence is more complicated.

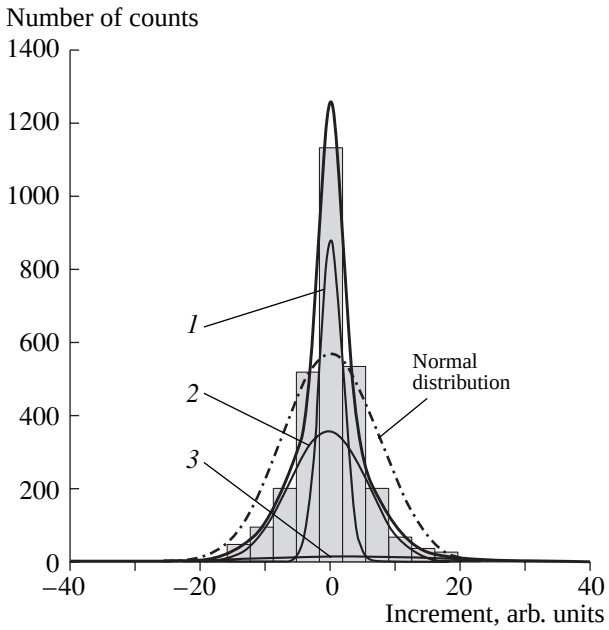


**Fig. 11.** Modeling the PDF of a time sample of the increments of the local flux in the low-temperature plasma of L-2M (shot no. 44487) by a scale mixture of three Gaussian distributions marked by *1*, *2*, and *3*.

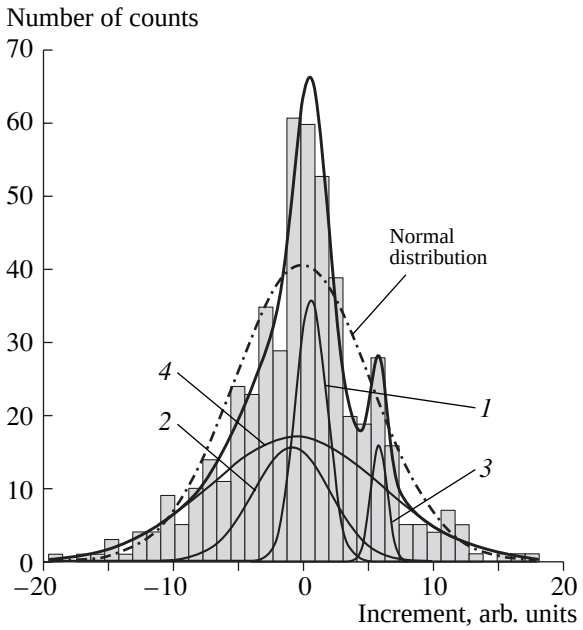


**Fig. 12.** Modeling the PDF of a short (0.5 ms) time sample of the increments of the local flux in TAU-1 (discharge no. 47) by a scale mixture of four Gaussian distributions marked by *1*, *2*, *3*, and *4*.

sis as any other stochastic process. The PDF of the local flux in all the experiments was leptokurtic and had heavier tails as compared to a Gaussian distribution [9, 16, 49].

Similarly to time samples of density fluctuations in a high-temperature plasma, time samples of the magnitudes of local fluxes in TAU-1 and L-2M are not homogeneous and independent (see [9, 16]). In contrast, time samples of the increments of local fluxes are independent. For this reason, when analyzing local fluxes, it is reasonable to use time samples of the increments of local fluxes rather than time samples of their magnitudes. Stationary time samples of local fluxes consisted of $5 \times 10^3$ data points for the edge plasma of L-2M and of up to $10^5$ data points for TAU-1.

Figure 11 shows the histogram of a time sample of the flux increments measured in L-2M; the sample consists of 2000 data points. The hypothesis of a normal distribution with $\mu = -0.000786$ and $\sigma = 7.379012$ is discarded because the P value equals zero. The histogram is fitted with a probability of 97% (the P value is 0.9747) by a mixture of three normal components with $p_1 = 0.3955$, $\mu_1 = 0.1416$, $\sigma_1 = 1.8930$, $p_2 = 0.5171$, $\mu_2 = -0.3335$, $\sigma_2 = 6.0149$; $p_3 = 0.0874$, $\mu_3 = 1.3239$, and $\sigma_3 = 19.7521$. However, in contrast to the modeling of density fluctuations in stellarators, we failed to fit the measured distribution by a mixture of two normal components. This may be explained by the presence of the third component with a large average and a dispersion that is significant in spite of the small weight of the component (≈0.09).

Figures 12 and 13 show histograms of the increments of the local flux in a steady TAU-1 discharge for samples consisting of 500 and 20000 data points (which corresponds to time intervals of 0.5 and 20 ms, respectively). Both samples can be adequately described by mixtures of four normal components with P values of 0.9975 and 0.9986, respectively.

Investigations of LF SS turbulence in the low-temperature plasma of TAU-1 have shown that there are two types of turbulence that are coupled to each other through ensembles of stochastic structures: drift turbulence with wave packets and ion-acoustic turbulence with solitons [12–14, 50]. We have measured the characteristic temporal parameters (incremental, autocorrelational, etc.) of all the plasma processes in LF SS turbulence. Note that, for the above two types of turbulence, these parameters turned out to differ by one order of magnitude or more. As is well known, the increments of the local flux in the frequency range below 500 kHz (this frequency range is determined by the 1-MHz sampling rate used in this series of experiments) are completely determined by LF SS turbulence. Therefore, in view of the fact that the probability distributions of the time samples of the increments of the local flux in TAU-1 are well fitted by mixtures of four normal distributions, we can relate the Brownian motion of plasma particles to plasma processes with certain time scales. In analyzing this relation, we will use the mathematical expectations and root-mean-square deviations of the processes described by mixtures of normal distributions for two samples of the flux increments of different length (see Table 3).

It can be assumed that variations in increments that occur on the characteristic times of the plasma processes determine the inertia (memory) of these processes. On the other hand, the rate of these variations is proportional to the root-mean-square deviations of the mixture components. The difference between the characteristic times of the plasma processes in LF SS turbulence (such as inverse growth rates of instabilities, the lifetimes and drift times of nonlinear plasma structures, etc.) can be related to the root-mean-square deviations of the mixture components. On the other hand, the number of rare events (i.e., events with abnormally fast rise/drop of the local flux) increases with increasing sample length or, in other terms, with increasing intensity of the control process $\Lambda(t)$.

It should be noted that only in process no. 1 do the root-mean-square deviations increase with increasing sample length; this indicates that the number of rare events in LF SS turbulence increases. A sample of length 0.5 ms is clearly insufficient to obtain a statistically consistent result for this process of normal random walk. Only one process with a characteristic time exceeding 1–2 ms was previously identified in SS turbulence—the process of nonlinear interaction between ion-acoustic solitons corresponding to the direct and inverse stages of tree-wave (three-structure) interaction. Since this process possesses a kind of memory, it was previously assumed that its contribution to anomalous diffusion might be significant because the random particle walk can be rather intense due to the particle exchange between the structures.

In the mixture of process nos. 2 and 3, an increase in the sample length does not change the root-mean-square deviations, but the average tends to zero as the sample length increases. This can be explained the particle walk over ensembles of ion-acoustic solitons with a characteristic correlation time of 50–100 μs or over ensembles of drift wave packets with a characteristic correlation time of 5–10 μs. As the sample length increases and, accordingly, the statistical estimate is improved, a tendency is observed for the balance of the processes of increments for a random walk related to the trapping/detrapping of particles by the structures.

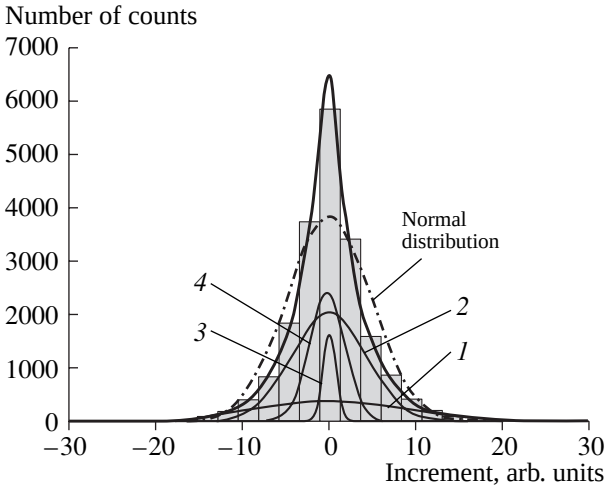


**Fig. 13.** Modeling of the PDF of a long (20 ms) time sample of the increments of the local flux in TAU-1 (discharge no. 47) by a scale mixture of four Gaussian distributions marked by *1*, *2*, *3*, and *4*.

Note that the root-mean-square deviations of the components also differ by one order of magnitude.

Finally, we consider mixture no. 4, which is characterized by a negative mathematical expectation in both the short and long samples. This process corresponds to a negative average increase in the particle number in the flux and may be interpreted, e.g., as the trapping of particles by a soliton and their subsequent transverse drift (the characteristic time of the process is 10–30 μs, depending on the soliton length). This process calls for additional analysis.

## 6. DISCUSSION AND INTERPRETATION OF THE RESULTS OF A STATISTICAL ANALYSIS

(i) Nonhomogeneous (over time) continuous-time random walks (e.g., those described by compound Cox processes) turn out to be convenient and adequate mathematical models for describing the processes under consideration on a microscopic level. These models make it possible to apply Gaussian processes (e.g., Wiener processes) with a random time (the so-

**Table 3**

| Number of the process (see Figs. 12, 13) | Length of the sample of increments of the local flux is 0.5 ms (500 data points) | | | Length of the sample of increments of the local flux is 20 ms (20000 data points) | | |
|---|---|---|---|---|---|---|
| | *p* (probability of a process in the mixture) | μ (mathematical expectation) | σ (dispersion) | *p* (probability of a process in the mixture) | μ (mathematical expectation) | σ (dispersion) |
| 1 | 0.2036 | 0.6844 | 1.2284 | 0.1847 | 0.2656 | 8.6550 |
| 2 | 0.2192 | –0.7849 | 3.0276 | 0.4742 | 0.0146 | 4.3499 |
| 3 | 0.0483 | 5.9305 | 0.6541 | 0.0693 | 0.0588 | 0.8016 |
| 4 | 0.5289 | –0.4877 | 6.6860 | 0.2718 | –0.2217 | 2.1183 |

called *subordinated Gaussian processes*) to describing the observed processes. Since the one-dimensional distributions of the increments of these processes are modeled by *finite* mixtures of normal distributions, the subordinated processes describing the intensity of local events have discrete distributions. This means that, in the processes observed in LF SS plasma turbulence, a finite number of characteristic processes can be distinguished, each of which is characterized by its own intensity of the local events.

(ii) In this study, we used the EM algorithm to model the increments of density fluctuations of high-temperature plasmas of L-2M, LHD, and TJ-II and the increments of the local fluctuating flux in TAU-1 and in the edge plasma of L-2M. Distributions of the increments are well fitted by finite mixtures of *normal* distributions with the same number of the mixture components in L-2M, LHD, and TJ-II, which have different magnetic field configurations. In the high-temperature central plasma and the low-temperature edge plasma of L-2M, LF SS turbulence is well described by scale mixtures of normal distributions with the same number of mixture components. This allows us to assume that the common features of turbulent fluctuations in a toroidal magnetic confinement system are associated with the existence of ensembles of interacting stochastic structures over the entire plasma volume.

(iii) It follows from the asymptotic properties of compound Cox processes (see Theorems 1 and 2) that the observed heavy non-Gaussian tails of the PDFs of the increments of turbulent processes can exist only if the relative accumulated intensity of local events is *random*. Hence, the intermittence of plasma turbulent pulsations can be explained on the basis of a physical model that is alternative to the model explaining such an intermittence by variations in the local plasma density gradient, governing the growth rate of the original instability [23, 51, 52]. According to the former model, the intermittence should be accompanied by the heavy tails of the distributions of the signal magnitudes, as is actually observed in experiments. On the other hand, variations in the local gradient have not yet been observed experimentally; therefore, the latter model can only be regarded as a theoretical guess not supported by experiment. In the steady-state phase of discharges in toroidal confinement systems, slightly varying canonical profiles of the density and temperature are usually observed [53, 54]. Moreover, the intermittence of turbulent signals in our experiments has the same form not only in the edge plasma, where the density and temperature gradients are maximal, but also at the mid-radius of the plasma column, where the gradients are considerably smaller, and in the central region, where the density profile is flat and the temperature profile is peaked (see [55], Fig. 16). Heavy tails are observed in the PDFs of homogeneous and independent time samples of increments of LF SS turbulence over the entire plasma volume, and a large spread in increments is seen even from their time samples. This means that the combined effect of three to four normal processes estimated in this paper, which specify the ensembles of increments in turbulence (the control discrete process), can naturally lead to heavy tails in the PDF of their aggregate increment. Our model implies that the local gradient resulting in the onset of plasma instabilities in the steady-state phase of a discharge remains constant, and the instability threshold is always exceeded. Mixed processes that govern the development of turbulence—the generation and nonlinear interaction of plasma structures, as well as their damping and drift—lead to the observed intermittence of turbulent signals. It is evident that this mechanism can be triggered by any type of LF instability when its threshold is exceeded, thereby resulting in the formation of stochastic plasma structures. We recall that this model is intended to explain the intermittence of *steady-state* LF SS turbulence. We do not consider here transient processes, such as discharge disruptions or transitions from one confinement mode to another [56, 57] (L–H transitions, the generation of internal transport barriers, etc.), which are accompanied by experimentally observed changes in the plasma density and temperature profiles.

(iv) Since the distributions of the increments of the LF SS turbulent processes are well fitted by finite mixtures of normal distributions, the local (in time and space) character of these processes is described by classical normal (Gaussian) diffusion. This does not mean, however, that the resulting motion of particles will also be Brownian. The increments of these processes are associated with a finite number of types of diffusion. Since each type of dynamic structures in plasma turbulence is characterized by its own diffusion coefficient, the separation of the mixture into a finite number of components means that the stochastic character of the observed plasma turbulence is related to a finite number of dynamic structures (a finite number of the main interacting processes). This is confirmed by the modeling of the local particle flux in LF SS turbulence by finite mixtures of normal distributions. In TAU-1, a relationship is established between the mixture of four normal distributions modeling the time sample of increments of the local flux and four plasma processes: stochastic convection of particles by nonlinear drift waves, their stochastic convection by solitons, random particle walk in the field of drift wave packets and ion-acoustic solitons, and random particle walk accompanying the nonlinear interaction of solitons in ion-acoustic turbulence.

## 7. CONCLUSIONS

In this paper, we have proposed a mathematical model for the probability distributions of the characteristics of the processes observed in turbulent plasmas. The model is based on formal theoretical considerations related to probabilistic limit theorems for a nonhomogeneous stochastic walk and has the form of a finite mixture of Gaussian distributions. The reliability

of the model is confirmed by the results of a statistical analysis of the experimental data on density fluctuations in high-temperature plasmas of the L-2M, LHD, and TJ-II stellarators and the local fluctuating flux in the TAU-1 linear device and in the edge plasma of the L-2M stellarator with the use of the EM algorithm. An efficient new method for the statistical analysis of SS plasma turbulence has been developed on the basis of the statistical separation of mixtures. The use of this method allows us (i) to show that LF SS turbulence in a magnetized plasma is related to anomalous transport, which is determined by the characteristic temporal and spatial scales of the ensembles of stochastic plasma structures, and (ii) to indicate mechanisms that can be responsible for the random nature of time samples of the local turbulent flux. A new physical concept of the intermittence of plasma turbulent pulsations has been developed. The intermittence of plasma pulsations is shown to be associated with the generation of plasma structures (solitons and vortices) and their nonlinear interaction, as well as with their damping and drift.

## ACKNOWLEDGMENTS

This work was supported in part by the Russian Foundation for Basic Research (project nos. 03-02-17269 and 01-02-16527), the LIME program (Japan), and the Russian Federal Program for State Support of Leading Scientific Schools (project no. 00-15-96676).

## REFERENCES

1. *Proceedings of the 30th EPS Conference on Plasma Physics and Controlled Fusion, St. Petersburg, 2003*; http://eps2003.ioffe.ru/public/pdfs/.
2. *Proceedings of the XXXI Zvenigorod Conference on Plasma Physics and Controlled Fusion, Zvenigorod, 2004*; http://www.fpl.gpi.ru/Zvenigorod/XXXI/Zven_XXXI.html.
3. *Proceedings of the 13th International Toki Conference on Plasma Physics and Controlled Nuclear Fusion, Toki, 2003*, J. Plasma Fusion Res. SERIES **7** (in press).
4. J. W. Connor, P. Burraffi, J. G. Cordey, *et al.*, Plasma Phys. Controlled Fusion **41**, 693 (1999).
5. A. Yoshizawa, S.-I. Itoh, K. Itoh, and N. Yokoi, Plasma Phys. Controlled Fusion **43**, R1 (2001).
6. U. Stroth, K. Itoh, S.-I. Itoh, H. Hartfuss, *et al.*, Phys. Rev. Lett. **86**, 5910 (2001).
7. A. Fujisawa, H. Iguchi, T. Minami, *et al.*, Phys. Rev. Lett. **82**, 2669 (1999).
8. Y. R. Martin, M. A. Henderson, S. Alberti, *et al.*, Plasma Phys. Controlled Fusion **45**, A351 (2003).
9. G. M. Batanov, V. E. Bening, V. Yu. Korolev, *et al.*, Pis'ma Zh. Éksp. Teor. Fiz. **78**, 974 (2003) [JETP Lett. **78**, 502 (2003)].
10. B. Saoutic, Plasma Phys. Controlled Fusion **44**, B11 (2002).
11. G. M. Batanov, K. A. Sarksian, A. V. Sapozhnikov, *et al.*, in *Proceedings of the IV International Conference on Nonlinear and Turbulent Processes in Physics, Kiev, 1989*, Vol. 1, p. 231.
12. K. A. Sarksyan, N. N. Skvortsova, N. K. Kharchev, and B. F. Milligen, Fiz. Plazmy **25**, 346 (1999) [Plasma Phys. Rep. **25**, 312 (1999)].
13. N. K. Kharchev, N. N. Skvortsova, and K. A. Sarksyan, J. Math. Sci. **106**, 2691 (2001).
14. A. E. Petrov, K. A. Sarksyan, N. N. Skvortsova, and N. K. Kharchev, in *Stochastic Models of Structural Plasma Turbulence*, Ed. by V. Yu. Korolev and N. N. Skvortsova (MAKS-Press, Moscow, 2003), p. 7.
15. G. M. Batanov, V. E. Benin, V. Yu. Korolev, *et al.*, in *Stochastic Models in Structural Plasma Turbulence*, Ed. by V. Yu. Korolev and N. N. Skvortsova (MAKS-Press, Moscow, 2003), p. 92.
16. G. M. Batanov, A. E. Petrov, A. A. Pshenichnikov, *et al.*, in *Stochastic Models in Structural Plasma Turbulence*, Ed. by V. Yu. Korolev and N. N. Skvortsova (MAKS-Press, Moscow, 2003), p. 151.
17. M. I. Gikhman and A. V. Skorokhod, *Stochastic Differential Equations* (Naukova Dumka, Kiev, 1968).
18. V. I. Klyatskin, *Stochastic Equations by the Physicist's Eyes* (Fizmatlit, Moscow, 2001).
19. V. M. Zolotarev, *One-Dimensional Stable Distributions* (Nauka, Moscow, 1983).
20. V. Kolokoltsov, V. Korolev, and V. Uchaikin, J. Math. Sci. **6**, 2569 (2001).
21. V. E. Bening, V. Yu. Korolev, T. A. Sukhorukova, *et al.*, in *Stochastic Models of Structural Plasma Turbulence*, Ed. by V. Yu. Korolev and N. N. Skvortsova (MAKS-Press, Moscow, 2003), p. 291.
22. V. Yu. Gonchar, A. V. Chechkin, É. L. Sorokovoĭ, *et al.*, Fiz. Plazmy **29**, 413 (2003) [Plasma Phys. Rep. **29**, 380 (2003)].
23. B. Ph. Van Milligen, R. Sanchez, and B. A. Carreras, Phys. Plasmas **11**, 2272 (2004).
24. A. I. Saichev and G. M. Zaslavsky, Chaos **7**, 753 (1997).
25. G. M. Zaslavsky, Phys. Rep. **371**, 461 (2002).
26. V. V. Uchaikin and V. V. Zolotarev, *Chance and Stability: Stable Distributions and Their Applications* (VSP, Utrecht, 1999).
27. V. Bening and V. Korolev, *Generalized Poisson Models and Their Applications in Insurance and Finance* (VSP, Utrecht, 2002).
28. J. Grandell, *Mixed Poisson Processes* (Chapman & Hall, London, 1997).
29. V. Yu. Korolev, Teor. Veroyatn. Primen. **43**, 786 (1998).
30. B. V. Gnedenko and V. Yu. Korolev, *Random Summation: Limit Theorems and Applications* (CRC, Boca Raton, 1996).
31. B. V. Gnedenko and A. N. Kolmogorov, *Limit Distributions for the Sums of Independent Random Quantities* (GITTL, Moscow, 1949).
32. V. Yu. Korolev, in *Stochastic Models of Structural Plasma Turbulence*, Ed. by V. Yu. Korolev and N. N. Skvortsova (MAKS-Press, Moscow, 2003), p. 183.
33. V. Yu. Korolev, *Mixed Gaussian Probabilistic Models of Real Processes* (MAKS-Press, Moscow, 2003).
34. V. V. Abrakov, D. K. Akulina, E. D. Andryukhina, *et al.*, Nucl. Fusion **37**, 233 (1997).

35. C. Alejaldre, J. Alonco, I. Almoguera, *et al.*, Plasma Phys. Controlled Fusion **41**, B109 (1999).
36. O. Motojima, H. Yamada, A. Komori, N. Ohyabu, *et al.*, Phys. Plasmas **6**, 1843 (1999).
37. G. M. Batanov, L. M. Kovrizhnykh, L. V. Kolik, *et al.*, Tr. FIAN **160**, 122 (1985).
38. G. M. Batanov, A. E. Petrov, K. A. Sarksyan, *et al.*, Pis'ma Zh. Éksp. Teor. Fiz. **67**, 634 (1998) [JETP Lett. **67**, 662 (1998)].
39. G. M. Batanov, K. M. Likin, K. A. Sarksyan, and M. G. Shats, Fiz. Plazmy **19**, 1199 (1993) [Plasma Phys. Rep. **19**, 628 (1993)].
40. G. M. Batanov, L. V. Kolik, A. E. Petrov, *et al.*, Pis'ma Zh. Éksp. Teor. Fiz. **72**, 250 (2000) [JETP Lett. **72**, 174 (2000)].
41. G. M. Batanov, L. V. Kolik, M. I. Petelin, *et al.*, Fiz. Plazmy **29**, 1099 (2003) [Plasma Phys. Rep. **29**, 1019 (2003)].
42. N. K. Kharchev, G. M. Batanov, K. A. Sarksian, *et al.*, J. Math. Sci. **112**, 3846 (2002).
43. N. N. Skvortsova, Pis'ma Zh. Éksp. Teor. Fiz. **70**, 203 (1999) [JETP Lett. **70**, 201 (1999)].
44. S. A. Aĭvazyan, V. M. Bukhshtaber, I. S. Enyukov, and L. D. Meshalkin, *Applied Statistics: Classification and Reduction of Dimensions* (Finansy i Statistika, Moscow, 1989).
45. G. M. Batanov, V. E. Bening, V. Yu. Korolev, *et al.*, Fiz. Plazmy **28**, 128 (2002) [Plasma Phys. Rep. **28**, 111 (2002)].
46. N. N. Skvortsova, G. M. Batanov, L. V. Kolik, *et al.*, J. Plasma Fusion Rev. Series **5**, 328 (2002).
47. G. M. Batanov, O. I. Fedianin, N. K. Kharchev, *et al.*, Plasma Phys. Controlled Nucl. Fusion Res. **40**, 1241 (1998).
48. L. A. Esipov, I. E. Sakharov, E. O. Chechik, *et al.*, Zh. Tekh. Fiz. **67** (4), 48 (1997) [Tech. Phys. **42**, 367 (1997)].
49. C. Hidalgo, Plasma Phys. Controlled Fusion **37**, A53 (1995).
50. A. E. Petrov, K. A. Sarksyan, N. N. Skvortsova, and N. K. Kharchev, Fiz. Plazmy **27**, 58 (2001) [Plasma Phys. Rep. **27**, 56 (2001)].
51. B. A. Karreras, D. Newman, V. E. Lynch, and P. H. Diamond, Fiz. Plazmy **22**, 819 (1996) [Plasma Phys. Rep. **22**, 740 (1996)].
52. K. Itoh, S.-I. Itoh, A. Fukuyama, and M. Yagi, Fiz. Plazmy **22**, 798 (1996) [Plasma Phys. Rep. **22**, 721 (1996)].
53. Yu. N. Dnestrovkij and G. M. Pereverznev, Plasma Phys. Controlled Fusion **30**, 47 (1988).
54. Yu. N. Dnestrovskij, A. Yu. Dnestrovskij, S. E. Lysenko, and S. V. Cherkasov, Fiz. Plazmy **28**, 963 (2002) [Plasma Phys. Rep. **28**, 887 (2002)].
55. G. M. Batanov, L. V. Kolik, A. E. Petrov, *et al.*, Fiz. Plazmy **29**, 395 (2003) [Plasma Phys. Rep. **29**, 363 (2003)].
56. S. V. Mirnov, *Physical Processes in Tokamak Plasmas* (Énergoatomizdat, Moscow, 1985).
57. S.-I. Itoh, K. Itoh, H. Zushi, and A. Fukuyama, Plasma Phys. Controlled Fusion **40**, 879 (1998).

*Translated by N.F. Larionova*

*Plasma Physics Reports, Vol. 31, No. 1, 2005, pp. 75–91. Translated from Fizika Plazmy, Vol. 31, No. 1, 2005, pp. 84–101.*


**LOW-TEMPERATURE PLASMA**

# The Effect of a Corona Discharge on a Lightning Attachment

**N. L. Aleksandrov*, E. M. Bazelyan**, and Yu. P. Raizer*****

**Moscow Institute of Physics and Technology, Institutskiĭ pr. 9, Dolgoprudnyĭ, Moscow oblast, 141700 Russia*
***Krzhizhanovskiĭ Rower Engineering Institute, Leninskiĭ pr. 19, Moscow, 117927 Russia*
****Institute for Problems of Mechanics, Russian Academy of Sciences, pr. Vernadskogo 101, Moscow, 117526 Russia*

Received June 30, 2004

**Abstract**—The interaction between the lightning leader and the space charge accumulated near the top of a ground object in the atmospheric electric field is considered using analytical and numerical models developed earlier to describe spark discharges in long laboratory gaps. The specific features of a nonstationary corona discharge that develops in the electric field of a thundercloud and a downward lightning leader are analyzed. Conditions for the development of an upward lightning discharge from a ground object and for the propagation of an upward-connecting leader from the object toward a downward lightning leader (the process determining the point of strike to the ground) are investigated. Possible mechanisms for the interaction of the corona space charge with an upward leader and prospects of using it to control downward lightning discharges are analyzed.


## 1. INTRODUCTION

Lightning discharges are the most frequent and most dangerous effect of atmospheric electricity on ground objects. During the lightning season, each square kilometer of the Earth's surface suffers one to ten lightning strikes (two to four strikes in moderate-climate regions of Russia). Intracloud lightning discharges occur three to four times more frequently. The frequency of lightning strikes increases with the height of a ground object. On the flat ground near Moscow, narrow objects ~30 m in height (like radio masts or towers) suffer, on average, one lightning strike every ten years; a 100-m high building undergoes a strike nearly every year; and such an extremely high structure as the Ostankino TV tower suffers 25–30 lightning strikes every year.

Unlike Benjamin Franklin, modern experts on lightning protection are acquainted with mechanisms for the development of lightning; however, the means that are at their disposal differ little from Franklin's lightning rods. Being above an object to be protected, the lightning rods intercept the approaching lightning channel. However, conventional methods of lightning protection often do not meet the needs of modern practice. Lightning rods are capable of efficiently protecting a certain point of the object, e.g., its easily flammable or explosive element. It is this purpose for which they were proposed by Franklin two and a half centuries ago. Modern buildings, however, contain almost no flammable elements. Precast or monolithic concrete does not burn, whereas its metal armature efficiently conducts the lightning current to the ground. In this respect, modern buildings need no lightning protection. The most dangerous effect for them is the electromagnetic field excited by the lightning current, rather than its thermal effect. The lightning current increases at a rate of more than $10^{11}$ A/s and gives rise to dangerous overvoltages in the electric circuits of the object under protection. Among the elements that are in most danger are low-voltage control and automation circuits and microelectronic devices, as well as channels for information transfer and processing.

It makes little sense to set lightning rods on the roof to protect a building from electromagnetic strays. After intercepting the lightning discharge, the rod will anyway direct the current into the building armature; as a result, the overvoltage level will be almost the same as in the case of an unprotected roof. To significantly reduce electromagnetic strays, it is necessary to eliminate lightning strikes in the close proximity of the protected object. For this purpose, lightning discharges must be either intercepted (or redirected) far away from the object. In principle, distant lightning interception is feasible. This requires the creation of long-range lightning protectors covering a sufficiently large area. General considerations naturally lead to the idea of using very tall lightning rods. However, mounting such rods is rather expensive. Moreover, the radius of the protected region increases rather slowly with the height of the lightning conductor. For example, lightning strikes to the ground were observed at distances as short as 200 m from the 540-m-high Ostankino TV tower, which can be regarded as an extremely tall lightning rod. For ordinary lightning rods, the radius of the protected region (at the ground level) is close to the rod height, whereas in the case of the Ostankino TV tower, it is nearly three times smaller. Obviously, substantially increasing the height of conventional lightning rods would have no significant effect. This is why methods for actively influencing lightning discharges have been searched over the last few decades.

1063-780X/05/3101-0075$26.00 © 2005 Pleiades Publishing, Inc.

Two approaches that yield diametrically opposite effects have been developed concurrently. The aim of the first approach is to increase the attraction of lightning to the lightning rod as much as possible, whereas the aim of the second approach is to hinder the propagation of lightning toward the protected object. Both approaches are based on Golde's hypothesis about the lightning attachment (the place of the lightning strike) [1, 2]. According to this hypothesis, lightning propagates toward a ground object because of the development of a highly conducting plasma channel (the so-called upward-connecting leader) from its top. The upward leader channel is produced in a strong electric field of a thundercloud enhanced by the approaching leader of downward lightning. The mutual attraction between these leaders of opposite polarities results in their merging, thereby determining the point of strike.

All methods for controlling lightning discharges with the aim of lightning protection can be ultimately reduced to either exciting (as early as possible) an upward-connecting leader from the lightning rod or, alternatively, hampering its development from the protected object. However, the development of these seemingly clear ways of affecting lightning discharges encounters great difficulties and is thus far from being complete. The point is that Golde's hypothesis has not yet been confirmed theoretically. For a number of principal issues, the process of mutual attraction between the leaders and the problem of the lightning attachment are still poorly understood even at a qualitative level. Laboratory experiments fail to shed light on these phenomena because of the significant difference in the spatial scales and the absence of justified scaling laws. Until recently, theory was not able to estimate the efficiency of nonconventional approaches to lightning protection. It is only in recent years that certain progress has been made owing to the parallel use of experimental data on laboratory spark discharges, theoretical models (often semi-empirical) of such discharges, and results from natural lightning observations and computer simulations of different stages of the lightning formation. However, this problem is still the subject of vigorous debate among practical engineers and also "pure" geophysicists (see, e.g., [3–6]). The fact that the authors of the present review are involved in this dispute might to a certain extent deprive the text of the paper of its chronicle neutrality.

The focus of our review is one aspect of the problem of the lightning attachment: the interaction of the lightning leader with the corona space charge that is accumulated near the top of the protected object in the atmospheric electric field. Based on the results of analytical considerations and numerical simulations, we analyze different ways of affecting the lightning trajectory and demonstrate the feasibility of their practical implementation with the help of specially designed corona systems.

The problem can be divided into several more or less independent physical tasks. First, it is necessary to understand to what extent the attachment of the leader channel of downward lightning is related to the origin and stable development of an upward leader from the top of the protected object. Second, there is a need for a quantitative description of a nonstationary corona that is first formed in the thundercloud electric field and then in the field of a downward leader with quite a large channel charge. Third, one must find out to what extent the redistribution of the electric field in the vicinity of the corona electrode is able to affect the origin and stable development of the upward leader that gives rise to an upward lightning discharge. As is well known, skyscraper objects with a height of 200 m and more are mainly subject to upward lightning flashes. Finally, it is necessary to reveal a possible mechanism for the influence of the corona space charge on the downward lightning leader. Here, the point is either the delayed origin (or termination) of an upward-connecting leader or such a change in its trajectory that eliminates the strike to the protected object. At present, the above issues are at different stages of their development and require further investigation. The general picture, however, is clear enough to predict prospects of new lightning protection technologies.

## 2. ATTACHMENT OF LIGHTNING TO A GROUNDED OBJECT IN THE CASE OF A CONVENTIONAL LIGHTNING ROD

### *2.1. Development of a Leader from a Grounded Object in the Atmospheric Electric Field*

The development of a leader from a grounded object due to the enhancement of the atmospheric electric field by the charge of the approaching channel of a downward leader is a real phenomenon. It can easily be modeled under laboratory conditions [7, 8]. The leader starts after the initial flash of a pulsed corona—a bunch of streamers with a common stem. It is the streamer flash from which the leader channel begins to develop. The streamer-flash current flowing through the stem delivers an energy sufficient for the heating of the cold streamer plasma to the temperature of ~5000 K. Electrons are then produced mainly due to the processes whose rate depends slightly on the electric field, and a longitudinal electric field of $\sim 10^2$ V/cm is quite sufficient to maintain the channel in the conducting state over a fairly long time [9–11]. Theoretical predictions and experimental data show that, under normal atmospheric conditions, the necessary gas heating in the stem can be achieved if the voltage drop over the streamer branch is no lower than $\Delta U_{cr} \approx 400$ kV [8, 12]. Such a voltage drop is sufficient to form a branch of cathode-directed streamers with a length $l_{st}$ of about 1 m.

The formal criterion for initiating a leader in the stem of the streamer flash can be written as

$$\Delta U(l_{st}) > \Delta U_{cr} \approx 400 \text{ kV}. \quad (1)$$

This criterion can easily be satisfied under real conditions even for relatively low grounded objects without assistance of the electric field of the downward leader. For example, when the thundercloud electric field near the ground is $E_{0cl}$ = 20 kV/m (which is quite realistic), a grounded rod of height $h$ = 20 m enables a voltage drop of $\Delta U = E_{0cl}h \sim 400$ kV near the top of the rod. Nevertheless, no one has ever observed leader development from such a low grounded object located on flat ground in the absence of a close cloud-to-ground lightning discharge. The reason is that the leader development must be preceded by a streamer flash starting from the rod top. There is no problem in exciting a streamer flash under laboratory conditions when the rise time of a pulsed voltage is from a few microseconds to a few milliseconds. However, the actual thundercloud electric field increases very slowly between the lightning discharges (over tens to hundreds of seconds). In such a field, a quiet streamerless corona occurs over a long period of time. This kind of corona has also been observed under laboratory conditions. Such a corona consists of a thin (less than a few millimeters) ionization zone and the outer region occupied by the drifting ions [13]. The length of the outer zone can be very large—up to tens or even hundreds of meters.

The most important feature of the streamerless corona (it is sometimes called an ultra corona [14]) is the stabilization of the electric field at the surface of the corona electrode at the level of corona ignition, $E_{cor}$. For the simplest electrode configurations, this field can be calculated by the empiric Peek formula [15]. This circumstance and the fact that the ionization zone is narrow allowed one to develop a simple and widely used numerical model of a corona in a long air gap (see [13, 16]). The model assumes that the ions are emitted directly from the surface of the corona electrode of radius $r_0$ and the boundary condition $E(r_0) = E_{cor} = \text{const}$ is satisfied on the electrode surface. This allows one to ignore the processes occurring in the ionization zone and to restrict oneself with an analysis of the ion drift in the outer region. For this purpose, the continuity equation for the density of the ions, which drift with a given mobility,

$$\frac{\partial n_j}{\partial t} + \nabla \cdot (n_j \mu_j \mathbf{E}) = S,$$

is solved together with Poisson's equation for electric field **E**,

$$\nabla \cdot \mathbf{E}(\mathbf{r}) = \rho/\varepsilon_0.$$

Here, $\rho = e\Sigma n_j$ is the space charge density, $n_j$ and $\mu_j$ are the density and mobility of the $j$th ion species, and $S$ is the term describing the production and loss of ions in ion–molecular reactions.

Analytic solutions to these equations were earlier obtained for the simplest electrode systems with a spherically symmetric or an axisymmetric electric field (concentric spheres or coaxial cylinders of unlimited length) and one ion species. The solutions were obtained for a steady-state operating mode, assuming that the discharge voltage was constant and the drifting ions had time to cross the discharge gap.

Steady-state solutions cannot be used to analyze the corona in an atmospheric electric field because the field itself varies significantly over time, whereas the ions have time to cover only a minor fraction of the gap between the grounded electrode and the cloud over the characteristic time of the electric field variations. As the electric field increases, the space charge front propagates away from the top of the corona electrode; this clearly indicates that the discharge is nonstationary.

An approximate analytical description of a nonstationary corona performed in [17, 18] is in good agreement with the results of numerical simulations carried out for conditions typical of a streamerless corona in a thundercloud field [18]. The details of analytical studies and numerical simulations are beyond the scope of the present study. Below, we will consider only those features of a nonstationary corona that are important for analyzing the conditions for the origin and stable development of the leader from a grounded object.

### *2.2. Features of a Nonstationary Corona*

A nonstationary corona can be observed in gaps of any length. The discharge remains nonstationary until the space charge front reaches the opposite electrode and the applied voltage ceases to change. All other factors being the same, the duration of the transient regime is a function of the gap length. In the ground–cloud gap, steady-state regime may not be established at all. The main difference between nonstationary and stationary coronas is that, in the former, the current is determined not only by the instantaneous value of the applied voltage but also its growth rate [17, 18]. As a result, the current in a nonstationary corona can be many times higher than that in a stationary corona. This is illustrated in Fig. 1, which shows the results of the numerical solution of the above equations for a 5-m-long laboratory gap. The unsteady current exceeds its steady-state value when the voltage rise time is much shorter than the propagation time of the space charge front across the gap. The approximate analytical theory gives similar results [17, 18]. It will be shown below that the dependence of the current on the field growth rate is of crucial importance for the initiation of a leader from the grounded electrode.

A nonstationary corona is also characterized by a much weaker dependence of the current on the ion mobility $\mu$. Instead of the direct proportionality between the steady-state corona current $i_{cor}$ and $\mu$, the functional dependence of the current on the ion mobility in a nonstationary corona is determined by the gap geometry: $i_{cor} \sim \mu^{1/2}$ for spherical geometry and $i_{cor} \sim \ln(\mu^{1/2})$ for cylindrical geometry. For the limiting case of plane geometry, the current does not depend on the

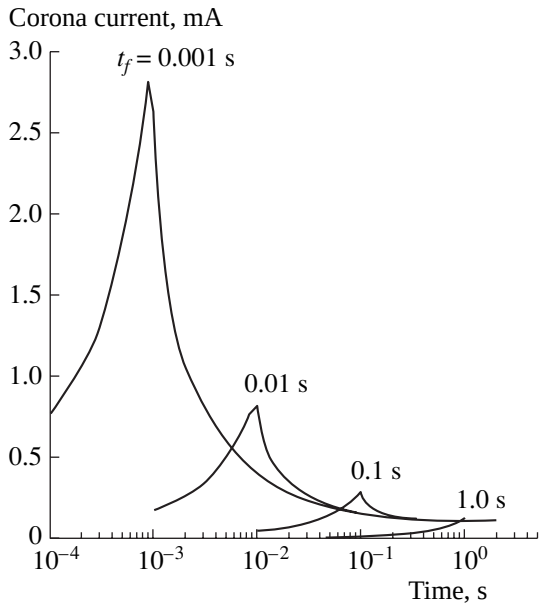


**Fig. 1.** Numerical simulations of the current of a transient corona in a gap between concentric spheres with radii of 1 cm and 5 m. The voltage increases linearly to 300 kV over a time $t_f$ and is kept constant at $t > t_f$.

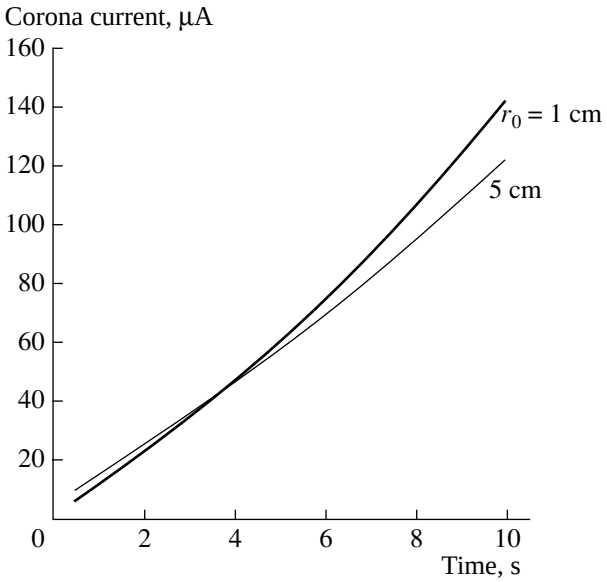


**Fig. 2.** Time evolution of the corona current from a 50-m-high rod electrode in a thundercloud field linearly increasing to 20 kV/m over 10 s.

mobility at all [19]. The weak dependence on the mobility allows one to simplify the calculation model of a corona in a thundercloud field; in this case, the lightning protection can almost always be calculated with allowance for only one ion species.

To sustain the current of a nonstationary corona at a fixed level, one has to continuously increase the gap voltage (the thundercloud electric field). The law according to which the field should increase over time is again determined by the geometry of the corona system. For a spherical electrode, the corona current will remain constant if the electric field increases as $E_0(t) \sim t^{1/3}$, and in the limiting case of a plane system, it should vary as $E_0(t) \sim t$. A long conductor of small radius occupies an intermediate place between these cases [19]. In a constant electric field $E_0$, the more uniform the field of the corona electrode, the faster the decrease in the corona current. In the limiting case of a plane electrode whose own electric field is uniform, the current almost instantaneously drops to zero. The decay of the corona current at $E_0(t)$ = const impedes the accumulation of a significant space charge near the top of the corona electrode.

Analytical studies and numerical simulations show that, if the thundercloud electric field significantly exceeds the external field $E_{0\mathrm{cor}}$ required for corona onset, then the corona current $i_{\mathrm{cor}}$ depends weakly on the electrode radius. According to the calculated time dependences $i_{\mathrm{cor}}(t)$ presented in Fig. 2, the fivefold increase in the radius of the rod electrode leads to the 15% decrease in the current amplitude. The main cause for the decrease in the current is an increase in the threshold field $E_{0\mathrm{cor}}$ for corona onset. Even if one increases the electrode radius to a few meters, provided that the condition $E_{0\mathrm{cor}} \ll E_{0\mathrm{max}}$ is satisfied (e.g., by placing short needles over the electrode top), then the corona current changes by no more than a few tens of percent. According to analytical estimates and numerical simulations performed for grounded electrodes a few tens of meters high (such as conventional lightning conductors and protected objects), the maximum corona current in a thundercloud field is about $10^{-4}$ A. Therefore, over a corona lifetime of ~10 s, a charge of $\sim 10^{-3}$ C is injected into the atmosphere. Although the front of the charged ion cloud can propagate from the corona surface over a distance of up to $10^2$ m, the ion density exceeds the natural background of $\sim 10^3$ cm$^{-3}$ only at distances of shorter than ~10 m from the top of the grounded electrode [18].

The approaching downward leader intensifies the corona due to a significant increase in the field growth rate $dE_0/dt$, rather than to the amplification of the atmospheric electric field by the leader charge. This is illustrated by the results of numerical simulations presented in Fig. 3. The calculations were performed for a 5-cm-radius rod with a height of $h$ = 50 m. The downward leader started from the height of 3000 m, when a linearly increasing thundercloud field had already reached a value of 20 kV/m over 10 s. The radial deviation of the downward leader with respect to the grounded rod was $r$ = 150 m. The electric charge per unit length of the downward leader was assumed to be constant and equal to 0.5 mC/m, which corresponded to an ordinary lightning. It can be seen that, even for a significant radial

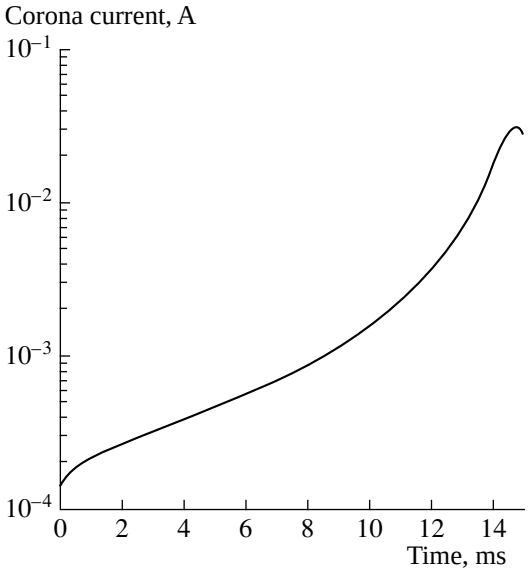


**Fig. 3.** Time evolution of the corona current during the propagation of the downward leader with a linear charge of 0.5 mC/m. The time is reckoned from the instant of the leader start.

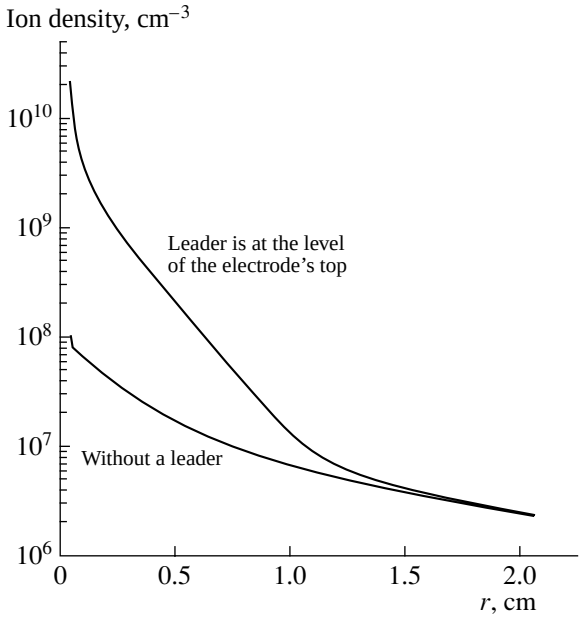


**Fig. 4.** Ion density near the top of a corona electrode for the conditions of Fig. 3 as a function of the distance from the top.

deviation of the leader ($r/h$ = 3), the corona current increases by nearly three orders of magnitude. However, this does not result in a significant increase in the corona charge because of the short development time of the downward leader, which propagates with an average velocity of $2 \times 10^5$ m/s and reaches the ground over 15 ms. In the case under consideration, the total corona charge increases by only 10%. Nevertheless, this additional charge plays an important role. Since this charge has no time to propagate far from the electrode, it is concentrated near the surface of the corona electrode, thereby greatly increasing the local ion density (Fig. 4). As a result, the point at which the electric field is maximal leaves the corona surface and begins to propagate into the gap. This effect can be regarded as the propagation of an ionization wave. From this instant, the corona discharge cannot be treated as streamerless and the model used fails to be adequate.

The condition for the termination of a streamerless corona can be derived from the relation $(dE/dr)_{r = r_0} \geq 0$ using the approximate solution for the electric field in a spherical corona system [17, 18]

$$E = E_{\text{cor}} \sqrt{\frac{r_0^4}{r^4} + \frac{i(r^3 - r_0^3)}{6\pi\varepsilon_0 \mu r^4 E_{\text{cor}}^2}}. \quad (2)$$

The critical current is [17]

$$i_{\text{cr}} \approx 8\pi\varepsilon_0 \mu r_0 E_{\text{cor}}^2. \quad (3)$$

For the above case of an electrode with a top radius of $r_0$ = 5 cm and for a typical ion mobility of $\mu$ = 1.5 $cm^2/V$ s, we have $i_{\text{cr}} \approx 15$ mA, which is comparable to the critical current of 10 mA obtained in numerical simulations for a rod electrode with the same radius.

Inequality (1), which determines the conditions for the development of an upward leader, can be applied only after the termination of the streamerless corona and the onset of a streamer flash.

### *2.3. Viability of an Upward Leader*

We are interested here in viable upward leaders that are capable of growing in the external electric field after emitting from the top of a grounded electrode. For a leader to grow, it is necessary that the field in the leader channel be weaker than the undisturbed external electric field [20, 21]. Only in this case will the increase in the length $l_L$ of a vertically growing leader be accompanied by an increase in the difference $\Delta U_{\text{tip}} = U_{\text{tip}} - U_0$ between the potential of the leader tip $U_{\text{tip}} = -E_L l_L$ and the potential of the undisturbed external electric field $U_0 = -E_0(h + l_L)$ at the position of the leader tip. It is $\Delta U_{\text{tip}}$ that determines the growth rate of the charge of the propagating leader and, consequently, its current $i_L$ and velocity $v_L$.

If we ignore the disturbance of the external electric field by the corona space charge, then the viability condition for the nascent leader can be found from the charge conservation law

$$i_L = \tau_L v_L = C_1 \Delta U_{\text{tip}} v_L, \quad (4)$$

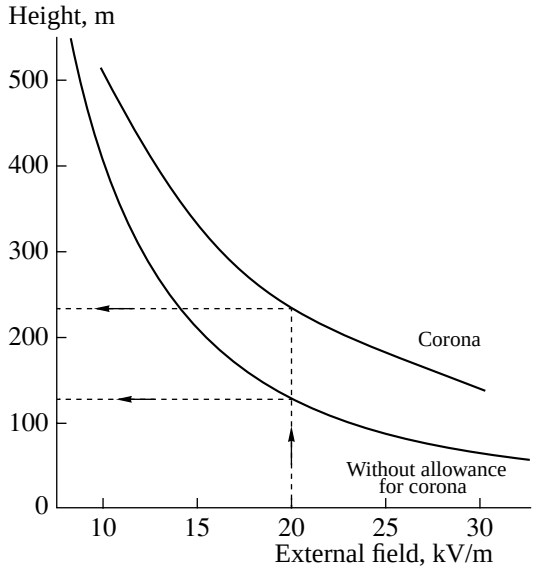


**Fig. 5.** The height of a ground object at which a viable leader can develop from the top of the object vs. external electric field.

and following semi-empiric formulas [8]:

$$E_L = \frac{b}{i_L}; \quad b = 300 \text{ V/(cm A)}, \tag{5}$$

$$v_L = a(\Delta U_{\text{tip}})^{1/2}; \quad a = 1500 \text{ cm/(s V}^{1/2}), \tag{6}$$

where $\tau_L$ and $C_1$ are the charge and capacitance per unit length of the leader channel, respectively. These formulas were shown to adequately describe leaders in long laboratory gaps with lengths of up to 100 m [8, 20, 22]. Substituting expressions (4)–(6) into the inequality $E_0 > E_L$, we obtain an estimate for the external electric field that is necessary to sustain a leader propagating from a grounded electrode of height $h$ [23]:

$$E_{0\text{cr}} \geq \frac{3.7 \times 10^5}{h^{3/5}} \text{ V/m}. \tag{7}$$

Under the thundercloud, near the ground, the electric field undisturbed by the corona space charge of grounded objects can be as high as 20 kV/m. According to criterion (7), this field is able to sustain a nascent upward leader propagating from an object whose height is no less than $h$ = 130 m. For ordinary objects with a height of $h$ = 20–30 m, the required external field must be much higher, $E_{0\text{cr}}$ = 50–60 kV/m. Such a strong field cannot be produced by a thundercloud.

The actual critical field is significantly higher than that predicted by criterion (7) because of the influence of the corona space charge (Fig. 5). Thus, computer simulations [23] show that, for a leader to grow from a corona electrode in an external field of 20 kV/m, the electrode must be higher than 225 m. In the absence of a corona, a height of 135 m is quite enough.

These estimates allow us to conclude that the main cause for the propagation of an upward leader from the top of a moderately high grounded object is the field of the approaching channel of a downward lightning leader, whereas an upward leader starting from a skyscraper object can develop even in a weaker thundercloud field. The effect of a corona on the emission of a viable leader under the action of the thundercloud field has been confirmed by experiments with lightning triggered by rockets drawing a grounded wire [24].

### *2.4. Phenomenology of the Downward Lightning Attachment*

Observations of lightning and experiments with long laboratory sparks have shown that the discharge channel undergoes many accidental deflections. Nevertheless, on the average, it propagates along the external electric field. Hence, in order to deflect the leader of downward lightning from the vertical direction, the disturbing field must be comparable to the thundercloud field $E_0$. This is also true for an upward leader propagating from a grounded object. Therefore, if the field generating the upward leader is mainly produced by the downward leader (rather than the thundercloud charge), then the attachment of downward lightning, which ends in the lightning strike to the object, indeed begins with the emission of a viable upward leader. In this case, the nascent upward channel will propagate toward the downward leader and, sooner or later, will direct it to the object top. According to the above estimates, this takes place for moderately high grounded objects near which the thundercloud field is a few times lower than $E_{0\text{cr}}$ and the necessary field is mainly produced by the charge of the approaching downward leader.

It should be noted that the direct influence of the charge of a grounded object on downward lightning is significantly weaker than that required for the deflection of the channel trajectory toward this object. Indeed, a linear charge $\tau_{\text{el}}(z)$ that is induced on the surface of a grounded electrode with a height $h$ and radius $r_0 \ll h$ in a uniform external field $E_0$ linearly increases from the base of the electrode to its top:

$$\tau_{\text{el}}(z) = \frac{4\pi\varepsilon_0 z E_0}{\ln\frac{2h}{r_0} - 2}.$$

Even if all the charge of the grounded electrode

$$q_{\text{el}} = \frac{2\pi\varepsilon_0 h^2 E_0}{\ln\frac{2h}{r_0} - 2}$$

were concentrated at its top, the horizontal component of the field induced by this charge at the position of the downward leader tip (with a height $H$ and radial deviation $r$) would not exceed

$$\Delta E_{\text{hor}} = \frac{q_{\text{el}} r}{4\pi\varepsilon_0}\left\{\frac{1}{[(H-h)^2 + r^2]^{3/2}} - \frac{1}{[(H+h)^2 + r^2]^{3/2}}\right\}.$$

For example, if $H = r = 3h$ and $h/r_0 = 10^3$, we then have $\Delta E_{\text{hor}} \approx 0.01E_0$, which is much lower than the thundercloud field. Such a disturbance is too weak to deflect the downward leader toward the grounded electrode. Hence, the lightning attachment is indeed provoked by the emission of an upward leader directed towards the downward leader tip. As the leaders approach one another, the disturbing effect of the upward leader on the downward one increases in an avalanche manner; as a result, the latter gets redirected toward the grounded object.

For skyscraper-type objects, the situation is different. Here, the thundercloud field can be quite enough to maintain a viable upward leader that has started from the top of a grounded object. It follows from criterion (7) that, for $E_0 \approx 20$ kV/m, this becomes possible for grounded objects higher than $h \approx 130$ m. The nascent leader will not necessarily develop toward the downward leader, whose influence is yet weak. There is no reason to call it an upward-connecting leader since, being controlled by the thundercloud field, the leader channel will propagate mainly upward, thereby forming a ground-to-cloud lightning discharge, rather than toward the downward leader.

Note that, in this case, the downward lightning discharge also is not affected by the upward leader. The disturbance of the external electric field near the tip of the downward leader is much smaller than the thundercloud field and is not able to deflect the leader channel toward the grounded object. On the average, the downward leader keeps propagating downward.

Thus, Golde's hypothesis is not applicable to skyscraper-type grounded objects, because, in this case, the downward leader does not control the propagation of the nascent upward leader. According to the results of numerical simulations presented in Fig. 5, this is the case for objects higher than 200 m. Observations show that it is these objects that most often undergo upward lightning strikes [25].

Nevertheless, the emission of an upward leader is hardly possible without a downward lightning discharge because the slowly varying thundercloud field is not able to increase the corona current from the top of a grounded object to the threshold value $i_{\text{cr}}$ corresponding to the excitation of a streamer flash. To show this, it suffices to consider an approximate analytical solution for an isolated sphere of radius $r_0$ [17, 18]. According to this solution, the current of a nonsteady corona with a linearly increasing voltage $U(t) = A_U t$ is

$$i(t) \approx 2\pi\varepsilon_0 t\sqrt{\frac{\mu A_U^3}{3}}. \quad (8)$$

This formula holds for the quite high effective voltage $U(t) \gg r_0 E_{\text{cor}}$ that is usually observed during a thunderstorm. In this case, the corona current is almost independent of the sphere radius. The critical current, determined by formula (3), is reached at a voltage amplitude of $U_{\max} = U(t_f) = A_U t_f$, which is equal to

$$U_{\max} \approx \sqrt[3]{\frac{3 i_{\text{cr}}^2 t_f}{4\pi^2\varepsilon_0^2\mu}}. \quad (9)$$

For a typical critical current of $i_{\text{cr}} = 10$ mA, we have $U_{\max} \approx 18.5$ MV. Even for such an extremely high object as the Ostankino TV tower ($h = 540$ m) and for the maximum possible regeneration rate of the thundercloud charge ($t_f \approx 10$ s), the required voltage drop can be reached in an external field as high as $E_{0\max} = U_{\max}/h \approx 34.5$ kV/m. Such a high field is hardly expected to frequently occur during a thunderstorm without involving downward lightning discharges.

### *2.5. The Frequency of Lightning Strikes to a Grounded Object*

Here, we consider lightning strikes to an isolated grounded object whose height is much larger than its transverse dimensions, e.g., a conventional lightning rod. The frequency of lightning strikes can be most easily determined for relatively low objects that do not excite upward lightning discharges and suffer only downward lightning strikes. As was shown above, the attachment of downward lightning proceeds via the development of an upward-connecting leader. Hence, the main problem is to find the instant at which the upward leader starts and to test its viability taking into account the design features of the grounded object and the space charge injected from its top into the atmosphere under the action of a corona discharge. As soon as the start instant of a viable upward leader has been found, the height $H_0$ of the tip of the downward lightning channel at the beginning of the attachment process can be determined by solving a purely electrostatic problem. The radius of the attraction zone can then be found using the equidistance principle [20]. As a result, we obtain an estimate for the frequency of lightning strikes to an object of a given height and configuration.

Note that, in spite of its primitivity, the equidistance principle is widely used for estimates in lightning protection. According to this principle, a downward lightning leader does not feel the ground until its tip comes down to a certain height $H_0$ called the attractive height. The lightning channel then propagates along the shorter of the two paths: along the path of length $H_0$ toward the ground or along the path of length $\sqrt{(H_0 - h)^2 + r^2}$ (where $r$ is the radial deviation of the downward leader tip with respect to the top of the object of height $h$) toward the grounded object. The equality of these

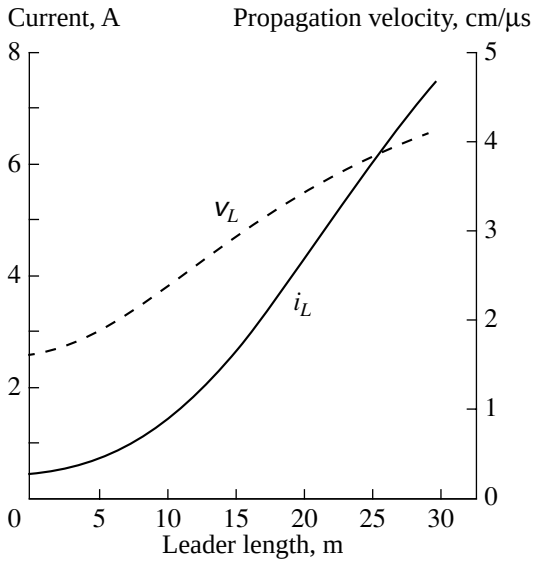


**Fig. 6.** Current and propagation velocity of an upward leader starting from a 30-m-high electrode as functions of the leader length.

lengths determines the attractive radius of a downward lightning,

$$R_{at} = \sqrt{2H_0h - h^2}. \quad (10)$$

The calculation algorithm is as follows:

(i) Determining the characteristics of a nonstationary corona at the top of a grounded rod electrode first in a thundercloud field that varies in a specified way and then in the field of a downward leader approaching the ground.

(ii) Calculating the position of the downward leader tip at the instant when the corona current becomes equal to the critical value that is necessary for a streamer flash to occur.

(iii) Checking whether condition (1) for the origin of an upward leader in the stem of the initial streamer branch is satisfied.

(iv) Calculating the parameters of the upward leader propagating in the space charge layer of the corona and checking its viability.

The computer code developed [18] allowed us to calculate the corona current from a rod electrode in an arbitrarily varying thundercloud electric field. When simulating a corona in the sum of the thundercloud field and the field produced by a downward leader, the leader was represented by an infinitely thin vertical charged channel. The propagation velocity of the leader was assumed to be constant. In the simplest version of the code, the distribution of the linear charge density along the leader channel was also assumed to be constant, $\tau_L(z) = \text{const}$. However, the code also allowed us to perform calculations with an arbitrary distribution $\tau_L(z)$, e.g., with a charge density linearly increasing from the base to the tip of the leader channel (such a distribution corresponds to the polarization of an ideal conductor in a uniform electric field). To check the viability of the nascent upward leader, we used the above simplified semi-empiric theory, which relates the leader current, the leader propagation velocity, and the longitudinal electric field in the channel to the difference $\Delta U_{tip}$ between the leader tip potential and the potential of the undisturbed external field at the position of the leader tip. In calculations, the nascent upward leader was represented by a straight charged channel. At every time step, the charge distribution along the channel was determined by solving a set of integral equations with potential coefficients. The equations related the potential of each channel segment with its charge, the charges of all the other channel segments, the space charge in the gap, and the external field created by the thundercloud and the downward leader. The images of the charges in the ground were taken into account. The obtained charge distribution was used to find the potential of the upward leader tip. Using this potential, the running values of the leader current, the leader propagation velocity, and the field in the leader channel were then determined.

Figure 6 presents the result of simulations (similar to those described in [26]) of the development of an upward leader from a 30-m-high grounded electrode with a hemispherical 2-cm-radius top. The downward leader started at a height of 3000-m at the instant when the linearly increasing (over 10 s) thundercloud field reached 20 kV/m near the ground. The downward leader propagated toward the ground with a velocity of $2 \times 10^5$ m/s. The radial deviation of the downward leader with respect to the grounded electrode was 90 m. The density of a uniformly distributed linear charge was 0.5 mC/m. The corona current exceeded its critical value 13.7 ms after the start of the downward leader, when its tip had already propagated down to a height of 225 m and the voltage drop across the streamer zone was nearly three times higher than $\Delta U_{cr} \approx 400$ kV, which was required for the emission of an upward leader. The leader was stable since the very beginning of its propagation. The propagation velocity of the upward leader and its current increased relatively slowly only over the first several meters of its path, where the corona space charge was maximum. Over 1 ms, the leader passed about 30 m, went beyond the space charge layer, and then propagated freely.

Figure 7 shows the calculated height $H_{tip}$ of the downward leader tip at the start instant of a viable upward leader as a function of the radial deviation $r$. The calculations were performed for a grounded electrode with a height $h = 30$ m for the same conditions as in Fig. 6. The solution to the equidistance equation $H_{tip} = [r^2 + (H_{tip} - h)^2]^{1/2}$ determines the limiting radial deviation $r = R_{at}$ at which downward lightning is yet attached towards the object and the height $H_{tip}(r = R_{at}) = H_0$ from which it starts to be attached. In Fig. 7, $H_0 = 8h$

and $R_{at} \approx 3.8h$, which corresponds to an attraction area of $S_{at} = \pi R_{at}^2 \approx 0.04$ km$^2$ (one lightning strike per twelve years of operation for a lightning strike frequency of about two strikes per year per kilometer squared, which is characteristic of central Russia). Similar calculations for a 100-m-high object with a 2-cm-radius top give $H_0 = 5h$ and $R_{at} \approx 3h$. The ratio $R_{at}/h$ decreases with increasing $h$ over the entire range of the practically important heights and for different densities of the linear charge of the downward lightning leader used in the model.

The above method for determining the start instant of an upward leader is applicable to objects with heights from a few tens of to a few hundred meters. Numerical simulations allow one unambiguously determine the conditions for the origin of a viable upward leader. Quite another matter is the role it plays in the lightning attachment. Our results show that the development of an upward leader from a sky-scraper object does not necessarily affects the downward lightning discharge. There may be a situation in which the upward and downward leaders will not sense one another, i.e., there will be no attraction between them. The leader of the downward lightning discharge will propagate towards the ground or some another grounded object. The evolution of the excited upward leader is not known in advance. It can decay or convert into an upward lightning flash. Since upward lightning is almost as dangerous as downward lightning, it is important to find the conditions under which it can develop from different objects.

As was shown above, an upward leader can arise from objects as low as 10–20 m owing to the amplification of the electric field by a nearby downward leader. There may be a situation in which downward lightning does not strike a grounded object but, nevertheless, stimulates the development of an upward leader from it. For low objects, such a leader will develop as long as the strong electric field of the downward leader exists. This field disappears when the downward leader touches the ground and the current wave of the return stroke is excited. This wave propagates upward from the ground at a velocity of about 30% of the speed of light. It recharges the lightning channel and substantially reduces its electric field [20]. As a result, the upward leader ceases to propagate. In Fig. 8, the leader starting from a 30-m-high object stops developing as early as 3 μs after the downward lightning leader has reached the ground.

For sky-scraper objects, the situation is quite different. We simulated the development of an upward leader from a 200-m-high grounded rod electrode with a top radius of 2 cm [27]. The process was induced by a downward leader with a linear charge density of 0.5 mC/m. The radial deviation of the downward leader was 750 m. The upward leader started when the tip of the downward leader came down to a height of 520 m and was at a distance of 860 m from the electrode top.

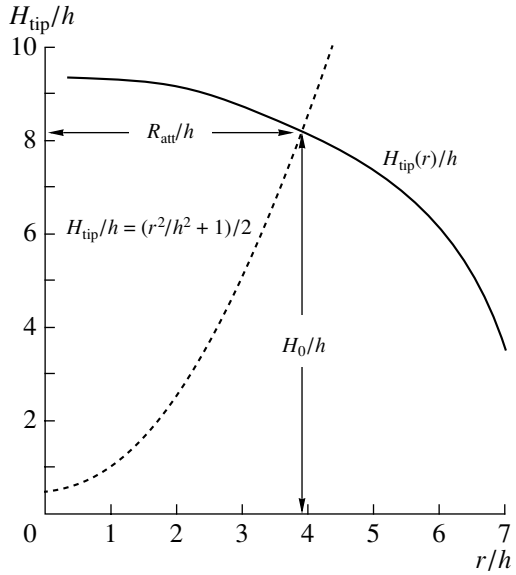


**Fig. 7.** Height of the downward leader tip at the instant of the excitation of an upward leader from a grounded electrode of height 30 m and radius 2 cm as a function of the radial deviation of the downward leader with respect to the electrode. The downward leader charge is uniformly distributed along the leader channel with a linear density of $\tau_L$ = 0.5 mC/m. The dashed curve shows the locus of points corresponding to the equal distances from the downward leader tip to the ground and to the object top.

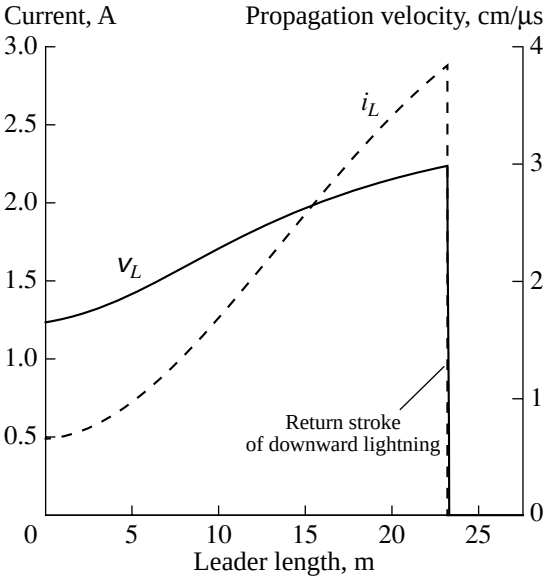


**Fig. 8.** Current and propagation velocity of an upward leader vs. leader length. The height of the grounded electrode is 30 m, and the radial deviation of the downward leader with a linear charge of $\tau_L$ = 0.5 mC/m is 150 m.

Such a distant lightning discharge was not able to strike the electrode; however, it efficiently sustained the development of the upward leader. By the instant when the return stroke of the downward lightning discharge

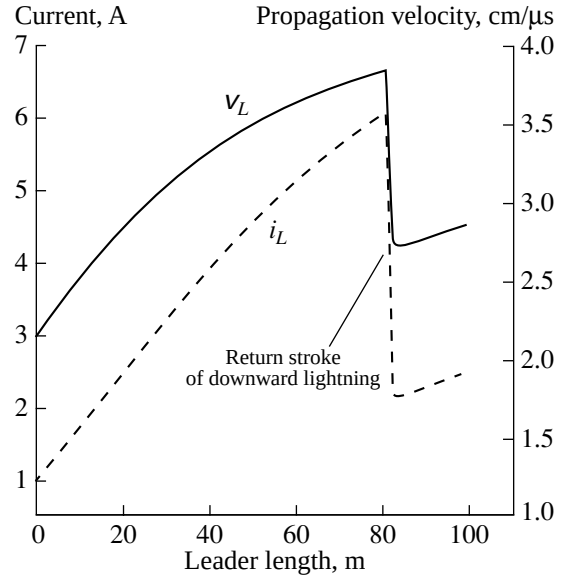


**Fig. 9.** Current and propagation velocity of an upward leader vs. leader length. The radial deviation of the downward leader with a linear charge of $\tau_L = 0.5$ mC/m is 750 m, and the height of the grounded object is 200 m.

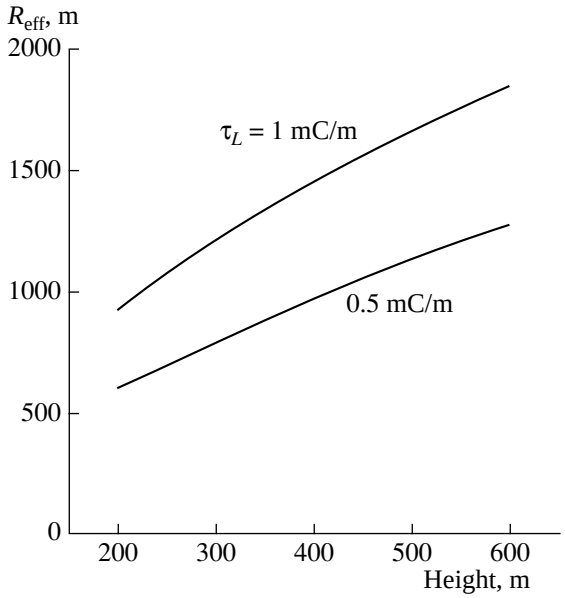


**Fig. 10.** Effective interaction radius $R_{eff}$ of a grounded object as a function of its height.

began, the upward leader had grown to approximately 80 m, i.e., it had gone beyond the cloud of the corona space charge. For a freely propagating leader, the presence of the corona charge leads to the amplification (rather than the attenuation) of the external field. No longer restrained, the upward leader continues to develop even after the neutralization of the charge of the downward leader during the return stroke of lightning. The only effect is that the propagation velocity and current of the upward leader decrease for a short time, after which these again begin to increase (Fig. 9). This process finally results in the origin of upward lightning, which strikes the ground object.

Because of the lack of data on the attachment mechanism, it is impossible to predict with certainty the further evolution of an upward leader starting from a high grounded object. It can either be attracted to the downward leader (in this case, the development of a downward lightning leader completes with a strike to the object) or, as was shown above, continue to propagate toward the cloud, thus converting into an upward lightning discharge. If one does not distinguish between downward and upward lightning strikes, the total frequency of strikes can be found using computer simulations. As long as one searches for the maximum possible radial deviation of the downward leader at which a viable leader can develop from the top of a grounded object of a given height, the algorithm for solving this problem is identical to that discussed above. This deviation determines the effective interaction radius $R_{eff}$—the radius of the area within which any downward lightning either strikes the grounded object or induces an upward lightning discharge from its top. Figure 10 shows the calculated values of $R_{eff}$ [27] for two different linear charges of the leader of downward lightning.

The number of lightning strikes estimated from the effective interaction radius ($N_{lightn} = n_0 \pi R_{eff}^2$, where $n_0$ is the number of lightning strikes per unit area of the ground surface) can be verified experimentally. In particular, one can use the representative data from observations over the Ostankino TV tower [25]. For the average yearly number of lightning strikes to the ground near Moscow of $n_0 = 2.5$–$3.0$ km$^{-2}$, the tower suffers about 30 lightning strikes over the lightning season. Our calculations provide a similar result for the $R_{eff}$ value corresponding to that shown in Fig. 10 for a linear charge of a downward leader of ~1 mC/m.

## 3. PROSPECTS FOR CONTROLLING THE FREQUENCY OF LIGHTNING STRIKES TO A GROUNDED OBJECT

As was mentioned in the Introduction, there are two approaches to the problem of lightning protection that yield diametrically opposite effects: the reduction of the number of lightning strikes to the protected object and, alternatively, the increase in the attraction of lightning to the lightning rod. The implementation of these approaches should not be related to the use of such exotic, expensive, and not quite reliable means as a high-power laser that lengthens the grounded electrode with a long plasma channel or chemical reagents destroying the thundercloud. It seems that the only acceptable means may be a counter discharge that is formed in a relatively weak electric field, is character-

ized by a moderate voltage drop, and can operate in a controllable regime, e.g., a streamer or streamerless corona discharge.

Attempts to excite an early counter discharge with the aim of emitting an upward-connecting leader that should intercept downward lightning are described in [5, 28, 29]. On the other hand, the grounded corona systems have been considered that should delay or almost completely prevent the emission of an upward-connecting leader [30]. Such systems are supposed to guarantee that downward lightning will not notice the object under protection.

Below, both these approaches are analyzed using the results of numerical simulations.

### *3.1. Lightning Protection Systems Based on the Early Streamer Emission*

The concept of lightning protection on the basis of early streamer emission (ESE) is very simple. The top of the lightning rod is shaped in such a way as to enable the earliest excitation of a streamer flash; i.e., the radius of curvature of the electrode top is made as small as possible. It is assumed that the early initiation of a streamer flash stimulates the early development of an upward-connecting leader. As it propagates toward the downward lightning leader, it intercepts the channel of the latter. To boost this effect, extra voltage (usually, a few tens of kilovolts) is applied to the top of the corona electrode. To obtain this extra voltage without employing an external power supply, the current flowing through the electrode top in the early stage of the counter discharge can be used. For example, this current may charge a storage capacitance, which then discharges through the forming *LC* circuit. The extra voltage thus obtained is applied to the top of the corona electrode (for this purpose, the top is insulated from the ground). The efficiency of ESE lightning rods is claimed to be many times higher than that of conventional lightning rods.

Unfortunately, there are no reliable statistical data on the efficiency of ESE lightning rods in the literature. Moreover, there are no works on laboratory studies that could clarify (at least at a qualitative level) the relation between the conditions for the excitation of a counter discharge from a grounded electrode and the probability of striking this electrode by a long downward spark. Nevertheless, as early as in the mid 1970s, a series of experimental studies aimed at determining the so-called critical radius of a high-voltage electrode in long air gaps were carried out in [31, 32]. It was shown that, when a positive pulsed voltage with a rise time of several hundred microseconds was applied to a rod–plane or sphere–plane gap, the electrical strength varied only slightly with increasing anode radius $r_0$ until the radius exceeded a certain critical value $r_{cr}$. The critical radius was found to be fairly large and to be a function of the interelectrode distance. For example, in a gap of length

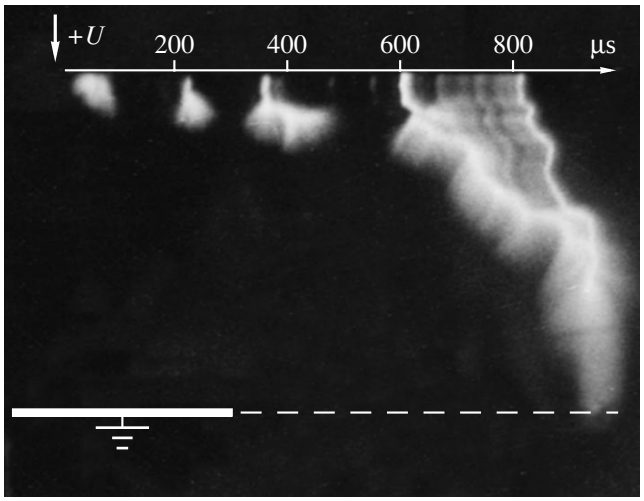


**Fig. 11.** Streak image of a leader in a 8-m-long rod–plane gap after a positive voltage pulse with a rise time of about 3 ms is applied to the rod.

~10 m, the critical radius is as large as $r_{cr} \approx 30$ cm. The explanation of this effect was given in [33]. In brief, the essence of the effect is that the too early excitation fails to provide the required viability of the leader. It first forms in the so-called flash mode (with long pauses between the flashes) [34], and its stable continuous propagation begins only after increasing the applied voltage (Fig. 11).

The fact that the critical radius $r_{cr}$ is rather large casts some doubt on the concept of ESE lightning protection. In [26], numerical simulations were performed of the excitation of a counter discharge from a grounded electrode of given height, starting with the generation of a nonstationary corona in a slowly increasing thundercloud field up to the initiation of a streamer flash due to the field amplification by the charge of an approaching downward leader. The probability of emitting an upward leader and the viability of the nascent leader while it propagates in the cloud of the corona space charge were estimated. The calculations were performed for different top radii of the grounded electrode. The results presented in Fig. 12 show that varying the electrode top radius within the range $r_0 = 0.1$–1 cm (which is typical of the lightning protection practice) affects the conditions for the excitation of a streamer flash but does not influence the viability of the upward leader.

The above effect of the electrode top radius $r_0$ on the excitation of a streamer flash is quite expectable because, according to formula (3), the critical current nearly linearly depends on $r_0$ for spherical electrodes as long as the corona threshold field $E_{cor}$ can be considered constant. However, for small electrode top radii, just after the excitation of a streamer flash, either condition (1) for the origin of an upward leader is not met or the

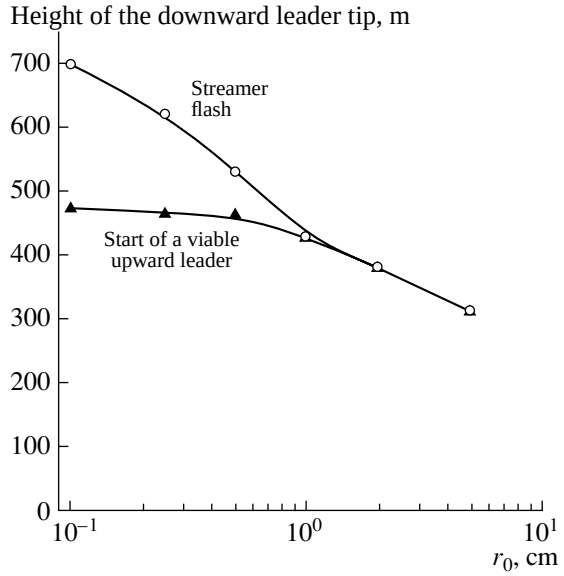


**Fig. 12.** Height of the downward leader tip at the instant of a streamer flash and at the start instant of a viable upward leader propagating from the top of a 50-m-high lightning rod vs. top radius. The downward leader with a linear charge of 0.5 mC/m starts from a height of 3000 m at the instant when a thundercloud field linearly increasing over 10 s has reached a value of 20 kV/m. The radial deviation of the downward leader is 50 m.

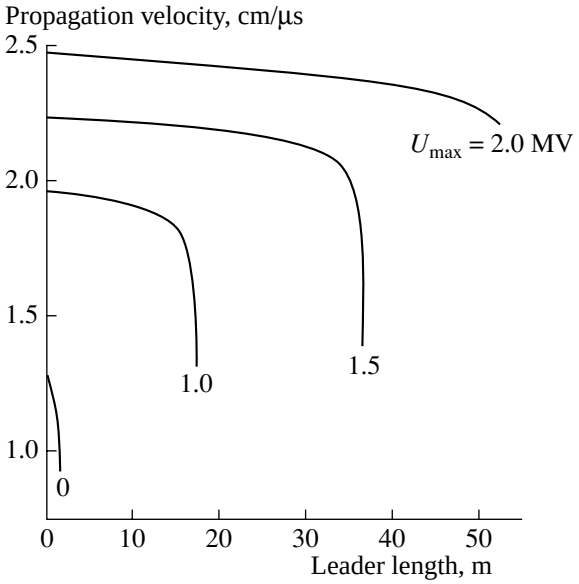


**Fig. 13.** Propagation velocity of an upward leader emitted from the top of a 150-m-high grounded rod under the action of a 1-ms controlling voltage pulse vs. leader length. The leader starts at the instant when a thundercloud field linearly increasing over 10 s has reached a value of 20 kV/m.

nascent leader is not able to penetrate through the layer of the corona space charge in a still relatively weak external field. Hence, the sharpening of the electrode does not increase the efficiency of the lightning rod. In this respect, it worth noting the results of field experiments [35, 36], which did not reveal any advantage of lightning rods with a pointed top against those with a blunt top (on a number of principal issues, those experiments need a more thorough analysis, which is beyond the scope of this study).

Besides a decrease in the top radius, ESE from the top of a grounded electrode can also be provoked by applying an additional voltage between the top of the electrode and its grounded base. There is no doubt in the efficiency of this method. The only problem is to determine the required value of this controlling voltage. Attempts to resolve this problem experimentally were made several decades ago. In recent years, numerical simulations have been used for this purpose.

The results of numerical simulations presented in Fig. 13 demonstrate how an upward leader developed from a 150-m-high grounded electrode grows under the combined action of a thundercloud field that increases to 20 kV/m over 10 s near the ground surface and the field produced by applying an additional (controlling) voltage $U_{max}$ to the electrode top. The full width at half-maximum of the additional voltage pulse is 1 ms. It was shown that, for the leader to propagate without bound, the amplitude $U_{max}$ of the additional voltage pulse should exceed 2 MV, which is much higher than the 20–30 kV voltage that can be obtained by accumulating energy from the atmospheric electric field due to the corona current (as is assumed to happen in ESE lightning rods).

To qualitatively estimate the effect of the increase in the potential of the lightning electrode top by this quite a moderate value provided by the internal scheme of an ESE lightning rod, it is necessary to consider the following circumstances. First, this value is less than 10% of the threshold voltage drop $\Delta U_{cr} \approx 400$ kV required to enable the leader emission from a grounded electrode. Second, it is quite easy to increase the voltage drop by 20–30 kV in a natural way. For this purpose, it is enough to increase the height of the lightning rod by only 1.0–1.5 m in a thundercloud field of ~20 kV/m. Finally, to produce an electric field comparable to the above controlling field due to the effect of an approaching downward leader, it is quite sufficient that the leader pass a relatively short additional distance toward the ground. Indeed, in the first approximation, the leader field near the ground, just under the leader tip, can be estimated as follows:

$$E_L \approx \frac{\tau_L}{2\pi\varepsilon_0 H_{tip}},$$

where $H_{tip}$ is the height to which the leader came down. The drop between the zero potential of the top of a grounded lightning rod of height $h$ and the potential

induced at the position of the top by the charge of the downward leader is

$$\Delta U_L \approx \frac{\tau_L h}{2\pi\varepsilon_0 H_{\text{tip}}}.$$

For example, if $H_{\text{tip}}/h = 5$, which is typical for the initial stage of lightning attachment, and $\tau_L = 0.5$ mC/m, then we have $\Delta U_L \approx 1.8$ MV. The controlling voltage provided by the internal scheme of an ESE lightning rod is less than 2% of this value. To increase $\Delta U_L$ by 2%, it is sufficient that the length of the downward leader increase by approximately the same amount, which is too small to lead to any significant consequences.

Finally, let us consider the experience acquired in the use of electric-power transmission lines. The energized wires of these lines are at a certain potential with respect to the shield wires, the wires of dc power transmission lines having potentials of opposite polarities. Nevertheless, no difference in using lightning wires to protect ground objects and high-voltage power transmission lines (at least, up to voltages of 500 kV) has been observed. Moreover, no difference has been observed in the number of lightning strikes to the positive and negative wires of a dc power transmission line, although about 90% of all downward lightning discharges carry a negative charge.

According to the above, the increase in the potential of the lightning rod by a few tens of kilovolts cannot significantly affect its protecting ability. Thus, to date, there are no experimental data or theoretical predictions indicating the increased efficiency of ESE lightning rods against conventional ones.

### *3.2. Lightning Protection Systems Based on Suppressing the Upward-Connecting Leader*

Systems of this kind are being actively discussed now [5, 6]. These are multipoint corona systems with a total radius of up to 10 m. The corona needles with a height of about 10 cm and radius $r_{\text{ndl}} \sim 1$ mm (or less) uniformly fill a surface that has the shape of an umbrella. The total number of the needles can be as high as several thousands. The corona space charge is assumed to suppress the emission of an upward leader and thus to prevent lightning strikes to the object above which the system is placed.

The main objection to employing this method is that the increase in the number of the corona points slightly affects the space charge injected into the atmosphere by a well-developed corona. Indeed, if the atmospheric electric field greatly exceeds the threshold level $E_{0\text{cor}}$ corresponding to corona onset, then a continuous corona is formed over the surface of the system so that the corona space charge covers the entire system. As was noted above, under these conditions, the corona current depends slightly on the radius of the corona surface. This is also true if the surface of the system is divided into many separate corona sites. Figure 14 shows the calculated time evolution of the corona current from an isolated hemispherical 2-cm-radius electrode and from a multipoint corona system of radius 2 m in a thundercloud electric field. The needle dimensions are chosen such that the coronas from these needles are excited at the same value of the thundercloud electric field (about 1.4 kV/m), which increases linearly to 20 kV/m over 10 s. One can see that, in a well-developed corona, the corona current through the rod differs from that through the multipoint system by no more than 15%.

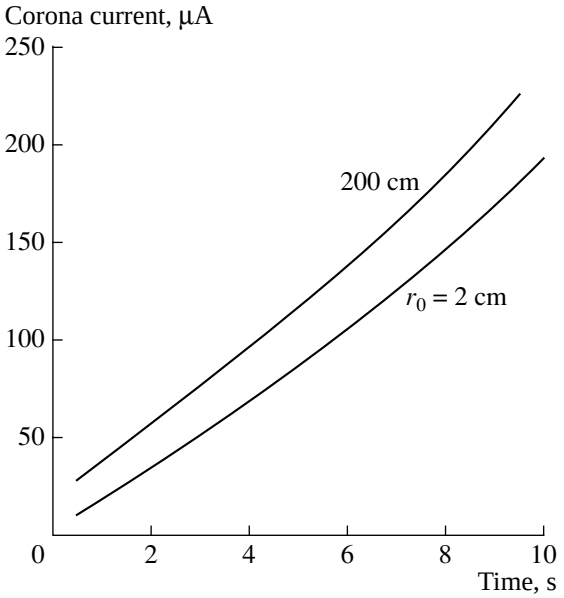


**Fig. 14.** Time evolution of the corona current through an isolated rod electrode and from a multipoint corona system of radius 2 m at the same corona threshold field $E_{0\text{cor}}$.

However, the increase in the injected charge is of minor importance for the protection ability of a multipoint corona system. The most important point is that the corona current is nearly uniformly distributed over the needles. Therefore, the current flowing through a needle decreases in proportion to the needle number $N_{\text{ndl}}$; as a result, it does nor reach the critical value $i_{\text{cr}}$ corresponding to the excitation of a streamer flash. To illustrate, for a needle radius of $r_{\text{ndl}} = 0.1$ cm (which corresponds to $E_{\text{cor}} \approx 75$ kV/cm and $i_{\text{cr}} \approx 2$ mA) and for $N_{\text{ndl}} = 5000$ (which is quite realistic), the total corona current must exceed 10 A for a streamer flash to be excited at any needle tip. To compare, for a single electrode with a typical radius of 2 cm, this would occur at a corona current as low as 10 mA.

Figure 15 shows the total corona current from a multipoint corona system as a function of the height of the downward leader tip for a radial deviation of $r = 50$ m with respect to the grounded electrode. As before, the leader is represented by an infinitely thin vertical charged channel with a linear charge of $\tau_L = 0.5$ mC/m. The propagation velocity of the leader is assumed to be

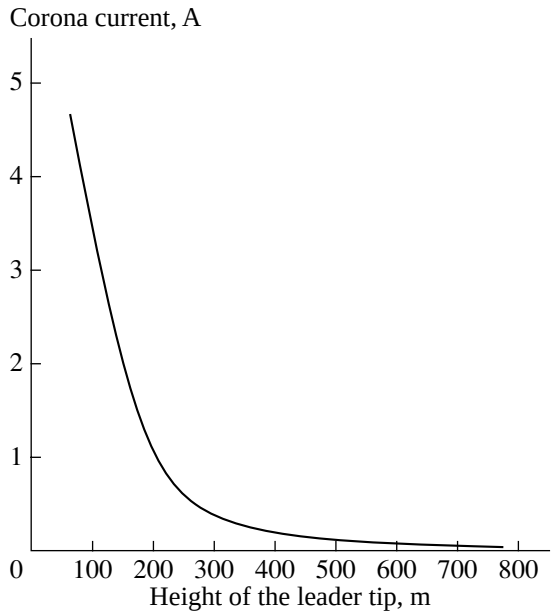


**Fig. 15.** Total current from a multipoint corona system of radius 2 m and height 50 m as a function of the height of the downward leader tip. The linear charge of the downward leader is 0.5 mC/m, and its radial deviation is 50 m.

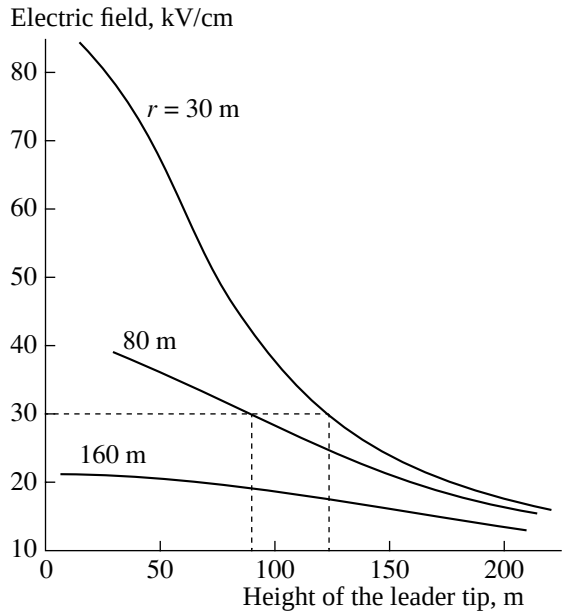


**Fig. 16.** Maximum electric field on the surface of a hemispherical multipoint corona system of radius 5 m as a function of the height of the downward leader tip.

$2 \times 10^5$ m/s. Simulations show that, under these conditions, the current flowing through a single needle cannot exceed the critical value. For this to occur, the tip of the downward leader should more closely approach the corona electrode. By choosing the size of the corona system and the number of needles, it is always possible to keep the current flowing through the corona points below the critical level $i_{cr} = 8\pi\varepsilon_0\mu r_{ndl}E_c^2$ and thus to prevent streamer emission. The only exception is the case of the zero radial deviation of the downward leader, when its tip is just above the corona system.

The situation becomes critical when the ionization condition is satisfied not only at the needles but also at the surface of the system. In this case, the streamer flash may be excited at any point on the surface or even at a point near the surface where the electric field can be much higher than that on the surface. Such an anomalous disturbance of the electric field is caused by an intensely accumulated space charge. As was mentioned above, this charge does not have time to propagate by a significant distance during the development of a downward lightning leader and is thus accumulated near the grounded top. Figure 16 shows the electric field between the needles on the surface of a multipoint corona system as a function of the height of the downward leader tip. The simulations were performed for a hemispherical corona system of radius 2 m placed at a height of $h = 50$ m. By the start instant of the downward leader with a linear charge of 1 mC/m (a high-power lightning discharge), the thundercloud field has increased to 10 kV/m. For a radial deviation of $r = 160$ m of the downward leader with respect to the system axis, the electric field near the surface of the system does not exceed 22 kV/cm. This means that no streamer flash accompanied by a subsequent upward leader can occur in this case. For $r = 80$ m ($r/h = 1.6$), the field near the surface of the corona system increases to 30 kV/cm as the downward leader tip comes down to $H_0 = 90$ m ($H_0/h = 1.8$). Such a situation corresponds to the approximate equality of the distances from the downward leader tip to the ground ($H_0$) and to the corona system ($\sqrt{(H_0 - h)^2 + r^2}$). Recall that this equality determines the lightning attractive radius $R_{at}$. Finally, for $r = 30$ m, the condition for the emission of an upward leader is satisfied already at a height of $H_0 = 125$ m, when $H_0 > \sqrt{(H_0 - h)^2 + r^2}$; this definitely ensures a lightning strike to the corona system.

Thus, employing a large-radius multipoint corona system substantially (severalfold) decreases the attractive height of the leader of downward lightning and, consequently, the attractive radius $R_{at}$ as compared to a conventional lightning rod of the same height. Note that the number of lightning strikes to a grounded object decreases in proportion to $R_{at}^2$.

All other factors being the same, the calculated attractive height $H_0$ depends strongly not only on the leader linear charge $\tau$ but also on its distribution along the channel. It is these lightning parameters that are still poorly investigated. To avoid the uncertainty related to

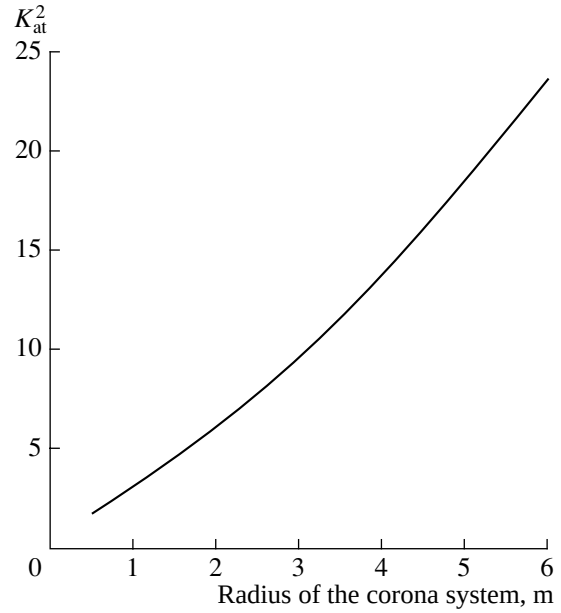


**Fig. 17.** Reduction factor of the lightning strike number for a 50-m-high object as a function of the radius of a multipoint corona system.

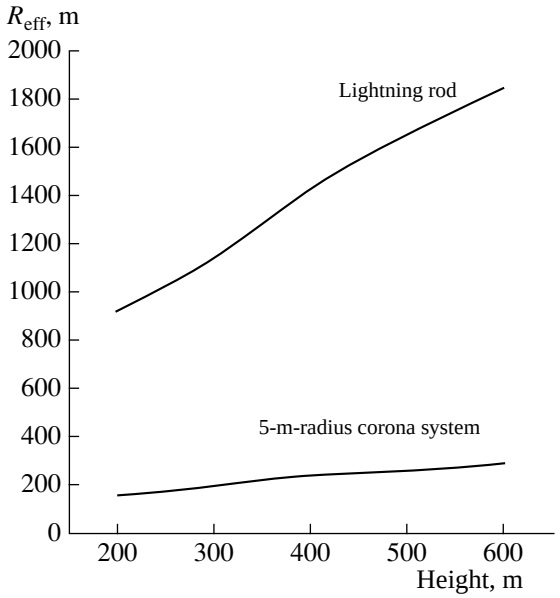


**Fig. 18.** Effective interaction radius $R_{eff}$ as a function of the height of an object protected by a lightning rod and that protected by a multipoint corona system of radius 5 m.

this, it is reasonable to deal with the ratio between the attractive radius of a conventional lightning rod ($R_{at0}$) and that of a large-radius multipoint corona system ($R_{at}$) rather than with the absolute value of the lightning attractive radius. Obviously, both $R_{at0}$ and $R_{at}$ should be determined with allowance for the effect of the corona space charge as was described in Section 2. Computer simulations show that the uncertainty in determining the parameter $K_{at} = R_{at0}/R_{at}$ is much lower than in determining the attractive radius itself. This parameter is convenient for an analysis because the lightning attraction area is proportional to $R_{at}^2$; hence, the quantity $K_{at}^2$ is, in fact, the factor by which the number of lightning strikes to an object is reduced when the object is protected by a multipoint corona system instead of a conventional lightning rod. Figure 17 shows the protection efficiency of such a system installed at 50-m height as a function of the system radius. It can be seen that, for a system of radius 4–6 m, the number of strikes by downward lightning discharges can be reduced by one order of magnitude and more.

The results presented in Fig. 18 give an idea of to what extent the effective interaction radius $R_{eff}$ decreases for sky-scraper objects protected by a multipoint corona system. For example, setting a multipoint corona system with a radius of 5 m at the top of the Ostankino TV tower would decrease $R_{eff}$ by a factor of 6.4, which corresponds to a nearly fortyfold decrease in the total number of lightning strikes.

Such a high expected efficiency of a multipoint protection systems deserves further thorough investigation. The main attention should be paid to the experimental study of the conditions for the conversion of a streamerless corona into a streamer one that gives rise to an upward leader propagating from the top of a grounded electrode. The analytical estimates used in this paper have not yet been confirmed even under laboratory conditions.

It should be noted that above multipoint corona systems can in no way be regarded as a panacea that will resolve the problem of the lightning protection of sky-scraper objects. Such systems provide only local lightning protection. They reduce the number of lightning strikes onto their own surface and the object components directly covered by it. Beyond the protecting "umbrella," the protecting effect of a corona charge decreases very rapidly. This does not allow one to use it to protect large-area objects. Note that, for extended corona conductors, the effect of a corona space charge has not yet been studied.

## 4. CONCLUSIONS

(i) The development of an upward leader from the top of a grounded object is determined by the amount and distribution of the space charge injected into the atmosphere by a corona discharge in the thundercloud electric field and the field of a downward lightning leader.

(ii) Theoretical analysis and computer simulations have shown that the corona discharge in the atmospheric electric field is nonstationary. In contrast to a steady corona, its current depends not only on the instantaneous value of the electric field but also on the rate of its time variations. This dependence, as well as

the dependence of the corona current on the ion mobility, is strongly affected by the geometry of the discharge gap. The current of a well-developed nonstationary corona depends only weakly on the radius of the corona electrode.

(iii) The critical current of a nonstationary corona above which it cannot occur in a streamerless mode has been estimated. The formation of a streamer flash from a grounded electrode can result in the development of an upward leader if the voltage drop along the streamer branches exceeds a certain threshold value.

(iv) The corona space charge impedes the propagation of the nascent upward leader inside the ion cloud formed by the corona discharge. Consequently, any simulations of the leader propagation from stationary grounded objects without allowance for a corona discharge are invalid.

(v) Golde's hypothesis that the attachment of the leader of downward lightning is affected by an upward leader developing from a grounded object is valid only for moderately high objects that are incapable of exciting upward lightning. Generally, the development of an upward leader from a grounded sky-scraper object only slightly affects the attachment of downward lightning, although it is usually the lightning field that is the reason for the leader origin. The nascent upward leader propagates toward the thundercloud (in the form of a separate upward lightning discharge) rather than toward the leader of downward lightning.

(vi) A numerical model has been developed for estimating the frequency of the lightning strikes to grounded objects of various heights with allowance for the effect of the corona space charge. The estimates obtained agree with the results from observations of skyscraper-type objects.

(vii) Analytic results and computer simulations show that ESE lightning rods are unable to provide the expected manyfold increase in the protecting efficiency. This is because a substantial decrease in the top radius of the lightning rod, as well as an additional increase in the potential of the rod top by a few tens of kilovolts, does not provoke the early onset of a viable upward leader.

(viii) Setting a large-radius multipoint corona system on the object insignificantly increases both the corona current and the space charge formed near the corona top. Nevertheless, the use of such systems can reduce the frequency of lightning strikes by one order of magnitude or more. The reason is that the corona current is nearly uniformly distributed over numerous corona points; as a result, the current of any point does not exceed the critical value corresponding to the origin of a streamer flash followed by the initiation of an upward leader. In contrast to conventional lightning rods, the efficiency of multipoint corona systems does not decrease when placing them on sky-scraper objects.

(ix) Multipoint corona systems provide only local lightning protection. They reduce the number of lightning strikes onto their own surface and the object components directly covered by them. The question of extending the protection area of such systems still remains open.

## REFERENCES


1. R. H. Golde, J. Franklin Inst. **286**, 451 (1967).
2. R. H. Golde, *Lightning Protection* (Edward Arnold, London, 1974).
3. R. H. Golde, *Lightning* (Academic, New York, 1977), Vols. 1, 2.
4. A. M. Mousa, IEEE Trans. Power Delivery **13**, 1120 (1998).
5. M. A. Uman and V. A. Rakov, Bull. Am. Meteorol. Soc., No. 12, 1809 (2002).
6. *Proceedings of the IEEE Power Engineering Society General Meeting, Toronto, 2003*, Panel "Nonconventional Lightning Mitigation: Fact or Fiction," IEEE Catalogue No. 03CH37491C (CD-ROM), Library of Congress, 2003106706.
7. Les Renardieres Group, Electra, No. 53, 31 (1977).
8. E. M. Bazelyan and Yu. P. Raizer, *Spark Discharge* (MFTI, Moscow, 1997; CRC, Boca Raton, 1998).
9. N. L. Aleksandrov, E. M. Bazelyan, I. V. Kochetov, and N. A. Dyatko, J. Phys. D **30**, 1616 (1997).
10. N. L. Aleksandrov and E. M. Bazelyan, Plasma Sources Sci. Technol. **8**, 285 (1999).
11. N. L. Aleksandrov, É. M. Bazelyan, and A. M. Konchakov, Fiz. Plazmy **27**, 928 (2001) [Plasma Phys. Rep. **27**, 875 (2001)].
12. É. M. Bazelyan, Élektrichestvo, No. 5, 20 (1987).
13. N. A. Kaptsov, *Electrical Phenomena in Gases and Vacuum* (Gostekhizdat, Moscow, 1950).
14. C. A. Uhlig, in *Proceedings of the High-Voltage Symposium of the National Research Council of Canada, Ottawa, 1956*, p. 15-1.
15. Yu. P. Raizer, *Gas Discharge Physics* (Nauka, Moscow, 1987; Springer-Verlag, Berlin, 1991).
16. L. B. Loeb, *Electrical Coronas* (Univ. California Press, Berkeley, 1965).
17. N. L. Aleksandrov, E. M. Bazelyan, R. B. Carpenter, Jr., *et al.*, J. Phys. D **34**, 3256 (2001).
18. N. L. Aleksandrov, É. M. Bazelyan, M. M. Drabkin, *et al.*, Fiz. Plazmy **28**, 1032 (2002) [Plasma Phys. Rep. **28**, 953 (2002)].
19. N. L. Aleksandrov, E. M. Bazelyan, R. B. Carpenter, Jr., *et al.*, in *Proceedings of XXVI International Conference on Physics of Ionized Gases, Greifswald, 2003*, Vol. 4, p. 19.
20. E. M. Bazelyan and Yu. P. Raizer, *Lightning Physics and Lightning Protection* (Nauka, Moscow, 2001; IOP, Bristol, 2000).
21. P. Lalande, A. Bondiou-Clergerie, G. Bacchiega, and I. Gallimberti, C. R. Physique **3**, 1375 (2002).
22. N. L. Aleksandrov, E. M. Bazelyan, and Yu. P. Raizer, in *Proceedings of the 26th International Conference on Lightning Protection, Cracow, 2002*, Vol. 1, p. 279.

23. N. L. Aleksandrov, E. M. Bazelyan, and Yu. P. Raizer, in *Proceedings of the 12th International Conference on Atmospheric Electricity, Versailles, 2003*, Vol. 2, p. 451.
24. V. A. Rakov and M. A. Uman, *Lightning: Physics and Effects* (Cambridge Univ. Press, Cambridge, 2003).
25. É. M. Bazelyan, B. N. Gorin, and V. I. Levitov, *Physical and Engineering Principles of Lightning Protection* (Gidrometeoizdat, Leningrad, 1978).
26. N. L. Aleksandrov, E. M. Bazelyan, F. D'Alessandro, and Yu. P. Raizer, in *Proceedings of the 27th International Conference on Lightning Protection, Avignon, 2004*, Vol. 1, p. 427.
27. N. L. Aleksandrov, E. M. Bazelyan, R. B. Carpenter, Jr., *et al.*, in *Proceedings of the 27th International Conference on Lightning Protection, Avignon, 2004*, Vol. 1, p. 407.
28. D. Mackerras, M. Darveniza, and A. C. Liew, IEEE Proc. Sci. Meas. Technol. **144**, 1 (1997).
29. I. D. Chalmers, J. C. Evans, and W. H. Siew, IEEE Proc. Sci. Meas. Technol. **146**, 57 (1999).
30. N. L. Aleksandrov, E. M. Bazelyan, R. B. Carpenter, Jr., *et al.*, in *Proceedings of IX Symposium on Gaseous Dielectrics, Ellicott City, 2002*, Ed. by L. G. Christophorou and J. K. Olthoff (Plenum, New York, 2002), p. 149.
31. G. Carrara and L. Thione, in *Proceedings of the IEEE Summer Meeting, 1974*, Paper CH 0910-0-PWR.41.
32. G. Carrara and L. Thione, IEEE Trans. Power App. Syst. **95**, 512 (1976).
33. É. M. Bazelyan, Elektrichestvo, No. 7, 22 (1977).
34. B. N. Gorin and A. V. Shkilev, Elektrichestvo, No. 2, 29 (1974).
35. C. B. Moore, G. D. Aulich, and W. Rison, Geophys. Res. Lett. **27**, 1487 (2000).
36. C. B. Moore, W. Rison, J. Mathis, and G. Aulich, J. Appl. Meteorol. **39**, 593 (2000).

*Translated by N.N. Ustinovskiĭ*